Structural and biophysical investigation of +TIPs in yeast and -TIPs in higher eukaryotes

Inauguraldissertation

zur
Erlangung der Würde eines Doktors der Philosophie
vorgelegt der
Philosophisch-Naturwissenschaftlichen Fakultät
der Universität Basel

von

Marcel Mateo Stangier

aus Frankfurt am Main, Deutschland

Basel, 2018

Originaldokument gespeichert auf dem Dokumentenserver der Universität Basel
edoc.unibas.ch

Genehmigt von der Philosophisch-Naturwissenschaftlichen Fakultät
auf Antrag von

Prof. Dr. Michel Steinmetz, Prof. Dr. Timm Maier

Basel, den 13.11.2018

Prof. Dr. Martin Spiess
Dekan

Table of Contents

Table of Contents .... **III**
Abbreviations .... **IV**
Summary .... **V-VI**
Zusammenfassung .... **VII-VIII**
1. Introduction **1-29**
  1.1 The cytoskeleton 1-2
  1.2 Microtubules 2-9
    1.2.1 Introduction into microtubules 2-6
    1.2.2 Dynamics of microtubules 4-6
    1.2.3 Structural details of tubulin and microtubules 6-8
    1.2.4 Microtubule associated proteins (MAPs) and ligands 8-9
  1.3 Microtubule plus-end tracking proteins (+TIPs) 9-18
    1.3.1 Overview of +TIPs 10-13
    1.3.2 The +TIP Bik1 in yeast 13-15
    1.3.3 Further + TIPs in yeast 15-18
  1.4 Kinesins 18-25
    1.4.1 Introduction into kinesins 18-20
    1.4.2 Regulation of microtubule dynamics by kinesins 20-22
    1.4.3 The kinesin Kip2 in yeast 22-23
    1.4.4 The kinesin Kip3 in yeast 23-24
  1.5 Microtubule minus-end tracking proteins (-TIPs) 25-27
    1.5.1 Overview of -TIPs 25
    1.5.2 The -TIP CAMSAP 25-27
  1.6 Aim of this thesis 27-29
2. Structure-function relationship of the Bik1-Bim1 complex **30-49**
  2.1 Declaration of contribution 32
  2.2 Publication 33-49
3. The kinesin Kip2 acts as a microtubule polymerase at plus-ends **50-80**
  3.1 Declaration of contribution 52
  3.2 Draft of the manuscript 53-80
4. Characterization of the tubulin-binding domain of Kip3 .... **81-104**
  4.1 Declaration of contribution 82
  4.2 Draft of the manuscript 83-104
5. A structural model for microtubule minus-end recognition by CAMSAPs **105-151**
  5.1 Declaration of contribution 106
  5.2 Publication 107-151
6. Conclusion and outlook **152-164**
  6.1 The +TIP network in yeast with Bik1 as a major contributor 153-156
  6.2 The kinesins Kip2 and Kip3 in the regulation of microtubule dynamics 156-161
  6.3 Emerging regulation of the minus-end by -TIPs as CAMSAPs 161-163
  6.4 Final outlook 163-164
7. Further manuscripts in preparation **164**
8. References **165-173**
9. Acknowledgments **174**

Abbreviations

ADP	Adenosine diphosphate
ASPM	Abnormal spindle-like microcephaly-associated protein
ATP	Adenosine triphosphate
Bim1	Binding to microtubules 1
Bik1	Bilateral karyogamy defect 1
CAMSAP	Calmodulin-regulated spectrin-associated
CAP-Gly domain	Cytoskeleton-associated protein-glycine-rich domain
CD spectroscopy	Circular dichroism spectroscopy
CENP-E	Centromere protein E
CH domain	Calponin homology domain
CKK	C-terminal domain common to CAMSAP1, KIAA1078 and KIAA1543
CPAP	Centrosomal P4.1-associated protein
Cryo-EM	Cryogenic electron microscopy
DARPin1	Designed ankyrin repeat protein 1
DTT	Dithiothreitol
EB	End-binding protein
EBH domain	End binding homology domain
EGTA	Ethylene glycol-bis(β-aminoethyl ether)-N,N,N′,N′-tetraacetic acid
F-actin	Filamentous actin
G-actin	Globular actin
GDP	Guanosine diphosphate
GFP	Green fluorescent protein
GTP	Guanosine triphosphate
HEPES	(4-(2-hydroxyethyl)-1-piperazineethanesulfonic acid)
IPTG	Isopropyl β-D-1-thiogalactopyranoside
ITC	isothermal titration calorimetry
Kar9	Karyogamy protein KAR9
K_D	Dissociation constant
MALS	Multi angle light scattering
MAP	Microtubule-associated protein
PIPES	Piperazine-N,N′-bis(2-ethanesulfonic acid)
RB3	Stathmin-Like-Protein RB3
SAXS	Small-angle X-ray scattering
SEC	Size exclusion chromatography
TCEP	Tris(2-carboxyethyl)phosphin
Tris	Tris(hydroxymethyl)-aminomethan
TOG domain	Tumor Overexpressed Gene domain
+TIPs	Microtubule plus-end tracking proteins
-TIPs	Microtubule minus-end tracking proteins
XMAP215	Xenopus microtubule associated protein 215 kDa

Summary

In eukaryotic cells, microtubules represent a highly dynamic protein filament system that is involved in cellular processes as cell division or transport of cargo. Microtubules oscillate between growth and shrinking, and the switch between these states is caused by catastrophe and rescue events. The building block of microtubules is the heterodimer tubulin, which polymerizes into tubular structures and switches from a curved state in the soluble form to a straight state in microtubules. Due to the polarity of tubulin, microtubules feature a plus-end and a minus-end. The highly dynamic plus-end is regulated by the plus-end tracking proteins (+TIPs). Certain +TIPs can function as a microtubule polymerase or rescue shrinking microtubules. Since budding yeast contains only a small number of microtubules, this organism is predestinated to study +TIPs and microtubule dynamics by microscopy on the system level.

The exact function and mechanism of yeast +TIPs such as Bik1 remain unresolved. In addition, it is unexplained how kinesins such as Kip2 or Kip3 can act as a microtubule polymerase or rescue factor. In my thesis, the budding yeast +TIPs Bik1, Kip2 and Kip3 were investigated to understand the role of these proteins in the formation of the +TIP network and how these proteins are capable of influencing microtubule dynamics. Recently, it has been discovered that minus-end tracking proteins (-TIPs) recognize the minus-end in cells such as neuronal cells. However, it is enigmatic how -TIPs target the microtubule minus-end. In order to elucidate the mechanism how -TIPs track the minus-end, my work focused on the discovered first -TIP class of CAMSAPs. In all projects, biophysical methods were applied, and besides for Kip2 crystal structures were determined to unravel mechanistic details of the proteins.

In budding yeast, Bik1 plays an important role especially in the dynein pathway, which is one of two major pathways for spindle positioning. Bim1 localizes Bik1 to the microtubule plus-end because Bik1 cannot autonomously track the plus-end. Here, we biophysically and structurally describe the interaction of the Bik1 CAP-Gly domain with the C-terminal tail of the +TIP Bim1. The crystal structure of the complex showed that Bik1 CAP-Gly binds specifically to C-terminal phenylalanine residues with a different binding mode compared to CAP-Gly domains of higher eukaryotes. Based on the structure, two different mutants were conceived to perturb the Bik1-Bim1 interaction. Then, the effect of this perturbation on Bik1 localization, microtubule length and Kar9 function was analyzed in yeast cells. Besides, we proved that the coiled-coil of Bik1 interacts with the C-terminal tail of microtubule polymerase Stu2, establishing Bik1 as an adaptor protein between Bim1 and Stu2.

Apart from Bim1, the budding yeast kinesin Kip2 also has the ability to transport Bik1 to the plus-end. We biophysically characterized the interaction of the Bik1 coiled-coil with the Kip2 coiled-coil. The C-terminal unstructured part of Kip2 turned out to be essential for the Bik1-Kip2 interaction, allowing an elegant way to disrupt this interaction without removing the Kip2 coiled-coil. In addition, Kip2 functions as a microtubule polymerase. By studying the interaction of the Kip2 motor domain with soluble tubulin, we were able to postulate a mechanism how Kip2 can polymerize microtubules. Furthermore, we identified the importance of the Bik1-Kip2 interaction for the polymerase activity.

The budding yeast kinesin Kip3 can depolymerize microtubules but exhibits the ability to rescue them as well. The N-terminal motor domain of Kip3 is responsible for the depolymerization activity. We discovered that Kip3 possesses a C-terminal tubulin-binding domain (TBD), followed by a weak microtubule-binding domain. The crystal structure of the Kip3 TBD was solved, and a sophisticated assembly of alpha-helices was revealed. Furthermore, the combination of the Kip3 motor domain together with the Kip3 TBD was identified as the minimal construct that can rescue microtubules. Therefore, we proposed that the Kip3 motor domain can also act as an anchor at the microtubule plus-end so that the Kip3 TBD can fulfill its rescue function by either increasing the tubulin concentration or facilitating the exchange of tubulin.

Most microtubules minus-ends are attached to the centrosome. However, some microtubules can occur with free minus-ends because not all microtubules are attached to the centrosome or cells such as neuronal cells entirely lack the centrosome. Thus, -TIPs like CAMSAPs can stabilize these free minus-ends. CAMSAP proteins have a CKK domain that can autonomously track the microtubule minus-end. In this study, we determined the crystal structure of this CKK domain. Our collaborator used this structure for fitting into a cryo-EM map of microtubules decorated by the CKK domain. Combined with other experimental results, we found that the CKK domain recognizes a unique curved state of tubulin that only occurs at the microtubule minus-end.

Overall, important insights into the mechanisms of Bik1 Kip2, Kip3 and CAMSAP were obtained. In the +TIP network, the understanding of Bik1 as a critical adaptor protein was considerably increased. Furthermore, we revealed new insights into the function of Kip2 as a microtubule polymerase. For Kip3, a mechanism for its microtubule rescue function was postulated. In the case of CAMSAP, it was discovered how this protein can recognize the microtubule minus-end. This represents the first described mechanism of a -TIP.

Zusammenfassung

In eukaryotischen Zellen stellen die Mikrotubuli ein extrem dynamisches System dar, welches in zelluläre Prozesse wie die Zellteilung oder Transportvorgängen involviert ist. Mikrotubuli oszillieren zwischen einem wachsenden und schrumpfenden Zustand. Der Übergang zwischen diesem Zustand wird durch Catastrophe und Rescue Ereignisse verursacht. Der Baustein von Mikrotubuli ist das Protein Tubulin, das polar in tubuläre Strukturen polymerisiert. Dabei wechselt es von einem „curved" Zustand in der löslichen Form in eine „straight" Konformation in den Mikrotubuli. Aufgrund der Polarität weisen Mikrotubuli ein Plus-End und ein Minus-End auf. Das sehr dynamische Plus-End wird reguliert durch sogenannte Plus-End tracking Proteins (+TIPs). Da S. cerevisiae nur eine geringe Anzahl an Mikrotubuli aufweist, ist dieser Organismus prädestiniert +TIP, um die Dynamik von Mikrotubuli mittels Mikroskopie zu untersuchen. Kürzlich ist entdeckt worden, dass sogenannte Minus-End tracking Proteins (-TIPs) das Minus-End in Zellen wie neuronalen Zellen erkennen können.

Die exakte Funktion und der Mechanismus von +TIPs wie Bik1 sind ungeklärt. Daneben ist es rätselhaft, auf welche Weise Kinesine wie Kip2 oder Kip3 Mikrotubuli polymerisieren oder Rescue-Events bewirken können. In meiner Promotion wurden die +TIPs Bik1, Kip2 und Kip3 des Organismus S. cerevisiae untersucht, um die Rolle dieser Proteine im +TIP network zu verstehen. Darüber hinaus waren wir interessiert, wie diese Proteine die Dynamik von Mikrotubuli beeinflussen können. Um den Mechanismus aufzuklären, wie -TIPs das Minus-End identifizieren können, wurde die Arbeit auf die erste entdeckte -TIP Gruppe der CAMSAP Proteine fokussiert. In allen Projekten wurden biophysikalische Methoden wie MALS oder ITC eingesetzt und außer für das Kip2 Projekt wurden Kristallstrukturen bestimmt, um die Mechanismen der Proteine zu entschlüsseln.

In S. cerevisiae spielt das +TIP Bik1 besonders eine wichtige Rolle im Dynein Pathway, welcher einer der zwei Pathways für die Positionierung der Spindel ist. Bim1 lokalisiert Bik1 an das Mikrotubuli Plus-End, weil Bik1 dieses nicht autonom verfolgen kann. In dieser Arbeit beschreiben wir mit biophysikalischen Methoden und Röntgenkristallographie die Interaktion der Bik1 CAP-Gly Domäne mit dem C-terminalen Tail des +TIP Bim1. Die Kristallstruktur des Komplexes zeigte, dass Bik1 spezifisch C-terminale Phenylalaninreste bindet mit einem anderen Bindungsmodus im Vergleich zu den CAP-Gly Domänen in höheren Eukaryoten. Basierend auf der Struktur des Komplexes wurden zwei Mutanten entworfen, um die Interaktion zwischen Bik1 und Bim1 zu inhibieren. Anschließend wurde der Effekt dieser Pertubation auf die Bik1 Positionierung, die Länge der Mikrotubuli und Kar9-Funktion analysiert. Daneben konnten wir beweisen, dass die

Coiled-coil Domäne von Bik1 mit dem C-terminalen Tail der Mikrotubuli-Polymerase Stu2 interagiert und damit konnte Bik1 als Adaptorprotein zwischen Bim1 und Stu2 etabliert werden

Abgesehen von Bim1 besitzt auch das S. cerevisiae Kinesin Kip2 die Fähigkeit, Bik1 zu dem Mikrotubuli Plus-End zu transportieren. Mittels biophysikalischer Methoden charakterisierten wir die Interaktion des Bik1 Coiled-coil mit dem Kip2 Coiled-coil. Es stellte sich heraus, dass die C-terminale unstrukturierte Region von Kip2 essentiell für die Interaktion mit Bik1 ist. Dies erlaubte uns auch die Interaktion aufzuheben, ohne den Kip2 Coiled-coil zu entfernen. Zusätzlich fungiert Kip2 als Mikrotubuli-Polymerase. Durch die Untersuchung der Interaktion der Kip2 Motordomäne mit löslichem Tubulin konnten wir einen Mechanismus postulieren, wie Kip2 Mikrotubuli polymerisieren kann. Des Weiteren wurde die Wichtigkeit der Bik1-Kip2 Interaktion für die Polymeraseaktivität erkannt.

Das S. cerevisiae Kinesin Kip3 kann Mikrotubuli depolymerisieren, besitzt aber auch die Fähigkeit sogenannte Rescue-Events hervorzurufen. Die N-terminale Motordomäne des Proteins Kip3 bewerkstelligt die Depolymeraseaktivität. Wir entdeckten, dass Kip3 eine C-terminale Tubulin-Binding Domain (TBD) besitzt, der eine Domäne für die Bindung von Mikrotubuli folgt. Die Kristallstruktur der Kip3 TBD wurde gelöst und die Struktur enthüllte eine komplexe Anordnung von alpha-Helices. Darüber hinaus wurde die Kombination der Kip3 Motordomäne und der Kip3 TBD als das minimale Konstrukt identifiziert, welches in der Lage ist, Rescue-Events zu bewirken. Aus diesem Grund schlagen wir vor, dass die Kip3 Motordomäne als Anker fungieren kann, so dass die Kip3 TBD die Rescue-Events verursachen kann. Dies könnte durch die Erhöhung der lokalen Tubulinkonzentration oder dem Austausch von Tubulin innerhalb der Mikrotubuli passieren.

Die meisten Mikrotubuli Minus-Ends sind an das Zentrosom verankert. Trotz dessen existieren manche Miktrotubuli mit freien Minus-Ends und bestimmten Zellen, wie neuronalen Zellen, fehlt das Zentrosom. Darum sind -TIPs wie CAMSAPs in der Lage, diese freien Minus-Ends zu stabilisieren. CAMSAP Proteine weisen eine CKK-Domäne auf, die in der Lage ist, autonom das Minus-End zu verfolgen. In dieser Arbeit wurde die Kristallstruktur der CKK-Domäne determiniert. Unser Kooperationspartner nutzte diese Struktur für die Platzierung in einer Cryo-EM Map von Miktrotubuli, die mit der CKK-Domäne dekoriert waren. Zusammen mit anderen experimentellen Ergebnissen fanden wir heraus, dass die CKK-Domäne einen einzigartigen „curved“ Zustand von Tubulin erkennt, der nur am Miktrotubuli Minus-End auftritt.

Insgesamt wurden wichtige Erkenntnisse für die Proteine Bik1, Kip2, Kip3 und CAMSAP gewonnen.

1. Introduction

1.1 The cytoskeleton

Living cells perform fascinating processes such as cell division and can differentiate into highly different shapes. Therefore, the elucidation of the factors responsible for processes like cell division has fascinated biologists and biochemists for over 100 years (Frixione, 2000). In 1903, Nikolai K. Koltsov conceived the idea that cells exhibit a kind of skeleton responsible for the shape of cells (Gordon and Gordon, 2017). The term cytoskeleton was introduced by Paul Wintrebert in 1931 (Zampieri et al., 2014). Each cell possesses a cytoskeleton, which represents a complex and dynamic network of various components. The cytoskeleton of cells participates in such diverse processes as cell division, cell polarity, cell motility, maintenance of mechanical properties of cells and endocytosis (Bezanilla et al., 2015; Huber et al., 2013). In eukaryotic cells, the cytoskeleton can be divided into actin filaments, intermediate filaments and microtubules (Figure 1.1) (Fletcher and Mullins, 2010). Each of these components can form long polymers by polymerization of their distinct subunits. Actin filaments, which are also called microfilaments, are assembled from the subunit actin, which polymerizes into filaments of 8 nm diameter (Blanchoin et al., 2014). On the other hand, intermediate filaments consist of various proteins but are also filamentous structures of around 11 nm diameter (Herrmann and Aebi, 2016). In contrast, the subunit of microtubules, tubulin, polymerizes into tubular structures, which have a diameter of around 25 nm (Desai and Mitchison, 1997). All three groups of the cytoskeleton are regulated by a large number of specific proteins, which can, for instance, increase the rate of polymerization (Huber et al., 2013). Prokaryotic cells feature three similar major components of the cytoskeleton, which are related to the eukaryotic elements (Erickson, 2007).

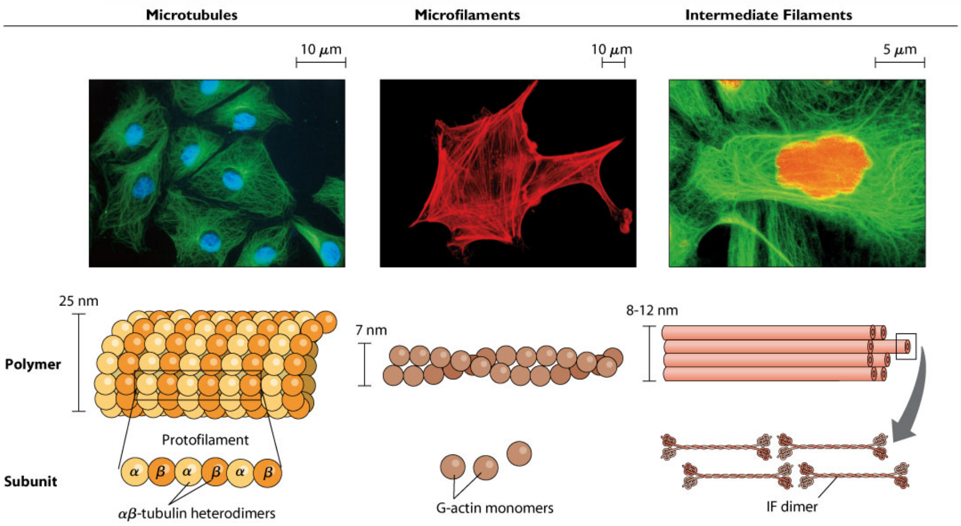

Figure 1.1 Overview of the cytoskeletal components.

Representations of microtubules, microfilaments (actin filaments) and intermediate filaments. Upper part: eukaryotic cells were immuno-stained to display the respective cytoskeletal component. Lower part: the composition of the respective cytoskeletal component is illustrated. Figure taken from (Hardin et al., 2012).

The actin filaments are primarily involved in cell motility, cytokinesis, maintenance of cell morphology, cell division and contraction of muscles (Blanchoin et al., 2014; Winder and Ayscough, 2005). An actin filament (F-actin) consists of the ATPase actin, a 42 kDa large α-helical protein, which assembles into double-stranded filaments and is described as the most common protein in mammalian cells (Blanchoin et al., 2014; Dominguez and Holmes, 2011). Unpolymerized actin (G-actin) contains mainly ATP, which is hydrolyzed after the incorporation of G-actin into filaments (Dominguez and Holmes, 2011). F-Actin exhibits a growing barbed end where further ATP-bound G-actin is added. In addition, the filaments feature a shrinking pointed end that is characterized by the removal of ADP-bound G-actin (Lee and Dominguez, 2010). Therefore, F-actin is a polar polymer, and a so-called treadmilling state of F-actin can occur when the growth rate at the barbed end matches the shrinkage rate of the pointed end. The polymerization of F-actin can be regulated by various actin-binding proteins (Blanchoin et al., 2014). Moreover, the protein formin can promote the nucleation of F-actin (Dominguez and Holmes, 2011), and the protein complex Arp2/3 is capable of inducing the formation of branched F-actin (Davidson and Wood, 2016).

In contrast to actin filaments and microtubules, intermediate filaments are composed of various proteins that are encoded by over 70 genes (Herrmann et al., 2009). These proteins share a common domain organization in the form of long coiled-coils domains (Herrmann and Aebi, 2016). Depending on the cell type, the composition of the intermediate filaments varies greatly. As an example, the large family of keratins in epithelial cells can be mentioned. Intermediate filaments represent non-polar polymers. Since their diameter ranges between the diameters of the other cytoskeleton groups (Herrmann and Aebi, 2016), they were termed intermediate filaments. They are mainly involved in ensuring cell plasticity and can function as stress absorbers as well. The polymerization of intermediate filaments takes place in three consecutive phases. First, eight tetramers of the respective component laterally associate into so-called unit-length filaments (ULF) (Herrmann et al., 2009). Afterward, the ULFs bind longitudinally to each other by end-to-end assembly so that filaments are formed. In the last phase, the filaments undergo compaction, in which the diameter shrinks from 17 nm to 11 nm (Herrmann and Aebi, 2016).

1.2 Microtubules

After a short overview of actin filaments and intermediate filaments, this chapter will introduce microtubules, their dynamic behavior, the structure of tubulin and the structural organization of microtubules. Moreover, proteins and ligands interacting with tubulin or microtubules will be described.

1.2.1 Introduction into microtubules

Microtubules are crucial for cell division, in which they form a key component of the mitotic spindle (Forth and Kapoor, 2017). Furthermore, they play a major role as tracks for transporting proteins, as an integral component of cilia and for obtaining cell polarity (Forth and Kapoor, 2017; Ishikawa and Marshall, 2013; Li and Gundersen, 2008). In the 1950s, researchers discovered microtubules by transmission electron microscopy when they observed these long filaments in the cell (Brinkley, 1997). The term “microtubules” originated in 1963 after improvements in sample fixation that enhanced the quality of electron microscopy studies of cells. At this time, it was observed that microtubules are ubiquitous in all eukaryotic cells, and first proofs for their tubular structure were obtained. Microtubules consist of the protein tubulin, which is a heterodimer of the two approximately 50 kDa large subunits α- and β-tubulin (Nogales, 2000). Gary Borisy and other researchers identified tubulin in 1967 by searching for the protein that binds to the cell division-inhibiting drug colchicine (Wells, 2005). This research was mainly motivated by the aim of understanding cell division and the mitotic spindle.

Tubulin heterodimers polymerize into microtubules, which are linear and polar protofilaments with the tubulin packed in a 25 nm wide hollow cylindrical arrangement (Desai and Mitchison, 1997). In order to assemble this structure, tubulin needs to interact both laterally and longitudinally with other tubulins (Brouhard and Rice, 2018). Furthermore, unpolymerized tubulin can be called “soluble” or “free” tubulin. In vitro assembled microtubules from mammalian brain tubulin consist of 10-15 protofilaments, but the majority exhibits 14 protofilaments (Chaaban and Brouhard, 2017). However, in most cell types, 13 protofilaments form microtubules because this number is determined by the γ-tubulin ring complex, which acts as a nucleation factor (Kollman et al., 2011). In addition, the 13 protofilaments represent the only geometry that permits a straight assembly of protofilaments because other numbers of protofilaments result in a supertwist (Chaaban and Brouhard, 2017). The polarity of microtubules is achieved by the head-to-tail binding of the tubulin heterodimers so that each β-subunit of tubulin longitudinally attaches to an α-subunit of tubulin (Desai and Mitchison, 1997). Due to the polarity, the two ends of a microtubule polymer are not equivalent. Inside cells, it was observed that one end of microtubules can grow considerably faster than the other end (Howard and Hyman, 2003). The so-called plus-end is the fast-growing end, in which the β-subunits are exposed (Akhmanova and Steinmetz, 2015). The other slow-growing end was named minus-end, and on this side, the α-subunits are exposed (Desai and Mitchison, 1997). Besides a growing state, both ends can also shrink. α-Tubulin laterally associates with α-tubulin, and the same applies to β-tubulin. However, in the 13 protofilaments, a seam occurs where α-tubulin binds β-tubulin in the lateral interaction and vice versa (Kollman et al., 2011).

1.2.2 Dynamics of microtubules

Both α- and β-tubulin are GTPases (Howard and Hyman, 2003). The GTP in the α-subunit normally remains non-hydrolyzed. In contrast, the GTP in the β-subunit can be hydrolyzed easily after the incorporation of tubulin into microtubules, leading to GDP-bound tubulin (Nogales, 2000) (Figure 1.2). At the ends of microtubules, the level of bound GTP is significantly higher compared to within microtubules because tubulin heterodimers attach to the ends with the β-subunit in the GTP-bound state (Brouhard, 2015). Therefore, the ends maintain a so-called "GTP cap" (Mitchison and Kirschner, 1984). This GTP cap is a distinct feature that helps proteins to recognize the ends of microtubules (Akhmanova and Steinmetz, 2015).

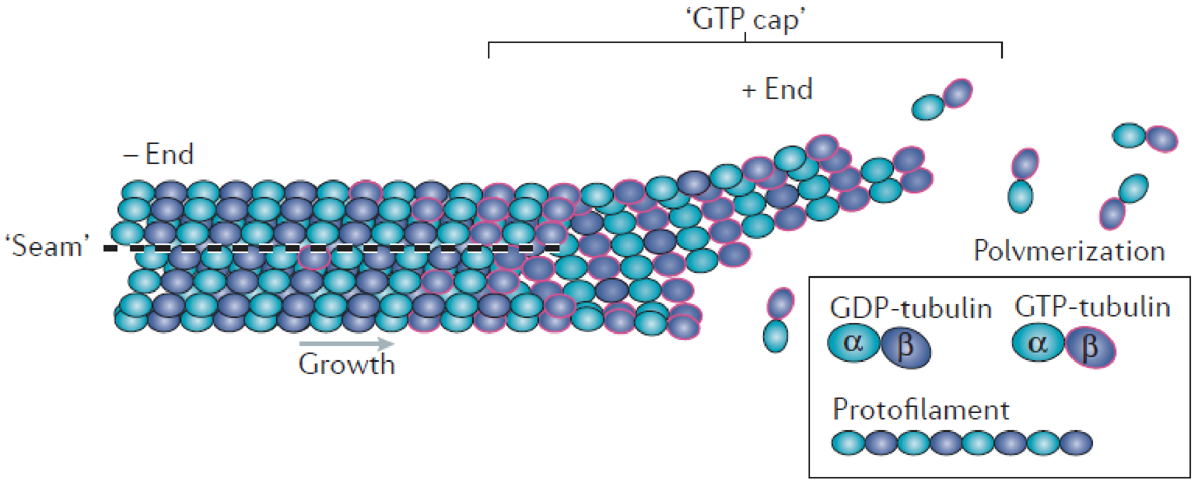

Figure 1.2 Illustration of the growth of microtubules.
Soluble GTP-bound tubulin is added to the microtubule plus-end. In addition, the seam and the GTP cap are displayed. Figure adapted from (Roostalu and Surrey, 2017).

In in vitro experiments, microtubules are capable of growing from both ends with a faster growth rate of the plus-end (Akhmanova and Hoogenraad, 2015). Since microtubules are polar polymers, there exists a difference between the plus-end and the minus-end. The exposure of the β-tubulin and further features of the plus-end seem to permit a faster growth rate of the plus-end than the minus-end when the GTP cap is present (Tran et al., 1997). Inside cells, the minus-end of microtubules is static due to its attachments to the γ-tubulin at the centrosome (Kollman et al., 2011). In vitro, the minus-end with a GTP cap grows slower due to differing properties of this end such as the exposure of α-tubulin instead of β-tubulin (Tran et al., 1997).

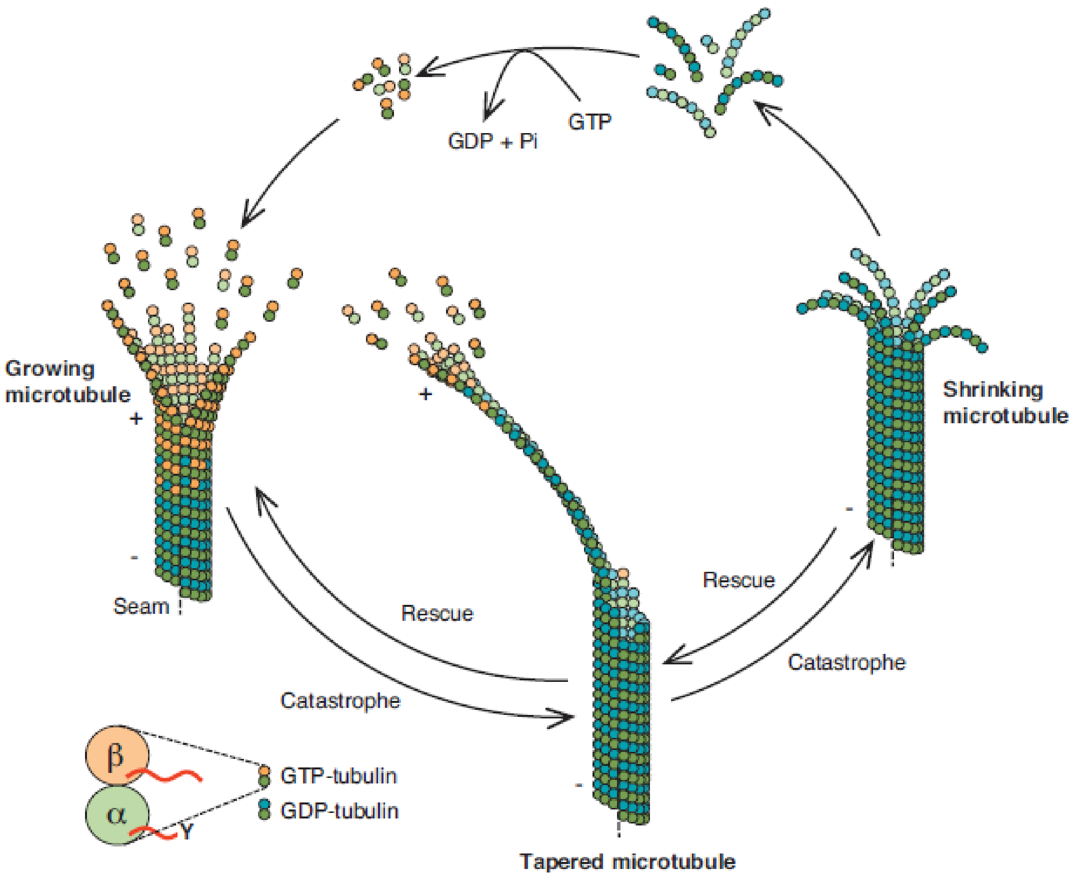

Figure 1.3 Illustration of the dynamic instability of microtubules.
Microtubules oscillate between a growing and a shrinking state. The transitions between these two states are termed as "catastrophe" and "rescue". Growing microtubules exhibit GTP-bound tubulin at their ends. In contrast, shrinking microtubules contain GDP-bound tubulin at their ends. Figure taken from (Aher and Akhmanova, 2018).

Due to the hydrolysis of GTP and the polarity of microtubules, it was assumed that microtubules would exist primarily in a treadmilling state that was observed for actin filaments (Desai and Mitchison, 1997) because the minus-end can be released from the centrosome and can shrink. This would mean that approximately the same amount of GTP-bound tubulin would bind to the plus-end as GDP-bound tubulin is disassembled from the minus-end. However, this was in stark contrast to experimental evidence because the treadmilling behavior was nearly never observed. Based on experimental observations, a new model was proposed that microtubules mainly switch between extended phases of polymerization and depolymerization (Figure 1.3) (Brouhard, 2015; Mitchison and Kirschner, 1984). This change of state can occur both at the plus-end and the minus-end (Akhmanova and Hoogenraad, 2015). In addition, the spontaneous loss of the GTP cap can induce the rapid shrinkage of the plus-end, also called "catastrophe" (Brouhard and Rice, 2018). Sometimes these rapidly shrinking microtubules are "rescued" by proteins, and they start to grow again. In addition, small islands of GTP-bound to β-tubulin within the microtubule lattice could be responsible for rescue events (Gardner et al., 2013). Overall, the oscillating behavior of microtubules between growth, shrinkage, catastrophe and rescue was termed as "dynamic instability" and is supposed to be an important mechanism by which microtubules can fulfill their various roles like the segregation of chromosomes (Aher and Akhmanova, 2018; Brouhard and Rice, 2018). The plus-end appears to be much more dynamic because of its faster growth, but the loss of the GTP cap induces a faster shrinkage compared to the minus-end (Akhmanova and Hoogenraad, 2015; Akhmanova and Steinmetz, 2015).

1.2.3 Structure of tubulin and microtubules

To better understand the dynamic instability of microtubules, structural information of tubulin and microtubules was essential. Since microtubules are filamentous structures, they are not suitable for structural studies by X-ray crystallography. In the year 1998, the first structure of tubulin was obtained by electron crystallography of zinc-induced tubulin sheets (Nogales et al., 1998). This structure showed that both subunits of tubulin exhibit high similarity and can be superimposed well. Each tubulin subunit consists of two β-sheets that are composed of 6 or 4 strands surrounded by 12 α-helices (Figure 1.4). In addition, three different functional domains can be assigned to each monomer (Lowe et al., 2001; Nogales et al., 1998). The N-terminal domain (residues 1-205) features the fold of a nucleotide binding domain. This domain is followed by the intermediate domain (residues 206-381) and the C-terminal domain, which contains an important loop between helices 11 and 12 for the longitudinal contact to the next subunit in the protofilament (Nogales, 2000; Nogales et al., 1998). The last residues in the C-terminal domain were not visible in the structure because at the C-terminus the last residues are unstructured (Lowe et al., 2001). The GTP bound to α-tubulin is buried in the intradimer interface that connects longitudinally α-tubulin to β-tubulin. This explains why this GTP cannot be hydrolyzed. In contrast, the GTP or GDP bound to β-tubulin appears to be partially exposed in a free tubulin heterodimer (Nogales et al., 1998).

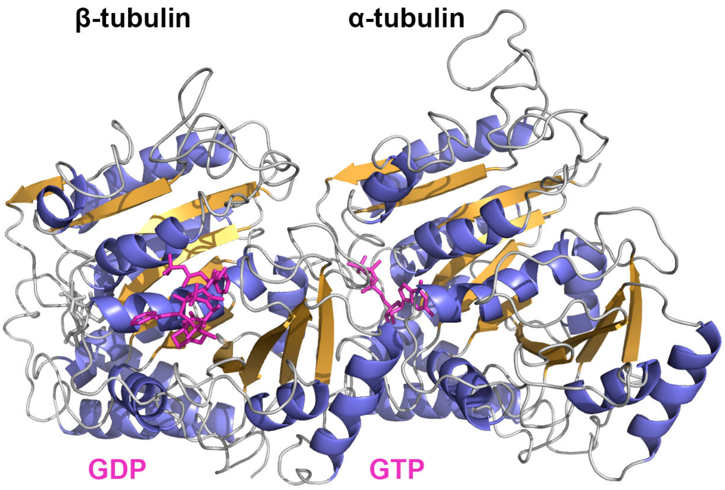

Figure 1.4 Electron crystallography structure of tubulin.
The α-helices and β-sheets are highlighted in blue and orange, respectively. In addition, the bound nucleotides are colored in magenta. The figure was prepared in PyMOL based on the PDB entry 1TUB.

Free tubulin turned out to be impossible to crystallize alone. However, in combination with proteins like stathmin that connects longitudinally two tubulin heterodimers and prevents polymerization, it became possible to co-crystallize the complex of tubulin and stathmin with a resolution of around 4 Å (Gigant et al., 2000). In addition, the structure of microtubules has been extensively investigated by cryo-EM (Figure 1.5). Recent cryo-EM structures have reached a resolution of around 4 Å, providing atomic resolution of microtubules (Zhang et al., 2015).

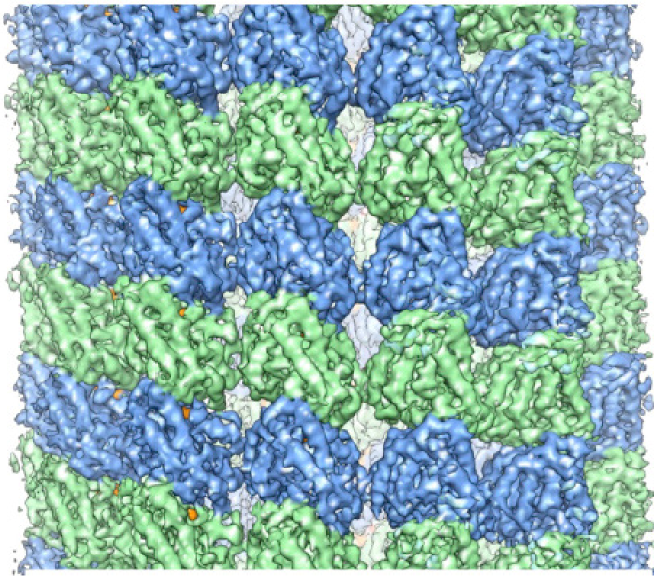

Figure 1.5 Cryo-EM structure of a microtubule.
The cryo-EM structure of a microtubule at a resolution of 4.7 Å shows the arrangement of the tubulin heterodimers inside microtubules in which tubulin exists in the straight conformation. The longitudinal and lateral interactions between tubulin heterodimers (α-tubulin in blue and β-tubulin in green) can be observed. Figure taken from (Nogales and Scheres, 2015).

By comparing tubulin in the soluble state and in microtubules, it was discovered that the angle between the α-subunit and the β-subunit decreases from 11° to 0° degree (Brouhard and Rice, 2014; Pecqueur et al., 2012; Ravelli et al., 2004). Therefore, soluble tubulin is also described as curved tubulin. In microtubules, tubulin exists as "straight tubulin" (Akhmanova and Steinmetz, 2015). The assembly of microtubules requires that tubulin switches from the curved state to the straight state (Brouhard and Rice, 2018). Soluble tubulin is normally incorporated into microtubule ends in the GTP-bound state (Brouhard and Rice, 2014). The ends of microtubules are in general not blunt, but single protofilaments or several of them together protrude in a curved manner (Chretien et al., 1996; Guesdon et al., 2016). The tubulin that attaches to these tapered ends can initially remain in the curved state (Brouhard and Rice, 2014), and the transition to the straight state only happens after several protofilaments laterally connect (Brouhard and Rice, 2018; Guesdon et al., 2016). Due to this straightening, the tubulin heterodimer expands. After a while, the GTP bound to β-tubulin is hydrolyzed. This is accompanied by structural rearrangements inside the tubulin heterodimer that lead to compaction by the shortening of the length of the tubulin heterodimer. (Brouhard and Rice, 2018). Furthermore, this process incorporates strain into the lattice (Zhang et al., 2015). The induction of catastrophe is associated with the loss of the GTP cap, and this loss results in the relaxation of GDP-bound tubulin heterodimers back to the curved state due to the strain and their dissociation from the ends. This illustrates that both GTP-bound and GDP-bound tubulin can exist in the curved state (Brouhard and Rice, 2014). The angle of the curved GDP-bound tubulin amounts to 13°, which is slightly higher compared to the 11° of GTP-bound curved tubulin. In the case of straight GDP-bound tubulin, it is assumed that the strain in the microtubule lattice increases the probability of dissociation to release the strain by switching to the curved state. Overall, this process is not understood well because how this strain destabilizes the lattice is unknown (Brouhard and Rice, 2018). Similarly, a detailed understanding of the features of microtubule ends like their tapered structure is lacking. In addition, the ends can also be blunt, and how the characteristics of the ends are regulated needs further investigation.

1.2.4 Microtubule interacting proteins and ligands.

Microtubules represent an inherently dynamic system, and their dynamicity is regulated by a class of proteins interacting with them. These proteins allow cells to precisely control length and the growth/shrinkage rate of microtubules depending on the stage of the cell cycle and the individual cell type. A large group of these proteins is called microtubule-associated proteins (MAPs) (Amos and Schlieper, 2005). The first MAPs that have been discovered were copurified together with tubulin from mammal brains during the tubulin isolation. It was observed that these MAPs, which are also called structural MAPs, promote polymerization of microtubules and help to stabilize microtubules by binding along their lattice. (Mandelkow and Mandelkow, 1995). The group of structural MAPs consists of the twelve proteins MAP1A, MAP1B, MAP1S, MAP2-9 and tau (Tortosa et al., 2016), which is well known for its involvement in Alzheimer's disease (Wang and Mandelkow, 2016). Overall, neuronal cells primarily express these MAPs, and they are essential for neuronal microtubules. All these MAPs contain at least one microtubule-binding domain (Tortosa et al., 2016). Additionally, most of them feature a coiled-coil domain for dimerization. However, the mechanism of binding to the microtubule lattice differs among various MAPs. For instance, Map1b primarily binds via positively charged repeats in the unstructured N-terminal microtubule-binding domain to the negatively charged surface of microtubules (Amos and Schlieper, 2005). In contrast, MAP2 and the related tau protein interact with microtubules by four 18-residue long microtubule-binding repeats, which become structured upon binding with microtubules (Al-Bassam et al., 2002). Recently, a high-resolution cryo-EM structure of tau attached to microtubules has been reported (Kellogg et al., 2018). This structure showed that tau longitudinally binds across several tubulin heterodimers and tethers several of them together to reduce the dissociation rate of tubulin from microtubules. This structurally explains how tau can both stabilize microtubules and enhance polymerization.

Besides the previously discussed structural MAPs, four additional groups of proteins (Tortosa et al., 2016) belong to the family of MAPs of which various proteins will be described in detail in the next sections. The first group consists of the motor proteins kinesin and dynein, which walk along microtubules (Endow et al., 2010). The second group represents proteins that possess specificity for the growing microtubule plus-end (Akhmanova and Steinmetz, 2010). These proteins are called microtubule plus-end tracking proteins (+TIPs) and can regulate microtubule dynamics. To the third group proteins that assist in nucleation of microtubules or sever microtubules and the microtubule minus-end tracking proteins (-TIPs) are counted (Akhmanova and Hoogenraad, 2015). Finally, the fourth group contains proteins that post-translationally modify tubulin (Janke, 2014).

Both to free tubulin and tubulin in microtubules, various small molecules can bind, and they either stabilize microtubules or promote the depolymerization of them (Steinmetz and Prota, 2018). These microtubule-targeting agents (MTAs) are widely applied as cytotoxic agents in the therapy of cancer. Tubulin exhibits two sites for the interaction with microtubule-stabilizing agents (MSAs) (Steinmetz and Prota, 2018). The most prominent MSA represents the drug taxol that binds to the taxol site in β-tubulin and induces the formation of a short helix from the M-loop, which is normally unstructured in free tubulin (Prota et al., 2013). By the involvement of this helix in lateral contacts in microtubules, taxol stabilizes microtubules and promotes their polymerization. Due to their stability, taxol-stabilized microtubules are widely used in in vitro experiments of microtubules (Campbell and Slep, 2011). On the other hand, microtubule-destabilizing agents (MDA), which target four different sites in tubulin, inhibit the assembly of tubulin into microtubules and lead to microtubule depolymerization (Steinmetz and Prota, 2018). MDAs like colchicine keep tubulin in the curved state by preventing the transition to the straight state (Dorleans et al., 2009), or MDAs like eribulin preclude the longitudinal attachment of two tubulin heterodimers by blocking the inter-dimer interface on the surface of β-tubulin (Doodhi et al., 2016).

1.3 Microtubule plus-end tracking proteins (+TIPs)

This chapter will provide insights into the proteins that target the plus-end of microtubules with examples of these proteins in higher eukaryotes, followed by examples of these proteins in budding yeast.

1.3.1 Overview of +TIPs

Microtubule plus-end tracking proteins (+TIPs), which are a group of MAPs, specifically target the microtubule plus-end by recognizing of special features of the plus-end (Akhmanova and Steinmetz, 2010). Depending on the cell type and the stage of the cell cycle, microtubules have to change their length and dynamics to perform processes such as chromosome segregation. +TIPs can regulate the dynamics of microtubules by increasing or decreasing their growth/shrinkage rate and by inducing catastrophes or rescues.

Various members of +TIPs are capable of autonomously tracking the microtubule plus-end by sensing specific chemical or structural features such as the GTP cap or the curvature of tubulin (Akhmanova and Steinmetz, 2015). In contrast to this, the second class of +TIPs needs to interact with an autonomously tracking +TIP to be located to the plus-end. Therefore, they are also described as hitchhiking +TIPs, which can additionally interact with each other. The composition of +TIPs at the plus-end significantly changes depending on the cell cycle, and +TIPs can either compete for the same position or cooperate with each other. This illustrates that a highly dynamic network of various proteins is involved in controlling microtubule plus-end dynamics.

1.3.2 Examples of +TIPs in higher eukaryotes

+TIPs do not share a common domain and vary significantly in their length, domain organization and amount of unstructured parts. This indicates a high functional diversity (Akhmanova and Steinmetz, 2010). It is possible to classify +TIPs according to their function and domains/motifs that are found in the respective subgroup of TIPs. A very prominent protein family of +TIPs represents the so-called end-binding proteins (EBs) that autonomously localize to the microtubule plus-end by their N-terminal calponin homology (CH) domain (Slep and Vale, 2007). In addition, the CH domain is followed by a linker, a coiled-coil for dimerization and an EB-homology (EBH) domain, which consists of a four-helix bundle (Honnappa et al., 2005; Slep et al., 2005). At the C-terminus, an unstructured tail ending with a conserved EEY/T motif can be found. This motif and the EBH domain allow EBs to interact with other +TIPs and recruit them to the plus-end. In mammals, three different EBs are expressed (EB1, EB2 and EB3), whereas in yeast only one EB with the name Bim1 exists (Akhmanova and Steinmetz, 2015).

The crystal structure of the EB1 CH domain, which shares a high similarity with actin-binding CH domains, revealed that this domain is formed by six α-helices (Hayashi and Ikura, 2003). Two additional short helices are also present. Furthermore, crystal structures showed high conservation between the Bim1 and the EB1 CH domain (Slep and Vale, 2007). In addition, various positively charged residues were identified to be essential for microtubule binding. From cryo-EM structures of microtubules decorated with EBs, it was determined that the CH domain binds at the interface between four tubulin heterodimers (Figure 1.6) (Maurer et al., 2012) so that this domain is located between the protofilaments. The CH domain recognizes the nucleotide state of microtubules and preferentially binds close to the GTP cap (Maurer et al., 2012). In the past, it was believed that EBs target specifically the GTP cap, but recent research has elucidated that they sense a conformation of tubulin that occurs in a transient GTP hydrolysis state (Maurer et al., 2014; Zhang et al., 2015).

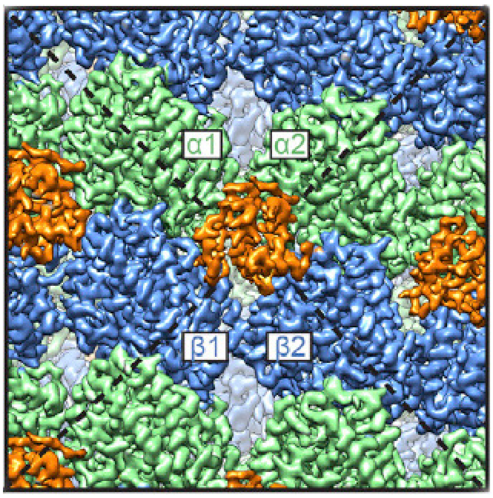

Figure 1.6 Illustration of the binding of EB3 to microtubules.
The cryo-EM map of microtubules decorated with EB3 is shown. The +TIP EB3 recognizes an interface that is formed by four tubulin dimers. Figure taken from (Zhang et al., 2015).

The binding of EBs to microtubules induces the hydrolysis of GTP-bound tubulin with the accompanied compaction of the microtubule lattice (Zhang et al., 2018). Therefore, EBs lead to an increased catastrophe frequency of microtubules in vitro (Maurer et al., 2014). In cells, EBs enhance the dynamics of microtubules as well (Rogers et al., 2002), but they also appear to promote the formation of longer microtubules (Komarova et al., 2009). This difference is not well understood (Akhmanova and Steinmetz, 2010). One hypothesis for such different behavior could be that the various proteins recruited by EBs lead overall to the increased length of microtubules in the cell. This highlights the importance of EB proteins as a hub to recruit various other +TIPs.

How different proteins sharing no obvious similarity can bind to EBs was solved by the discovery of the conserved SxIP peptide motif, which binds to the EBH domain of EBs (Akhmanova and Steinmetz, 2015; Honnappa et al., 2009). The amino acids of the SxIP motif form an extensive network of hydrogen bonds with the four-helix bundle of the EBH domain, and each EBH domain can bind to two SxIP motifs due to the symmetry of the EBH domain (Honnappa et al., 2009). Since EBs recruit already a peptide containing just the SxIP motif to the microtubule plus-end, this motif is also called a microtubule tip localization signal (MtLS) (Honnappa et al., 2009). In addition, the composition of the residues surrounding the SxIP motif influences the affinity of the SxIP motif to the EBH domain because positively charged residues such as arginine and lysine can interact with negatively charged residues of the EBH domain (Buey et al., 2012) so that certain proteins have a higher affinity for EBs. On the other hand, the phosphorylation of serines surrounding the SxIP motif decreases the binding affinity to the EBH domain (Honnappa et al., 2009). This allows cells to control which protein that harbors an SxIP motif primarily attaches to EBs depending on the stage of the cell cycle. Furthermore, it has been recently discovered that besides the SxIP motif a conserved LxxPTPh motif can interact with the EBH domain in a similar fashion (Kumar et al., 2017).

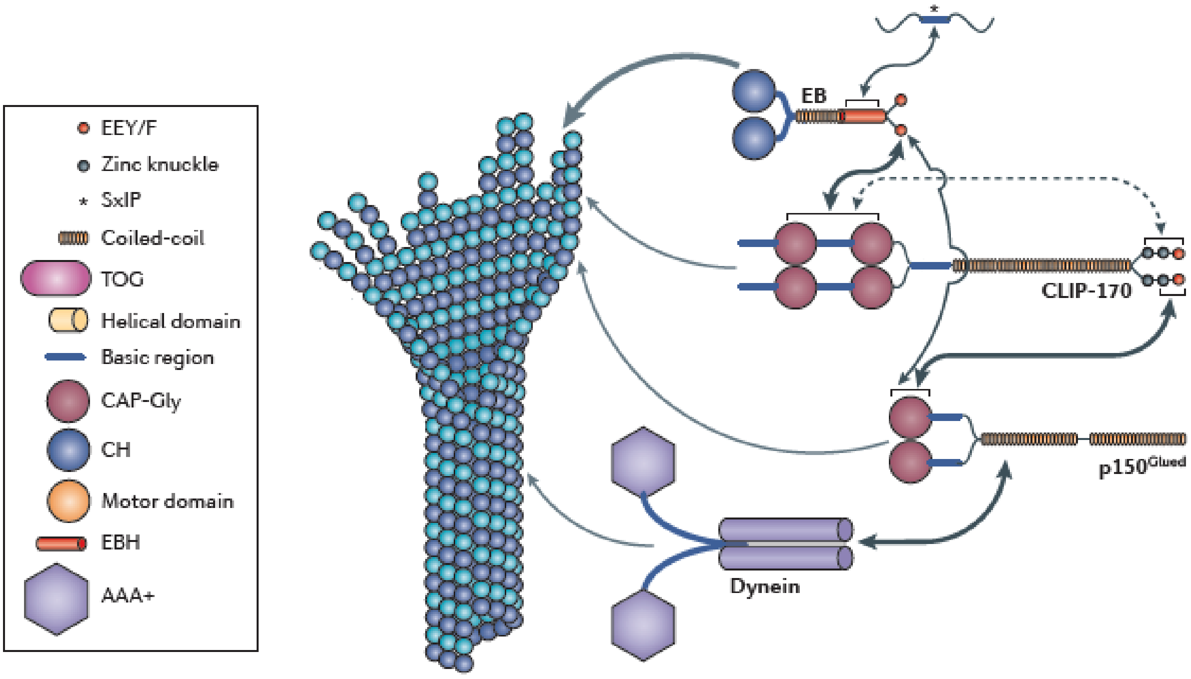

Figure 1.7 Schematic overview of various +TIPs in higher eukaryotes.
The +TIPs EB, CLIP-170, p150Glued, dynein and their interaction with each other and microtubules are displayed. Their domain organization is illustrated, and arrows show the interactions between the respective domains. Figure adapted from (Akhmanova and Steinmetz, 2015).

As the first reported +TIP, the mammalian cytoplasmic linker proteins (CLIP) with a molecular weight of 170 kDa can be mentioned (Perez et al., 1999). This protein is called CLIP-170 or CLIP1 and can act as a rescue factor for microtubules (Arnal et al., 2004). Moreover, it is involved in the targeting of dynein to microtubule plus-ends by the +TIP p150Glued. CLIP-170 belongs to the family of CLIPs that comprise four members. CLIP-170 consists of two N-terminal cytoskeleton-associated protein-glycine-rich (CAP-Gly) domains that are surrounded by positively charged linkers, followed by a long coiled-coil, two zinc knuckles and an EEY/F motif at the C-terminus (Figure 1.7) (Lansbergen et al., 2004). CAP-Gly domains form a highly twisted, antiparallel β-sheet, which encompasses five strands, surrounded by a small β-hairpin (Figure 1.8) (Steinmetz and Akhmanova, 2008). The large number of glycine residues in CAP-Gly domains is responsible for the loops connecting the β-strands (Figure 1.8). The +TIP p150Glued, which is a subunit of the dynactin complex, also possesses a CAP-Gly domain.

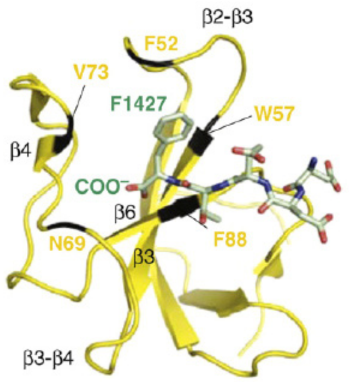

Figure 1.8 Structure of the p150Glued CAP-Gly domain in complex with an EEF peptide.
The p150Glued CAP-Gly domain structure shows the arrangement of β-sheets that is characteristic for CAP-Gly domains. Furthermore, the EEF peptide binds in a cavity of the CAP-Gly domain formed by β-sheets and loops. Figure taken from (Steinmetz and Akhmanova, 2008).

In addition, the CAP-Gly domains of the proteins CLIP-170 and p150Glued recognize the EEY/F motif of proteins such as EBs (Steinmetz and Akhmanova, 2008) The co-crystal structures of the CLIP-170 or p150Glued CAP-Gly domain with the EEY/F motif showed that the respective CAP-Gly domain binds the EEY/F motif via a cavity that contains a conserved GKDNG motif, which is essential for the binding (Honnappa et al., 2006; Weisbrich et al., 2007). The interaction with EBs targets CLIP-170 and p150Glued to the microtubule plus-end. A short construct of a single CLIP-170 CAP-Gly domain together with one positively charged unstructured linker can track the plus-end via binding to EBs (Gupta et al., 2009). Microtubules also feature EEY/F motifs at the C-terminus of α-tubulin so that proteins like CLIP-170 can decorate microtubules on their own and diffuse along them. However, the specificity for the plus-end is only achieved by binding to additional proteins like EBs. In the EEY/F motif, the aromatic residue is crucial for the binding of CAP-Gly domains because CLIP-170 does not directly interact anymore with detyrosinated microtubules (Peris et al., 2006). Interestingly, the +TIP p150Glued CAP-Gly domain can attach to the EEY/F motif of CLIP-170 (Weisbrich et al., 2007). In this interaction, the second zinc knuckle of CLIP-170 also participates in the binding to the p150Glued CAP-Gly domain. Overall, p150Glued can be recruited to EBs by CLIP-170 that can function as an adaptor.

1.3.3 The yeast +TIP Bik1

In the mating of yeasts, the word karyogamy defines the fusion of two haploid nuclei to a diploid nucleus (Kurihara et al., 1994). During research on mating, the protein bilateral karyogamy defect 1 (Bik1), which is the budding yeast orthologue of the +TIP CLIP-170, was discovered as an essential protein for nuclear fusion (Trueheart et al., 1987). The knockout of Bik1 is viable in haploid cells but becomes lethal in polyploid cells, illustrating the importance of Bik1 (Lin et al., 2001). Inside the cell, Bik1 accumulates both at astral and spindle microtubules, the kinetochore and the spindle pole body (SPB) (Carvalho et al., 2004; Lin et al., 2001). Furthermore, Bik1 plays an important role in microtubule dynamics because haploid yeast cells with a Bik1 deletion display extremely shortened astral microtubules (Berlin et al., 1990). As an additional function, the movement of dynein to the microtubule plus-end is dependent on Bik1 (Roberts et al., 2014).

Bik1 exhibits a similar molecular architecture as CLIP-170 and consists of an N-terminal CAP-Gly domain, followed by a positively charged linker, a long coiled-coil, a C-terminal zinc knuckle and a C-terminal QQFF motif (Figure 1.9, page 15) (Miller et al., 2006). However, the coiled-coil in Bik1 is much shorter than the coiled-coil in CLIP-170 (roughly 200 aa instead of 1000 aa). Moreover, Bik1 also lacks the second CAP-Gly domain. In the same fashion as CLIP-170, Bik1 interacts with the tails of the yeast EB orthologue Bim1 and α-tubulin (Badin-Larcon et al., 2004; Blake-Hodek et al., 2010). The interaction takes places between the CAP-Gly domain of Bik1 and the ETF tail of Bim1 or the EEF tail of α-tubulin (Wolyniak et al., 2006). Across various yeast species, this C-terminal phenylalanine is conserved, indicating a substitution of tyrosine to phenylalanine in the tails that interact with CAP-Gly domains. After attachment to microtubules, Bik1 can diffuse along them, and the binding of Bik1 to Bim1 recruits Bik1 to the microtubule plus-end (Caudron et al., 2008). Furthermore, the coiled-coil of Bik1 interacts with the coiled-coil of the kinesin motor Kip2, which is a plus-end-directed kinesin (Roberts et al., 2014). Kip2 is capable of transporting Bik1 to the microtubule plus-end independent of Bim1 (Caudron et al., 2008). Therefore, Bik1 can track the microtubule plus-end by binding to Bim1 and Kip2. The interaction of the CAP-Gly domain with microtubules seems to be important because the deletion of the C-terminal phenylalanine of α-tubulin abrogates the plus-end tracking of Bik1 (Caudron et al., 2008). This illustrates that interactions with Bim1 and Kip2 are not sufficient to load Bik1 on microtubules when Bik1 cannot localize itself to the microtubule lattice.

Since Bim1 and Kip2 attach to different domains of Bik1, they can form a ternary complex to which dynein binds via the adaptor protein Pac1, the Lis1 orthologue in yeast, which also interacts with the zinc knuckle of Bik1 (Roberts et al., 2014; Sheeman et al., 2003). The Bim1-Bik1-Kip2 complex can target dynein to the microtubule plus-end in a tug-of-war between this complex and the minus-end-directed motor dynein. During anaphase, the mitotic spindle can be positioned by dynein to the bud neck that is the junction between the mother cell and the bud (Moore et al., 2009). This mechanism is called the dynein pathway, for which the correct function of Bik1 is indispensable (Miller et al., 2006). The disruption of the dynein pathway is not lethal because the so-called Kar9 pathway can also fulfill the spindle positioning (see also next chapter) (Moore et al., 2009). Interestingly, a putative interaction between Bik1 and the C-terminal part of the protein Kar9 has been described, and both the phosphorylation and asymmetric positioning of Kar9 could be influenced by Bik1 (Moore et al., 2006). In addition, the deletion of Bik1 seems to have a non-lethal effect on the Kar9 pathway. Therefore, it appears that Bik1 plays a role not only in the dynein pathway but also in the Kar9 pathway (Miller et al., 2006).

The coiled-coil of Bik1 is reported to interact with the C-terminal region of the microtubule polymerase Stu2 as well (Wolyniak et al., 2006), and this interaction can subsequently recruit Bik1 to the kinetochore in an independent manner of the Bik1 binding to microtubules (Lin et al., 2001). The binding of Bik1 to Stu2 probably helps to increase the dynamics of kinetochore microtubules, but this interaction shows no relevance for the behavior of astral microtubules (Wolyniak et al., 2006). In total, the functional role of the Bik1-Stu2 interaction is still not well understood.

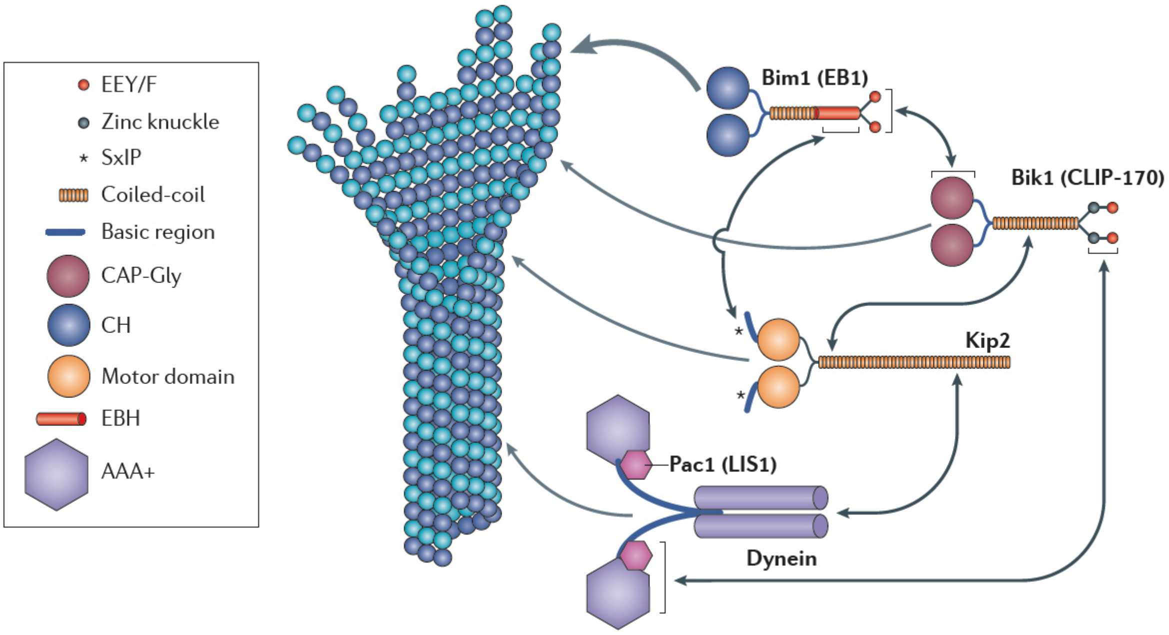

Figure 1.9 Schematic overview of various +TIPs in budding yeast.
The +TIPs Bim1, Bik1, Kip2, dynein and their interaction with each other and with microtubules are displayed. Their domain organization is depicted, and interactions between the respective domains are presented by arrows. Figure adapted from (Akhmanova and Steinmetz, 2015).

1.3.4 Further +TIPs in yeast

In yeast, the mitotic spindle is positioned by both the Kar9 pathway in the pre-anaphase stage and the dynein pathway during anaphase (Moore et al., 2009). Although these pathways are partially redundant, the perturbation of both pathways is lethal, highlighting the importance of these two pathways (Miller and Rose, 1998). The Kar9 pathway consists of the proteins Kar9, a crucial factor for spindle alignment (Liakopoulos et al., 2003), Bim1, the yeast orthologue of EBs, and the myosin motor Myo2 (Kusch et al., 2003) that can orient the mitotic spindle along polarized actin cables (Yin et al., 2000). The deletion of Kar9 results in a reduced number of cells with correct spindle alignment (Manatschal et al., 2016). Kar9 interacts with the EBH domain of the +TIP Bim1 via SxIP or LxxPTPh motifs present in the unstructured C-terminal tail of Kar9, and Bim1 targets Kar9 to the microtubule plus-ends and the spindle pole body (SPB) (Manatschal et al., 2016). In addition, Kar9 localizes only to the new SPB of the two SPBs, establishing a prerequisite for asymmetric cell division (Liakopoulos et al., 2003). At the old SPB, the absence of Kar9 is caused by phosphorylation because this post-translational modification abrogates binding to Bim1 (Leisner et al., 2008). Moreover, the N-terminal α-helical domain of Kar9 dimerizes, and this permits Kar9 to interact with multiple Bim1 proteins by the two C-terminal tails of the Bim1 dimer. (Manatschal et al., 2016). Furthermore, the N-terminal domain appears to be responsible for the interaction with the C-terminal domain of Myo2 (Yin et al., 2000). By the interactions with Bim1 and Myo2, Kar9 functions as an adaptor that connects astral microtubule plus-ends to actin cables (Figure 1.10) (Dasso, 2016; Liakopoulos et al., 2003).

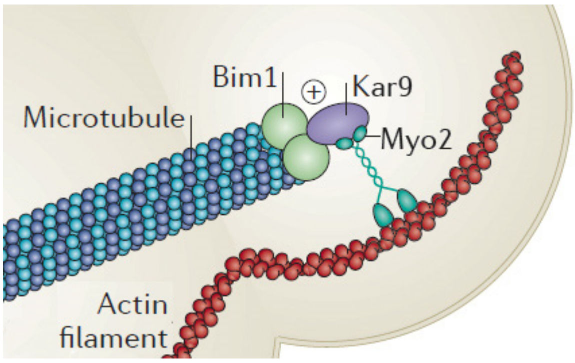

Figure 1.10 Schematic illustration of the Kar9-pathway.
The adaptor protein Kar9 interacts with Bim1 and Myo2. By linking microtubules and actin cables, the Bim1-Kar9-Myo2 complex can facilitate the spindle positioning. Figure adapted from (Akhmanova and Steinmetz, 2015).

Bim1, which is the budding yeast orthologue of EBs, induces faster GTP hydrolysis so that Bim1 can promote catastrophe of microtubules by its destabilizing effect (Howes et al., 2017, 2018). Deletion of Bim1 results in less dynamic microtubules in vivo because of a decrease of catastrophe and rescue events and a reduced shrinkage rate (Tirnauer et al., 1999). Interestingly, Bim1 is not capable of tracking the plus-end of mammalian microtubules in vitro, pointing towards subtle differences between yeast and mammalian microtubules (Howes et al., 2018). The domain architecture of Bim1 is equivalent to the one of EB proteins (see chapter 1.3.1), but the C-terminal tail features an ETF motif instead of the EEY motif at its end and is 20 amino acids longer (Manatschal et al., 2016; Zimniak et al., 2009). The ETF tail of Bim1 interacts with the Bik1 CAP-Gly domain (see chapter Bik1). In addition, the EBH domain of Bim1 can bind to SxIP or LxxPTPh motifs of +TIPs such as Kar9 (Kumar et al., 2017). Proteins associated with Bim1 can track the plus-end by the autonomous plus-end tracking of Bim1 (Blake-Hodek et al., 2010), and these various interactions emphasize the role of Bim1 as a hub at the microtubule plus-end. In addition, Bim1 attaches to the kinesin Kip2 by recognizing the N-terminal SxIP motif in the unstructured C-terminal tail of Kip2 (Drechsler et al., 2015). Therefore, in the ternary Bik1-Bim1-Kip2 complex each protein interacts with each other (Roberts et al., 2014).

The budding yeast protein Stu2, which belongs to the XMAP215 family, functions as a microtubule polymerase (Podolski et al., 2014). The impairment of Stu2 yields both very short astral and spindle microtubules (Al-Bassam et al., 2006). For the elongation of the mitotic spindle during anaphase, Stu2 plays a crucial role (Severin et al., 2001). Stu2 is composed of two tumor overexpressed gene (TOG) domains that interact both with soluble tubulin and microtubules. These are followed by an unstructured basic linker, a subsequent coiled-coil for dimerization and an unstructured C-terminal tail (Al-Bassam et al., 2006). The basic linker appears to increase affinity to microtubules by the interaction of positively charged residues with the negatively charged microtubules (Al-Bassam et al., 2006; Wang and Huffaker, 1997). The TOG domain specifically binds to the curved state of tubulin that exists both in free tubulin and at microtubule ends (Ayaz et al., 2012).

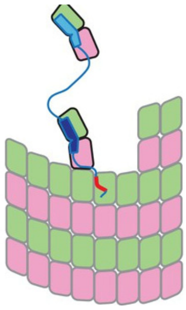

Figure 1.11 Proposed microtubule polymerization mechanism of Stu2.
Stu2 attaches with some TOG domains and basic linker to the very end of microtubules. Other TOG domains recruit soluble tubulin to polymerize microtubules. Figure taken from (Ayaz et al., 2014).

Surprisingly, an isolated TOG domain depolymerizes microtubules in vitro, but the full-length Stu2 is a polymerase (Podolski et al., 2014) because more than one TOG domain is required for correct function of Stu2 (Figure 1.11) (Ayaz et al., 2014). By its four TOG domains, Stu2 is capable of concentrating tubulin at the microtubule plus-end with the help of a tethering mechanism because some of the TOG domains are bound to soluble unpolymerized curved tubulin, and some of them are associated with the polymerized curved tubulin at the microtubule plus-end (Ayaz et al., 2014). Due to this mechanism, Stu2 can autonomously track the microtubule plus-end, and the arrangement of the second TOG domain and the linker permits Stu2 to discriminate between the plus-end and the minus-end (Ayaz et al., 2012). In contrast to the binding of EBs slightly away from the very end of microtubules, proteins of the XMAP215 family as Stu2 are located at the very end of the plus-end due to the binding to curved protofilaments (Maurer et al., 2014). The interactions of Stu2 with the yeast +TIPs Bik1 has been described in the preceding chapter. Furthermore, Stu2 appears to bind to the N-terminal part of Kar9, and this interaction promotes the accumulation of Kar9 at the SPBs (Moore and Miller, 2007). In addition, it has been reported that Stu2 could directly interact with Bim1, but it is unclear if this interaction is direct or indirect via Bik1 (Wolyniak et al., 2006). In the Kip3 paragraph (chapter 1.4.3), the association of Stu2 with the kinesin Kip3 is discussed.

1.4 Kinesins

In this chapter, an overview of kinesins will be provided. After the introduction, this chapter will focus on the regulation of microtubule dynamics by kinesins, and the yeast kinesins Kip2 and Kip3 will be described in detail.

1.4.1 Introduction into kinesins

Kinesins represent molecular motor proteins that can walk along microtubules by the hydrolysis of ATP (Endow et al., 2010). The main function of kinesins is the transport of cargo along microtubules, but various kinesins also regulate microtubule dynamics, for instance, as a depolymerase in cellular processes like mitosis (Welburn, 2013). The first kinesin was discovered by the observation of their movement along microtubules in the axons of squid (Allen et al., 1982). Kinesins are categorized into fourteen different families according to their function and domain organization (Lawrence et al., 2004). Each kinesin contains a motor domain that is responsible for the binding to microtubules and hydrolysis of ATP (Wang et al., 2015). Furthermore, most kinesins dimerize via a coiled-coil stalk, and this dimerization is essential for the processive movement of kinesins. The motor domain is connected to the stalk by a flexible neck region that features a linker but can also exhibit a short coiled-coil for dimerization in addition to the stalk. Moreover, kinesins can possess additional domains for the binding of cargo or other functions.

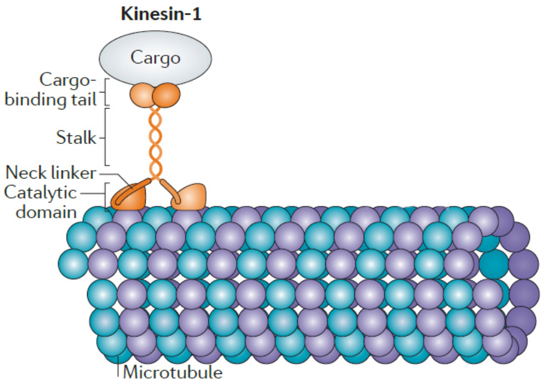

Figure 1.12 Illustration of the kinesin-1 binding to a microtubule.
Kinesin-1 consists of the motor domain (here denoted as catalytic domain), the neck linker, a stalk and a cargo binding domain. The binding of both motor domains to microtubules permits the detachment of one motor domain so that the kinesin can walk along microtubules. Figure adapted from (Veigel and Schmidt, 2011).

The first kinesin motor domain attaches to a single tubulin in microtubules, and the second motor domain of a kinesin dimer binds longitudinally neighboring tubulin (Figure 1.12) (Wang et al., 2015). Additionally, the motor domain can occupy three different states during the hydrolysis cycle of ATP. Both the apo-state and the ATP-bound state bind to microtubules with a high affinity. The ADP-bound state only weakly associates with microtubules (Cross, 2004). The dissociation of the ADP and the phosphate results in a strong microtubule binding of the motor in the apo-state. Afterward, ATP binds to the motor domain, and this induces conformational changes of the motor domain such as the docking of the neck linker to the motor domain (Wang et al., 2015). The ATP hydrolysis is stimulated by microtubule binding. After the hydrolysis of ATP, the motor domain dissociates from the microtubule and can step along them by binding to the after next tubulin. The second motor domain of the kinesin remains associated so that kinesins displays a high processivity in their movement.

The first structures of kinesin motor domains have been solved in the nineties by X-ray crystallography (Kozielski et al., 1997). Today, a high second digit number of structures that encompass the motor domain of all fourteen kinesin families exist. Overall, the motor domain is highly conserved across the families, and differences in regions like the microtubule binding regions are primarily responsible for the different functions. The kinesin motor domain features an eight-stranded β-sheet core that is surrounded by six α-helices (Kull et al., 1996). The ATP binding site represents a Walker fold (Walker et al., 1982) and contains four motifs that are also found in the motor domain of myosin (Marx et al., 2009). The two motifs switch-1 (NxxSSR) and switch-2 (DxxGxE) adapt their conformation depending if the γ-phosphate is present or not (Marx et al., 2009).

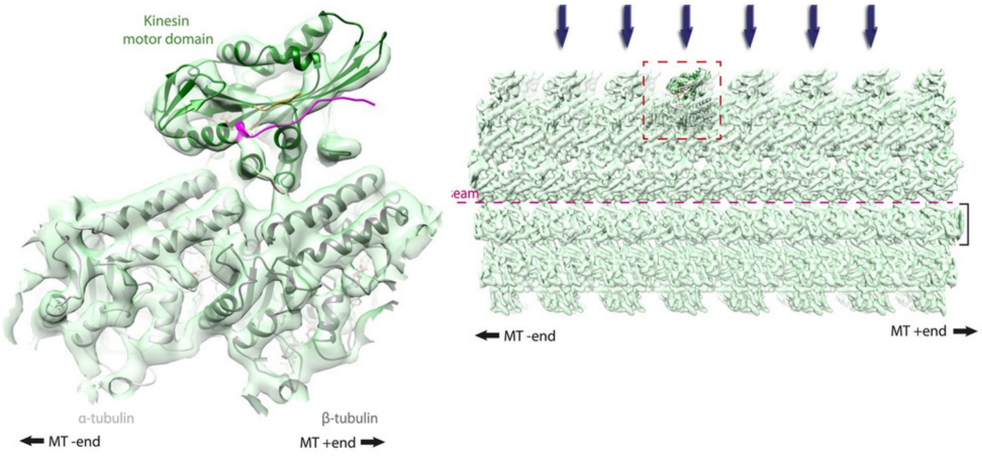

Figure 1.13 Cryo-EM structure of the kinesin-1 motor domain bound to a microtubule.
On the left side, the structure displays the details of the interaction between the kinesin-1 motor domain with the tubulin heterodimer inside microtubules. On the right side, a microtubule decorated with the kinesin-1 motor domain is shown. Figure adapted from (Atherton et al., 2014).

Cryo-EM structures of microtubules decorated with kinesin motor domains showed that the motor domain binds microtubules primarily by the α-helices and two loop regions (Figure 1.13) (Atherton et al., 2014; Hirose et al., 2006). Interestingly, it was possible to co-crystallize two kinesin motor domains together with tubulin by using a system of tubulin capped on the β-tubulin by a small artificial protein called DARPin (Figure 1.14) (Gigant et al., 2013; Wang et al., 2017). These structures confirmed the findings of the cryo-EM structures. The curved state of tubulin does not significantly interfere with the binding of the kinesin-1 motor domain that normally has a high preference for straight tubulin in microtubules (Gigant et al., 2013).

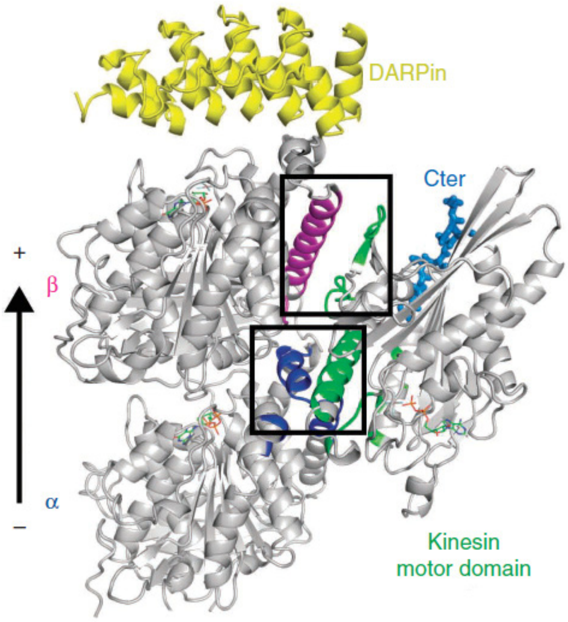

Figure 1.14 Crystal structure of the kinesin-1 motor domain in complex with tubulin-DARPin1.
The kinesin-1 motor domain laterally binds the tubulin heterodimer. The protein DARPin1 (yellow) stabilizes the soluble curved tubulin. No significant difference was observed between straight and curved tubulin for the binding of the motor domain. Figure adapted from (Gigant et al., 2013).

One major function of kinesins represents the transport of cargo, and the kinesin-1, 2 and 3 families are mainly involved in this function (Verhey and Hammond, 2009). For instance, kinesin-1 carries synaptic vesicles along axonal microtubules. The next chapter will describe additional functions of kinesins besides cargo transport.

1.4.2 Regulation of microtubule dynamics by kinesins

As their major function, some kinesins can either promote polymerization of microtubules or induce catastrophe that leads to depolymerization (Drummond, 2011). Therefore, they represent potent regulators of microtubule dynamics in cellular processes like mitosis. In addition, a class of kinesins is capable of rescuing depolymerizing microtubules (Su et al., 2011). The microtubule dynamic regulating kinesins can be further differentiated into motile kinesins that can walk along microtubules and non-motile kinesins that attach directly to the ends of microtubules (Drummond, 2011). The mammalian kinesin-7 family member CENP-E, which is a motile kinesin, belongs to the class of microtubule polymerases, which enhance the growth rate of microtubules, and has the orthologue Kip2 in yeast (Verhey and Hammond, 2009). CENP-E tethers microtubules to the kinetochore (Wood et al., 1997) and can move chromosome as well to reach their correct alignment (Kapoor et al., 2006). In vitro experiments proved that purified CENP-E increases the rate of polymerization of microtubules without the help of additional proteins (Sardar et al., 2010). How CENP-E functions as a polymerase is still unclear, but it is suggested that CENP-E could stabilize the straight conformation of tubulin, and thus favors microtubule assembly (Sardar et al., 2010). A similar mechanism has been proposed for the kinesin-5 family that acts as a microtubule polymerase as well (Chen and Hancock, 2015).

The kinesin-13 family consists of non-motile kinesins like the mammalian protein MCAK (Endow et al., 2010) whose motor domain depolymerizes microtubules under hydrolysis of ATP by stabilizing the curved state of tubulin (Wang et al., 2017). At microtubule ends, the kinesin-13-bound curved tubulin resembles the tubulin state that dissociates from microtubules. Hence, the kinesin-13-bound tubulin is quickly released. The structural details of this mechanism were elucidated by the crystal structure of the kinesin-13 protein MCAK bound to tubulin that was capped by DARPin1 (Wang et al., 2017). MCAK decreases the length of spindle microtubules (Domnitz et al., 2012), and this process is important for amending incorrect attachments between microtubules and kinetochores (Tulu et al., 2006; Verhey and Hammond, 2009).

The motile kinesin-8 family, whose members are plus-end directed motors, depolymerize microtubules in a length-dependent manner (Varga et al., 2009). This means that the activity is higher at the ends of longer microtubules due to the high processivity because more kinesins can accumulate on long microtubules. In mammals, the kinesin-8 family member KIF18A reduces the oscillation of chromosomes during anaphase (Stumpff et al., 2008), and KIF19A (kinesin-8 family) can control the length of microtubules in cilia (Niwa et al., 2012). The best-studied kinesin-8 family member is the budding yeast kinesin Kip3, which regulates the length of the mitotic spindle (Su et al., 2013). In addition, Kip3 depolymerizes microtubules in vitro by its motor domain (Arellano-Santoyo et al., 2017; Varga et al., 2009). Similar depolymerization of microtubules by the motor domain has been reported for both KIF18A and KIF19A (Locke et al., 2017; Niwa et al., 2012). Kip3 will be discussed in more detail in chapter 1.4.4.

All kinesin-8 proteins comprise an N-terminal motor domain, followed by the neck-linker, a coiled-coil region and a C-terminal unstructured tail (Su et al., 2011; Wang et al., 2016). A microtubule-binding site was identified in the C-terminal tail that helps to tether kinesins like Kif18a at the microtubule plus-end (Stumpff et al., 2011; Weaver et al., 2011). Based on a crystal structure and a cryo-EM reconstitution of KIF19a, it is assumed that the motor domains of the kinesin-8 family can both walk along microtubules and stabilize the curved state of tubulin at the plus-end by two different interfaces (Wang et al., 2016). This would imply a dual function of the kinesin-8 family. At the plus-end, the depolymerase mechanism by promoting curved tubulin through ATP hydrolysis would be similar to kinesin-13 proteins (Wang et al., 2016). Details of the kinesin-8 depolymerase mechanism are still unclear because a cryo-EM structure of Kif18 attached to microtubules indicated that the mechanism is ATP independent (Locke et al., 2017). Nevertheless, this result confirms the stabilization of the curved tubulin as the depolymerase mechanism.

1.4.3 The yeast kinesin Kip2

The yeast kinesin Kip2, which belongs to the kinesin-7 family, supports the correct position of the mitotic spindle by participating both in the dynein pathway (Carvalho et al., 2004) and Kar9 pathway (see also chapter 1.3.3 and 1.3.4) (Maekawa et al., 2003). Kip2 transports the +TIP Bik1 to the astral microtubule plus-end (Roberts et al., 2014). By the Bik1-Kip2 complex, dynein itself can also be carried to the plus-end, and this localization of dynein is important for spindle positioning. In addition, it has been described that Kip2 helps to ensure the correct amount of Kar9 at the bud neck (Maekawa et al., 2003)

Besides its involvement in spindle positioning, the yeast kinesin Kip2 is capable of stabilizing microtubules (Miller et al., 1998). The deletion of Kip2 causes very short microtubules in yeast cells (Cottingham and Hoyt, 1997). On the other hand, the overexpression of Kip2 yields hyper-elongated cytoplasmic microtubules (Carvalho et al., 2004). Furthermore, it was observed in vitro that the addition of full-length Kip2 to microtubules results in faster growth rate and longer microtubules (Hibbel et al., 2015). Therefore, it is assumed that Kip2 can function as a microtubule polymerase. For the human orthologue of Kip2, CENP-E, similar properties have been reported.

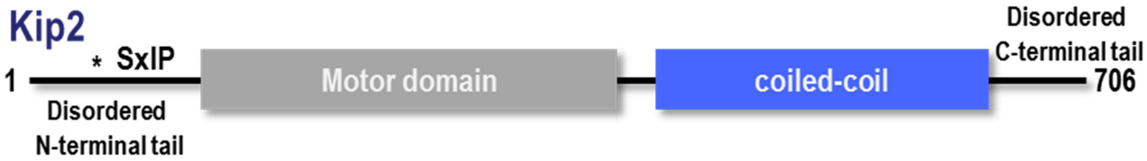

Figure. 1.15 Domain Organization of the budding yeast kinesin Kip2.
The various domains and unstructured regions of kinesin Kip2 are depicted.

Kip2 consists of an unstructured N-terminal part, followed by the motor domain and a C-terminal region that is described to form a coiled-coil (Figure 1.15) (Drechsler et al., 2015; Roberts et al., 2014). In the N-terminus of Kip2, an SxIP motif can be found so that Kip2 can interact with the EBH domain of Bim1 by this motif. Various serines in the Kip2 N-terminus can be phosphorylated, and this phosphorylation reduces the affinity of Kip2 both for Bim1 and astral microtubules (Drechsler et al., 2015). This could be a mechanism to induce dissociation of the Bik1-Kip2 complex and offloading of dynein. During the cell cycle, the amount of Kip2 attached to microtubules highly varies, and low levels of Kip2 correspond to short astral microtubules. At the beginning of the cell cycle, the level of Kip2 attached to microtubules is low, and it increases during the M phase. By regulating the level of Kip2, the cell seems to have one option to control the length of astral microtubules and to ensure correct separation of spindle pole bodies (SPBs) while the astral microtubules exist in a short state.

The motor domain of Kip2 shows high sequence conservation with the motor domains of other kinesins. In addition, the motor domain of Kip2 appears to be high processive because full-length Kip2 exhibits a high processivity (Hibbel et al., 2015). The proteins Bik1 and Bim1 further increase the processivity of Kip2 (Roberts et al., 2014). However, the motor domain in isolation has not been investigated comprehensively.

The predicted coil-coil domain of Kip2 can interact with the coiled-coil domain of Bik1 (Newman et al., 2000) so that Bik1 is enriched by Kip2 at the microtubule plus-end (Caudron et al., 2008; Roberts et al., 2014) (see also the Bik1 chapter). In addition, the binding of Bik1 enhances the processivity of Kip2 (Hibbel et al., 2015). In contrast to the interaction with Bik1, Kip2 seems not to directly interact with Kar9. The positive effect of Kip2 on Kar9 accumulation at astral microtubules plus-ends seems to be indirect and could be mediated via Bim1, which binds both to Kip2 and Kar9 (Drechsler et al., 2015). Since Kar9 is supposed to interact with Bik1 as well (Moore et al., 2006) , Bik1 could also play a role by its interactions both with Kip2 and the putative Kar9 interaction.

1.4.4 The yeast kinesin Kip3

The correct length of the mitotic spindle is essential to guarantee correct chromosome segregation. In yeast, the major function of the kinesins Kip3, which is part of the kinesin-8 family, represents the control of microtubule dynamics in dependence on the microtubule length (Su et al., 2011). This allows Kip3 to regulate the length of the mitotic spindle by both depolymerization and antiparallel sliding of microtubules (Su et al., 2013). In the case of long microtubules, Kip3 acts as a microtubule depolymerase and induces catastrophe. On the other hand, Kip3 serves as a rescue factor for short microtubules. The switch from the role as a rescue factor to a catastrophe factor seems to be correlated to the increase of the Kip3 concentration at the microtubule plus-end (Su et al., 2011). Kip3 has the ability to significantly accumulate on the microtubule plus-end because the kinesin Kip3 features a very long run-length (Varga et al., 2009). This means that nearly all Kip3 motors that attach to a microtubule manage to reach the plus-end. The additional implication of this is that more Kip3 can enrich on longer microtubules and a shift from a rescue factor to a microtubule depolymerase occurs (Su et al., 2011). Due to this, Kip3 is also described as a length-dependent microtubule depolymerase that is crucial in yeast to maintain the correct length of microtubules. In line with this, the deletion mutant of Kip3 exhibits extremely long cytosolic microtubules and a hyper-elongated spindle. (Cottingham and Hoyt, 1997; Rizk et al., 2014)

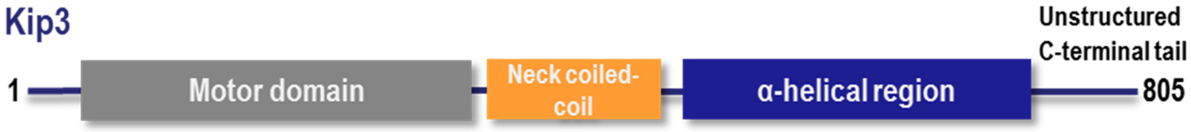

Figure. 1.16 Domain Organization of the budding yeast kinesin Kip3.
The various domains and unstructured regions of kinesin Kip3 are depicted.

Kip3 consists of an N-terminal motor domain that is responsible for the depolymerase function (Figure 1.16) (Fukuda et al., 2014), followed by a neck linker, a neck coiled-coil and a C-terminal part (Su et al., 2011). The C-terminal part is essential for rescuing shrinking microtubules (Fukuda et al., 2014) and can interact both with soluble tubulin and microtubules (Su et al., 2011). The C-terminal part of Kip3 can be separated into a structured α-helical region and an unstructured C-terminal tail. Only the α-helical region appears to be required for microtubule rescue (Dave et al., 2018). However, the C-terminal tail that is partially disordered seems to prevent premature spindle disassembly. Since no structural or detailed biochemical information exists for the C-terminal domain, the rescue mechanism is poorly understood. For the motor domain, it is described that the depolymerization activity is achieved by the stabilization of the curved tubulin conformation (Arellano-Santoyo et al., 2017), as reported for other kinesin-8 family members in mammals and kinesin-13. However, structural information is missing for the motor domain of Kip3.

Furthermore, Kip3 can interact by its motor domain with the microtubule polymerase Stu2 that is transported by Kip3 along microtubules (Gandhi et al., 2011). Stu2 can rescue microtubules, and the interaction of a microtubule polymerase with a depolymerase looks counterintuitive. However, shrinking microtubules can often lose their connection to the kinetochore, and the rescue by Stu2 provides a mechanism to keep the kinetochore attached to the microtubule end (Gandhi et al., 2011).

1.5 Microtubule minus-end-tracking proteins (-TIPs)

This chapter will provide an introduction into proteins that target the microtubule minus-end. Afterward, the CAMSAP proteins, which track the microtubule minus-end, will be described.

1.5.1 Introduction into -TIPs

In various higher eukaryotic cells, not all microtubule minus-ends are attached to the centrosome because a large spatial distance between the centrosome and microtubules can occur, or the cells can even lack the centrosome like neuronal cells (Akhmanova and Hoogenraad, 2015). The microtubules that do not bind to γ-tubulin of the centrosome, the major microtubule-organizing center, are called non-centrosomal microtubules that exhibit free minus-ends (Martin and Akhmanova, 2018). Therefore, it was enigmatic how the minus-ends of these non-centrosomal microtubules are stabilized because free microtubule minus-ends are prone to depolymerization (Keating et al., 1997). In the last years, several microtubule minus-end-tracking proteins (–TIPs) have been identified that are capable of targeting the minus-end and regulating dynamics of the microtubule minus-end (Akhmanova and Hoogenraad, 2015; Tanaka et al., 2012).

1.5.2 The -TIP CAMSAP

The first family of discovered -TIPs is the calmodulin-regulated spectrin-associated proteins (CAMSAPs) that occur in species from *C. elegans* to mammals but not in yeast (Akhmanova and Hoogenraad, 2015). The CAMSAP proteins stabilize microtubule minus-ends by preventing both depolymerization and polymerization. This could explain why growing minus-ends of non-centrosomal microtubules are observed very rarely in contrast to in vitro experiments with microtubules alone. CAMSAP proteins can autonomously track the microtubule minus-end by their globular CKK domain (Hendershott and Vale, 2014). The abbreviation CKK is derived from the name C-terminal domain common to CAMSAP1, KIAA1078 and KIAA1543 (Baines et al., 2009). In mammals, three different homologs of the CAMSAP proteins, named CAMSAP1, CAMSAP2 and CAMSAP3, exists. The two last generic names in the description of the CKK domain were later replaced by the CAMSAP names (Akhmanova and Hoogenraad, 2015). The CKK domain is unique for CAMSAP proteins and defines this protein family, (Jiang et al., 2014). In organisms as *C. elegans*, only one CAMSAP protein occurs that is named Patronin, and in *D. melanogaster* the sole CAMSAP protein is called Nezha.

All CAMSAP proteins consist of an N-terminal CH domain that is not involved in microtubule binding in contrast to the microtubule-binding CH domains of EBs (Figure 1.17). However, the CAMSAP CH domain seems to promote actin polymerization in endocytosis (Gong et al., 2018). After a long unstructured region, which also possesses a binding site for the microtubule-severing enzyme katanin (Jiang et al., 2018), three coiled-coils are present that dimerize the CAMSAP proteins (Akhmanova and Hoogenraad, 2015). This dimerization enhances the minus-end tracking of the CKK domain because the dimerization results in an avidity effect. Without the coiled-coil, the CKK domain only weakly tracks the minus-end (Jiang et al., 2014). The coiled-coils, of which the third one features a consecutive α-helix as well, are followed by the conserved CKK domain. In the case of CAMSAP2 and CAMSAP3, a positively charged unstructured microtubule-binding domain (MBD) can be found between the second and third coiled-coil. The MBD can decorate microtubule on its own but has no specificity for the minus-end (Jiang et al., 2014) so that this domain appears to increase the overall affinity of CAMSAP2/3 for microtubules. Besides the minus-end tracking, CAMSAP2/3 stabilize the microtubule minus-end by decoration through a combination of the MBD and the CKK domain (Jiang et al., 2014). In addition, microtubules grown in vitro show that the CAMSAP2/3 decorate not only the minus-end but remains at positions of the former minus-end before growing due to the high affinity of CAMSAP2/3 for microtubules (Akhmanova and Hoogenraad, 2015). The MBD helps to explain the different behaviors of CAMSAP 1 compared to CAMSAP2/3 because CAMSAP1 tracks the minus-end by the CKK but does not stabilize the minus-end due to the lack of the MBD (Hendershott and Vale, 2014; Jiang et al., 2014). For CAMSAP3, the MBD is partially redundant because the α-helix also binds microtubules. Due to this, CAMSAP3 has the strongest ability to stabilize the minus-end and to prevent polymerization (Akhmanova and Hoogenraad, 2015).

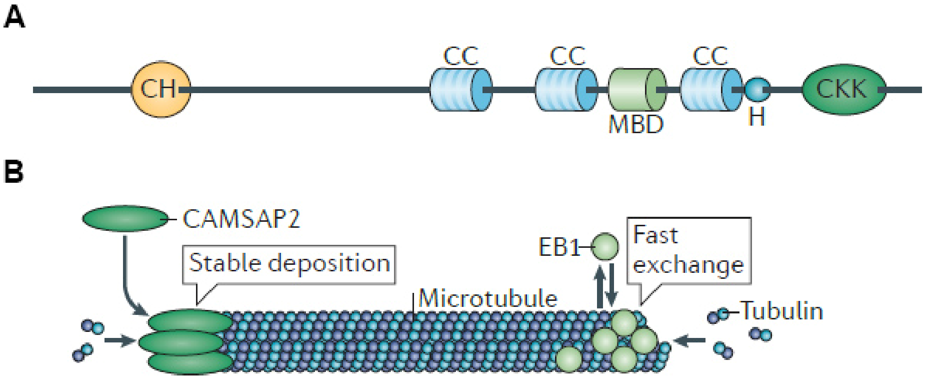

Figure 1.17 Domain organization of CAMSAP proteins and illustration of their microtubule binding. *In the upper panel, the domain organization of the -TIP CAMSAP3 is displayed. The abbreviation stands for a coiled-coil domain, and MBD describes the microtubule-binding domain. The CKK domain is shown in dark green. In the lower panel, the tracking of the microtubule minus-end by CAMSAP proteins is illustrated. EBs exchange fast at the microtubule plus-end. In contrast to this, CAMSAPs bind more stable to the minus-end. Figure adapted from (Akhmanova and Steinmetz, 2015).*

Although CAMSAP proteins bind to the microtubule minus-end, they do not block integration of tubulin into microtubules by a capping mechanism but significantly slow down the polymerization of microtubules so that it looks like a stop of growth of the minus-end (Jiang et al., 2014). This clarifies why in cells growing microtubule minus-ends are very rare. (Akhmanova and Hoogenraad, 2015). In addition, CAMSAP proteins compete with the depolymerizing kinesin-13 for the same binding site to preclude depolymerization by this kinesin (Hendershott and Vale, 2014). As CAMSAP proteins do not cap the microtubule minus-end, they cannot sense the minus-end by binding to the longitudinal interface of α-tubulin (Jiang et al., 2014). It is presumed that the CKK domain of CAMSAPS recognizes a special feature of the minus-end like the curvature, but the orientation or another feature of the tubulin at the minus-end also seems to be important because CAMSAP proteins do not target the plus-end that exhibits curved tubulin as well (Akhmanova and Hoogenraad, 2015). This illustrates a fundamental difference between the CKK domains of CAMSAPs and CH domains of EBs because EBs can track both growing microtubule plus-ends and minus-ends by targeting a region around the GTP cap (Akhmanova and Steinmetz, 2015).

1.6 Aim of this thesis

The research on +TIPs was able to answer a lot of important biological questions in the last ten years (Akhmanova and Steinmetz, 2015). However, various significant questions are still open like the details of the interaction of a +TIP with other proteins in the +TIP network or the mechanistic details of various +TIPs. For instance, it remains enigmatic how a kinesin can function as a microtubule polymerase (Hibbel et al., 2015). Furthermore, the recently discovered -TIPs are poorly understood because fundamental insights into their mechanism of minus-end recognition are lacking (Jiang et al., 2014).

Yeast represents an excellent model organism to perform research on microtubules and proteins interacting with them because in yeast only a small number of microtubules exist that can be analyzed well by microscopy. In addition, mutations or deletions can be easily introduced in yeast +TIPs to study their effect on phenomena such as the tracking of the plus-end or microtubule dynamics. Therefore, biophysical and structural research on a protein target can be ideally combined with the in vivo research to obtain a holistic picture of the yeast +TIPs.

In order to understand the yeast +TIP network, a thorough understanding of the important factors is required. The +TIP Bik1 constitutes an integral component of the dynein pathway, but the structural and biophysical details of the interactions of Bik1 with Bim1, Stu2 and Kip2 are lacking. Especially, the implications of the Bik1-Bim1 interaction on the function of Bik1 and the positioning of Kar9 are open. For these reasons, the investigation of the Bik1 interaction network was defined as the first research aim to increase our understanding of the +TIP network in yeast and the interplay between the various proteins. Based on the findings of a potential Bik1-Bim1 structure, we planned to perturb the Bik1-Bim1 interaction in vivo to investigate the effect on Bik1 localization, microtubules dynamics and Kar9 localization.

The mechanisms of kinesins that function as microtubule polymerases are unresolved. In terms of the kinesin Kip2, it is unknown which parts of this protein participate in the polymerase function and if Kip2 increase the polymerization rate by a similar mechanism as Stu2 that locally enriches the concentration of soluble tubulin. In this context, the interaction of the coiled-coil of Kip2 with the coiled-coil with Bik1 could play a significant role in the polymerase function of Kip2. These points illustrate why the elucidation of the Kip2 function is the second research aim to significantly improve the overall understanding of microtubule polymerases.

Overall rescue of microtubules remains poorly understood. The induction of rescue by kinesins such as the budding yeast Kip3 is even more unexplained. For Kip3, it has been resolved that the motor domain possesses a crucial role in the activity of Kip3 as a microtubule depolymerase at the plus-end, but Kip3 is a length-dependent depolymerase that can also rescue microtubules. The function and the regulation of the C-terminal part of Kip3 in the rescue of collapsing microtubules is unclear. The C-terminal part appears to interact both with tubulin and microtubules. Biochemical and structural details of this interaction are missing, and it is not known if only certain regions like the structured domain are involved in this interaction. Due to this, the third research aim involves the investigation of the C-terminal part of Kip3 to understand how this protein can function as a rescue factor for microtubules. Additionally, insights into the rescue function of Kip3 would increase our general knowledge of microtubule dynamics.

In a significant part of my Ph.D. thesis, I have focused on the yeast proteins Bik1, Kip2 and Kip3 to structurally and biophysically investigate the role of Bik1 in the +TIP network in yeast and the function of the two kinesins Kip2 and Kip3 in the regulation of microtubule dynamics. Complementary cell biology experiments were performed by the group of Yves Barral (ETH Zürich). Since orthologues of the proteins Bik1, Kip2 and Kip3 exist in higher eukaryotes as well, functional insights on the yeast proteins can help to answer important questions for the proteins in higher eukaryotes as for Kip3 orthologue KIF18a that is overexpressed in various types of cancer(Zhang et al., 2010).

To comprehensively understand microtubules and their dynamics, the minus-end should not be neglected because proteins like CAMSAPs can stabilize the minus-end and protect them from depolymerization (Akhmanova and Hoogenraad, 2015). In contrast to +TIPs such as EBs, no information exists how -TIPs mechanistically function to target the microtubule minus-end. CAMSAP proteins have been identified as the first -TIPs, and the CAMSAP CKK domain is capable of autonomously tracking the minus-end. It is enigmatic which structural elements of microtubules are recognized and how the CKK domain binds to microtubules. Therefore, studies on the CKK domain itself and on microtubules decorated with the CKK were chosen as the fourth research aim to elucidate the mechanism for the targeting of the CKK domain to the minus-end of microtubules and the microtubule-stabilizing effect of CAMSAPs. The CKK domain and its interaction were supposed to be investigated biochemically and structurally in this work. To reveal the binding mode to microtubules, a potentially obtained crystal structure was supposed to be inserted in cryo-EM maps of microtubules decorated with the CKK domain recorded in the group of Carolyn Moore (Birkbeck College). Moreover, the group of Anna Akhmanova (University Utrecht) envisaged to perform in vivo work on the CKK domain and in vitro reconstitutions of microtubules with the CKK domain.

2. Structure-Function Relationship of the Bik1-Bim1 Complex

2. Structure-Function Relationship of the Bik1-Bim1 Complex

2.1 Declaration of contribution

In the Bik1 project, all in vitro work was performed by me together with support from Dr. Anil Kumar for ITC experiments and crystallization experiments. Prof. Dr. Michel Steinmetz and I designed and analyzed the in vitro experiments. I cloned, expressed and purified all constructs besides Bim1C that was purified by Anil Kumar. Most of the ITC experiments were conducted by me, and some ITC experiments like with SxIP or LxxPTPh peptide were done together with Anil Kumar. I set up all crystallization trials and received help from Anil Kumar to prepare crystals for the beam line. At the beam line, data sets were collected together by Anil Kumar and me. Anil Kumar solved the Bik1 apo-structure and the Bik1-Bim1 complex structure, and I also participated in this process. In yeast, Dr. Xiuzhen Chen and Dr. Ana-Maria Farcas conducted the in vivo experiments, and Prof. Dr. Yves Barral supervised this part. Prof. Dr. Michel Steinmetz and I wrote together the manuscript with input from all other authors.

The paper about Bik1 was published in the year with the title “Structure-Function Relationship of the Bik1-Bim1 Complex” in the journal Structure in 2018.

Bibliographic information:

Stangier, M.M., Kumar, A., Chen, X., Farcas, A.M., Barral, Y., and Steinmetz, M.O. (2018). Structure-Function Relationship of the Bik1-Bim1 Complex. Structure 26, 607-618.e604.

Article

Structure

Structure-Function Relationship of the Bik1-Bim1 Complex

Graphical Abstract

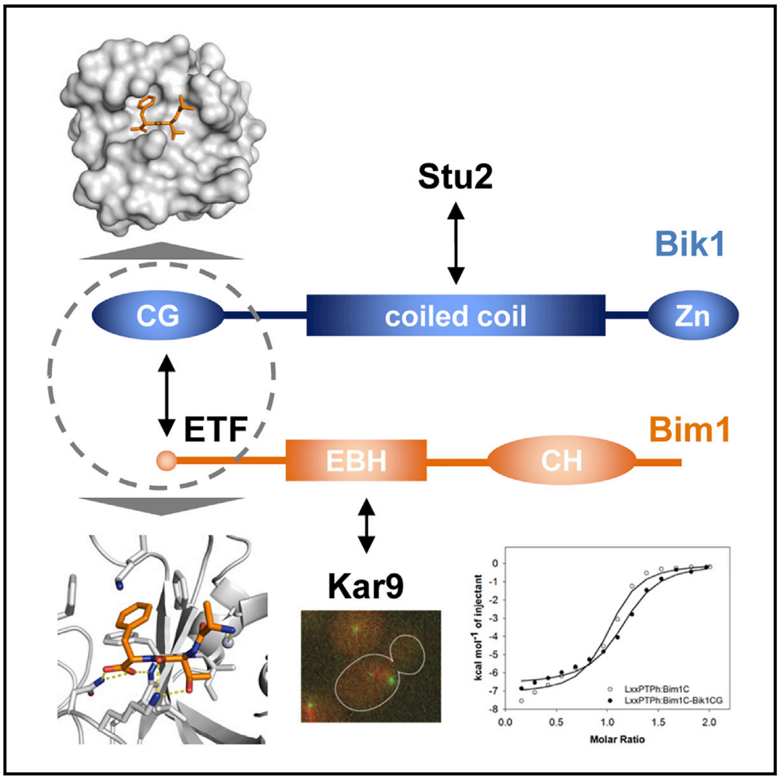
Stu2
Bik1
CG
coiled coil
Zn
ETF
Bim1
EBH
CH
Kar9
kcal mol^{-1} of injectant
0
-1
-2
-3
-4
-5
-6
-7
-8
0.0
0.5
1.0
1.5
2.0
Molar Ratio
○ LxxPTPh:Bim1C
● LxxPTPh:Bim1C-Bik1CG

Highlights

- The CAP-Gly domain of Bik1 is a C-terminal phenylalanine recognition domain
- The Bik1-Bim1 complex interacts with the EB1-binding motifs SxIP and LxxPTPh
- Perturbation of Bik1-Bim1 affects Bik1 localization and astral microtubule length
- The Bik1/CLIP-170-Bim1/EB1 module is evolutionarily flexible

Authors

Marcel M. Stangier, Anil Kumar, Xiuzhen Chen, Ana-Maria Farcas, Yves Barral, Michel O. Steinmetz

Correspondence

michel.steinmetz@psi.ch

In Brief

Stangier et al. show that the CAP-Gly domain of Bik1 is a C-terminal phenylalanine recognition domain. Bik1-Bim1 forms ternary complexes with the EB1-binding motifs SxIP and LxxPTPh. The results provide insight into the role of the Bik1-Bim1 interaction in cell division, and demonstrate that the Bik1/CLIP-170-Bim1/EB1 module is evolutionarily flexible.

Stangier et al., 2018, Structure *26*, 607–618
April 3, 2018 © 2018 Elsevier Ltd.
https://doi.org/10.1016/j.str.2018.03.003

Structure
Article

CellPress

Structure-Function Relationship of the Bik1-Bim1 Complex

Marcel M. Stangier,[1] Anil Kumar,[1,4] Xiuzhen Chen,[2,4] Ana-Maria Farcas,[2,4] Yves Barral,[2] and Michel O. Steinmetz[1,3,5,*]
[1]Laboratory of Biomolecular Research, Division of Biology and Chemistry, Paul Scherrer Institut, 5232 Villigen PSI, Switzerland
[2]Institute of Biochemistry, ETH Zürich, 8049 Zürich, Switzerland
[3]University of Basel, Biozentrum, 4056 Basel, Switzerland
[4]These authors contributed equally
[5]Lead Contact
*Correspondence: michel.steinmetz@psi.ch
https://doi.org/10.1016/j.str.2018.03.003

SUMMARY

In budding yeast, the microtubule plus-end tracking proteins Bik1 (CLIP-170) and Bim1 (EB1) form a complex that interacts with partners involved in spindle positioning, including Stu2 and Kar9. Here, we show that the CAP-Gly and coiled-coil domains of Bik1 interact with the C-terminal ETF peptide of Bim1 and the C-terminal tail region of Stu2, respectively. The crystal structures of the CAP-Gly domain of Bik1 (Bik1CG) alone and in complex with an ETF peptide revealed unique, functionally relevant CAP-Gly elements, establishing Bik1CG as a specific C-terminal phenylalanine recognition domain. Unlike the mammalian CLIP-170-EB1 complex, Bik1-Bim1 forms ternary complexes with the EB1-binding motifs SxIP and LxxPTPh, which are present in diverse proteins, including Kar9. Perturbation of the Bik1-Bim1 interaction *in vivo* affected Bik1 localization and astral microtubule length. Our results provide insight into the role of the Bik1-Bim1 interaction for cell division, and demonstrate that the CLIP-170-EB1 module is evolutionarily flexible.

INTRODUCTION

In eukaryotic cells, various proteins localize to the plus-ends of microtubules where they regulate microtubule dynamics and attachment of microtubule ends to subcellular structures (reviewed in Howard and Hyman, 2003; Akhmanova and Steinmetz, 2015). As such, these microtubule plus-end tracking proteins (+TIPs) participate in key cellular processes, including cell division, cell motility, and intracellular trafficking. One key attribute of +TIPs is their ability to form complex and dynamic interaction networks. A detailed molecular understanding of these networks is crucial for deciphering how they support the large variety of microtubule-based processes and for rationally perturbing their architectures and functions.

Yeast is an excellent system to investigate the structure-function relationship of +TIP networks, as they are simpler than that of metazoans. In the yeast cytoplasm, +TIPs are implicated in two prominent pathways that align the mitotic spindle with the division axis of the cell, and are thus crucial for cell division: the pre-anaphase "Kar9 pathway," which involves the microtubule plus-end-F-actin crosslinking protein Kar9, and the anaphase "dynein pathway," which is supported by the microtubule minus-end directed motor protein dynein (Miller and Rose 1998; reviewed in Miller et al., 2006). Bik1 (ortholog of CLIP-170) is a crucial +TIP that acts together with proteins of both pathways (reviewed in Miller et al., 2006). It interacts directly and indirectly with microtubules (Badin-Larçon et al., 2004), with the GTP-cap-binding protein Bim1 (ortholog of the end binding [EB] protein EB1; Blake-Hodek et al., 2010), Stu2 (ortholog of the microtubule polymerase XMAP215/ch-TOG; Podolski et al., 2014), and Kar9 (Moore et al., 2006), and is thus a central player in +TIP networks. However, how these diverse interactions are orchestrated, whether they are simultaneous or mutually exclusive, and how they contribute to Bik1 function is poorly understood.

In this study, we assessed the structural basis and function of Bik1-Bim1-mediated interactions. Bik1 consists of an N-terminal cytoskeleton-associated protein glycine-rich (CAP-Gly) domain, which is followed by a positively charged unstructured region, a coiled-coil domain, and a zinc finger domain at its C terminus (Figure 1A; reviewed in Miller et al., 2006). The CAP-Gly domains of CLIP-170 and p150glued interact with the C-terminal EEY motif of EBs, whereby the terminal tyrosine residue is essential for binding (Weisbrich et al., 2007). However, this tyrosine can be substituted by a phenylalanine residue without compromising the binding strength toward the CAP-Gly domains of both CLIP-170 and p150glued (Weisbrich et al., 2007; Mishima et al., 2007). Notably, C-terminal EEY/F motifs that are targeted by CAP-Gly domains are also present in α-tubulin, CLIP-170, and SLAIN2 (reviewed in Slep, 2010; Steinmetz and Akhmanova, 2008). Based on these observations, CAP-Gly domains were defined as EEY/F motif recognition domains (reviewed in Steinmetz and Akhmanova, 2008). Besides CAP-Gly domains, EBs also interacts with linear SxIP and LxxPTPh motifs present in many +TIPs, including Kar9 (Honnappa et al., 2009; Kumar et al., 2017). Notably, binding of mammalian EB1 to both CAP-Gly and to SxIP are reciprocally exclusive, due to competition between these two elements for adjacent binding sites (Duellberg et al., 2014). The evolutionary flexibility of these modules, however, is unknown.

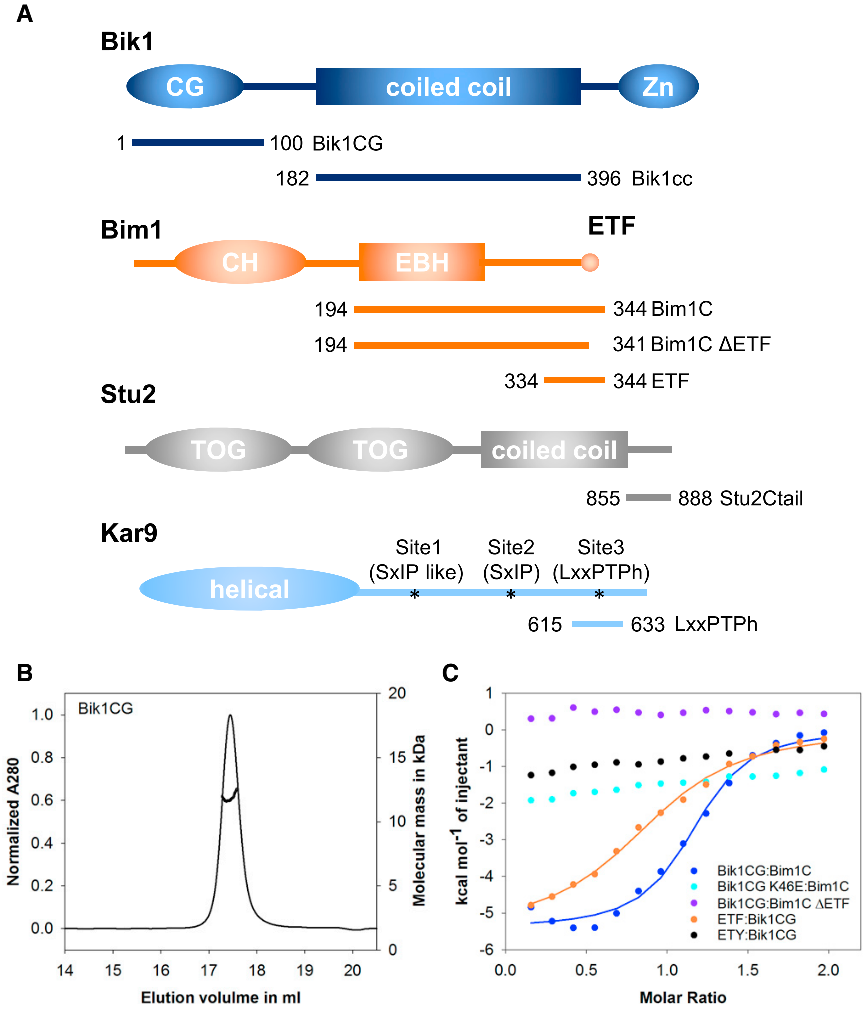

Figure 1. Schematic Representations of Proteins and Constructs Used in this Study

(A) Respective protein fragments are labeled and indicated by lines and residue boundaries. Asterisks in Kar9 indicate the positions of the Bim1-interacting site 1, site 2, and site 3 (Manatschal et al., 2016). CG, CAP-Gly; Zn, zinc finger; CH, calponin homology; EBH, end binding (EB) homology; TOG, tumor overexpressed gene.

(B) SEC-MALS experiment of Bik1CG. The UV absorption at 280 nm and the molecular masses across the peak determined by MALS are plotted.

(C) ITC experiments for Bik1CG:Bim1C (blue closed circles), Bik1CG K46E:Bim1C (cyan closed circles), Bik1CG:Bim1C ΔETF (purple closed circles), ETF:Bik1CG (orange closed circles), and ETY:Bik1CG (black closed circles). Solid lines are the fits that were obtained by using the monomeric concentrations of the proteins.

See also Table S1 and Figure S1.

Here, using biophysical methods in combination with mutagenesis, we found that the CAP-Gly domain of Bik1 (Bik1CG) binds to the C-terminal ETF peptide of Bim1 in the low-micromolar range. In contrast to the CAP-Gly domains of CLIP-170 and p150glued, the Bik1CG showed strict specificity, preventing it from binding to Bim1 when the terminal phenylalanine was substituted by a tyrosine residue. Furthermore, unlike CLIP-170-EB1 and p150glued-EB1, the Bik1-Bim1 complex allows SxIP and LxxPTPh motifs to bind. The crystal structures of the Bik1CG alone and in complex with an ETF peptide identifies essential residues for the formation of the Bik1-Bim1 complex in both Bik1 and Bim1. We used this structural information to assess the role of the Bik1-Bim1 interaction in controlling Bik1 localization, astral microtubule length, and spindle positioning.

RESULTS

Biophysical Characterization of the Bik1-Bim1 Interaction

To quantitatively analyze the interaction of the Bik1CG with the C terminus of Bim1 (Bim1C) (Figures 1A and S1) (Blake-Hodek et al., 2010), we purified these recombinant protein fragments from bacteria. Bim1C forms dimers in solution (Blake-Hodek et al., 2010; Hüls et al., 2012; Manatschal et al., 2016). As shown in Figure 1B, size-exclusion chromatography followed by multi-angle light scattering (SEC-MALS) revealed a molecular mass for Bik1CG of 11.6 kDa, consistent with the presence of a monomer (calculated molecular mass of the Bik1CG monomer construct: 11.2 kDa). Complex formation between Bik1CG monomers and Bim1C dimers was monitored by isothermal titration calorimetry (ITC). The data presented in Figure 1C demonstrate that two Bik1CG monomers bind one Bim1C dimer with an equilibrium dissociation constant (K_D) of 1.2 ± 0.3 μM.

Bim1C contains the EB-homology (EBH) domain and a C-terminal disordered tail region that terminates with an EEY/F motif (ETF in the case of Bim1C; Figure 1A). To test the exact interaction mode of Bik1CG with Bim1C, we performed ITC experiments with a Bim1C version that lacks the last three C-terminal residues (Bim1C ΔETF) and with a Bim1-derived peptide containing the ETF motif. As shown in Figure 1C, one Bik1CG monomer bound one ETF peptide with a K_D of 5.6 ± 0.8 μM. In contrast, no interaction was observed between Bik1CG and Bim1C ΔETF (Figure 1C). Thus, the interaction between Bik1CG and Bim1C is primarily mediated by the ETF motif of Bim1.

Crystal Structures of Bik1CG and the Bik1CG-Bim1C Complex

To obtain a detailed insight into how Bik1 and Bim1 interact with each other, we solved the structure of Bik1CG alone and in complex with the C-terminal ETF peptide of Bim1C (denoted Bik1CG-ETF) to 1.9 and 1.8 Å resolution, respectively (Table 1). As shown in Figure 2A, the globular apo Bik1CG structure contains a highly twisted, five-stranded antiparallel β sheet that is flanked by a small β hairpin on its convex side, structural features

Table 1. X-Ray Data Collection and Refinement Statistics

	Bik1CG	Bik1CG-ETF
Data collection[a]		
Space group	$P4_1 2_1 2$	$P4_1 2_1 2$
Cell dimension		
a, b, c (Å)	53.7, 53.7, 61.4	53.6, 53.6, 62.0
α, β, γ (°)	90, 90, 90	90, 90, 90
Resolution (Å)[b]	40.4–1.88 (1.95–1.88)	40.55–1.8 (1.87–1.8)
R_{meas} (%)	10.0 (97.8)	28.7 (438.0)
R_{pim} (%)	2.0 (19.9)	5.7 (88.5)
CC½[c]	99.9 (85.9)	99.8 (38.8)
I/σI	28.2 (3.4)	13.2 (0.9)
Completeness (%)	99.8 (98.4)	100 (99.8)
Redundancy	25.0 (22.5)	25.3 (24.1)
Refinement		
Resolution (Å)	40.4–1.88	40.54–1.8
No. of unique reflections	7,731	8,808
$R_{\text{work}}/R_{\text{free}}$ (%)	16.7/19.7	18.5/22.9
Average B factors	34.3	33.6
RMSD from ideality		
Bond length (Å)	0.02	0.02
Bond angles (°)	1.84	1.68
Ramachandran statistics (%)[d]		
Favored regions	97.6	97.6
Allowed regions	2.4	2.4
Outliers	0	0

[a] Highest-resolution shell statistics are in parentheses. RMSD, root-mean-square deviation.

[b] The resolution cutoff was selected based on I/σI and CC½ according to Karplus and Diederichs (2012).

[c] CC½ is the percentage of correlation between intensities from random half-datasets.

[d] As defined by MolProbity (Davis et al., 2004).

that are characteristic of the CAP-Gly fold (reviewed in Steinmetz and Akhmanova, 2008). The structure is complemented by two unique α helices that pack against the concave side of the central β sheet, secondary structure elements that have not been observed in any CAP-Gly structure solved until now. Most of the glycine residues that are highly conserved across CAP-Gly domains are involved in shaping the loop regions of the Bik1CG structure. Furthermore, a unique cluster of conserved hydrophobic residues that pack against each other forms a solvent-exposed cavity bordered by the distinctive GKNDG sequence motif (Figure 2B); this cavity binds C-terminal EEY/F motifs (reviewed in Steinmetz and Akhmanova, 2008).

Superimposition of Bik1CG with the first CAP-Gly domain of CLIP-170 (CLIP170CG1) (Weisbrich et al., 2007) and that of p150glued (p150CG) (Honnappa et al., 2006) revealed that, with the exception of helices H1 and H2, which are unique to Bik1CG, the domains are very similar (root-mean-square deviation $[\text{RMSD}]_{\text{Bik1CG-CLIP170CG1}}$: 0.7 Å over 43 Cα atoms; $\text{RMSD}_{\text{Bik1CG-p150CG}}$: 0.8 Å over 45 Cα atoms). However, inspection of the hydrophobic cavities of Bik1CG, CLIP170CG, and p150glued revealed a prominent difference in the β2-β3 loop that adopts a more “open” conformation in the case of Bik1CG (Figure 2C). This difference is most likely due to Thr30 of Bik1CG, which adopts an “outward,” exposed conformation. In contrast, the corresponding residue in CLIP170CG and p150CG is occupied by a phenylalanine that assumes an “inward” conformation and whose side chain packs against surrounding hydrophobic core CAP-Gly residues (Figure 2C). As a consequence, the hydrophobic cavities of CLIP170CG and p150CG, which are essentially identical, is shallower than that of Bik1CG. However, the open conformation of the β2-β3 loop as well as the N- and C-terminal flanking helices are very likely to be conserved in budding yeast Bik1 proteins (Figure S2), suggesting functional conservation across budding yeast species. Collectively, these observations indicate that the hydrophobic cavity of the Bik1CG is shaped distinctly from that of its metazoan ortholog CLIP-170.

Whereas CLIP170CG1 binds primarily the C-terminal EEY peptide of EB1, p150CG simultaneously binds both EEY and the EBH domain (Weisbrich et al., 2007; Honnappa et al., 2006; Mishima et al., 2007; Bjelić et al., 2012). The determinant discriminating between the single and bipartite binding mode is primarily a residue in the β2-β3 loop of the CAP-Gly domain, Ala49 and Glu79 of p150CG and CLIP170CG1, respectively (Figure 2E). In the case of p150CG, the Ala49 side chain packs against the hydrophobic groove of the EBH domain of EB1, while, in the case of CLIP170CG1, the Glu79 side chain is expected to inhibit such an interaction (Honnappa et al., 2006; Bjelić et al., 2012). In Bik1CG, the equivalent β2-β3 loop residue position is occupied by a proline (Pro27). To understand why Bik1CG does not interact with Bim1C-ΔETF in solution (Figure 1C), we superimposed the Bik1CG structure onto that of p150CG in complex with the C-terminal domain of EB1 (Honnappa et al., 2006; Bjelić et al., 2012). As illustrated in Figure 2D, this analysis reveals that Pro27 of Bik1CG substitutes well for the alanine in p150CG, thus making an interaction of the β2-β3 loop of Bik1CG with the EBH domain of Bim1 in principle possible. However, we observed that the unique N-terminal helix H1 of Bik1CG seriously clashes into the four-helix bundle of the EBH domain of EB1 (Figure 2D). This observation explains why Bik1CG does not interact with Bim1C ΔETF.

Next, we inspected the structure of the Bik1CG-ETF complex. Superimposition of Bik1CG and Bik1CG-ETF revealed that, besides an outward movement of the side chain of Lys31, which is needed to accommodate binding of the ETF peptide to Bik1CG, no additional conformational changes are observed ($\text{RMSD}_{\text{Bik1CG-Bik1CG-ETF}}$: 0.1 Å over 79 Cα atoms). As expected, the ETF peptide is bound to the hydrophobic cavity of Bik1CG, which is bordered by the highly conserved GKNDG motif (Figure 3A). Well-defined electron density is seen for the TF dipeptide and for the main chain of the glutamate residue of ETF. The side chain of Phe344 of the ETF peptide is deeply inserted into the hydrophobic cavity of Bik1CG, which is shaped by the side chains of Val28, Lys31, Phe35, Phe51, and Phe67 (Figure 3B). Three prominent hydrogen-bonding interactions are established between the carboxylate and main chain amide group of Phe344 of ETF and the side chain and main chain of Asn47 (the asparagine of the GKNDG motif) and Ph67 of Bik1CG (Figure 3C). Three additional hydrogen bonds are formed between the main chain of Phe344 and side chain of Thr343 of ETF and the side

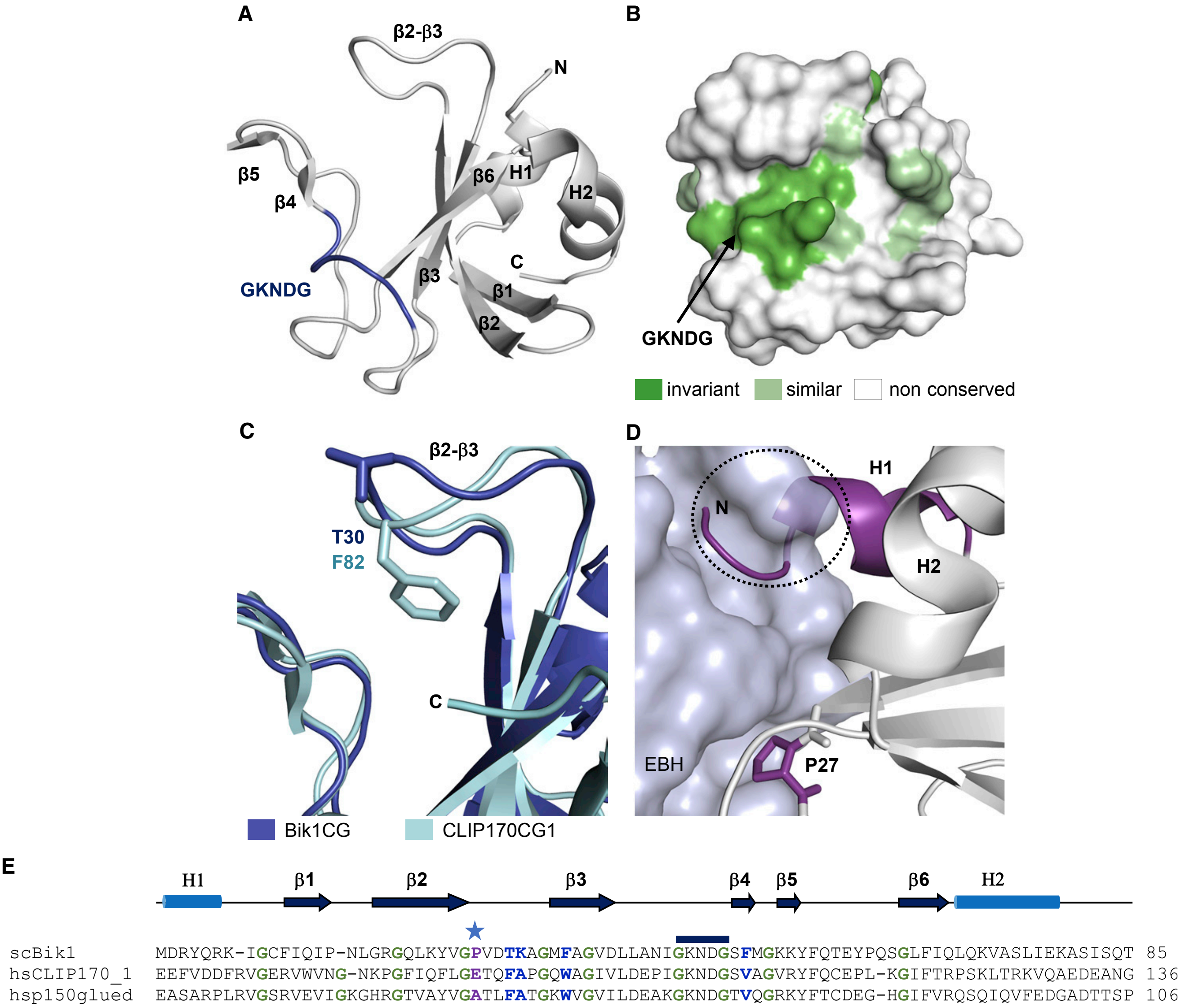
A
β2-β3
N
β5
β4
β6
H1
H2
GKNDG
β3
C
β1
β2
B
GKNDG
🟩 invariant
🟩 similar
☐ non conserved
C
β2-β3
T30
F82
C
🟦 Bik1CG
🟦 CLIP170CG1
D
H1
N
H2
EBH
P27
E
H1
β1
β2
β3
β4
β5
β6
H2
★
scBik1 MDRYQRK-IGCFIQIP-NLGRGQLKYVGPVDTKAGMFAGVDLLANIGKNDGSFMGKKYFQTEYPQSGLFIQLQKVASLIEKASISQT 85
hsCLIP170_1 EEFVDDFRVGERVWVNG-NKPGFIQFLGETQFAPGQWAGIVLDEPIGKNDGSVAGVRYFQCEPL-KGIFTRPSKLTRKVQAEDEANG 136
hsp150glued EASARPLRVGSRVEVIGKGHRGTVAYVGATLFATGKWVGVILDEAKGKNDGTVQGRKYFTCDEG-HGIFVRQSQIQVFEDGADTTSP 106

Figure 2. Crystal Structure of the Bik1CG

(A) Overall view of the Bik1CG structure in cartoon representation with the highly conserved GKNDG motif highlighted in light blue. Secondary structure elements are indicated. In contrast to the CAP-Gly domains of higher eukaryotes, Bik1CG possesses two additional helices (H1 and H2); see also (E).

(B) Surface representation of the Bik1CG structure with conserved residues between Bik1CG, CLIP170CG1, and p150CG highlighted in green.

(C) Superimposition of Bik1CG (dark blue) with CLIP170CG1 (cyan) (PDB: 2E3I) highlighting structural differences in the hydrophobic cavity of the two CAP-Gly domains.

(D) Close-up view of the superimposition of Bik1CG (cartoon representation) with p150CG (not shown for simplicity) in complex with the EBH domain of EB1 (surface representation; PDB: 2HKQ). The clash caused by the N-terminal helix H1 (shown in maroon) of Bik1CG with the EBH domain is highlighted with a dashed black circle. Pro27 of Bik1CG is shown in blue sticks representation.

(E) Sequence alignment of the CAP-Gly domains of Bik1, CLIP-170 (CG1), and p150glued. The characteristic glycine residues and GKNDG motif of CAP-Gly domains are indicated in green and with a black horizontal bar on top of the alignment, respectively. The position of the β2-β3 loop residue that in the case of p150CG interacts with the EBH domain of EB1 (Ala49; Honnappa et al., 2006) is highlighted with an asterisk, and the corresponding residues are shown in bold and purple. Key residues of the exposed hydrophobic cavity of CAP-Gly, which are discussed in the text, are shown in bold and dark blue. Note that helices H1 and H2 (indicated in light blue) are only found in Bik1.

See also Figure S2.

chain of Lys46 of Bik1CG (the lysine of the GKNDG motif), and through a water molecule between the main chain of Glu342 of ETF and the main chain of Gln69 and the side chain of Lys72 of Bik1CG (Figure 3C). The apparent importance of Lys46 of the GKNDG motif of Bik1CG for Bim1C binding was tested by mutagenesis. As documented in Figure 1C, mutating this residue to glutamate (Bik1CG K46E) is sufficient to abrogate binding of the mutant domain to Bim1C in ITC experiments.

Comparison of the Bik1CG-ETF binding mode with those seen in the complex structures formed between p150CG and the

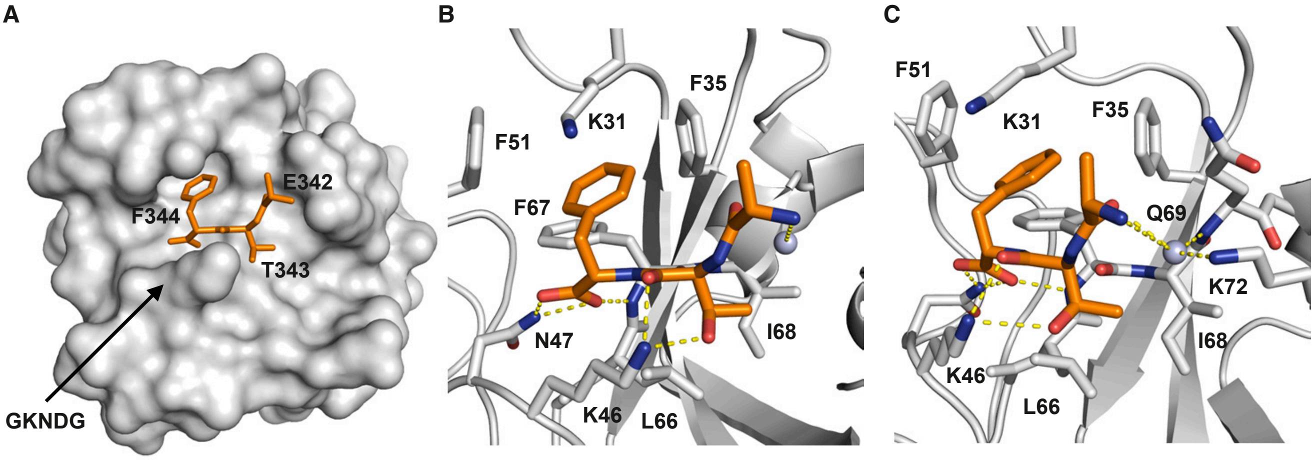

Figure 3. Crystal Structure of the Bik1CG-ETF Complex

(A) Overall view of the heterodimeric complex formed between Bik1CG (gray surface representation) and the ETF peptide of Bim1 (orange sticks representation).
(B and C) Two close-up views of the complex formed between Bik1CG (gray) and the ETF peptide of Bim1 (orange) 90° apart. Interacting residues are shown in sticks representation.

C-terminal EEY peptide of EB1 (Honnappa et al., 2006; Bjelić et al., 2012), between p150CG and the C-terminal ETF peptide of CLIP-170 (Weisbrich et al., 2007), and between CLIP170CG1 and the C-terminal GCY peptide of SLAIN2 (van der Vaart et al., 2011), revealed that the CAP-Gly-EEY/F motif binding modes are overall similar for all four complex structures (Figures 4A and B). However, and interestingly, we noted that the terminal Phe344 residue of the ETF peptide of Bim1C is much deeper inserted into the binding pocket compared with its aromatic residue counterparts of the other CAP-Gly-EEY/F motif complex structures. This deeper insertion of Phe344 is most likely achieved due to the open conformation of the β2-β3 loop, which widens the cavity. In addition, the side chains of Lys31 and Phe51 of Bik1CG, which are substituted by Ala and Val, respectively, in both p150CG and CLIP170CG1, allow for a more extensive packing with the C-terminal phenylalanine residue of the Bim1 ETF peptide (Figure 4C).

Modeling of the binding mode of the Bim1 ETF peptide in the context of CLIP170CG1 or p150CG revealed that the terminal phenylalanine side chain of ETF would clash into the phenylalanine residue forming the floor of the cavity (Phe52 in the case of p150CG; Figure 4C) due to the more closed conformation adopted by the β2-β3 loop of both these CAP-Gly domains (Figure 4D). Inversely, computational replacement of the phenylalanine residue of ETF in the Bik1CG-ETF complex structure by a tyrosine indicates that its polar side chain OH group would be placed in a strongly hydrophobic environment and would probably even clash into the protein domain (not shown). To test this hypothesis, we performed ITC experiments with a mutant C-terminal Bim1C ETF peptide variant in which the terminal phenylalanine was replaced by a tyrosine (ETY peptide). As shown in Figure 1C, binding of the ETY peptide to Bik1CG was essentially abrogated compared with the wild-type ETF peptide.

Taken together, these results reveal the structural basis of the Bik1-Bim1 interaction and establish the Bik1CG as a C-terminal phenylalanine recognition domain. Notably, the unique phenylalanine-binding pocket of Bik1 CAP-Gly enables the domain to achieve a 1–2 orders of magnitude higher affinity toward C-terminal EEF motifs compared with the CAP-Gly domains of CLIP-170 or p150glued, which target both EEY and EEF motifs (Weisbrich et al., 2007; Honnappa et al., 2006; Bjelić et al., 2012).

Interaction of the Bik1-Bim1 Complex with +TIP Partners

As mentioned in the Introduction, Bik1 has the capacity to interact directly or indirectly with additional +TIP partners, including Kar9 and Stu2 (Figure S1). For instance, the C-terminal unstructured domain of Kar9 interacts with Bim1C via SxIP and LxxPTPh motifs (Figure 1A), which bind to the EBH domain of Bim1C (Manatschal et al., 2016; Kumar et al., 2017). This observation suggests that Kar9 binds mainly indirectly to Bik1 via Bim1. To test this hypothesis, we performed ITC experiments with the Bik1CG-Bim1C complex and SxIP and LxxPTPh peptides. As shown in Figures 5A and B, and summarized in Table S1, the Bik1CG-Bim1C complex binds SxIP or LxxPTPh peptides with K_D values of 13 ± 0.6 and 2.7 ± 0.5 μM, respectively, values that are close to those obtained with Bim1C alone. We also assessed the affinity of the Bim1C-SxIP complex toward Bik1CG, and obtained a very similar K_D as for the Bim1C-Bik1CG interaction (Table S1). Collectively, these results suggest that Kar9 can indeed bind Bik1 indirectly via Bim1.

Next, we tested whether Stu2 binds Bik1 directly or indirectly. Two-hybrid, coimmunoprecipitation, and *in vitro* binding assays suggested an interaction between the predicted coiled-coil domain of Bik1 (Bik1cc) and the C-terminal disordered tail region of Stu2 (Stu2Ctail) (Wolyniak et al., 2006). To reconstitute a putative Bik1cc-Stu2Ctail complex, we purified the corresponding recombinant protein fragments from bacteria. The secondary structure and stability of Bik1cc were assessed by circular dichroism (CD) spectroscopy. As shown in Figure 6A, the far-UV CD spectrum of the protein recorded at 5°C displays minima at 208 and 222 nm, which is characteristic of α-helical

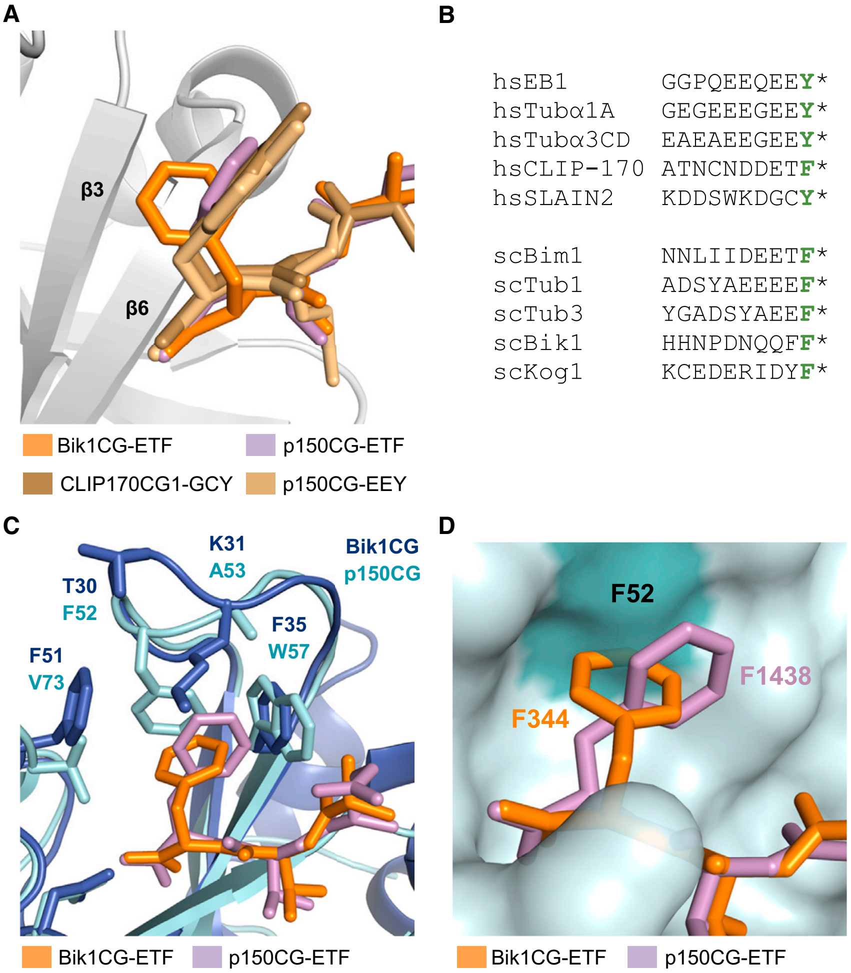

Figure 4. Analysis of the Bik1CG-ETF Complex

(A) Superimposition of Bik1CG-ETF compared with those complex structures formed between CLIP170CG1 and the C-terminal GCY peptide of SLAIN2 (CLIP170CG1-GCY) (PDB: 3RDV), between p150CG and the C-terminal ETF peptide of CLIP-170 (p150CG-ETF) (PDB: 3E2U), and between p150CG and the C-terminal EEY peptide of EB1 (p150CG-EEY) (PDB: 2HL3). For simplicity, only the structure of Bik1CG is shown in cartoon representation. The different peptide motifs are shown in sticks representation.

(B) Sequence alignment of human proteins containing C-terminal EEY motifs and yeast proteins containing C-terminal EEF motifs.

(C) Superimposition of the Bik1CG-ETF (dark blue) and p150CG-ETF (cyan) complex structures (cartoon representation). Interacting residues are shown in sticks representation.

(D) Close-up view of (C) with p150CG in semi-transparent surface representation.

proteins. Upon heating and recording of the CD signal at 222 nm, a cooperative thermal unfolding profile with a midpoint of the transition at 37°C was obtained for Bik1cc (Figure 6B). The oligomerization state of Bik1cc in solution was assessed by SEC-MALS, which yielded a molecular mass of 50.6 kDa, consistent with the formation of a dimer (calculated molecular mass of the Bik1cc monomer: 25.5 kDa; Figure 6C). These results suggest that Bik1cc folds into a two-stranded coiled-coil structure.

The interaction between Bik1cc and Stu2Ctail was subsequently assessed by ITC. The data shown in Figure 6D revealed that one Stu2Ctail peptide binds one Bik1cc dimer with a K_D of 0.6 ± 0.1 μM. Stu2Ctail has also been reported to interact with Bim1C (Wolyniak et al., 2006); however, we were not able to detect such an interaction in ITC experiments (Figure 5D). +TIP peptide regions that bind to the C-terminal domain of EB proteins typically contain SxIP or LxxPTPh motifs (Honnappa et al., 2009; Kumar et al., 2017). No such motifs were found in the Stu2Ctail sequence, explaining the inability of this Stu2 region to interact with Bim1C (Wolyniak et al., 2006). Taken together, these results establish a molecular and quantitative basis for understanding the indirect interaction between Bik1 and Kar9, the direct interaction between Bik1 and Stu2, and the indirect interaction between Stu2 and Bim1.

Role of Bik1 CAP-Gly Domain-Mediated Interactions *In Vivo*

Although it has been shown that the accumulation of Bik1 on microtubule plus-ends relies on both Bim1 and α-tubulin (Caudron et al., 2008), it is unknown whether this dependency stems from the direct interaction between the Bik1 CAP-Gly domain and the C-terminal EEF motifs of Bim1 and α-tubulin. To dissect the function of the Bik1-Bim1 complex and other Bik1 CAP-Gly domain-mediated interactions, we created yeast strains that specifically lose the Bik1-Bim1 interaction by deleting the C-terminal ETF peptide of Bim1 (Bim1 ΔETF) or strains bearing the K46E point mutation in the Bik1 CAP-Gly domain (Bik1 K46E), which fail to interact with EEY/F motifs. Interestingly, the Bim1 ΔETF cells did not show any growth defect on YPD plates, while Bik1 K46E mutant cells exhibited a severe growth defect, similar to the *bik1Δ* mutant cells (Figure 7A). This result suggests that the interaction of the Bik1CG with EEF is essential for Bik1 function. Furthermore, binding to the ETF peptide of Bim1 is not sufficient to express the full function of the CAP-Gly domain of Bik1.

We next assessed the impact of these mutations on the recruitment of Bik1-3xGFP to astral microtubule plus-ends. As shown in Figures 7B–7D, the disruption of Bik1-Bim1 interaction either by deleting BIM1 or its C-terminal ETF peptide, reduced the accumulation of Bik1-3xGFP on plus-ends by more than 35%. Interestingly, we noticed that a substantial amount of Bik1-3xGFP binds microtubule lattices upon loss of the Bik1-Bim1 interaction. This dramatic change is quantified by line scan analyses of Bik1-3xGFP fluorescence intensity along microtubules from plus-ends toward the spindle pole bodies (SPBs) (Figures 7B–7D). Furthermore, concomitant disruption of Bik1-Bim1 and Bik1-α-tubulin interactions by

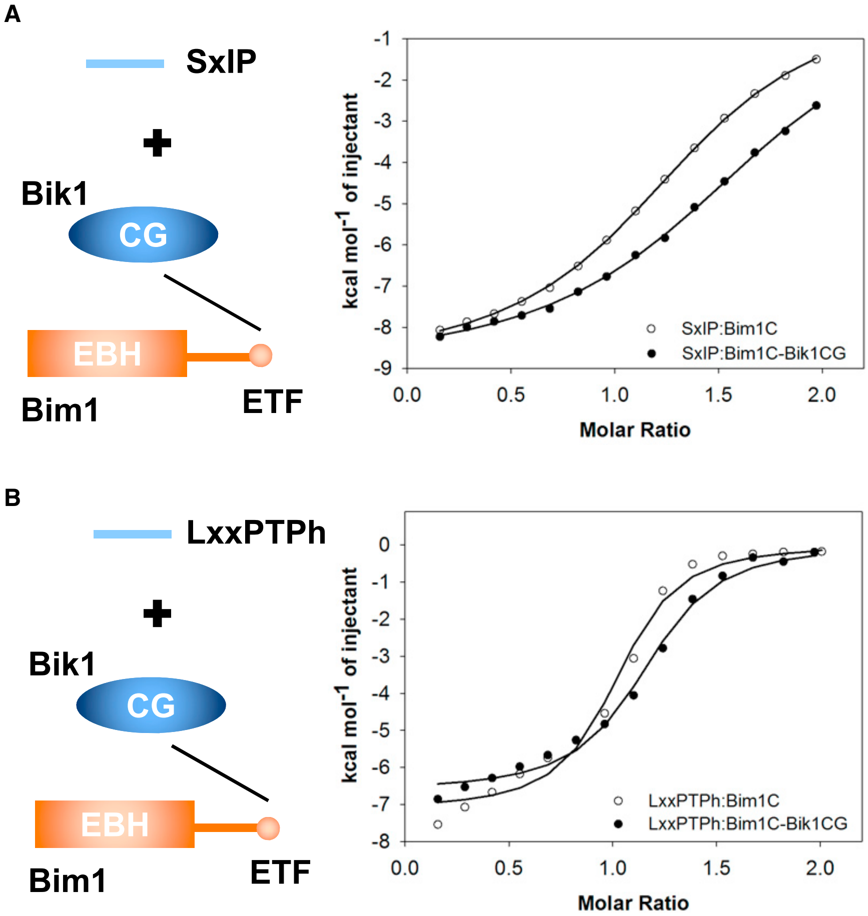

Figure 5. Ternary Complex Formation of Bik1-Bim1 with SxIP or LxxPTP Motifs

(A) ITC experiment for SxIP:Bim1C (open circles) and SxIP:Bim1C-Bik1CG (closed circles). Solid lines are the fits that were obtained by using the monomeric concentrations of the proteins.

(B) ITC experiments for LxxPTPh:Bim1C (open circles) and LxxPTPh:Bim1C-Bik1CG (closed circles).

Solid lines are the fits that were obtained by using the monomeric concentrations of the proteins and peptides.

See also Table S1 and Figure S1.

introducing the K46E substitution in the Bik1CG drastically reduced the Bik1 K46E-3xGFP intensity both at the plus-ends and along astral microtubules. Only around 17.7% of the Bik1 K46E-3xGFP mutant metaphase cells (77 out of 436) demonstrated detectable signal on astral microtubule plus-ends. In those cells, the Bik1 K46E-3xGFP focus on astral microtubule plus-ends was very faint. These observations establish two points. First, Bik1 interacts with microtubules essentially through binding to EEF motifs, i.e., to the C-terminal tails of Bim1 and α-tubulin. Second, somehow Bim1 helps displacing Bik1 from the microtubule shaft.

Next, we investigated the consequences of abrogating the Bik1-Bim1 interaction on microtubule dynamics in metaphase. Using Bik1-3xGFP and Spc72-GFP as microtubule plus-end and minus-end markers, respectively, we measured the maximum 3D length and lifetime of individual astral microtubules over an image acquisition window of 85.6 s. Deletion of BIM1 increased the maximum astral microtubule length from 2.08 ± 0.62 to 3.54 ± 0.76 μm (mean ± SD). The lifetimes of astral microtubules were also increased (Figures 7E and 7F). These observations support the idea of EB proteins being microtubule-destabilization factors by accelerating GTP hydrolysis in the GTP cap of growing microtubules (Maurer et al., 2014). Importantly, the loss of the Bik1-Bim1 interaction in Bim1 ΔETF cells increased the size of astral microtubules to 2.62 ± 0.72 μm (mean ± SD) (Figures 7E and 7F). Knowing that Bik1 functions as a microtubule-stabilizing factor *in vivo* (Carvalho et al., 2004; Caudron et al., 2008), together with the fact that the Bik1 amount is reduced on astral microtubule plus-ends in Bim1 ΔETF cells (Figures 7C and 7D), we reasoned that Bik1 could promote the microtubule-destabilizing activity of Bim1. Unfortunately, the very low intensity of Bik1 K46E-3xGFP on plus-ends prevented us from quantifying astral microtubule behavior in these cells. Together, these data demonstrate that the interaction of Bik1 with Bim1 and α-tubulin, mediated by the Bik1 CAP-Gly domain, ensures the accumulation of Bik1 on the plus-end of microtubules, while displacing it from the microtubule lattice. They further reveal that the Bik1-Bim1 interaction promotes astral microtubule destabilization.

To test whether the Bik1-Bim1 interaction contributes to spindle positioning during metaphase, we introduced the Bik1 K46E and Bim1 ΔETF mutations into strains expressing the Tub1 protein tagged with CFP to visualize the mitotic spindle, where the Kar9 protein was tagged with 3xsfGFP To assess the function of Kar9 during metaphase, we measured the relative spindle positioning to the mother-bud neck and the alignment along the mother-bud axis in wild-type cells. We then compared these results across strains bearing the *bik1 K46E*, the *bim1 ΔETF*, and the *kar9Δ* genotypes. As shown in Figures 7G and 7H, disrupting the Bik1-Bim1 interaction by either mutating Bik1 or Bim1 did not interfere with Kar9 localization and function. On the contrary, the mutations disrupting the Bik1-Bim1 interaction caused a slight improvement of spindle positioning compared with wild-type (Figure 7I). Thus, the disruption of the Bik1-Bim1 interaction impairs the proper localization of Bik1 at microtubule plus-ends, resulting in longer microtubules, whereas there is no significant effect on Kar9 localization, Kar9 asymmetry, and spindle positioning.

DISCUSSION

Although a rudimentary understanding of the interactions mediated by the CLIP-170 family member Bik1 with protein partners is available, it is unclear whether these interactions are direct or

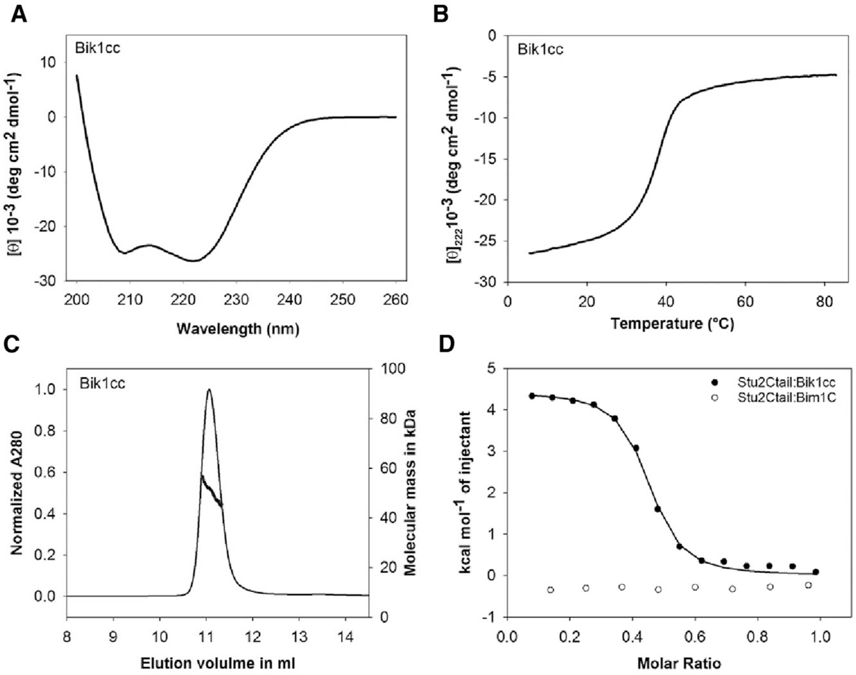

Figure 6. Biophysical Characterization of Bik1 Interactions

(A and B) CD spectrum (A) and thermal unfolding profile recorded at 222 nm (B) of Bik1cc.

(C) SEC-MALS experiment of Bik1cc. The UV absorption at 280 nm and the molecular masses across the peak determined by MALS are plotted.

(D) ITC experiments for Stu2Ctail:Bik1cc (closed circles) and Stu2Ctail:Bim1C (open circles). The solid line represents the fit that was obtained by using the monomeric concentrations of Bik1cc and Stu2Ctail.

See also Table S1 and Figure S1.

indirect. Furthermore, quantitative and structural information on Bik1-mediated complexes is largely missing. The availability of such information is, however, important to understand how Bik1 interactions contribute to its functions.

In this study, we found that the Bik1CG is a specific C-terminal phenylalanine recognition domain. Interestingly, besides Bim1 C-terminal phenylalanine residues that are targeted by the Bik1CG are also present in the budding yeast proteins α-tubulin and the TORC1 subunit Kog1/Raptor (Badin-Larçon et al., 2004; van der Vaart et al., 2017). In contrast, proteins that are targeted by the CAP-Gly domains of mammalian CLIP-170 and p150glued contain predominantly C-terminal tyrosine residues (Figure 4B). Thus, besides offering detailed structural insights into the Bik1-Bim1 complex, our results also provide a basis for understanding the Bik1-α-tubulin and Bik1-Kog1/Raptor interactions. We further found that the Bik1CG contains a unique N-terminal helix that prevents interaction with the EBH domain of EBs; CLIP-170 CAP-Gly achieves a similar effect, however, through the presence of an unfavorable residue located in the β2-β3 loop of the domain (Honnappa et al., 2006). Collectively, these observations highlight that, within the CLIP-170 protein family, the CAP-Gly domain structurally evolved along different routes to nevertheless achieve a similar binding mechanism toward proteins containing C-terminal EEY and/or EEF motifs.

We also report that the Bik1CG-ETF complex can interact with SxIP or LxxPTPh peptides. Ternary +TIP complexes are thus likely to be formed, for example, between Bim1-Bik1 and Kar9 or the yeast kinesin motor Kip2, two +TIPs that contain SxIP and/or LxxPTPh motifs and which are important for spindle alignment and proper function of the motor dynein (Roberts et al., 2014; Manatschal et al., 2016; Kumar et al., 2017). Interestingly, and in contrast to Bik1-Bim1, the CLIP-170-EB1 complex is not capable to bind SxIP peptides (Duellberg et al., 2014). This evolutionary flexibility can be explained by the significantly shorter C-terminal tail sequence of EB1 compared with Bim1 (19 compared with 67 residues, respectively), which, upon CLIP-170 CAP-Gly binding, apparently hinders access of SxIP to its EB1-binding site in the CLIP-170-EB1 complex.

In addition to the CAP-Gly domain that mediates the interaction of Bik1 with Bim1, α-tubulin and Kog1/Raptor, we found that the Bik1cc binds the C-terminal tail region of Stu2 with high affinity. The fact that Bik1 forms complexes with several protein partners through its different domains suggests that Bik1 acts as an adaptor protein that can link different activities to the same location. Although Stu2 is an autonomous +TIP (Podolski et al., 2014), the indirect interaction to Bim1 through Bik1 is likely relevant to enhance its localization to the otherwise crowded environment of the microtubule plus-end. Stu2 has also been reported to interact with Kar9 (Moore and Miller, 2007), which creates an additional indirect link between Stu2 and the Bik1-Bim1 complex. Interestingly, in fission yeast the Bim1 ortholog Mal3 is capable of directly interacting with the Stu2 paraloglog Dis1 via an LxxPTPh motif (Matsuo et al., 2016; Kumar et al., 2017). In higher eukaryotes, SLAIN2 forms an adaptor complex with CLIP-170 to indirectly link the Stu2 ortholog ch-TOG to EBs at growing microtubule plus-ends (van der Vaart et al., 2011). Taken together, these biophysical and structural considerations highlight the complex topology that +TIP networks can adopt at growing microtubule plus-ends, and whose connectivity and interaction strength of individual nodes can vary from one species to the other, although the involved domains and motifs belong to the same protein family.

The structure of the Bik1CG-ETF complex allowed us to rationally mutate residues with the aim to perturb the Bik1-Bim1 interaction *in vivo*. We found that deleting the ETF motif of Bim1 resulted in a reduction in Bik1 localization to microtubule plus-ends, and an increase in the amount of Bik1 decorating microtubule shafts, probably via the EEF motif of α-tubulin. The remaining tip-localized pool could be maintained through Stu2-binding, transport of Bik1 via the kinesin motor Kip2 (Carvalho et al., 2004), and through interactions

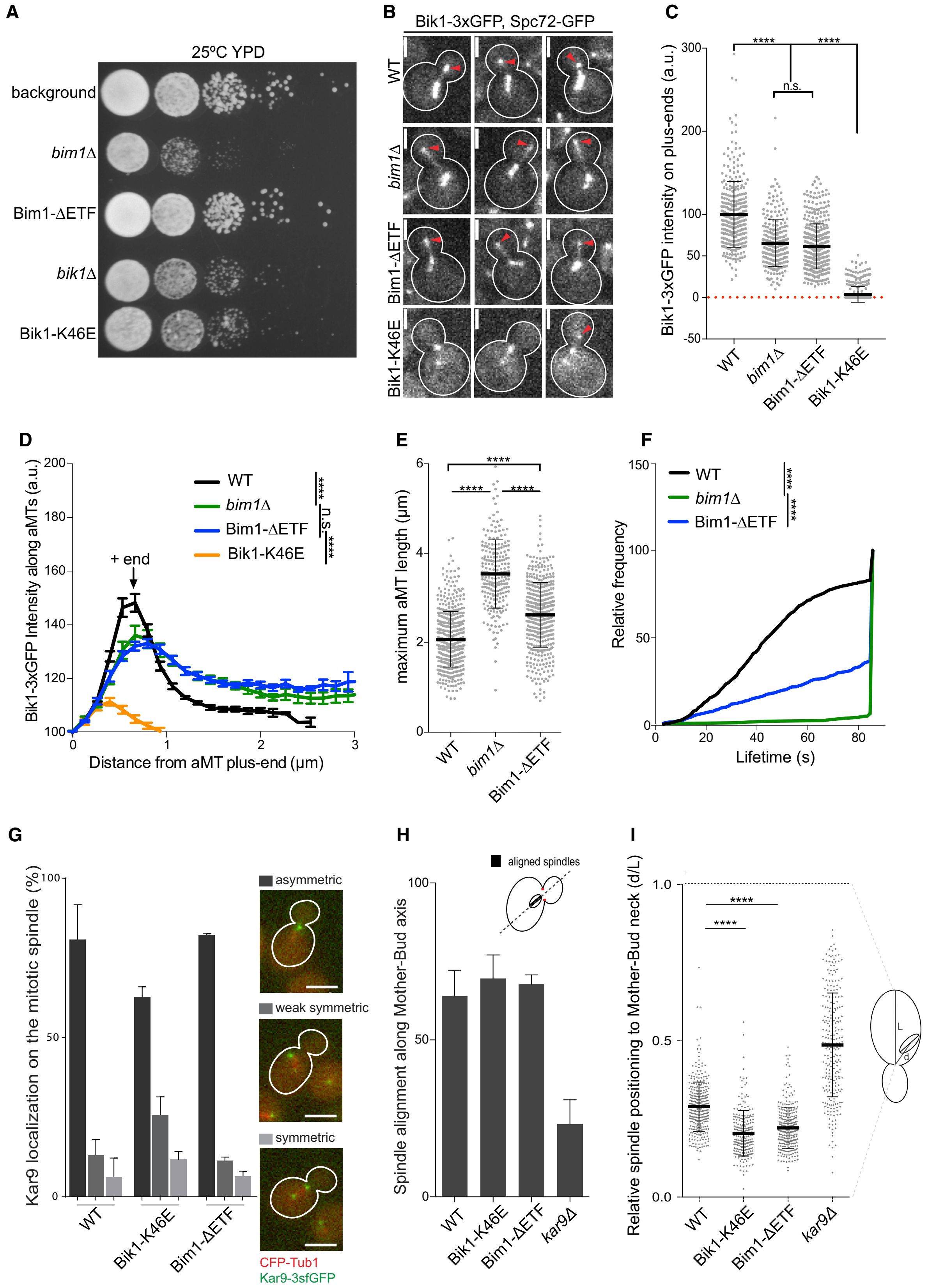

(legend on next page)

with the EEF motif of α-tubulin (Badin-Larçon et al., 2004). Thus, and as reported earlier (Caudron et al., 2008), it seems that Bik1 exhibits two partially redundant mechanisms for localizing to microtubule plus-ends. The increased levels of Bik1 on microtubule shafts suggests that somehow Bim1 helps removing Bik1 from microtubules, perhaps by competing with α-tubulin.

Interestingly, the average microtubule length was increased in a Bim1 ΔETF background, but remained still smaller than in the Bim1 delete strain. The most likely explanation for this intermediate phenotype is that, in the Bim1 delete background, many more Bim1-dependent interactions are perturbed compared with Bim1 ΔETF, thus resulting in a stronger microtubule length phenotype. The disruption of the Bik1-Bim1 interaction did not significantly perturb the asymmetric positioning of Kar9 and, accordingly, the positioning and alignment of the mitotic spindle. It has been reported that the deletion of Bik1 resulted in partial loss of Kar9 asymmetry (Moore et al., 2006). In this context, our data suggest that this Bik1-dependent Kar9 asymmetry does not rely on the Bik1-Bim1 interaction. In conclusion, our study provides detailed mechanistic and functional insights into key interactions mediated by Bik1 and protein partners. It further offers a basis to rationally perturb +TIP interactions *in vivo* with the aim to understand +TIP network functioning at the systems level.

STAR★METHODS

Detailed methods are provided in the online version of this paper and include the following:

- KEY RESOURCES TABLE
- CONTACT FOR REAGENT AND RESOURCE SHARING
- EXPERIMENTAL MODEL DETAILS
- METHOD DETAILS
    - ○ Protein and Peptide Preparations
    - ○ Circular Dichroism (CD) Spectroscopy
    - ○ Size Exclusion Chromatography Followed by Multi-Angle Light Scattering (SEC-MALS)
    - ○ Isothermal Titration Calorimetry (ITC)
    - ○ X-Ray Data Collection and Structure Determination
    - ○ Measurements of Astral Microtubule Behavior and Bik1-3xGFP Distribution in *S. Cerevisiae* Strains
    - ○ Localization of Kar9 in Bim1 ΔETF or Bik1 K46E *S. Cerevisiae* Strains
- QUANTIFICATION AND STATISTICAL ANALYSIS
- DATA AND SOFTWARE AVAILABILITY

SUPPLEMENTAL INFORMATION

Supplemental Information includes two figures and two tables and can be found with this article online at https://doi.org/10.1016/j.str.2018.03.003.

ACKNOWLEDGMENTS

We are indebted to Alain Blanc for help with mass spectrometry, to Natacha Olieric for support with protein purification, and to Ashwani Sharma for technical assistance at the synchrotron beamlines. The X-ray data were collected at beamline X06DA of the Swiss Light Source (Paul Scherrer Institut, Villigen, Switzerland). This work was supported by a Marie Curie COFUND fellowship (to A.K.), and by grants from the Swiss National Science Foundation (31003A_166608; to M.O.S.) and from SystemsX.ch (RTD-TubeX; to Y.B. and M.O.S.).

AUTHOR CONTRIBUTIONS

M.M.S., A.K., X.C., A.-M.F., Y.B., and M.O.S. designed the research. M.M.S., A.K., X.C., and A.-M.F., performed the research. M.M.S., X.Z., A.-M.F., A.K., Y.B., and M.O.S. analyzed the data. M.M.S. and M.O.S. wrote the paper with input from all authors.

DECLARATION OF INTERESTS

The authors declare no competing interests.

Received: December 20, 2017
Revised: February 9, 2018
Accepted: February 28, 2018
Published: March 22, 2018

Figure 7. Role of the Bik1-Bim1 Interaction *In Vivo*

(A) Spot growth assay of background (Bik1-3xGFP, Spc72-GFP), *bim1Δ*, Bim1 ΔETF, and Bik1 K46E cells grown for 2 days on solid YPD agar at 25°C. Spots are from log-phase growing cell samples that was sequentially diluted 10-fold.

(B) Representative images of wild-type (WT), *bim1Δ*, and Bim1 ΔETF metaphase cells expressing Bik1-3xGFP or Bik1 K46E-3xGFP and Spc72-GFP. Red arrowhead marks aMT plus-end. Scale bars, 2 μm.

(C and D) Quantification of Bik1-3xGFP fluorescence intensity (a.u.) on aMT plus-ends (n > 250 cells pooled from three independent clones for each mutant, mean ± SD) or Bik1-3xGFP distribution along aMTs by line scanning (n > 30 for each mutant, mean ± SEM, only cells positive with Bik1 K46E-3xGFP signal on plus-ends were used in line scanning analysis) in WT, *bim1Δ*, Bim1 ΔETF, and Bik1 K46E metaphase cells. Statistical significance was calculated using two-tailed Student's t test.

(E and F) Measurements of maximum three-dimensional aMT length and lifetime within the 85.6 s image acquisition window in WT, *bim1Δ*, Bim1 ΔETF, and Bik1 K46E metaphase cells using Bik1-3xGFP and Spc72-GFP as the plus- and minus-end markers, respectively (n > 250 cells pooled from three independent clones for each mutant, mean ± SD). Statistical significances for aMT length were calculated using two-tailed Student's t test. Differences among lifetime were demonstrated with cumulative distribution plot and assessed with the Kolmogorov-Smirnov test. For all panels, ****p > 0.0001; n.s., not significant (Bik1 K46E not shown because MT length was not measurable).

(G) Kar9 localization and its quantification in metaphase cells bearing the WT, Bik1- K46E, or the Bim1 ΔETF mutations. The mean ± SD of three independent clones was plotted. n > 235 cells per strain. Scale bars, 2 μm.

(H) Percentage of aligned spindles in metaphase cells bearing the WT, Bik1 K46E, Bim1 ΔETF, or kar9Δ alleles; same cells were quantified as shown in (B). The mean ± SD of three independent clones was plotted.

(I) Relative positioning of the mitotic spindle within the mother cell (d/L; d is the spindle to bud-neck distance and L is the length of the mother cell). The data of three independent clones is represented as a scattered dot plot, showing the mean value ± SD. Statistical significances for spindle positioning was calculated using two-tailed Student's t test; ****p > 0.0001.

See also Table S2.

REFERENCES

Akhmanova, A., and Steinmetz, M.O. (2015). Control of microtubule organization and dynamics: two ends in the limelight. Nat. Rev. Mol. Cell Biol. *16*, 711–726.

Badin-Larçon, A.C., Boscheron, C., Soleilhac, J.M., Piel, M., Mann, C., Denarier, E., Fourest-Lieuvin, A., Lafanechère, L., Bornens, M., and Job, D. (2004). Suppression of nuclear oscillations in *Saccharomyces cerevisiae* expressing Glu tubulin. Proc. Natl. Acad. Sci. USA *101*, 5577–5582.

Bjelić, S., De Groot, C.O., Schärer, M.A., Jaussi, R., Bargsten, K., Salzmann, M., Frey, D., Capitani, G., Kammerer, R.A., and Steinmetz, M.O. (2012). Interaction of mammalian end binding proteins with CAP-Gly domains of CLIP-170 and p150(glued). J. Struct. Biol. *177*, 160–167.

Blake-Hodek, K.A., Cassimeris, L., and Huffaker, T.C. (2010). Regulation of microtubule dynamics by Bim1 and Bik1, the budding yeast members of the EB1 and CLIP-170 families of plus-end tracking proteins. Mol. Biol. Cell *21*, 2013–2023.

Buey, R.M., Sen, I., Kortt, O., Mohan, R., Gfeller, D., Veprintsev, D., Kretzschmar, I., Scheuermann, J., Neri, D., Zoete, V., et al. (2012). Sequence determinants of a microtubule tip localization signal (MtLS). J. Biol. Chem. *287*, 28227–28242.

Carvalho, P., Gupta, M.L., Jr., Hoyt, M.A., and Pellman, D. (2004). Cell cycle control of kinesin-mediated transport of Bik1 (CLIP-170) regulates microtubule stability and dynein activation. Dev. Cell *6*, 815–829.

Caudron, F., Andrieux, A., Job, D., and Boscheron, C. (2008). A new role for kinesin-directed transport of Bik1p (CLIP-170) in *Saccharomyces cerevisiae*. J. Cell Sci. *121*, 1506–1513.

Chen, V.B., Arendall, W.B., 3rd, Headd, J.J., Keedy, D.A., Immormino, R.M., Kapral, G.J., Murray, L.W., Richardson, J.S., and Richardson, D.C. (2010). MolProbity: all-atom structure validation for macromolecular crystallography. Acta Crystallogr. D Biol. Crystallogr. *66*, 12–21.

Cordingley, M.G., Callahan, P.L., Sardana, V.V., Garsky, V.M., and Colonno, R.J. (1990). Substrate requirements of human rhinovirus 3C protease for peptide cleavage in vitro. J. Biol. Chem. *265*, 9062–9065.

Davis, I.W., Murray, L.W., Richardson, J.S., and Richardson, D.C. (2004). MOLPROBITY: structure validation and all-atom contact analysis for nucleic acids and their complexes. Nucleic Acids Res. *32* (Web Server issue), W615–W619.

DeLano, W.L. (2002). The PyMOL Molecular Graphics System (DeLano Scientific).

Duellberg, C., Trokter, M., Jha, R., Sen, I., Steinmetz, M.O., and Surrey, T. (2014). Reconstitution of a hierarchical +TIP interaction network controlling microtubule end tracking of dynein. Nat. Cell Biol. *16*, 804–811.

Emsley, P., Lohkamp, B., Scott, W.G., and Cowtan, K. (2010). Features and development of coot. Acta Crystallogr. D Biol. Crystallogr. *66*, 486–501.

Honnappa, S., Okhrimenko, O., Jaussi, R., Jawhari, H., Jelesarov, I., Winkler, F.K., and Steinmetz, M.O. (2006). Key interaction modes of dynamic +TIP networks. Mol. Cell *23*, 663–671.

Honnappa, S., Gouveia, S.M., Weisbrich, A., Damberger, F.F., Bhavesh, N.S., Jawhari, H., Grigoriev, I., van Rijssel, F.J., Buey, R.M., Lawera, A., et al. (2009). An EB1-binding motif acts as a microtubule tip localization signal. Cell *138*, 366–376.

Howard, J., and Hyman, A.A. (2003). Dynamics and mechanics of the microtubule plus end. Nature *422*, 753–758.

Hüls, D., Storchova, Z., and Niessing, D. (2012). Post-translational modifications regulate assembly of early spindle orientation complex in yeast. J. Biol. Chem. *287*, 16238–16245.

Kabsch, W. (2010). XDS. Acta Crystallogr. D Biol. Crystallogr. *66*, 125–132.

Knop, M., Siegers, K., Pereira, G., Zachariae, W., Winsor, B., Nasmyth, K., and Schiebel, E. (1999). Epitope tagging of yeast genes using a PCR-based strategy: more tags and improved practical routines. Yeast *15*, 963–972.

Kumar, A., Manatschal, C., Rai, A., Grigoriev, I., Degen, M.S., Jaussi, R., Kretzschmar, I., Prota, A.E., Volkmer, R., Kammerer, R.A., et al. (2017). Short linear sequence motif LxxPTPh targets diverse proteins to growing microtubule ends. Structure *25*, 924–932.

Karplus, P.A., and Diederichs, K. (2012). Linking crystallographic model and data quality. Science *336*, 1030–1033.

Krull, A., Steinborn, A., Ananthanarayanan, V., Ramunno-Johnson, D., Petersohn, U., and Tolić-Nørrelykke, I.M. (2014). A divide and conquer strategy for the maximum likelihood localization of low intensity objects. Opt. Express *22*, 210–228.

Laughery, M.F., Hunter, T., Brown, A., Hoopes, J., Ostbye, T., Shumaker, T., and Wyrick, J.J. (2015). New vectors for simple and streamlined CRISPR-Cas9 genome editing in *Saccharomyces cerevisiae*. Yeast *32*, 711–720.

Manatschal, C., Farcas, A.M., Degen, M.S., Bayer, M., Kumar, A., Landgraf, C., Volkmer, R., Barral, Y., and Steinmetz, M.O. (2016). Molecular basis of Kar9-Bim1 complex function during mating and spindle positioning. Mol. Biol. Cell *27*, 3729–3745.

Matsuo, Y., Maurer, S.P., Yukawa, M., Zakian, S., Singleton, M.R., Surrey, T., and Toda, T. (2016). An unconventional interaction between Dis1/TOG and Mal3/EB1 in fission yeast promotes the fidelity of chromosome segregation. J. Cell Sci. *129*, 4592–4606.

Maurer, S.P., Cade, N.I., Bohner, G., Gustafsson, N., Boutant, E., and Surrey, T. (2014). EB1 accelerates two conformational transitions important for microtubule maturation and dynamics. Curr. Biol. *24*, 372–384.

McCoy, A.J., Grosse-Kunstleve, R.W., Adams, P.D., Winn, M.D., Storoni, L.C., and Read, R.J. (2007). Phaser crystallographic software. J. Appl. Crystallogr. *40*, 658–674.

Miller, R.K., and Rose, M.D. (1998). Kar9p is a novel cortical protein required for cytoplasmic microtubule orientation in yeast. J. Cell Biol. *140*, 377–390.

Miller, R.K., D'Silva, S., Moore, J.K., and Goodson, H.V. (2006). The CLIP-170 orthologue Bik1p and positioning the mitotic spindle in yeast. Curr. Top. Dev. Biol. *76*, 49–87.

Mishima, M., Maesaki, R., Kasa, M., Watanabe, T., Fukata, M., Kaibuchi, K., and Hakoshima, T. (2007). Structural basis for tubulin recognition by cytoplasmic linker protein 170 and its autoinhibition. Proc. Natl. Acad. Sci. USA *104*, 10346–10351.

Moore, J.K., D'Silva, S., and Miller, R.K. (2006). The CLIP-170 homologue Bik1p promotes the phosphorylation and asymmetric localization of Kar9p. Mol. Biol. Cell *17*, 178–191.

Moore, J.K., and Miller, R.K. (2007). The cyclin-dependent kinase Cdc28p regulates multiple aspects of Kar9p function in yeast. Mol. Biol. Cell *18*, 1187–1202.

Olieric, N., Kuchen, M., Wagen, S., Sauter, M., Crone, S., Edmondson, S., Frey, D., Ostermeier, C., Steinmetz, M.O., and Jaussi, R. (2010). Automated seamless DNA co-transformation cloning with direct expression vectors applying positive or negative insert selection. BMC Biotechnol. *10*, 56.

Podolski, M., Mahamdeh, M., and Howard, J. (2014). Stu2, the budding yeast XMAP215/Dis1 homolog, promotes assembly of yeast microtubules by increasing growth rate and decreasing catastrophe frequency. J. Biol. Chem. *289*, 28087–28093.

Roberts, A.J., Goodman, B.S., and Reck-Peterson, S.L. (2014). Reconstitution of dynein transport to the microtubule plus end by kinesin. Elife *3*, e02641.

Sauter, N.K., Grosse-Kunstleve, R.W., and Adams, P.D. (2004). Robust indexing for automatic data collection. J. Appl. Crystallogr. *37*, 399–409.

Schneider, C.A., Rasband, W.S., and Eliceiri, K.W. (2012). NIH Image to ImageJ: 25 years of image analysis. Nat. Methods *9*, 671–675.

Slep, K.C. (2010). Structural and mechanistic insights into microtubule end-binding proteins. Curr. Opin. Cell Biol. *22*, 88–95.

Steinmetz, M.O., and Akhmanova, A. (2008). Capturing protein tails by CAP-Gly domains. Trends Biochem. Sci. *33*, 535–545.

van der Vaart, B., Manatschal, C., Grigoriev, I., Olieric, V., Gouveia, S.M., Bjelic, S., Demmers, J., Vorobjev, I., Hoogenraad, C.C., Steinmetz, M.O., and Akhmanova, A. (2011). SLAIN2 links microtubule plus end-tracking proteins and controls microtubule growth in interphase. J. Cell Biol. *193*, 1083–1099.

van der Vaart, B., Fischböck, J., Mieck, C., Pichler, P., Mechtler, K., Medema, R.H., and Westermann, S. (2017). TORC1 signaling exerts spatial control over microtubule dynamics by promoting nuclear export of Stu2. J. Cell Biol. *216*, 3471–3484.

Vagin, A.A., Steiner, R.A., Lebedev, A.A., Potterton, L., McNicholas, S., Long, F., and Murshudov, G.N. (2004). REFMAC5 dictionary: organization of prior chemical knowledge and guidelines for its use. Acta Crystallogr. D Biol. Crystallogr. *60*, 2184–2195.

Weisbrich, A., Honnappa, S., Jaussi, R., Okhrimenko, O., Frey, D., Jelesarov, I., Akhmanova, A., and Steinmetz, M.O. (2007). Structure-function relationship of CAP-Gly domains. Nat. Struct. Mol. Biol. *14*, 959–967.

Wolyniak, M.J., Blake-Hodek, K., Kosco, K., Hwang, E., You, L., and Huffaker, T.C. (2006). The regulation of microtubule dynamics in *Saccharomyces cerevisiae* by three interacting plus-end tracking proteins. Mol. Biol. Cell *17*, 2789–2798.

STAR★METHODS

KEY RESOURCES TABLE

REAGENT or RESOURCE	SOURCE	IDENTIFIER
Bacterial and Virus Strains		
BL21(DE3)	Novagen	Prod: #69450-3
Mach1	Thermo Fischer	Prod: #C862003
Chemicals, Peptides, and Recombinant Proteins		
ETF peptide (peptide sequences are specified in the methods)	This paper	N/A
ETY peptide	This paper	N/A
LxxPTPh peptide	Kumar et al., 2017	N/A
PreScission protease	produced in-house	N/A
Sodium cacodylate trihydrate	Hampton Research	HR2-241
SxIP peptide	Buey et al., 2012	N/A
TCEP	Sigma-Aldrich	646547
Deposited Data		
Crystal structure of Bik1CG	This paper	PDB: 6FC5
Crystal structure of Bik1CG-ETF complex	This paper	PDB: 6FC6
Experimental Models: Organisms/Strains		
All *S. cerevisiae* strains used in this study are listed in Table S2	This paper	N/A
Oligonucleotides for CRISPR		
Bim1-ΔETF guide RNA 5’-CAACAACTTGATCATCGACGAGG-3’	This paper	N/A
Bim1-ΔETF_F 5’-GGTGAGGTTGGCGTGAGCAACAACTTGATCATCGACGAGTAAGTTGAGAACTAAAAAGCAGTATTGTTTTCGAATATGT-3’	This paper	N/A
Bim1-ΔETF_R 5’-ACATATTCGAAAACAATACTGCTTTTTAGTTCTCAACTTACTCGTCGATGATCAAGTTGTTGCTCACGCCAACCTCACC-3’	This paper	N/A
Bik1_gRNA_125bp_O1 5’-GATCTCCATCGTTCTTACCAATGTGTTTTAGAGCTAG-3’	This paper	N/A
Bik1_K46E-F (template) 5’-GCTGGAATGTTTGCTGGTGTAGACTTACTTGCCAACATTGGTGAGAACGATGGATCATTCATGGGGAAGAAGTATTTTCAAACGGAGTATCCTC-3’	This paper	N/A
Bik1_K46E-R (template) 5’-GAGGATACTCCGTTTGAAAATACTTCTTCCCCATGAATGATCCATCGTTCTCACCAATGTTGGCAAGTAAGTCTACACCAGCAAACATTCCAGC-3’	This paper	N/A
Recombinant DNA		
Plasmid: Bik1CG (aa 1-100) in PSTcm9	This paper	N/A
Plasmid: Bik1CG K46E (aa 1-100) in PSTcm9	This paper	N/A
Plasmid: Bik1cc (aa 182-396) in PSTcm2	This paper	N/A
Plasmid: Bim1C (aa 194-344)	Manatschal et al., 2016	N/A
Plasmid: Bik1C ΔETF (aa 194-341) in PSTcm2	This paper	N/A
Plasmid: Stu2Ctail (aa 855-888) in PSTcm9	This paper	N/A

(*Continued on next page*)

Continued

REAGENT or RESOURCE	SOURCE	IDENTIFIER
Software and Algorithms		
ASTRA	Wyatt Technolgies	https://www.wyatt.com/products/software/astra.html
Coot	Emsley et al., 2010	http://www.ccp4.ac.uk
Chirascan	Applied Photophysics	http://www.photophysics.com/
ImageJ	Schneider et al., 2012	https://fiji.sc/
MolProbity	Chen et al., 2010	http://molprobity.biochem.duke.edu
Origin	OriginLab	https://www.originlab.com
PHASER	McCoy et al., 2007	http://www.ccp4.ac.uk
PHENIX	https://www.phenix-online.org/	https://www.phenix-online.org/
Pymol	Schrödinger, LLC	http://www.pymol.org
REFMAC5	Vagin et al., 2004	http://www.ccp4.ac.uk
VisiVIEW	Visitron Systems	http://www.visitron.de
XDS	Kabsch, 2010	http://xds.mpimf-heidelberg.mpg.de/
Other		
Agilent UltiMate3000 HPLC (full MALS setup in methods)	Agilent	N/A
HisTrap FF 5ml	GE Healthcare	Prod: #17531901
HiLoad 16/60 Superdex 75 pg column	GE Healthcare	Prod: #28989333
HiLoad 16/60 Superdex 200 pg column	GE Healthcare	Prod: #28989335
MicroCal ITC200 Isothermal Titration Calorimeter	MicroCal	N/A
Superdex 200 Increase 10/300 GL	GE Healthcare	Prod: #28990944

CONTACT FOR REAGENT AND RESOURCE SHARING

Further information and requests for resources and reagents should be directed to and will be fulfilled by the Lead Contact, Michel Steinmetz (michel.steinmetz@psi.ch)

EXPERIMENTAL MODEL DETAILS

In this study, all yeast strains (*S. cerevisiae*) were derived from the S288C background. Expression of recombinant proteins for *in vitro* studies were produced in the E. coli strain BL21(DE3).

METHOD DETAILS

Protein and Peptide Preparations

The DNA encoding the CAP-Gly domain of *S. cerevisiae* Bik1 (Bik1CG, residues 1-100; Uniprot ID: P11709) and the C-terminal part of *S. cerevisiae* Stu2 (Stu2Ctail, residues 855-888; Uniprot ID: P46675) were cloned into the pET-based bacterial expression vector PSTCm9, which encodes for an N-terminal thioredoxin, a 6x His-tag and a PreScission cleavage site using a positive selection method (Olieric et al., 2010). The coiled-coil domain of Bik1 (Bik1cc, residues 182-396; Uniprot ID: Q80VC9) was cloned into the PSTCm2 vector that encodes for an N-terminal 6x His-tag and a PreScission cleavage site (Olieric et al., 2010). The bacterial expression vector for the C-terminal domain of *S. cerevisiae* Bim1 (Bim1C, residues 194-344; Uniprot ID: P40013) has been reported previously (Manatschal et al., 2016). This plasmid was utilized to generate the Bim1C construct that lacked the C-terminal ETF motif of Bim1 (denoted Bim1C ΔETF, residues 194-341) by applying a standard PCR approach and cloning into the PSTCm2 vector. The mutant Bik1CG K46E clone was obtained by standard PCR-based site-directed mutagenesis.

Protein production was performed in the *E. coli* strain BL21(DE3) (Stratagene) in LB media containing 50 μg/ml of kanamycin. When the cultures had reached an OD_{600} of 0.6 at 37°C, they were cooled down to 20°C, induced with 1 mM isopropyl 1-thio-β-D-galactopyranoside (IPTG) and shaken for another 16 hours at 20°C. After harvesting and washing of the cells with Dulbecco PBS buffer (Millipore), the cells were sonicated in the presence of the protease inhibitor cOmplete cocktail (Roche) in lysis buffer (50 mM HEPES, pH 8, supplemented with 500 mM NaCl, 10 mM imidazole, 2 mM β-mercaptoethanol, 0.1% bovine deoxyribonuclease I).

Proteins were purified by immobilized metal-affinity chromatography (IMAC) on a HisTrap HP Ni^{2+}-Sepharose column (GE Healthcare) at 4°C following the instructions of the manufacturer. The column was equilibrated in IMAC buffer A (50 mM HEPES, pH 8, supplemented with 500 mM NaCl, 10 mM imidazole, 2 mM β-mercaptoethanol). Proteins were eluted by IMAC buffer B (IMAC buffer A containing 400 mM imidazole in total). In the case of Bik1CG, Bik1CG K46E or Bik1cc, the N-terminal fusion proteins and tags were cleaved off by an in-house produced HRV 3C protease (Cordingley et al., 1990) in IMAC buffer A for 16 hours at 4°C. The cleaved samples were reapplied on the IMAC column to separate cleaved from uncleaved protein.

Protein samples were concentrated and loaded onto a size exclusion chromatography (SEC) HiLoad Superdex 75 16/60 column (GE Healthcare), which was equilibrated in SEC buffer (20 mM Tris-HCl, pH 7.5, supplemented with 500 mM NaCl and 1 mM DTT). In the case of Bim1C, Stu2C and Bik1cc, the SEC buffer contained 150 mM NaCl. The fractions of the respective main peaks were pooled and concentrated to 10 mg/ml. Protein quality and identity were assessed by SDS-PAGE and mass spectrometry, respectively.

The ETF (residues 334-344 of *S. cerevisiae* Bim1), the ETY (F344 mutated to Y), SxIP (KPSKIPTLQRKSW, a derivative of MACFp1; Buey et al., 2012) and LxxPTPh (residues 615-633 of *S. cerevisiae* Kar9, Uniprot ID: P32526; Manatschal et al., 2016) peptides were produced by standard peptide chemistry. Peptide quality and identity were assessed by high performance liquid chromatography and mass spectrometry, respectively. Peptides were dissolved in PBS buffer pH 7.4 (137 mM NaCl, 2.7 mM KCl, 10 mM Na_2HPO_4 and 1.8 mM KH_2PO_4) at a typical concentration of 10 mM.

Circular Dichroism (CD) Spectroscopy

The CD spectrum of Bik1cc (0.25 mg/ml in PBS) was recorded at 5°C on a Chirascan-Plus spectrophotometer (Applied Photophysics Ltd.) equipped with a computer-controlled Peltier element using a quartz cuvette of 1 mm optical path length. Thermal unfolding profiles were recorded by CD at 222 nm by continuous heating at 1°C min^{-1}. The apparent midpoint of the transition, T_m, was determined by fitting of the data points using the R nonlinear least square fitting function based on a sigmoid model.

Size Exclusion Chromatography Followed by Multi-Angle Light Scattering (SEC-MALS)

For the SEC-MALS experiment at 25°C, a Superdex 10/30 column (GE Healthcare) was equilibrated in 20 mM Tris-HCl, pH 7.5, supplemented with 150 mM NaCl and 1 mM DTT (SEC buffer) at a flow rate of 0.5 ml/min on an Agilent UltiMate3000 HPLC. 30 μl of Bik1CG or Bik1cc protein solutions at 5 mg/ml were injected onto the column and the mass was determined using the miniDAWN TREOS and Optilab T-rEX refractive index detectors (Wyatt Technology). The Zimm model was chosen for data fitting, which was performed in the ASTRA 6 software.

Isothermal Titration Calorimetry (ITC)

All proteins and peptide samples were buffer-exchanged to ITC buffer (PBS buffer supplemented with 0.5 mM TCEP). ITC experiments were performed either at 20°C (experiments with Stu2-C) or 25°C (all other experiments) on an iTC 200 machine (MicroCal) using 15 injections of 2.6 μl. 50-100 μM of Bim1C, Bik1cc, Bim1C ΔETF, Bim1C-MACF SxIP or Bim1C-Kar9 LxxPTPh were loaded into the sample cell. 500-1000 μM Bik1CG, Bim1C ETF, Stu2C, MACF SxIP, Kar9 LxxPTPh or Bik1CG K46E were loaded into the syringe. In the case of Bik1 CG:Bim1 ETF, Bik1CG was present in the cell (50 μM) and Bim1 ETF in the syringe (500 μM). Fits of the binding isotherms were obtained by using a nonlinear least squares minimization method. The one set of site model provided in the software package of the calorimeter was utilized to determine the equilibrium dissociation constant, K_d. In most cases where a binding reaction took place, two independent experiments were performed. The determined K_d values are reported in Table S1. The K_d value of “Exp1” in Table S1 is reported in the main text. Standard errors were derived from the nonlinear least square fitting of the respective binding isotherms.

X-Ray Data Collection and Structure Determination

Bik1CG was concentrated to 20 mg/ml and DTT to a final concentration of 5 mM was added to the sample. The screening of crystallization conditions was performed using a Mosquito robot (TTP Labtech) in 96 well plates using the vapor diffusion hanging drop method at 20°C. Crystals appeared overnight in drops of a 1:1 (200 nl each) mixture of Bik1CG and mother liquor (0.1 M sodium cacodylate, pH 6.5, 1.0 M sodium citrate) The crystals were cryo-protected by transferring them into mother liquor supplemented with 25% glycerol and were flash frozen in liquid nitrogen.

In order to co-crystallize Bik1CG with the Bim1C ETF peptide, Bik1CG was mixed with Bim1C ETF that was also dissolved in the Bik1CG SEC buffer. The final concentration of the complex was 10 mg/ml and 5 mM DTT was added. Crystals were obtained at 0.1 M sodium cacodylate, pH 6.4, 1.0 M sodium citrate. The crystals were cryo-protected by transferring them into mother liquor supplemented with 25% glycerol and were flash frozen in liquid nitrogen.

X-ray diffraction data of Bik1 CG crystals were collected at the X06DA macromolecular crystallography beamline at the Swiss Light Source (Paul Scherrer Institut) at a wavelength of 1 Å. The data were indexed with LABELIT (Sauter et al., 2004), and refined and integrated with XDS (Kabsch, 2010). The Bik1CG structure was solved by molecular replacement with PHASER (McCoy et al., 2007) using the structure of the CAP-Gly domain of the p150glued structure (PDB ID 2HKN) as a search model. The Bik1CG structure was subsequently used to solve the structure of the Bik1CG-Bim1-ETF complex by molecular replacement. Several rounds of manual model building in COOT (Emsley et al., 2010) and refinement in REFMAC (Vagin et al., 2004). Both the Bik1CG and Bik1CG-Bim1C ETF structures were validated by MolProbity. Figures were prepared using PyMOL (DeLano, 2002). Data collection and refinement statistics are given in Table 1.

Measurements of Astral Microtubule Behavior and Bik1-3xGFP Distribution in *S. Cerevisiae* Strains

All yeast strains used in this study were derived from the S288C background. Yeast cells expressing the microtubule plus-end marker Bik1-3xGFP and SPB marker Spc72-GFP from endogenous loci were grown and imaged in synthetic complete (SC) medium at 25°C, except that at 30°C for aMT dynamics. Deletion of BIM1 and BIK1 was performed as described (Knop et al., 1999), the Bim1 ΔETF mutants and the point mutation Bik1 K46E were created with the CRISPR-cas9 system (Laughery et al., 2015) and sequenced to validate.

Time-lapse movies were acquired using a back-illuminated EM-CCD camera Evolve 512(Photometrics, Inc.) mounted on a spinning disk microscope with a motorized piezo stage (ASI MS-2000) and 100x 1.46 NA alpha Plan Apochromat oil immersion objective, driven by Metamorph based software VisiVIEW (Visitron Systems). 17 Z-section images separated by 0.24μm increments were captured every 1.07 sec for 85.6 sec. To determine the length of astral microtubules, three-dimensional coordinates of microtubule plus-end and the corresponding SPB were extracted with the Low Light Tracking Tool (Krull et al., 2014) and the distance between the plus-end and the SPB represents the length of a microtubule. The maximum length and lifetime of each microtubule within the recorded window were then recorded. For line scan analysis, sum slices projections of Z stacks were used, a 5px (666.7 nm) width line was used to scan aMTs from plus-ends toward SPBs. To quantify the fluorescence intensity of Bik1-3xGFP on plus-ends, a region of interest (ROI) was drawn around the area of interest (AOI) and the integrated density was quantified. An identically sized ROI was put next to the AOI to determine the background signal. The background intensity was subtracted from the ROI intensity to yield the fluorescent intensity (a.u.).

Localization of Kar9 in Bim1 ΔETF or Bik1 K46E *S. Cerevisiae* Strains

Specific Bik1 and Bim1 mutations were introduced at the endogenous locus via the CRISPR/Cas9 gene editing methodology (Laughery et al., 2015). The integration was confirmed by PCR and sequencing. The Kar9 protein was tagged at the endogenous locus with 3xsfGFP:KanMX cassette, while the CFP-Tub1 construct was inserted at the TRP1 locus using the integrative plasmid pRS304.

Yeast strains were exponentially grown in synthetic media lacking tryptophan. Cells were harvested by centrifugation at 600 x g for 2 minutes and taken onto microscopy slides. Strains were imaged on a Personal Delta Vision microscope, with z stacks of 11 layers (step size of 0.3 μm). Images were analyzed with Fiji (ImageJ) using sum projections.

All yeast strains generated in this study are summarized in Table S2.

QUANTIFICATION AND STATISTICAL ANALYSIS

In case of ITC, the standard errors were derived from the nonlinear least square fits of the respective binding isotherms. For the *in vivo* experiments in yeast, the statistical significance was calculated by applying the two-tailed student t-test.

DATA AND SOFTWARE AVAILABILITY

Atomic coordinates and structure factors for Bik1CG and Bik1CG-ETF have been deposited in the RCSB Protein Data Bank (PDB) under accession numbers 6FC5 and 6FC6.

3. The kinesin Kip2 acts as a microtubule polymerase at plus-ends

3. The kinesin Kip2 acts as a microtubule polymerase at plus-ends

3.1 Declaration of Contribution

For the Kip2 project, I contributed by conducting all in vitro experiments. Prof. Dr. Michel Steinmetz and I planned and analyzed the in vitro experiments. Cell biology experiments were performed by Dr. Xiuzhen Chen, and she and Lukas Widmer together evaluated the Kip2 positioning and microtubule dynamics data. I cloned, purified and expressed all proteins for in vitro experiments. By ITC and MALS experiments, I characterized the interaction of the Bik1 coiled-coil with the Kip2 coiled-coil. Three mutation sites of the Kip2 motor domain were conceived by me with the help of a homology model and sequence alignments. I analyzed the Kip2 motor domain wild-type and mutants by CD spectroscopy and investigated the tubulin binding of these constructs by MALS. This draft of the manuscript was written by Dr. Xiuzhen Chen, Lukas Widmer and me under the guidance of Prof. Yves Barral, Prof. Dr. Michel Steinmetz and Prof. Dr. Jörg Stelling. The material and methods about the in vivo experiments were taken from the Ph.D. thesis of Dr. Xiuzhen Chen. Furthermore, some figure legends of the in vivo results are adapted from the Ph.D. thesis of Dr Xiuzhen Chen. Before submission, the manuscript will be modified by all authors.

Since this paper is still in preparation, only preliminarily figure legends of the figures are presented. Longer preliminarily figure legends of the in vivo experiments are available in the Ph.D. thesis of Dr. Xiuzhen Chen (Diss. No. 25080, ETH Zürich).

The following section consists of the preliminary version of the manuscript draft with the title “The kinesin Kip2 acts as a microtubule polymerase at plus-ends “. It is intended to submit this manuscript in the next half year.

3.2 Draft of the manuscript

The kinesin Kip2 acts as a microtubule polymerase at plus-ends

Xiuzhen Chen[1], Marcel M. Stangier[2], Lukas A. Widmer[3,4], Jörg Stelling[3], Michel O. Steinmetz[2,5], Yves Barral[1*].

[1]Institute of Biochemistry, ETH Zürich, Otto-Stern-Weg 3, 8093 Zurich, Switzerland.
[2]Laboratory of Biomolecular Research, Department of Biology and Chemistry, Paul Scherrer Institut (PSI), 5232 Villigen, Switzerland.
[3]Department of Biosystems Science and Engineering, ETH Zürich, and SIB Swiss Institute of Bioinformatics, 4058 Basel, Switzerland.
[4]Systems Biology Ph.D. Program, Life Science Zurich Graduate School, Zurich, Switzerland.
[5]University of Basel, Biozentrum, 4056 Basel, Switzerland
*Correspondence to: yves.barral@bc.biol.ethz.ch

Abstract

The polymerization rate of tubulin into microtubules can be increased by so-called microtubule polymerases. Recently, it has been reported that the budding yeast Kip2, a member of the kinesin-7 family, functions as a microtubule polymerase. Here, we demonstrate that the motor domain of Kip2 interacts both with soluble tubulin and microtubules, and no other part of Kip2 is involved in these interactions. Furthermore, three mutants of the Kip2 motor domain tubulin/microtubule-binding interface were designed. We discovered that one of these mutants bound weakly to tubulin and lost the ability to polymerize microtubules in yeast cells but retained the motile function. Based on this evidence and further experiments, we propose that Kip2 is capable of increasing the tubulin concentration at the microtubule plus-end to enhance the polymerization rate. Besides, we characterized the interaction of Kip2 C-terminal part with the Bik1 coiled-coil. In addition, a Kip2 C-terminal truncated mutant was conceived that lost the ability to bind Bik1. Thereby, we found that the interaction of Kip2 with Bik1 is crucial for the polymerase function of Kip2. Overall, these new insights unravel the enigmatic role of kinesins as microtubule polymerases.

Introduction

Kinesins are emerging players in the control of microtubule dynamics, governing a wide range of cellular processes, including cell division, cargo transportation and organelle distribution. Non-motile kinesins from the kinesin-13 family were the first of their kind to be found as microtubule depolymerases (Walczak et al., 1996) that promote microtubule shrinkage (Rogers et al., 2004). Later on, motile kinesins such as kinesin-8 family members (budding yeast Kip3, fission yeast Klp5/6, human Kif18a and Kif18b) were reported to be microtubule depolymerases as well (Gupta et al., 2006). Extensive studies using in vitro reconstitution of purified components or acquiring structural details of their motor domains in complex with tubulin have greatly advanced our understanding of how these motor proteins possess both motility and microtubule depolymerase activities (Gardner et al., 2011; Su et al., 2011; Wang et al., 2017). Mechanistically, the emerging theme is that the motor domains of these kinesins evolved distinct ways to bind preferentially to the curved αβ-tubulin (hereafter: tubulin) on microtubule plus-ends, over the straight tubulin incorporated into microtubule lattices. Thereby, they stabilize the curved protofilaments on plus-ends and eventually lead to catastrophe (the transition from growth to shrinkage) (Arellano-Santoyo et al., 2017; Wang et al., 2017).

Kinesins can not only promote shrinkage, but some kinesins rather enhance microtubule growth, such as Kinesin-5 Eg5, Kinesin-7 CENPE and budding yeast Kip2 (Chen and Hancock, 2015; Sardar et al., 2010). These motile kinesins directly accelerate microtubule elongation in reconstituted systems, yet the mechanisms underlying their microtubule polymerase activity are largely unknown. The budding yeast cytoplasmic kinesin Kip2, a plus-end directed motor, is a prominent example. Kip2 has long been implicated in stabilizing microtubules, mainly because the deletion of *KIP2* results in extremely short and much less abundant astral microtubules (aMTs) (Cottingham and Hoyt, 1997). Conversely, overexpression of Kip2 leads to the formation of long aMTs (Carvalho et al., 2004). Recent reconstitution experiments demonstrated that Kip2 directly polymerizes microtubules and inhibits catastrophe to promote microtubule growth in vitro (Hibbel et al., 2015). In budding yeast, two proteins have been shown to physically associate with Kip2 and potentially control the proper its functions: Bik1, the yeast orthologue of CLIP-170, interacts with the C-terminal region of Kip2 and rides the motor protein to reach microtubule plus-ends (Carvalho et al., 2004; Caudron et al., 2008; Roberts et al., 2014). Bim1, the yeast orthologue of EBs, instead makes contact with the low-complexity N-terminus of Kip2. This interaction is negatively regulated by Kip2 phosphorylation (Drechsler et al., 2015). While Kip2 alone is already a highly processive motor both in vitro and in vivo (Hibbel et al., 2015), its processivity is increased further in vitro by supplementing both Bik1 and Bim1 (Roberts et al., 2014). Understanding how Kip2 powers and coordinates its motility and microtubule polymerase activities, as well as how cells orchestrate microtubule-associating proteins (MAPs) to regulate these activities of Kip2 will provide mechanistic insights into the regulation of microtubule dynamics by kinesins like Kip2.

Here, we focus on metaphase cells, which only have a limited number of aMTs (usually one) emanating from each spindle pole body (SPB, yeast microtubule organizing center, centrosome equivalent). Combining high spatial-temporal resolution microscopy-based quantification of microtubule behavior, biophysical characterization and mathematical modelling, we investigated which parts of the Kip2 motor are responsible for its different functions in cargo transportation and microtubule polymerization.

Results

Kinesin-tubulin interactions drive the microtubule polymerase activity of Kip2

To investigate the basis for Kip2 functions, we developed a homology model of its motor domain bound to a tubulin dimer, based on a Kif2C-tubulin complex structure (Wang et al., 2017). Three positively charged patches were predicted by the homology model to be potential kinesin-tubulin interfaces, and these patches could interact with the negatively charged regions of tubulin. The three patches that featured the positively charged residues Lys294Arg296, Arg384Arg385 and Arg446 were named interface 1, 2 and 3, respectively (Fig. 1A and Fig. S1A).

Interestingly, both interface 1 and 3 are predicted to bind β-tubulin. Then, we investigated the role of interfaces in vivo by substituting critical residues of each interface to alanine and monitored phenotypic consequences of these mutations. As described previously (Hibbel et al., 2015), the functional endogenous Kip2-3xsfGFP protein decorated aMT lattices and enriched on their plus-ends (Fig. 1B). This behavior also holds in heterozygous diploid cells in which the other wild-type copy of Kip2 was fused to mCherry (Kip2-mCherry) (Fig. S2). Interestingly, Kip2 bearing mutations in interface 2 or interface 3 diffused in the cytoplasm and barely interacted with microtubules. These mutant proteins only associated weakly with SPBs (Fig. 1B and Fig. S2). In contrast, the interface 1 mutant Kip2-K294AR296A-3xsfGFP bound to microtubules and accumulated on their plus-ends to the same level as wild-type proteins (Fig. 1B and Fig. S2). Quantifications of their accumulation on bud-directed aMT plus-ends are shown in Fig. 1C. Next, we purified Kip2 motor domains (Kip2-MD) bearing mutations in these interfaces from bacteria and performed circular dichroism (CD) experiments in which neither the CD spectrum nor the melting curve of any of the mutants was perturbed (Fig. S1CD). This validated that none of the mutations caused protein misfolding. Therefore, we concluded that interfaces 2 and 3 are both essential for Kip2 binding to microtubule lattices and translocating along them.

Figure 1:

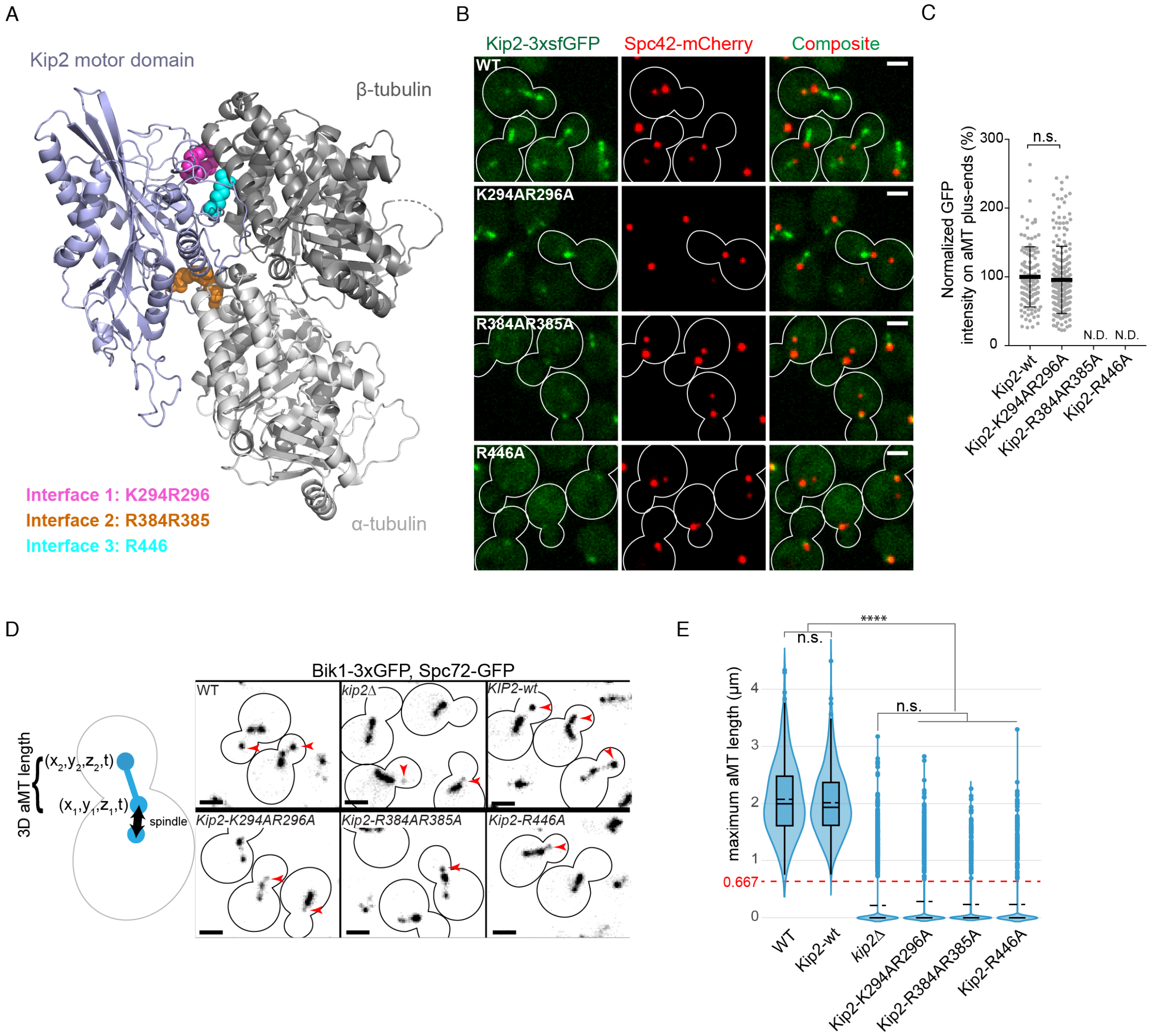

Figure 1. The three important interfaces of the Kip2 motor domain for tubulin and microtubule binding and their role for the polymerase function of Kip2.

(A) Homology model of the Kip2 motor domain (blue) in complex with the tubulin (grey) dimer. The three positively charged interfaces that are crucial for tubulin or microtubule binding are highlighted in various colors.

(B) Representative images of yeast cells expressing Spc72-GFP as a reference and wild-type Kip2-3xsfGFP or Kip2 harboring the respective mutation of the tubulin-binding interface. A scale bar of 2µm is displayed.

(C) The quantification of Kip2-3xsfGFP fluorescence levels at metaphase aMT plus-ends of the cells from figure 2B are shown

(D) Illustration of the measuring method to determine the aMT length.

(E) Quantification of the maximum aMT length of wild-type Kip2, kip2 delete or the respective Kip2 mutant.

Strikingly, aMTs decorated with Kip2-K294AR296A-3xsfGFP were much shorter than those of wild-type cells (Fig. 1B). To systematically evaluate the effect of each interface mutant on microtubule polymerization, we employed a previously reported microscopy-based assay (Stangier et al., 2018). This assay uses Bik1-3xGFP and Spc72-GFP as the plus-end and minus-end markers respectively. Time-lapse series were acquired with a spinning disk confocal microscope at an interval of 1.07 s. Three dimensional (3D) coordinates of both the plus-end and the minus-end of each microtubule overtime were extracted with the low light tracking tool (Krull et al., 2014), which allowed us to compute the maximum length and the lifetime of each recorded aMT. This assay worked well with wild-type cells in which Bik1-3xGFP molecules form bright foci on aMT plus-ends (Fig. 1D). It is known that Kip2 is required for efficient targeting of Bik1 to aMT plus-ends (Carvalho et al., 2004; Caudron et al., 2008). As a control, we tested whether the low Bik1-3xGFP intensity on aMT plus-ends of *kip2*Δ cells (53.93 ± 24.14 % in *kip2*Δ cells versus 100 ± 28.74 % in wt cells, mean ± s.d) was sufficient for faithfully tracking them. Using Bik1-3xGFP as the plus-end marker, we observed only around 15.09% (302 out of 2001) *kip2*Δ metaphase cells with visible aMTs in contrast to 100% (511 out of 511) of wild-type metaphase cells (Fig. 1D). Tracking of those visible aMTs was successful, except that in some cases the tracker lost the plus-ends when they shrank rapidly, faster than aMTs of wild-type cells (Fig. S3C). For this reason, all tracking was inspected by eye and manually curated if necessary. We marked all lengths of aMTs below the detection limit (666.7 nm owing to the microscope resolution) or aMTs from those 85% of cells with no visible aMTs as 0 µm. Accounting all metaphase cells, indeed, the loss of Kip2 resulted in extremely short aMTs (0.21 ± 0.02 μm, mean ± s.d., n = 3 independent clones, ****) comparing to that of the wild-type cells (2.08 ± 0.06 μm, mean ± s.d., n = 3 independent clones) (Fig. 1E). Further annotation of the catastrophe and rescue events of the tracked aMTs (around 15% of total *kip2*Δ metaphase cells) allowed us to compute the detailed parameters of microtubule dynamicity (Fig. S3). Importantly, loss of Kip2 resulted in higher frequency of catastrophe (5.09 events min^{-1} comparing to 2.81 events min^{-1} in wt cells) and slower microtubule growth (1.46 ± 0.92 μm min^{-1} comparing to 1.99 ± 1.84 μm min^{-1} in wt cells, mean ± s.d., *, 30 °C) (Fig. S3CD). This supports the idea that Kip2 functions as a microtubule polymerase in vivo. Interestingly, aMTs in *kip2*Δ cells also shrank faster (4.18 ± 2.08 μm min^{-1} comparing to 3.10 ± 1.50 μm min^{-1} in wt cells, mean ± s.d., ****, 30 °C) and had higher rescue frequency (1.68 events min^{-1} comparing to 0.97 events min^{-1} in wt cells) (Fig. S3CD), suggesting yet unknown regulatory functions of Kip2 on shrinking microtubules. In order to introduce the alanine substitutions into the endogenous *KIP2* locus, a selection marker *TRP1* was inserted downstream to it. The introduction of *TRP1* downstream of wild-type *KIP2* (marked as *KIP2-wt*) did not affect aMT dynamics, leaving the average microtubule length at 2.00 ± 0.15 μm (mean ± s.d., n = 3 independent clones, n.s.). Using this assay, we found that all three interface mutants pheno-copied *kip2*Δ cells (Fig. 1DE). The remarkably short aMTs of the interface 1 mutant cells (0.28 ± 0.01 μm, mean ± s.d., ****) indicates that the Kip2-K294AR296A molecules accumulating at aMT plus-ends are inactive in polymerizing microtubules. These results suggest that Kip2 promotes microtubule growth and inhibits catastrophe in vivo and this polymerase activity relies on interactions between Kip2 and tubulin.

Residues K294 and R296 of Kip2 mediate interaction with free tubulin dimers and are dispensable for motility

Different from the two other interfaces, mutations in interface 1 led to a polymerase-inactive phenotype without dissociating Kip2 from microtubules. Therefore, we asked whether the interface 1 might specifically mediate Kip2 interaction with free tubulin dimers rather than microtubule lattices. We purified wild-type and Kip2-K294AR296A motor domains (Kip2-MD) from bacteria and subjected them to a pelleting assay with Taxol-stabilized microtubules, in which the amount of proteins co-sedimenting with microtubules reflects their binding affinity to microtubules. Around half the amount of Kip2-MD co-sedimented with microtubules, and no significant reduction of affinity to microtubules was observed when using Kip2-K294AR296A-MD (Fig. 2A). To test the affinity between apo-state Kip2-MD and free tubulin dimers in solution, we performed size-exclusion chromatography coupled to multi-angle light scattering analysis (SEC-MALS: determines molecular mass by measuring light-scattering intensities and concentrations of particles in solution). These measurements indicated that the mass of the putative Kip2-MD-tubulin complex shifted to 153 kDa from 107 kDa of the free tubulin, corresponding to the mass of Kip2-MD of 44 kDa (Fig. 2B). Importantly, when using apo-state Kip2-K294AR296A-MD, the SEC-MALS measurement yielded nearly no peak shift anymore and a molecular mass of 137 kDa that was in between the mass of free tubulin and the mass of MD-tubulin complex (Fig. 2B). These results demonstrate that the residues K294 and R296 are required for Kip2 to bind free tubulin dimers with higher affinity and are dispensable for Kip2 binding to polymerized tubulin, i.e., to microtubules.

To this point, we predicted that interface 2 – which mediates contact with α-tubulin (Fig. 1A) – is paired either with interface 1 or interface 3 to bind to free tubulin dimers or to microtubules, respectively. We wondered whether loss of interaction with free tubulin dimers affects Kip2 interaction with microtubules in any way. Therefore, we inspected whether the motility of Kip2-K294AR296A differs from that of the wild-type protein. Kip2-3xsfGFP moves along microtubule lattices as fluorescent speckles, and we have previously assessed the speeds of those speckles by analyzing kymographs of aMTs decorated with Kip2-3xsfGFP computed from time-lapse series.

Figure 2:

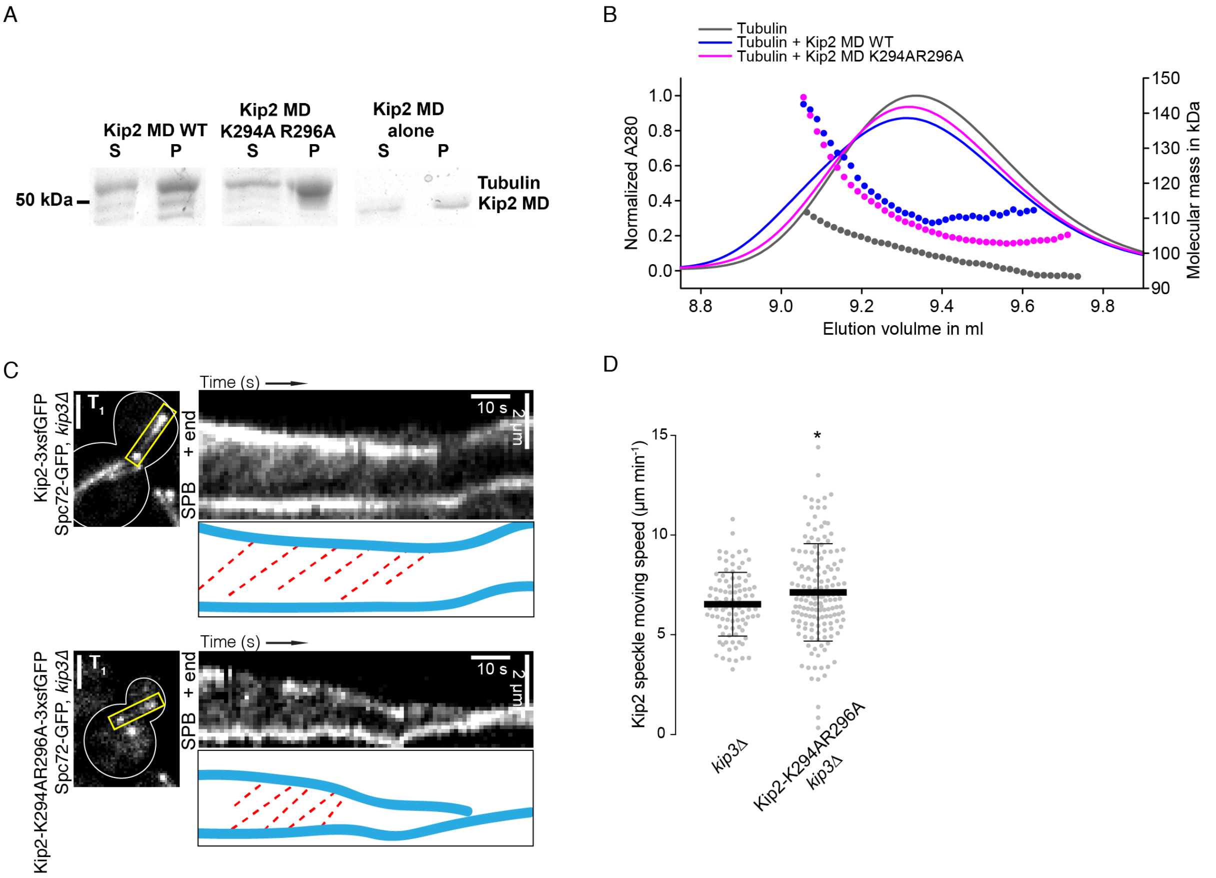

Figure 2. Microtubule and tubulin binding of the Kip2 motor domain (MD).

(A) Microtubule-pelleting assay in which the Kip2 MD wild-type (WT) and the Kip2 MD K294A R296A (interface 1 mutant) were mixed in an equimolar ratio with tubulin in BRB80 buffer. As controls, the Kip2 MD domain was processed alone. The supernatants (S) and pellets (P) were separated on a 12 % SDS-PAGE and stained with Coomassie.

(B) SEC-MALS experiments of Kip2 MD wild-type (WT) or the Kip2 MD K294AR294A with tubulin. As a reference, free tubulin was used. The UV absorption at 280 nm and the molecular masses across the peak determined by MALS are plotted.

(*C) Representative metaphase cells and kymographs of wild-type Kip2-3xGFP or Kip2-3xGFP-K294AR296A associated aMTs.*

(D) Quantification of the Kip2 speckle moving speed of data from (C).

The very short microtubules in Kip2-K294AR296A cells made it impossible for us to observe any moving speckles within such short ranges. To circumvent this difficulty, we deleted *KIP3*, which encodes a kinesin with strong microtubule depolymerase activity (Gupta et al., 2006) in both control and Kip2-K294AR296A cells. Cells lacking Kip3 produced longer aMTs in both cases and enabled us to observe plenty of Kip2-3xsfGFP or Kip2-K294AR296A-3xsfGFP speckles moving towards aMT plus-ends (Fig. 2C). We found a small but significant increase in speckle moving speed in the *kip3Δ KIP2-K294AR296A* double cells compared to *kip3Δ KIP2* cells (7.13 ± 2.44 μm min^{-1}, mean ± s.d., n = 159 speckles versus 6.53 ± 1.60 μm min^{-1}, mean ± s.d., n = 92 speckles in control cells, p = 0.036, 25 °C) (Fig. 2D). In parallel, we measured the speeds of Kip2-3xsfGFP and Kip2-

K294AR296A-3xsfGFP speckles in heterozygous diploid cells in which the other copy of Kip2 was wild-type, thus aMTs are longer (Fig. S2B). In this system, Kip2-3xsfGFP speckles (5.43 ± 1.70 μm min^{-1}, mean ± s.d., n = 120 speckles) instead moved slightly faster than the Kip2-K294AR296A-3xsfGFP speckles (4.76 ± 1.63 μm min^{-1}, mean ± s.d., n = 103 speckles, **) (Fig. S2C). In conclusion, K294 and R296 of Kip2 mediate interaction with free tubulin dimers and are not essential for Kip2 motility. Collectively, our results suggest that Kip2 has acquired a specialized interface dedicated to binding free tubulin dimers and to microtubule polymerization. We next asked whether Kip2-MD promoted microtubule polymerization in vitro and if so, whether Kip2-K294AR296A-MD lost this activity. Unfortunately, the recombinant Kip2-MD was not well-behaved enough to test this hypothesis. When we added ATP to the apo-state Kip2-MD-tubulin mixture, the solution became white, indicating aggregation or formation of various high-molecular-weight species. Therefore, it was not possible to perform in vitro microtubule polymerization assays, and this was the reason why the apo-state of the Kip2-MD was applied in the MALS experiments.

The motor domain and not the rest of Kip2, binds free tubulin dimers

We next sought to address whether the motor domain is the only part of Kip2 that is capable of recognizing and recruiting free tubulin dimers. We reasoned that if the low-complexity N-terminus was able to recruit free tubulin dimers, a construct of Kip2 lacking the N-terminus (Kip2-ΔN, illustrated in Fig. 3A) would not be fully active in microtubule polymerization. To our surprise, the removal of Kip2 N-terminus resulted in much longer (2.86 ± 0.17 μm, mean ± s.d., n = 3 independent clones, ****) aMTs in comparison to those of wild-type cells (2.00 ± 0.15 μm, mean ± s.d., n = 3 independent clones) (Fig. 3B). Thus, the N-terminus negatively regulates the microtubule polymerase activity of Kip2. Since the N-terminus of Kip2 is required to interact with Bim1 (Drechsler et al., 2015), we reasoned that Bim1 is certainly not required for Kip2's polymerase activity. We further removed the motor domain from the Kip2-ΔN construct. The resulting mutant protein, Kip2-CF (illustrated in Fig. 3A), was no longer able to polymerize aMTs (0.20 ± 0.06 μm, mean ± s.d., n = 3 independent clones, ****) (Fig. 3B). Although this result supports the importance of the motor domain, it could simply be a consequence of the loss of motility, thus, reduced amounts of Kip2 on microtubule plus-ends. Therefore, we fused the Kip3 motor domain to Kip2-CF and expressed the chimeric protein from the *KIP2* locus. The Kip3-Kip2 chimera was abundantly present at aMT plus-ends but was still incapable of polymerizing microtubules (0.26 ± 0.07 μm, mean ± s.d., n = 3 independent clones, ****) (Fig. 3B). The Kip3 motor domain intrinsically promotes catastrophe by stabilizing the curved conformation of tubulin on microtubule plus-ends (Arellano-Santoyo et al., 2017). For this reason, we measured the lengths of aMTs in *KIP2/Kip3-Kip2 chimera* heterozygous diploid cells to dissect whether Kip3-Kip2 chimera gained the Kip3 motor domain function in microtubule depolymerization. We observed similar aMT length in *KIP2/kip2*Δ (1.92 ± 0.09 μm, mean ± s.d., n = 3 independent clones, ****) and *KIP2/Kip3-Kip2 chimera* cells (1.91 ± 0.13 μm, mean ± s.d., n = 3 independent clones, ****), both shorter in comparison with wild-type diploid cells (2.59 ± 0.14 μm, mean ± s.d., n = 3 independent clones), suggesting that the short aMTs in Kip3-Kip2 chimera cells originated solely from the loss of the Kip2 motor domain. Again, these data support the indispensable role of the Kip2 motor domain and not its motility in microtubule polymerization.

Figure 3:

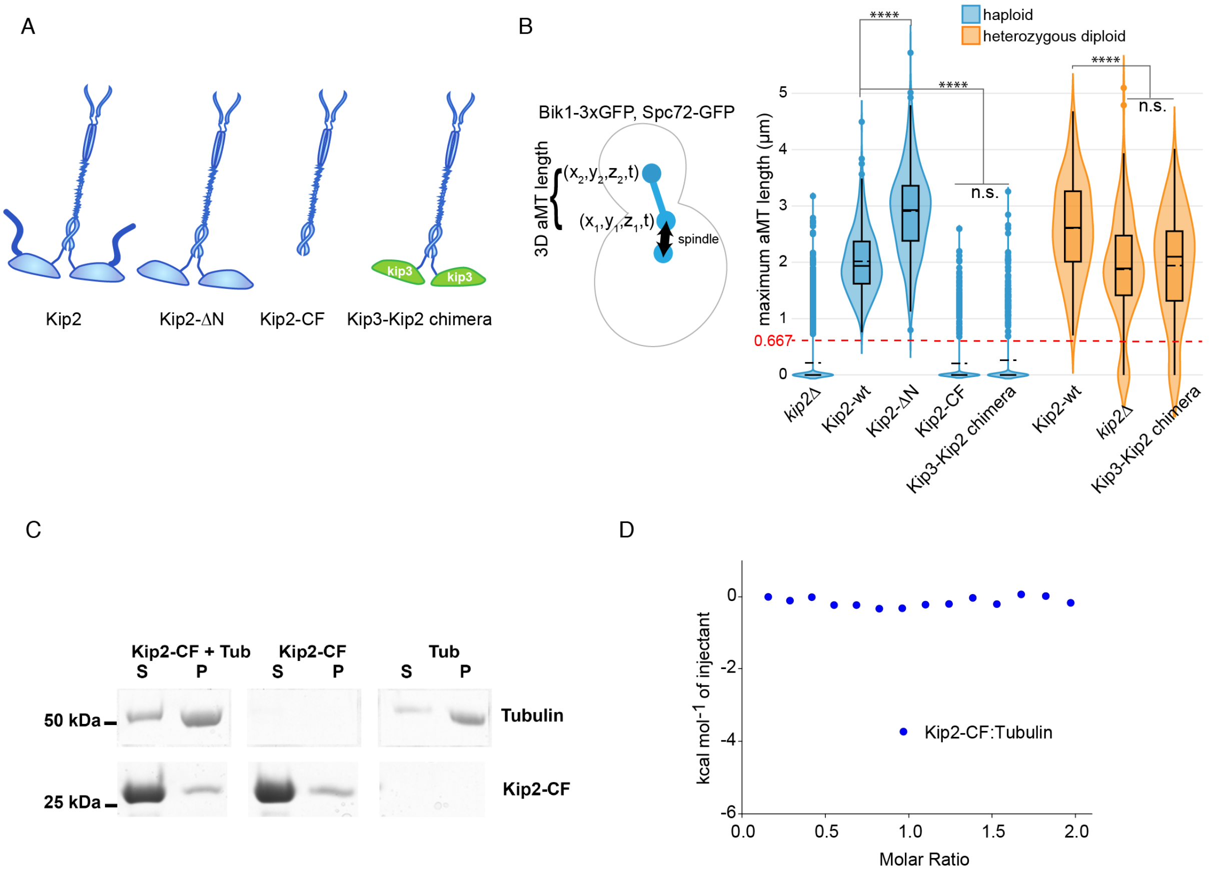

Figure 3. Effect of various truncated Kip2 constructs on microtubule length and probing of the binding of Kip2-CF to tubulin and microtubules.

(A) Illustration of the various truncated Kip2 constructs and the chimeric Kip2 construct.

(B) Quantification of the maximum aMT length applying Bik1-3xGFP and Spc72-GFP as the markers for the plus-end and minus-end.

(C) Microtubule-pelleting assay in which Kip2-CF was mixed in two-fold excess with tubulin in BRB80 buffer. As controls, Kip2-CF and tubulin were processed alone. The supernatants (S) and pellets (P) were separated on a 12 % SDS-PAGE and stained with Coomassie.

(D) ITC experiment for Kip2-CF:tubulin. The solid line represents the fit that was obtained by using the monomeric concentrations of Kip2-CF and tubulin.

To examine whether Kip2-CF could potentially interact with tubulin, we purified this fragment from bacteria and subjected it to the microtubule pelleting assay (Fig. 3C), which demonstrated no interaction between Kip2-CF and stabilized microtubules. Further isothermal titration calorimetry (ITC) and SEC-MALS analysis of Kip2-CF in solution with free tubulin dimers revealed no detectable interaction under our conditions (Fig. 3D and S4B). Importantly, the SEC-MALS analysis of Kip2-CF alone resulted in a molecular mass of 55 kDa, consistent with the formation of a dimer as predicted by a coiled-coil-prediction server (Fig. S4AC) (Lupas et al., 1991). Altogether, our results demonstrate that the motor domain contains the only kinesin-tubulin interface that recognizes free tubulin dimers and polymerizes microtubules.

Kip2's C-terminal tail confers the microtubule plus-end specific accumulation of Kip2

Given that the motor domains are essential for microtubule polymerization, we reckon that Kip2 should accumulate at microtubule plus-ends and that at least one of its motor domains should be free from microtubules for this function. Indeed, as reported previously (Hibbel et al., 2015), Kip2-3xsfGFP construct moves along microtubule lattices and GFP signal peaks specifically on their plus-ends (Fig. 4A). To quantitatively demonstrate the accumulation of Kip2-3xsfGFP at microtubule plus-ends, we devised the 'tip accumulation index' by dividing the mean GFP fluorescence at the plus-end with the mean fluorescence along the whole microtubule lattice, where the plus-end is defined as the location of the intensity peak ± 1 pixel (133.3 nm). The tip accumulation index adopts values close to 0 when the Kip2 intensity on plus-ends is substantially lower than that on lattices, to 1 when Kip2 intensity on plus-ends is the same as on the lattice, and greater than 1 when Kip2 accumulates at microtubule plus-ends. Analysis of the distribution of Kip2-3xsfGFP generated a mean index of 1.98 (1.91 - 2.06, 95% CI), demonstrating its extensive accumulation at microtubule plus-ends (Fig. 4B).

Strikingly, Kip2-ΔT-3xsfGFP, a mutant lacking the last 62 residues of Kip2's C-terminus failed to enrich itself to microtubule plus-ends as efficiently (Fig. 4AB). Measurements of Kip2-ΔT-3xsfGFP signal along microtubules generated a mean tip accumulation index of 1.43 (1.41 - 1.46, 95% CI), on average 28% decreased compared to wild-type proteins. The strong defect for Kip2-ΔT-3xsfGFP to accumulate on microtubule plus-ends does not stem from failing to assemble Kip2 homo-dimers, as the C-terminal tail is not required for forming homo-dimers (Fig. S4CDE). The possibility of Kip2-ΔT-3xsfGFP being defective in motility is also excluded by quantifying its moving speed along microtubules in vivo, which did not deviate from wild-type proteins (6.69 ± 2.31 μm min^{-1}, mean ± s.d., n = 107 speckles vs. 6.26 ± 2.07 μm min^{-1}, mean ± s.d., n = 192 speckles in wild-type cells, n.s.) (Fig. S5AB). Since Kip2-ΔT-3xsfGFP does not demonstrate any defect in targeting itself to microtubule plus-ends, we explored the possibility of the C-terminal tail actively retaining Kip2 on plus-ends. Loss of such ability will lead to dissociation of Kip2-ΔT from microtubule plus-ends prematurely. To test this possibility, we expressed Kip2-CF-3xsfGFP from the endogenous locus and used Kip2-CF-ΔT-3xsfGFP as a negative control. Although the majority of the GFP signal diffused in the cytoplasm, Kip2-CF-3xsfGFP was enriched on SPBs and at microtubule plus-ends (Fig. 4C). Remarkably, Kip2-CF-ΔT-3xsfGFP failed to associate with any specific structure (Fig. 4C). These results demonstrate that the C-terminal tail of Kip2 plays an important role in keeping Kip2 at where microtubule polymerization is needed, and this location is at the microtubule plus-end.

Figure 4:

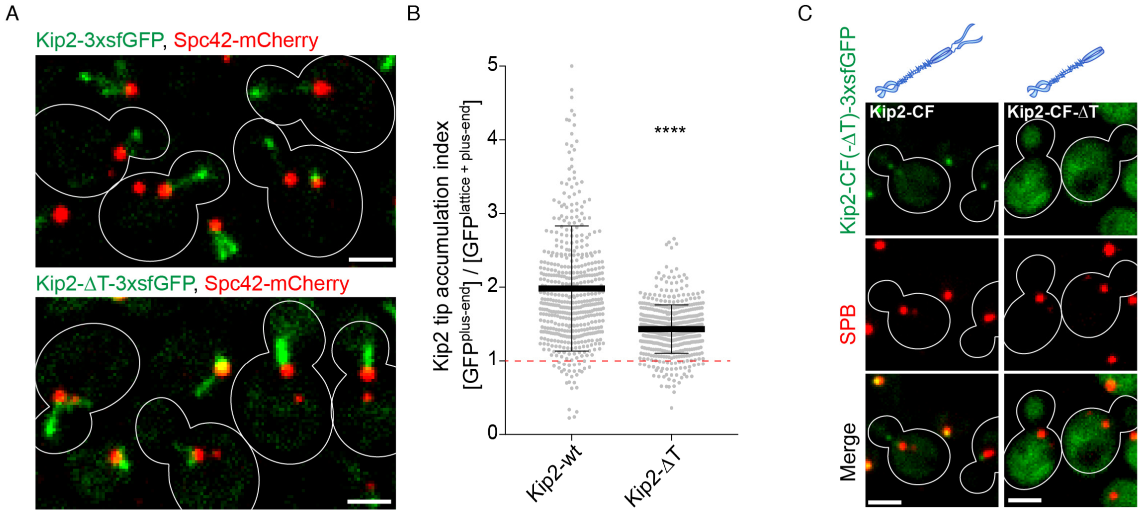
A
Kip2-3xsfGFP, Spc42-mCherry
Kip2-ΔT-3xsfGFP, Spc42-mCherry
B
Kip2 tip accumulation index
[GFPplus-end] / [GFPlattice + plus-end]
5
4
3
2
1
0
****
Kip2-wt
Kip2-ΔT
C
Kip2-CF(-ΔT)-3xsfGFP
SPB
Merge
Kip2-CF
Kip2-CF-ΔT

Figure 4. Influence of the Kip2 C-terminal tail on Kip2 enrichment at microtubules and localization of two Kip2 C-terminal fragments.

(A) Representative images of metaphase cells that expressed either wild-type Kip2-3xsfGFP or Kip2- Δ T-3xsfGFPand Spc42-mCherry.

(B) Quantification of the Kip2 accumulation at the microtubule tip for wild-type Kip2 and Kip2-ΔT

(C) Representative images of metaphase cells expressing either the C-terminal Kip2 fragments Kip2-CF 3xsfGFP or Kip2-CF- ΔT 3xsfGFP. Spc42-mCherry was used a marker.

The C-terminal tail is indispensable for the microtubule polymerase activity of Kip2

To examine the importance of retaining Kip2 on microtubule plus-ends, we measured the length of aMTs in Kip2-ΔT cells. We found that the loss of the Kip2 C-terminal tail led to extremely short aMTs (0.42 ± 0.11 *μ*m, mean ± s.d., n = 3 independent clones, ****) similar to those of *kip2*Δ cells, regardless of the presence of the N-terminus of Kip2 (0.29 ± 0.05 *μ*m in Kip2-ΔN-ΔT cells, mean ± s.d., n = 3 independent clones ****) (Fig. 5). Therefore, the negative regulatory function of Kip2's N-terminus for microtubule polymerization also requires the C-terminal tail. Given that Kip2's C-terminus is not required for recruiting free tubulin dimers, motility and homo-dimerization, the only plausible conclusion is that its role in retaining Kip2 on plus-ends is essential for the Kip2 motor domain to become an active microtubule polymerase.

Figure 5:

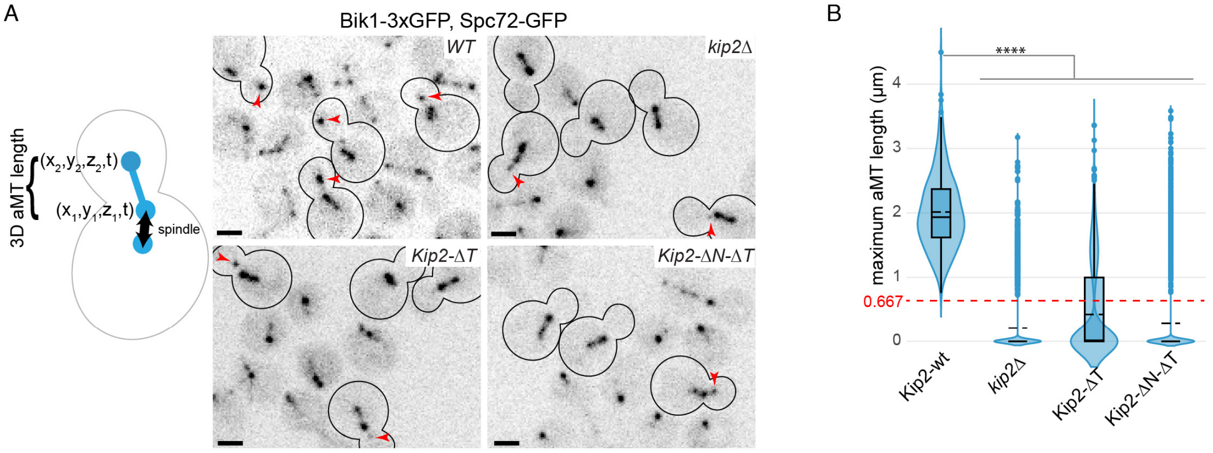

Figure 5. Influence of various Kip2 truncations on aMT length.

(A) Set-up and representative images that were applied to determine the aMTs length for wild-type Kip2 and various Kip2 truncations. The cells expressed Bik1-3GFP and Spc72-GFP as markers.

(B) Quantification of the aMT length of wild-type Kip2, the kip2 deletion and the truncated Kip2 versions Kip2- Δ T or Kip2- Δ N- Δ T.

Bik1 retains Kip2 on microtubule plus-ends through direct interaction

The observation that Kip2-CF-3xsfGFP specifically accumulated on aMT plus-ends was unexpected since Kip2-CF did not exhibit affinity to microtubules (Fig. 3C). Kip2-CF must do so by binding to other microtubule plus-end specific proteins, most likely Bik1, which has been established to interact with Kip2-CF and proposed to hitchhike on Kip2 to move along microtubules to reach their plus-ends (Caudron et al., 2008). Indeed, Kip2-CF-3xsfGFP failed to accumulate on aMT plus-ends in *bik1*Δ cells but not in *kip3*Δ cells (Fig. 6A).

In order to test whether Kip2-CF-ΔT-3xsfGFP dissociates from microtubule plus-ends due to the loss of interaction with Bik1, we purified the coiled-coil domain of Bik1 (Bik1-CC), Kip2-CF and Kip2-CF-ΔT expressed from bacteria. In a SEC-MALS analysis, the peak of Bik1-CC was shifted by the addition of Kip2-CF, whose molecular mass corresponds to two Bik1-CC and two Kip2-CF (2:2 complex) (Fig. 6B). We then subjected these two fragments to an ITC experiment, which allows quantitative measurement of binding isotherms by recording the heat change occurring upon complex formation. In agreement with the SEC-MALS analysis, the ITC experiment yielded a K_d below 100 nM ± 12 nM, suggesting the formation of an extremely tight complex (Fig. S6). It is an inherent property of ITC experiments that for strong interactions only the upper limit of the Kd can be determined. In contrast, Kip2-CF-ΔT no longer co-eluted with Bik1-CC, indicating that the C-terminal tail is essential for Bik1-Kip2 interaction (Fig. 6B). Altogether, we conclude that Kip2-CF-3xsfGFP tracks growing and shrinking microtubule plus-ends by directly binding to Bik1.

Next, we asked whether Bik1 retains full-length Kip2 on microtubule plus-ends as well. Firstly, we found that in *bik1*Δ cells Kip2-3xsfGFP moves along microtubules at a similar speed (6.45 ± 2.19 μm min^{-1}, mean ± s.d., n = 99 speckles, n.s.) to that of control cells (6.26 ± 2.07 μm min^{-1}, mean ± s.d., n = 192 speckles) (Fig. S5AB). Secondly, the tip accumulation index of Kip2-3xsfGFP distribution in *bik1*Δ cells reduced to 1.72 (1.68 - 1.76, 95% CI) (Fig. 6C), suggesting a reduction of Kip2 retention at microtubule plus-ends. Thirdly, we applied a previously established mathematical model for Kip2, which describes its binding at microtubule minus-ends and lattices, stepping of the motor, as well as its unbinding on the lattices and the plus-ends. (Fig. 6F). Fitting this model to the experimental data (Fig. 6DE) allowed us to estimate the loading rates at the minus-end and on the lattice as well as the unbinding rate at the plus-end. Upon deletion of *BIK1,* the estimate for the plus-end unbinding rate of increased significantly from 3.57 (95% CI: 3.06 – 4.56) S^{-1} to 15.7 (10.2 – YY) S^{-1}, i.e. 4.4-fold (Fig. 6C), indicating that removal of Bik1 leads to drastically increased release of Kip2 at microtubule plus-ends. Bik1-dependent retention of Kip2 on microtubule plus-ends activates the polymerase activity of Kip2.

Figure 6:

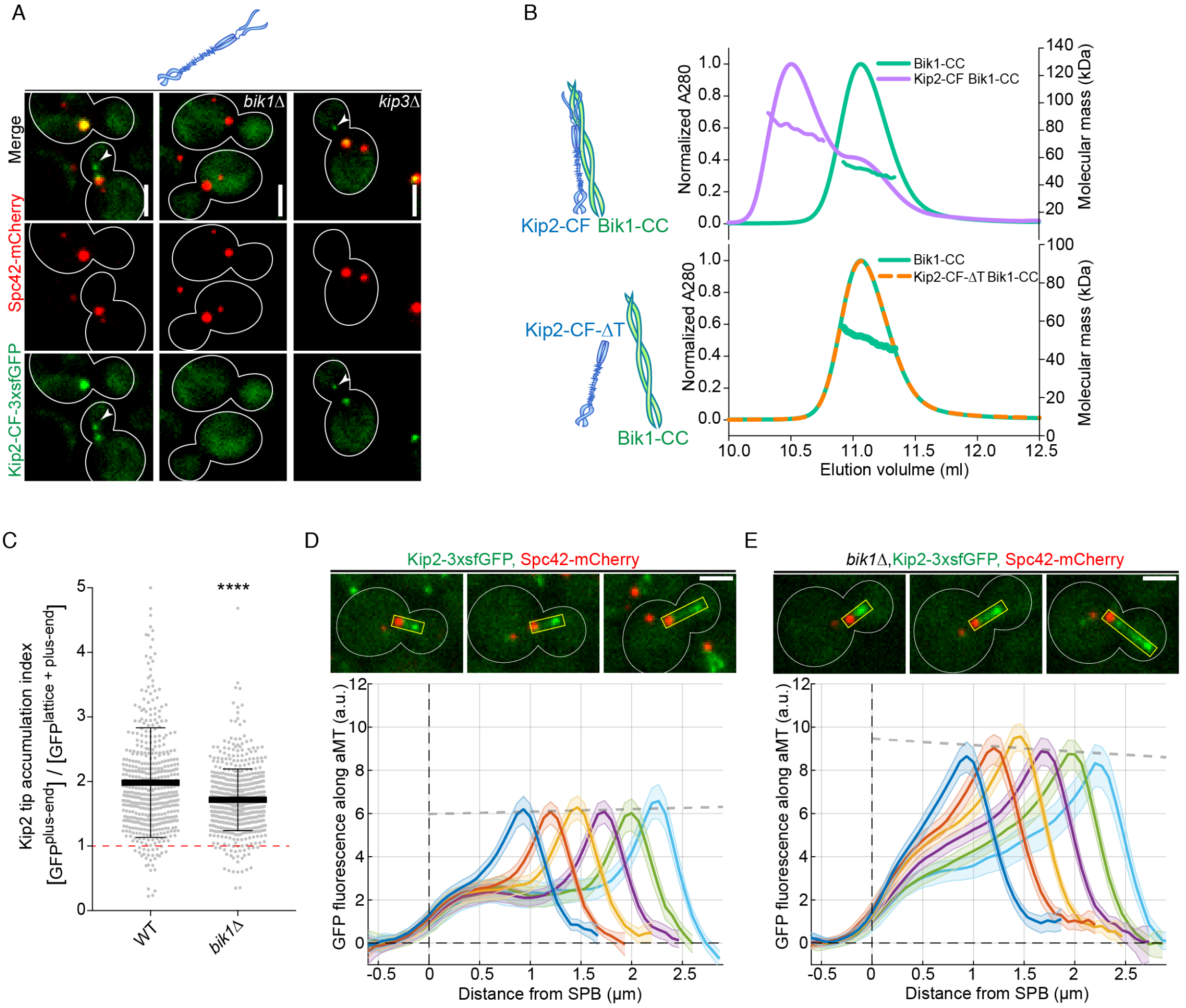

Figure 6. Role of the Bik1-Kip2 interaction for the Kip2 polymerase function.

(A) Representative images of metaphase cells that expressed Kip2-CF-3xsfGFP and Spc42-mCherry. Cells with no deletion, the bik1 deletion or the kip3 deletion were used.

(B) Upper part: SEC-MALS experiment of Kip2-CF with Bik1-CC (purple) and Bik1-CC as a reference (green). Lower part: SEC-MALS experiment of Kip2-CF-ΔT with Bik1-CC (orange) and Bik1-CC as a reference (green). The UV absorption at 280 nm and the molecular masses across the peak determined by MALS are plotted.

(C) Quantification of the Kip2 tip accumulation index in cells with or without the bik1 deletion.

(D) and (E) Representative images of metaphase cells expressing Kip2-CF-3xsfGFP (D) or Kip2-CF-3xsfGFP in cells with a bik1 deletion. Spc42-mCherry was used as a marker. In addition, the line scan analyses of the respective fluorescence profiles along aMTs are presented.

Discussion

Microtubule polymerases are enzymes that catalyze the addition of tubulin dimers to the end of a microtubule polymer. Our work demonstrates that kinesin Kip2 functions as a microtubule polymerase in vivo. Kinesin polymerases could potentially 'shuttle tubulin' to plus-ends by carrying them when moving along microtubule lattices, which cannot be the case for Kip2, simply because its free tubulin interface (interface 1) would not be accessible when bound to microtubules. The other possibility is that when a kinesin arrives at a microtubule plus-end, it dwells and fishes free tubulin dimers from the cytoplasm before dissociation, which is likely the case for Kip2. By this mechanism, Kip2 would locally enrich the tubulin concentration at the plus-end to promote polymerization of microtubules. We found a kinesin-tubulin interface that separates the activities of Kip2 motility and microtubule polymerization. One role of this interface could be to preferably bind to free tubulin dimers. Since the interface 1 mutant is still capable of binding to free tubulin with a weaker affinity than the wild-type, it can be concluded that the mutation could also affect the polymerization mechanism of the motor domain. One possibility is that the interface 1 stabilizes an intermediate state between 'curved' and 'straight' tubulin. More work is required to understand how the kinesin Kip2 functions as a polymerase, but we propose the following model: Tubulin adopt 'straight' conformations in the body of microtubules, whereas they remain to be curved in single protofilaments or unpolymerized (Brouhard and Rice, 2014). The differential curvature of tubulin is a fundamental property that kinesin depolymerases exploit to control microtubule length. Members from kinesin-13 family use their motor domains to preferentially bind to and to induce curved tubulin, thereby trigger catastrophe. Kip3, a member of kinesin-8, also preferably binds curved tubulin, and this property underlies its depolymerase activity. We suggest that kinesin polymerases could employ this property to separate polymerase activity from motility. In line with this hypothesis, an overlay of the Kip2 structure model with 'curved' and 'straight' tubulin structure places Kip2^{K294R296} at a position that is optimal for reaching the H12 helices of β-tubulin from a 'curved' but not a 'straight' conformation (Fig. S1B). This binding to curved tubulin would allow the Kip2 motor domain to locally enrich tubulin at the microtubule plus-end. As a non-exclusive alternative, the Kip2 motor domain could stabilize the transition from curved to straight tubulin. This mechanism has been reported for Eg5, a microtubule polymerase of the kinesin-5 family (Chen and Hancock, 2015).

A polymerase that actively recruits and incorporates tubulin on to microtubule plus-ends must follow the growing tracks. Stu2/XMAP215 family proteins are such examples, they use multiple 'TOG' domains to recruit free tubulin and a basic patch to diffuse along the lattice so that the polymerases can processively follow the growing end and perform multiple rounds of tubulin incorporation. We found that in living cells, Kip2 itself is insufficient to catch its motor domains at the growing plus-ends. Instead, it carries and makes use of Bik1 for this purpose. Bik1 substantially prolongs the time that Kip2 stays on plus-ends, where at least one of the motor domains is potentially free from microtubule lattices and efficiently recruits free tubulin. These findings explain why Bik1 should be required for Kip2 to prolong microtubules in vivo. Consistently, aMTs in *bik1*Δ cells have been reported to be extremely short. We observed around 40% to 50% reduction for Bik1-3xGFP intensity on aMT plus-ends in all conditions where Kip2 lost motility or interaction with Bik1. Therefore, the loss of Bik1 from plus-ends is somewhat correlated with microtubule behavior, but more work is required to dissect whether Bik1 can directly polymerize microtubules, which has been a model for CLIP-170. However, no strong interaction between Bik1 and free tubulin dimers has been observed in vitro (Blake-Hodek et al., 2010). CAP-Gly domains of proteins like Bik1 or CLIP-170 interacts primarily with the unstructured C-terminal tail of tubulin and not with the structured domain of tubulin. In a previous study, we found that Bik1 heavily decorates microtubule lattices in the absence of Bim1 or interaction between Bik1 and Bim1. This observation reflects the potential involvement of Bik1 in the incorporation of tubulin to stabilize the freshly incorporated tubulin. We speculate that Bik1 might not be directly involved in recruiting free tubulin dimers, rather facilitate their stable incorporation onto microtubule plus-ends. In addition, Bik1 has been shown to promote the processivity of Kip2 in the presence of Bim1 in vitro. However, we do not see an obvious processivity defect of Kip2 in cells lacking Bim1, Bik1, or the C-terminal tail of Kip2 (Fig. S5AB). Instead, we found that Bim1 is required to maintain the high rate of Kip2 moving along microtubules. Together, we reveal a novel function for the yeast CLIP-170 to activate microtubule polymerases on plus-ends.

The loading of Kip2 onto microtubules is subjected to sophisticated regulation in metaphase cells. The majority of the Kip2 molecules are deployed by SPBs, from microtubule minus-ends, with a steady rate, then walk towards microtubule plus-ends without falling down. Interestingly, this constant influx of Kip2 did not lead to uncontrolled accumulation of Kip2 on microtubule plus-ends (Fig. 6D), which suggests that the dissociation of Kip2 from the plus-ends is regulated as well. Given that Bik1 strongly retains Kip2 at microtubule plus-ends, regulation of the interaction between Bik1 and Kip2 might be a part of such an unloading mechanism. Another layer of the regulation is the phosphorylation of Kip2's N-terminus, which negatively regulates the association of Kip2 with microtubules. Understanding the mechanisms of how Kip2 unloads from microtubule plus-ends will move us closer to a full picture of how this motor protein is spatially controlled and fulfills its functions in cargo transportation and microtubule polymerization.

Supplementary Figures

Figure S1:

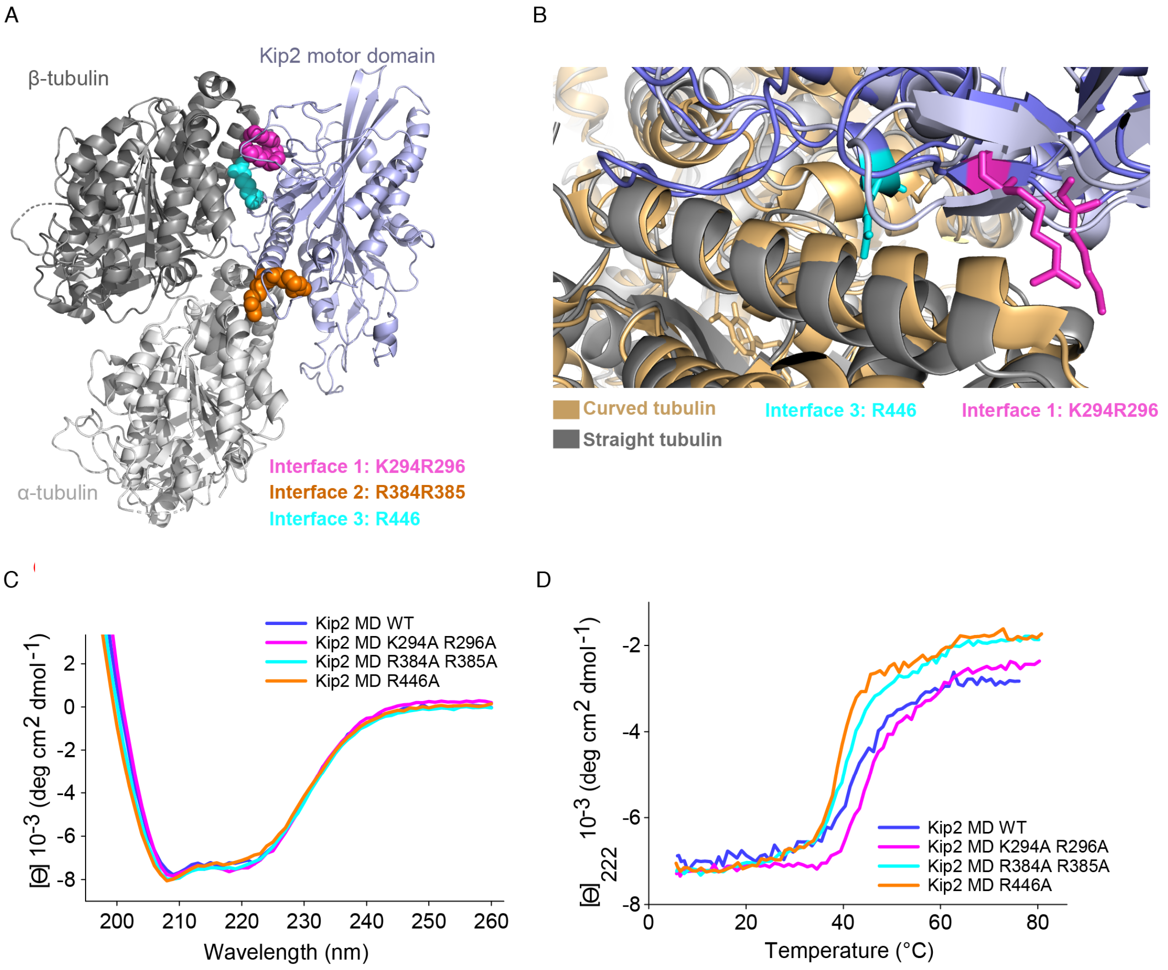

Figure S1. Details of the modeled Kip2 MD-complex and characterization of the wild-type Kip2 MD and the Kip2 MD mutants by CD spectroscopy.

(A) Rear view of the Kip2 motor domain homology model (blue) in complex with the tubulin (white) heterodimer. The three positively charged interfaces that are crucial for tubulin or microtubule binding are highlighted in various colors.

(B) Predicted binding of the Kip2 MD homology model to curved and straight tubulin. The residues K294R 296 (interface 1) and R446 (interface 3) residues are highlighted to illustrate the difference for interface 1.

(C) and (D) CD spectra (C) and thermal unfolding profiles recorded at 222 nm (D) of Kip2 MD wild-type (WT) and the three interface mutants.

Figure S2:

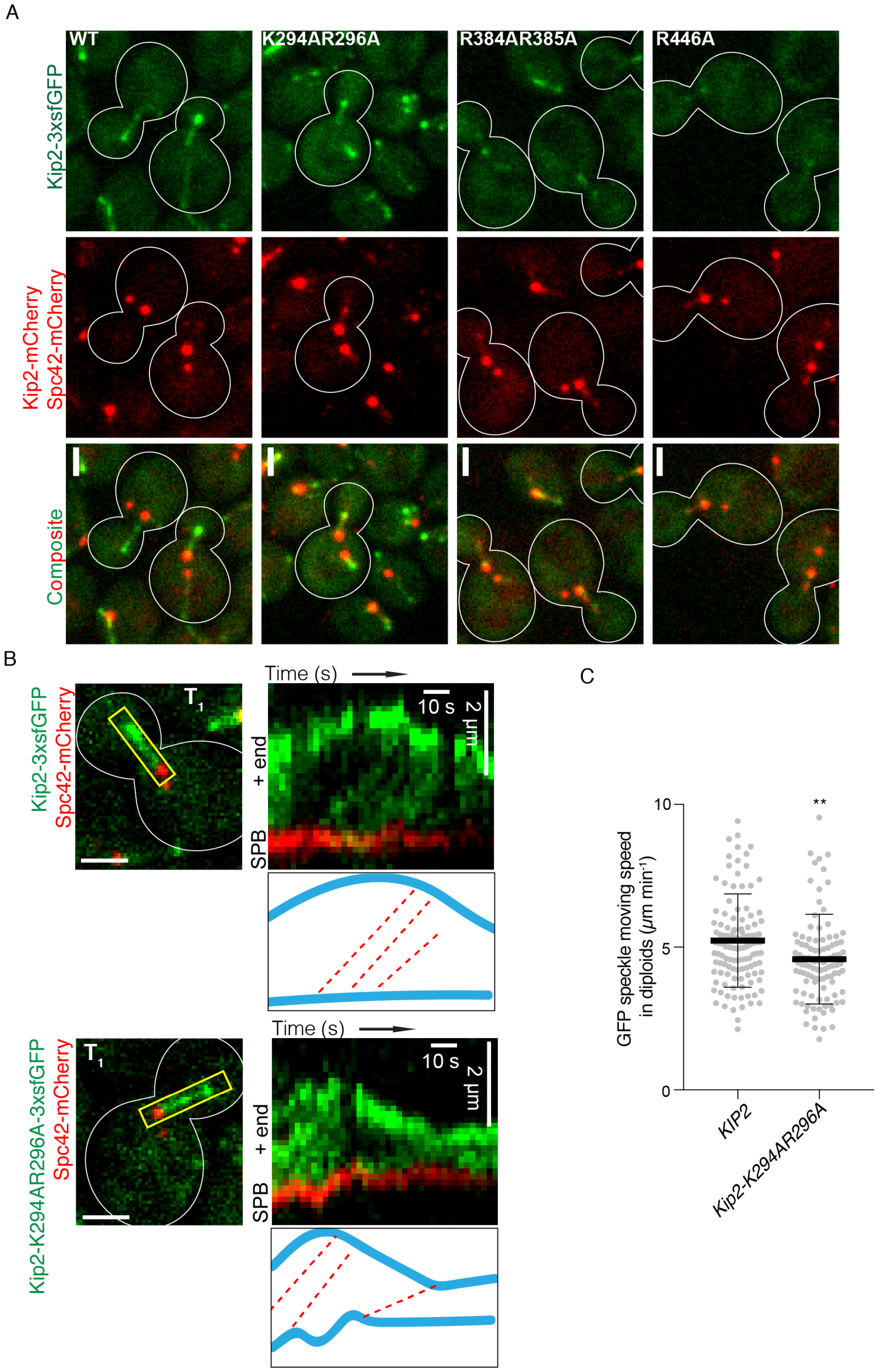
A
WT
K294AR296A
R384AR385A
R446A
Kip2-3xsfGFP
Kip2-mCherry
Spc42-mCherry
Composite
B
Kip2-3xsfGFP
Spc42-mCherry
T_1
Time (s)
10 s
2 µm
+ end
SPB
Kip2-K294AR296A-3xsfGFP
Spc42-mCherry
T_1
Time (s)
10 s
2 µm
+ end
SPB
C
GFP speckle moving speed in diploids (µm min⁻¹)
10
5
0
**
KIP2
Kip2-K294AR296A

Figure S2. Further images of the Kip2 motor domain mutants.

(A) Representative images of yeast cells expressing Kip2-mCherry and Spc42-mChery as references and wild-type Kip2-3xsfGFP or Kip2 harboring the respective mutation of the tubulin-binding interface. A scale bar of 2µm is displayed.

(B) Representative images of yeast cells expressing Kip2-mCherry and Spc42-mChery as references and wild-type Kip2-3xsfGFP or Kip2-3xsfGFP-K294AR296A. A scale bar of 2µm is displayed, the kymographs are shown.

(C) Quantication of the GFP speckle moving speed for wild-type Kip2 and Kip2-K294AR296A.

Figure S3:

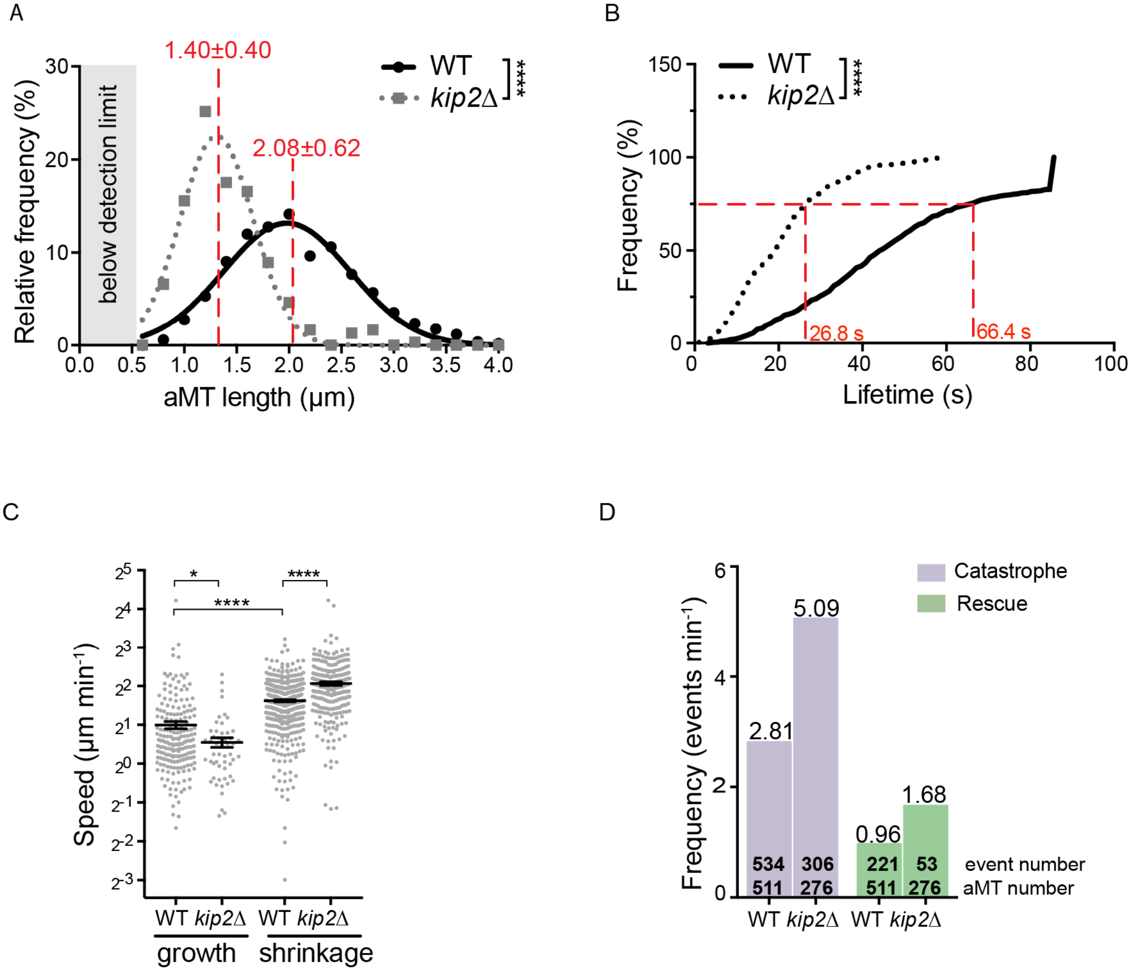

Figure S3. Illustration of how the catastrophe and rescue frequency were determined.

Description of the respective panels can be found in the result section.

Figure S4:

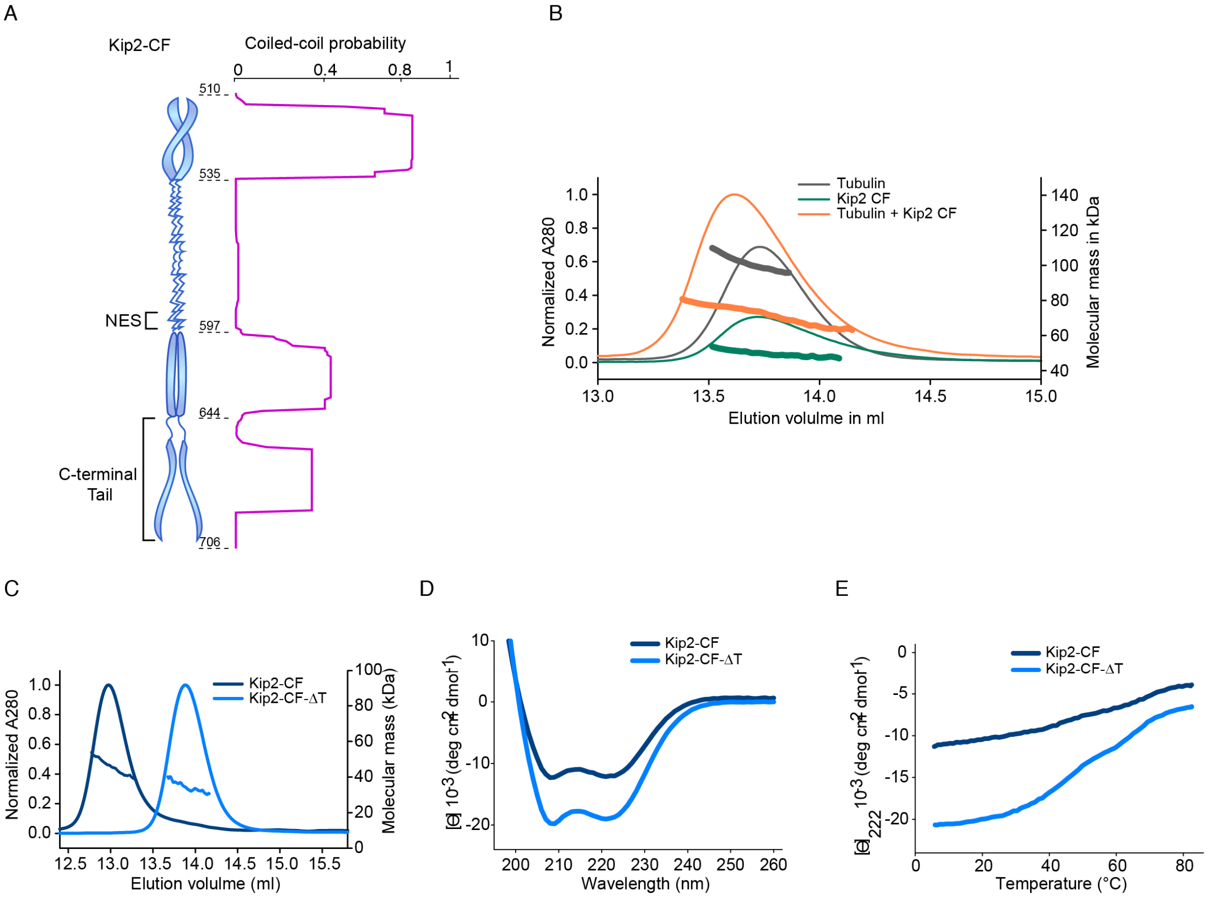

Figure S4. Characterization of Kip2-CF.

(A) Prediction of the coiled-coil probability of the Kip2 C-terminal part.

(B) SEC-MALS experiments of Kip2-CF with tubulin. As a reference, both Kip2-CF and free tubulin were used. The UV absorption at 280 nm and the molecular masses across the peak determined by MALS are plotted.

(C) SEC-MALS experiments of Kip2-CF or Kip2-CF-ΔT. The UV absorption at 280 nm and the molecular masses across the peak determined by MALS are plotted.

(D) and (E) CD spectrum (D) and thermal unfolding profile recorded at 222 nm (E) of Kip2-CF and the Kip2-CF-ΔT.

Figure S5:

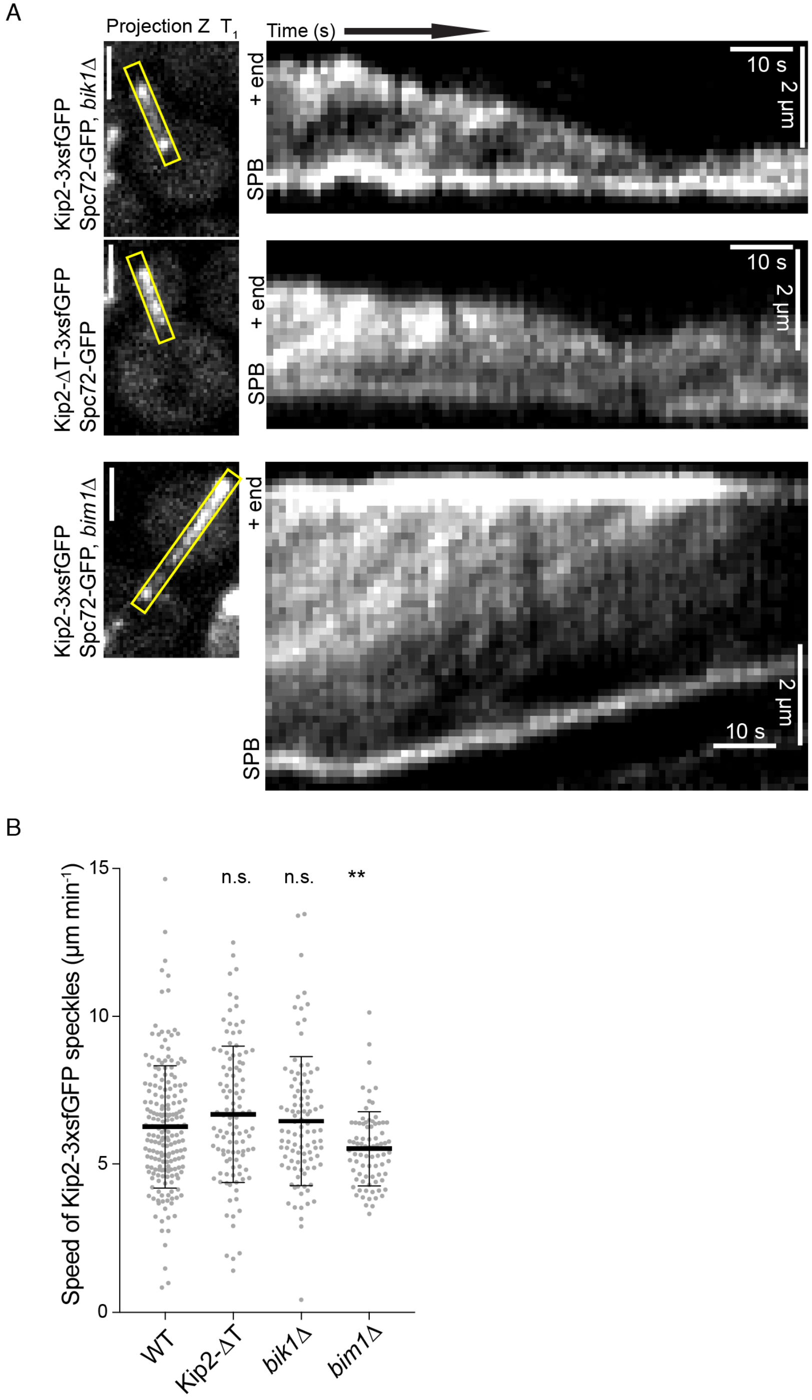

Figure S5. The movement speed of Kip2 is not impaired by the truncation.

(A) Representative metaphase cells and kymographs of wild-type Kip2-3xGFP or Kip2- Δ T-3xGFP associated aMTs. In addition, wild-type Kip2-3xGFP was analyzed in the bik1 delete strain as well.

(B) Quantification of the Kip2 speed for the wild-type Kip2 and Kip2- Δ T. In addition, wild-type Kip2 was also analyzed in the bik1 and bim1 delete strain.

Figure S6:

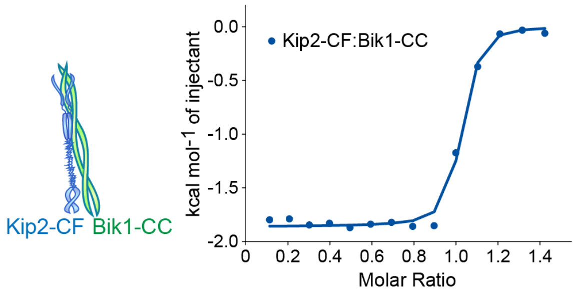

Figure S6. ITC experiments for Kip2-CF:Bik1-CC.
The solid line represents the fit that was obtained by using the monomeric concentrations of Kip2-CF and Bik1-CC.

Material and Methods

Protein preparations

The DNA encoding the motor domain of *S. cerevisiae* Kip2 (Kip2-MD residues 100-503; UniProt ID: P28743), the C-terminal part of *S. cerevisiae* Kip2 (Kip2-CF residues 504-706; UniProt ID: P28743) and a truncated version of the C-terminal part of *S. cerevisiae* Kip2 (Kip2-CF-ΔT residues 504-645; UniProt ID: P28743) were cloned into the pET-based bacterial expression vector PSPCm2, which encodes for an N-terminal 6x His-tag and a PreScission cleavage site using a positive selection method (Olieric et al., 2010). The vectors for mutants of the Kip2-MD were obtained by cloning the DNA bearing the respective mutation from the cell biology experiments in the PSPCm2 vector. The vector for the expression of the Bik1-CC was available from previous work (Stangier et al., 2018).

The production of the proteins was performed in the *E. coli* strain BL21(DE3) (Stratagene) in LB media containing 50 µg/ml of kanamycin. After the cultures had reached an OD_{600} of 0.6 at 37 °C, they were cooled down to 20 °C, induced with 1 mM isopropyl 1-thio-β-D-galactopyranoside (IPTG) and shaken for another 16 hours at 20 °C. Then, the cells were harvested and washed with Dulbecco PBS buffer (Millipore). As the next step, they were sonicated in the presence of the protease inhibitor cOmplete cocktail (Roche) in lysis buffer (50 mM HEPES, pH 8, supplemented with 500 mM NaCl, 10 mM imidazole, 2 mM β-mercaptoethanol, 0.1% bovine deoxyribonuclease I).

Proteins were purified by immobilized metal-affinity chromatography (IMAC) on a HisTrap HP Ni^{2+}-Sepharose column (GE Healthcare) at 4 °C according to the instructions of the manufacturer.

The column was equilibrated in IMAC buffer A (50 mM HEPES, pH 8, supplemented with 500 mM NaCl, 10 mM imidazole, 2 mM β-mercaptoethanol). Proteins were eluted by IMAC buffer B (IMAC buffer A containing 400 mM imidazole in total). In the case of the Kip2-CF and Kip2-CF-ΔT, the N-terminal 6x His-tag was cleaved off by an in-house produced HRV 3C protease (Cordingley et al., 1990) in IMAC buffer A for 16 hours at 4 °C. The cleaved samples were reapplied on the IMAC column to separate cleaved from uncleaved protein.

Protein samples were concentrated and loaded onto a size exclusion chromatography (SEC) HiLoad Superdex 200 16/60 column (GE Healthcare), which was equilibrated in SEC buffer (20 mM Tris-HCl, pH 7.5, supplemented with 150 mM NaCl and 1 mM DTT). In case of the Kip2-MD, the Kip2-MD SEC buffer (20 mM Tris-HCl, pH 7.5, supplemented with 500 mM NaCl, 1 $MgCl_2$, 1 mM EGTA and 1 mM DTT) was used. The fractions of the respective main peaks were pooled and concentrated to 5-20 mg/ml. Protein quality and identity were analyzed by SDS-PAGE and mass spectrometry, respectively.

Circular dichroism (CD) spectroscopy

The CD spectra of Kip2-MD, the Kip2-MD mutants, Kip2-CF and Kip2-CF-ΔT (0.2 mg/ml in PBS) were measured at 5 °C on a Chirascan-Plus spectrophotometer (Applied Photophysics Ltd.) equipped with a computer-controlled Peltier element using a quartz cuvette of 1 mm optical path length. Thermal unfolding profiles were recorded by CD at 222 nm by continuous heating at 1 °C min^{-1}.

Size exclusion chromatography followed by multi-angle light scattering (SEC-MALS)

For the SEC-MALS experiment at 25 °C, a Superdex200 10/30 column (GE Healthcare) was equilibrated in (20 mM Tris-HCl, pH 7.5, supplemented with 150 mM NaCl and 1 mM DTT) at a flow rate of 0.5 ml/min on an Agilent UltiMate3000 HPLC. 30 µl of the respective single protein or complex was injected onto the column, and the mass was determined using the miniDAWN TREOS and Optilab T-rEX refractive index detectors (Wyatt Technology). In the case of experiments of the Kip2-MD, a Superdex75 10/30 column (GE Healthcare) was used, and the SEC-MALS buffer was replaced by the Kip2-MD MALS buffer (40 mM PIPES, pH 6.8, supplemented with 60 mM KCl, 1 mM MgCl2, 1 mM EGTA and 1 mM DTT) The concentration in the injected volume was 5 mg/ml for tubulin and 2-3 mg/ml for the Kip2-MD or the respective mutant. For the Bik1-CC, Kip2-CF and Kip2-CF-ΔT, 5-8 mg/ml were applied. In case of the runs of the complexes, the individual concentrations of the components were maintained. The Zimm model was chosen for data fitting that was performed in the ASTRA 6 software.

Isothermal titration calorimetry (ITC)

All proteins samples were buffer-exchanged to Dulbecco PBS buffer (Millipore) supplemented with 0.5 mM TCEP. ITC experiments were performed on an iTC 200 machine (MicroCal) at 20 °C using 15 injections of 2.6 µl. 260 µM of Kip2-CF was loaded into the syringe. 15 µM Bik1-CC was put into the sample cell. Fits of the binding isotherms were obtained by using a nonlinear least squares minimization method. The one set of site model provided in the software package of the calorimeter was utilized to determine the equilibrium dissociation constant, K_d.

Microtubule-pelleting assay

Microtubule-pelleting assays of purified proteins were performed as previously described. Briefly, 10 mg/ml bovine brain tubulin was diluted in a 1×BRB80 buffer (80 mM K-PIPES, pH 6.8, supplemented, 1 mM EGTA, 1 mM MgCl2 and 1 mM DTT) to 2 mg/ml. In the case of the Kip2-MD constructs, a modified BRB40 buffer (40 mM K-PIPES, pH 6.8, supplemented with 100 mM NaCl, 1 mM EGTA, 1 mM MgCl2 and 1 mM DTT) was used. After the addition of 0.5 mM GTP, the sample was incubated on ice for 5 min. The microtubule polymerization was started by transfer to 37 °C. After 10 min, 0.1 µM, 1 µM and 10 µM paclitaxel were added stepwise with incubation times of 5 min each. Pelleting assays in the presence of Kip2-CF, Kip2-MD or Kip2-MD mutants were performed by mixing 3.8 µM of taxol-stabilized microtubules with an equimolar ratio of the respective protein. As control treatments, taxol-stabilized microtubules or the respective protein was applied alone. Samples were applied onto a taxol–glycerol cushion that contained 55% 2× BRB80, 44% glycerol and 6% 2 mM paclitaxel. After centrifugation at 174,500g for 30 min at 25 °C, an aliquot was taken from the supernatant. After removal of the supernatant, the pellet was resuspended in SDS sample buffer. Samples were loaded and analyzed on Coomassie-stained 12 % SDS gels.

The following material and methods of the in vivo experiments (pages 77-78) are taken from the Ph.D. thesis of our collaborator, Dr. Xiuzhen Chen (Diss No. 25080 ETH Zürich) because the in vivo methods for the paper were not available at the time of the writing of my thesis.

Strain and plasmids of in vivo experiments

Yeast strains and plasmids used in this study are listed in table S1 and tableS2 (see thesis Dr. Xiuzhen Chen) respectively. All strains are isogenic to S288C. All gene deletions were created using the PCR-based integration system (Janke et al., 2004) and gene deletions were verified by PCR analysis. Fluorescent or HA-tagged proteins were tagged at endogenous loci(Knop and Schiebel, 1998). Specific Kip2 mutations were introduced on a pRS314-Kip2-3xsfGFP:KanMX plasmid or a pRS304-Kip2:TRP1 plasmid via site-directed mutagenesis (pfu-Turbo, Stratagene). Kip2 locus was then amplified and integrated in a kip2D strain and the correct integration was verified by PCR and sequencing after integration. Some strains were created with CRISPR-Cas9 system as indicated (Laughery et al., 2015), the oligonucleotides used are in the supplement material of this thesis.

Media and growth conditions

Cells were cultured in YEPD (yeast extract peptone) or SC (synthetic medium) containing 2% glucose. Temperature sensitive mutant strains were diluted to OD600 0.15 and cultivated at 25"C for 4 hours then shifted to 37"C for 50min before analysis. For live cell imaging, overnight cultures in SC were diluted to OD600 0.15 and cultivated for 4 more hours before placed on an SC-medium agar patch for microscopy imaging.

Fluorescence microscopy

A Nipkow spinning disk (Carl Zeiss) equipped with an incubator for temperature was employed. Time-lapse movies were acquired using a back-illuminated EM-CCD camera Evolve 512 (Photometrics, Inc.) mounted on the spinning disk microscope with a motorized piezo stage (ASI MS-2000) and 100x 1.46 NA alpha Plan Apochromat oil immersion objective, driven by Metamorph based software VisiVIEW (Visitron Systems). 17 Z-section images separated by 0.24µm increments were captured with the exposure time of 30ms each, the whole stack took 1.07s. For imaging aMT dynamics,80 continuous repetitions were taken. For imaging strains with both GFP and mCherry signals, the GFP channel was always set to 30ms exposure time and the mCherry channel with 50ms exposure time. Images in figures represent sum fluorescence intensity Z-projections. Scale bars represent 2 µm.

Image and data analysis

Pre-anaphase cells were manually collected based on the shape of cells and the size of spindles. To determine the length of astral microtubules, three-dimensional coordinates of microtubule +ends and the corresponding SPB were extracted with the Low Light Tracking Tool [Krull et al., 2014]. The distance between +end and SPB represents the length of a microtubule, the distance between the proximal and distal SPB is the spindle length. Cells with spindles longer than 2 μm were excluded. All of the time series tracking results were analyzed with custom functions written in Matlab (MathWorks). For fluorescence intensity, a Region Of Interest (ROI) was drawn around the area of interest (AOI) and the integrated density was quantified. An identically sized ROI was put next to the AOI to determine the background signal. The background intensity was subtracted from the ROI intensity to yield the fluorescent intensity (AU). For every experiment that was performed for quantification of fluorescent intensity (AU), corresponding wild type cells were imaged and analysed for comparison to mutant cells. Average values of wild type cells of different experiments were used for normalisation and comparison between experiments. For analyzing the profiles of GFP fusion proteins along aMTs, the sum intensity projection of the images was used. A 5 pixel (666.7 nm) width line was used to scan aMTs from plus-ends toward SPBs.

Statistics of in vivo experiments

Each experiment was repeated with three or more independent clones (biological replicates). The standard deviation (s.d.) of independent clones is shown in the graphs, or as indicated. n.s. (not significant) or asterisks indicate P values from Student's t-test or one-way ANOVA as indicated. Except that the differences of cumulative distributions were evaluated by the Kolmogorov-Smirnov test. No statistical method was used to predetermine sample distribution.

References

Arellano-Santoyo, H., Geyer, E.A., Stokasimov, E., Chen, G.Y., Su, X., Hancock, W., Rice, L.M., and Pellman, D. (2017). A Tubulin Binding Switch Underlies Kip3/Kinesin-8 Depolymerase Activity. Dev Cell *42*, 37-51 e38.

Blake-Hodek, K.A., Cassimeris, L., and Huffaker, T.C. (2010). Regulation of microtubule dynamics by Bim1 and Bik1, the budding yeast members of the EB1 and CLIP-170 families of plus-end tracking proteins. Molecular biology of the cell *21*, 2013-2023.

Brouhard, G.J., and Rice, L.M. (2014). The contribution of alphabeta-tubulin curvature to microtubule dynamics. J Cell Biol *207*, 323-334.

Carvalho, P., Gupta, M.L., Jr., Hoyt, M.A., and Pellman, D. (2004). Cell cycle control of kinesin-mediated transport of Bik1 (CLIP-170) regulates microtubule stability and dynein activation. Dev Cell *6*, 815-829.

Caudron, F., Andrieux, A., Job, D., and Boscheron, C. (2008). A new role for kinesin-directed transport of Bik1p (CLIP-170) in Saccharomyces cerevisiae. Journal of cell science *121*, 1506-1513.

Chen, Y., and Hancock, W.O. (2015). Kinesin-5 is a microtubule polymerase. Nat Commun *6*, 8160.

Cottingham, F.R., and Hoyt, M.A. (1997). Mitotic Spindle Positioning inSaccharomyces cerevisiaeIs Accomplished by Antagonistically Acting Microtubule Motor Proteins. The Journal of Cell Biology *138*, 1041-1053.

Drechsler, H., Tan, A.N., and Liakopoulos, D. (2015). Yeast GSK-3 kinase regulates astral microtubule function through phosphorylation of the microtubule-stabilizing kinesin Kip2. Journal of cell science *128*, 3910-3921.

Gardner, M.K., Zanic, M., Gell, C., Bormuth, V., and Howard, J. (2011). Depolymerizing kinesins Kip3 and MCAK shape cellular microtubule architecture by differential control of catastrophe. Cell *147*, 1092-1103.

Gupta, M.L., Jr., Carvalho, P., Roof, D.M., and Pellman, D. (2006). Plus end-specific depolymerase activity of Kip3, a kinesin-8 protein, explains its role in positioning the yeast mitotic spindle. Nat Cell Biol *8*, 913-923.

Hibbel, A., Bogdanova, A., Mahamdeh, M., Jannasch, A., Storch, M., Schaffer, E., Liakopoulos, D., and Howard, J. (2015). Kinesin Kip2 enhances microtubule growth in vitro through length-dependent feedback on polymerization and catastrophe. eLife *4*.

Janke, C., Magiera, M.M., Rathfelder, N., Taxis, C., Reber, S., Maekawa, H., Moreno-Borchart, A., Doenges, G., Schwob, E., Schiebel, E., *et al.* (2004). A versatile toolbox for PCR-based tagging of yeast genes: new fluorescent proteins, more markers and promoter substitution cassettes. Yeast (Chichester, England) *21*, 947-962.

Knop, M., and Schiebel, E. (1998). Receptors determine the cellular localization of a gamma-tubulin complex and thereby the site of microtubule formation. Embo j *17*, 3952-3967.

Krull, A., Steinborn, A., Ananthanarayanan, V., Ramunno-Johnson, D., Petersohn, U., and Tolic-Norrelykke, I.M. (2014). A divide and conquer strategy for the maximum likelihood localization of low intensity objects. Optics express *22*, 210-228.

Laughery, M.F., Hunter, T., Brown, A., Hoopes, J., Ostbye, T., Shumaker, T., and Wyrick, J.J. (2015). New vectors for simple and streamlined CRISPR-Cas9 genome editing in Saccharomyces cerevisiae. Yeast (Chichester, England) *32*, 711-720.

Lupas, A., Van Dyke, M., and Stock, J. (1991). Predicting coiled coils from protein sequences. Science *252*, 1162-1164.

Olieric, N., Kuchen, M., Wagen, S., Sauter, M., Crone, S., Edmondson, S., Frey, D., Ostermeier, C., Steinmetz, M.O., and Jaussi, R. (2010). Automated seamless DNA co-transformation cloning with direct expression vectors applying positive or negative insert selection. BMC biotechnology *10*, 56.

Roberts, A.J., Goodman, B.S., and Reck-Peterson, S.L. (2014). Reconstitution of dynein transport to the microtubule plus end by kinesin. eLife *3*, e02641.

Rogers, G.C., Rogers, S.L., Schwimmer, T.A., Ems-McClung, S.C., Walczak, C.E., Vale, R.D., Scholey, J.M., and Sharp, D.J. (2004). Two mitotic kinesins cooperate to drive sister chromatid separation during anaphase. Nature *427*, 364-370.

Sardar, H.S., Luczak, V.G., Lopez, M.M., Lister, B.C., and Gilbert, S.P. (2010). Mitotic kinesin CENP-E promotes microtubule plus-end elongation. Curr Biol *20*, 1648-1653.

Stangier, M.M., Kumar, A., Chen, X., Farcas, A.M., Barral, Y., and Steinmetz, M.O. (2018). Structure-Function Relationship of the Bik1-Bim1 Complex. Structure (London, England : 1993) *26*, 607-618.e604.

Su, X., Qiu, W., Gupta, M.L., Jr., Pereira-Leal, J.B., Reck-Peterson, S.L., and Pellman, D. (2011). Mechanisms underlying the dual-mode regulation of microtubule dynamics by Kip3/kinesin-8. Mol Cell *43*, 751-763.

Walczak, C.E., Mitchison, T.J., and Desai, A. (1996). XKCM1: a Xenopus kinesin-related protein that regulates microtubule dynamics during mitotic spindle assembly. Cell *84*, 37-47.

Wang, W., Cantos-Fernandes, S., Lv, Y., Kuerban, H., Ahmad, S., Wang, C., and Gigant, B. (2017). Insight into microtubule disassembly by kinesin-13s from the structure of Kif2C bound to tubulin. Nat Commun *8*, 70.

4. Characterization of the tubulin-binding domain of the kinesin Kip3

4. Characterization of the tubulin-binding domain of the kinesin Kip3

4.1 Declaration of contribution

In the Kip3 project, I performed all the in vitro experiments that are included in this thesis. The crystallization experiments were done by me with support from Dr. Anil Kumar. The design and analysis of the in vitro experiments was conducted by Prof. Dr. Steinmetz and me. I cloned, purified and expressed all the constructs. Furthermore, I characterized the binding of Kip3 to tubulin by MALS and ITC experiments. I performed the microtubule-pelleting assays of Kip3 and the microtubule polymerization assay. Crystallization trials were conducted by me, and Anil Kumar helped to prepare crystals for the beam line. At the beam line, Anil Kumar and I together collected data sets. Afterward, I solved the Kip3 TBD structure by Se-Met phasing. The model building and refinement was conducted by me. Dr. Xiuzhen Chen investigated the microtubule dynamics of Kip3 in yeast cells under the guidance of Prof. Dr. Yves Barral. The material and methods of the in vivo experiments can be found in the Ph.D. thesis of Dr. Xiuzhen Chen. Furthermore, the method section of Kip2 manuscript in chapter 4.2 describes the in vivo methods that also were used for Kip3. This draft of the manuscript was written by me under the guidance of Prof. Dr. Michel Steinmetz.

The following section consists of the preliminary version of the manuscript draft with the title “Biochemical, structural and functional characterization of the Kip3 tubulin-binding domain “. It is intended to submit this manuscript in the next year.

4.2 Draft of the manuscript

Biochemical, structural and functional characterization of the Kip3 tubulin-binding domain

Marcel M. Stangier[1], Xiuzhen Chen[2], Anil Kumar[1], Yves Barral[2], Michel O. Steinmetz[1,3*]

[1]Laboratory of Biomolecular Research, Division of Biology and Chemistry, Paul Scherrer Institut, CH-5232 Villigen PSI, Switzerland,

[2]Institute of Biochemistry, ETH Zürich, CH-8049 Zürich, Switzerland

[3]University of Basel, Biozentrum, CH-4056 Basel, Switzerland

*Corresponding author and lead contact: michel.steinmetz@psi.ch

Abstract

The yeast kinesin Kip3, a member of the kinesin-8 family, acts as a microtubule depolymerase that can also rescue microtubules from shrinkage. This microtubule rescue activity was found to be dependent on the non-motor domains. Here, we report a novel tubulin-binding domain (TBD) outside of the Kip3 motor domain and determined its crystal structure. The structure revealed a dimer that is formed by a sophisticated arrangement of α-helices. By screening mutants and performing competition ITC experiments, a potential interaction interface between Kip3 and tubulin was suggested. We further found that this tubulin-binding domain is indispensable for the microtubule rescue activity of Kip3. Experiments in living yeast showed that the Kip3 TBD together with the motor domain forms the minimal construct that can rescue microtubules. We propose that the motor domain of Kip3 functions as an anchor on the microtubules plus-end so that the Kip3 TBD can increase the tubulin concentration at the plus-end or facilitate the exchange of GDP-bound tubulin to GTP-bound tubulin, leading to the rescue of shrinking microtubules. In addition, the unstructured C-terminal tail of Kip3 appears to possess a microtubule-binding domain that is not involved in the rescue function. However, the Kip3 C-terminal tail seems to serve as a tether to increase the processivity of the motor domain, and this enhances the catastrophe-inducing activity of the motor domain.

Introduction

The kinesin-8 family consists of microtubule depolymerases that play crucial roles in cellular processes such as mitosis by restricting the length of microtubules (Gupta et al., 2006; Stumpff et al., 2008). The correct length and assembly of the mitotic spindle are essential for achieving correct chromosome segregation. In budding yeast, the kinesin Kip3, a member of the kinesin-8 family, controls the length of the mitotic spindle (Su et al., 2013). Kip3 depolymerizes microtubules in a length-dependent manner (Su et al., 2011) because this kinesin accumulates at the microtubule plus-end due to its high processivity (Varga et al., 2009). In contrast to Kip3, the depolymerase activity of the kinesin-13 family member MCAK does not depend on the length of microtubules (Gardner et al., 2011). In the microtubule lattice, tubulin occurs in the so-called straight conformational state (Brouhard and Rice, 2018). On the other hand, soluble tubulin and tubulin at the very end of microtubules exist in a curved state (Brouhard and Rice, 2014). Therefore, the stabilization of the curved state by the motor domain of Kip3 or MCAK can promote the disassembly of microtubules (Arellano-Santoyo et al., 2017; Wang et al., 2017). The Kip3 catastrophe mechanism appears to be ATP independent and introduces a second function of the motor domain besides motility through the hydrolysis of ATP. The dimeric protein Kip3 comprises an N-terminal motor domain, followed by the coiled-coil neck and a C-terminal part. The motor domain is capable of depolymerizing microtubules by the stabilization of curved tubulin dimers at the microtubule plus-end (Arellano-Santoyo et al., 2017).

However, Kip3 can also rescue shrinking microtubules by its C-terminal part (Fukuda et al., 2014). Rescue of microtubule means that they switch from shrinkage back to a growing state (Gardner et al., 2013). Rescue factors can facilitate microtubule rescue by mechanisms like recruiting and enriching soluble tubulin locally at the plus-end (Al-Bassam et al., 2010). Since growing microtubules exhibit a GTP cap and the loss of the GTP cap induces catastrophes (Akhmanova and Steinmetz, 2015), it is believed that the recruitment of soluble GTP-bound tubulin can rescue microtubules by the formation of a new GTP cap (Brouhard and Sept, 2012; Seetapun et al., 2012). Furthermore, microtubules feature GTP islands, which are small areas of GTP-bound tubulin inside the microtubule lattice (Akhmanova and Steinmetz, 2015; Gardner et al., 2013). It is postulated that rescue factors can utilize these GTP islands to promote the rescue of microtubules (Aumeier et al., 2016), and a GTP island could function as a seed to establish a new GTP cap (Cassimeris, 2009). Microtubule-severing enzymes like katanin can introduce GTP islands through their severing activity so that these enzymes induce rescue of microtubules as a side effect (Vemu et al., 2018). Therefore, rescue factors could also exchange GDP-bound tubulin to GTP-bound tubulin inside the microtubule lattice to create GTP islands.

It is assumed that the rescue function prevails at low concentrations of Kip3 and high concentrations induce a shift to the depolymerase activity (Su et al., 2011). In in vitro experiments, the C-terminal part of Kip3 interacts both with soluble tubulin and microtubules, and it is proposed that two different binding sites for tubulin and microtubules exist. Furthermore, it has been reported that the C-terminal part of Kip3 can be functionally divided into an α-helical proximal region that appears to be important for the rescue activity and a partially unstructured C-terminal tail (Dave et al., 2018); destabilization of the spindle midzone seems to be prevented by this region (Dave et al., 2018). Interestingly, a similar C-terminal tail of the Kip3 orthologue, Kif18A, can bind microtubules on its own (Stumpff et al., 2011; Weaver et al., 2011).

Structural information about the C-terminal part of Kip3 or any orthologue are not available, and the rescue mechanism of microtubules of Kip3 is poorly understood. In order to decode the rescue mechanism of Kip3, it is required to know in which ways regions of Kip3 can interact with microtubules and tubulin. It remains unclear if both the proximal and distal regions of the Kip3 C-terminal part feature an own binding interface for tubulin and microtubules. Therefore, structural and biochemical studies of these regions of the Kip3 C-terminal part can help to elucidate the rescue mechanism.

Here, we determined that a region that is similar to the proximal region of Kip3 functions as a tubulin-binding domain (TBD) that binds tubulin with a high affinity. We solved the crystal structure of the Kip3 TBD and characterized the tubulin-binding interface. Furthermore, we discovered that the C-terminal tail (Ctail) is a microtubule-binding domain. Additionally, the influence of the Kip3 TBD and the Kip3 Ctail on microtubule dynamics was investigated in yeast cells.

Results

The C-terminal part of Kip3 contains a tubulin-binding domain

A construct of the structured C-terminal part of Kip3 (residues: 445-693) was recombinantly expressed and purified. This construct contained the neck coiled-coil and the α-helical region. Since the full C-terminal pat of Kip3 has been reported to bind to tubulin (Su et al., 2011), we assumed a putative tubulin-binding interface in the structured C-terminal part of Kip3 and called this construct Kip3 tubulin-binding domain (TBD) (Figure 1A). A shorter construct of only the α-helical region (residues: 488-693) could not be successfully purified. A MALS run of the Kip3 TBD showed that the protein is a dimer (Figure 1B), and the mass was measured as 55 kDa, corresponding well to the theoretical mass of the dimer of 59 kDa. Moreover, the CD spectrum indicated a folded protein with an all α-helical fold (Figure 1C), and a cooperative unfolding was observed (Figure 1D).

Figure 1

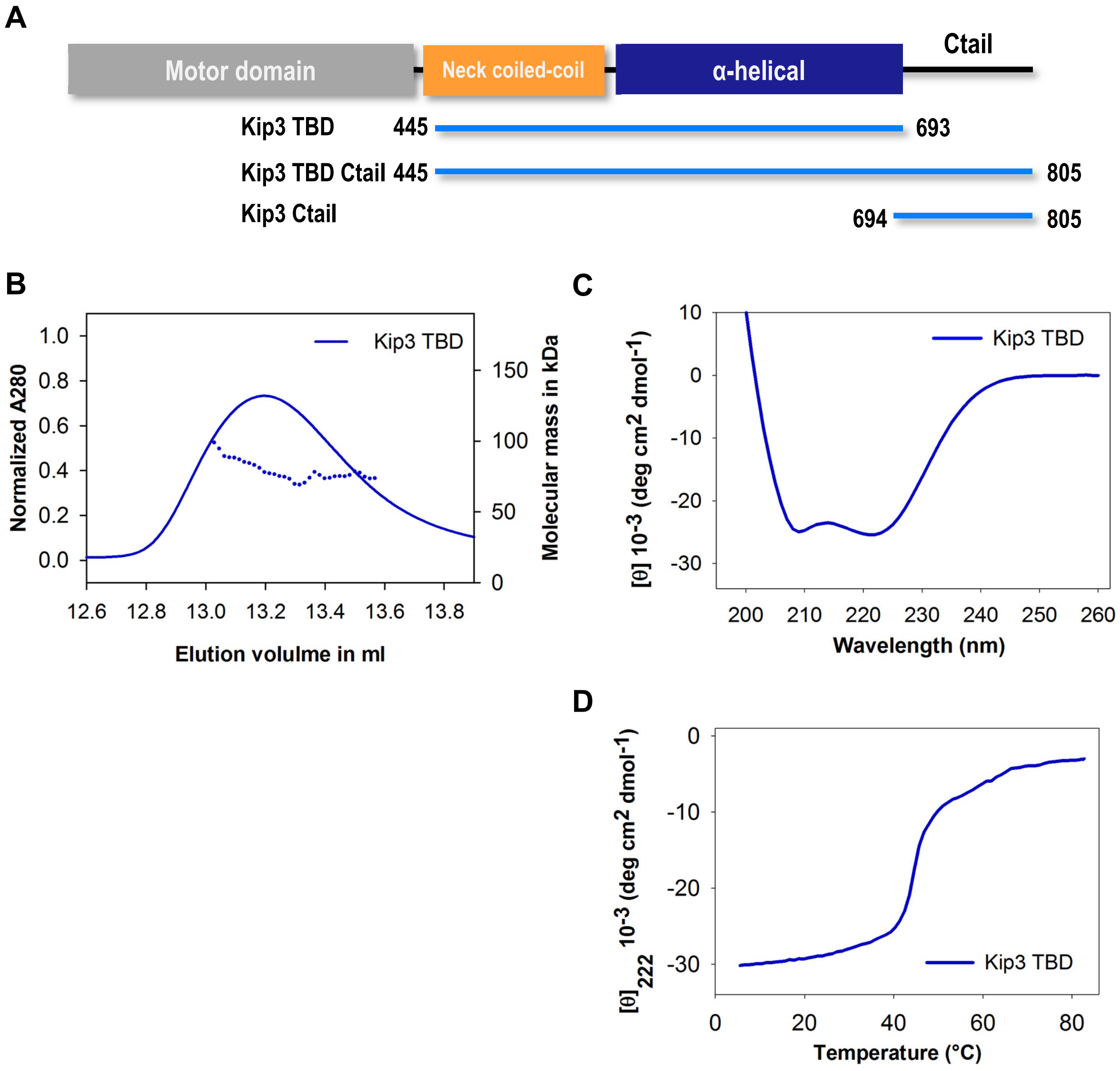

Figure 1. Overview of the Kip3 constructs used in this study and dimerization of the Kip3 TBD.

(A) Domain organization of Kip3. The protein fragments Kip3 tubulin-binding domain (TBD), Kip3 Ctail and Kip3 TBD Ctail are labeled and indicated by lines and residue boundaries.

(B) SEC-MALS experiment of the Kip3 TBD. The UV absorption at 280 nm and the molecular masses across the peak determined by MALS are plotted.

(C) and (D) CD spectrum (C) and thermal unfolding profile recorded at 222 nm (D) of the Kip3 TBD.

In order to investigate the potential tubulin binding of the Kip3 TBD, an ITC experiment of the Kip3 TBD against tubulin was performed. The ITC revealed that the Kip3 TBD can bind soluble tubulin with a high affinity (K_D 400 nM) (Figure 2A). Based on the N-value of 1.74, one Kip3 TBD dimer interacted with a single tubulin heterodimer, and this ratio was confirmed by a MALS run of the Kip3 TBD together with tubulin (Figure 2B). The calculated average mass of 155 kDa corresponded well to the predicted mass of 170 kDa for the Kip3-tubulin complex.

Then, we asked if the Kip3 C-terminal tail (Ctail) increases the tubulin-binding affinity or binds on its own to tubulin. To answer this, the Kip3 TBD Ctail (residues 445-805, consisting of the Kip3 TBD and the Ctail) was chosen. In the ITC titration of tubulin with the Kip3 TBD Ctail, no increase of the binding affinity was observed (Figure 2C), and the N-value was not significantly changed (data available upon request). Therefore, the Kip3 Ctail neither enhances the Kip3 TBD binding affinity to tubulin nor strongly interacts on its own with soluble tubulin.

Next, we investigated the effect of the Kip3 TBD on taxol-stabilized microtubules by a microtubule-pelleting assay. The addition of the Kip3 TBD caused depolymerization of these microtubules, indicating an increase of soluble tubulin compared to the microtubule control without the Kip3 TBD (Figure 2D). This result highlights the strong affinity of the Kip3 TBD for the curved conformational state of tubulin. Furthermore, the addition of the Kip3 TBD to soluble tubulin prevented the polymerization of microtubules probably by sequestering soluble tubulin (Figure 2E). These results seem to be counterintuitive to the proposed rescue function of the Kip3 C-terminal part. However, a single TOG domain of the microtubule polymerase Stu2 showed the same behavior in vitro (Ayaz et al., 2012). This provides evidence that the Kip3 TBD cannot be responsible for the rescue activity alone.

Interestingly, the Kip3 TBD Ctail mixed with microtubules exhibited less microtubule depolymerization activity (Figure 2F) so that the combination of the Kip3 TBD together with the Ctail behaves differently on microtubules than the Kip3 TBD alone. In the microtubule-pelleting assay, the Kip3 Ctail (residues 694-805, fused N-terminally to thioredoxin) co-pelleted with microtubules especially at lower ionic strength of the buffer (Figure 2F). Due to this, it can be proposed that the C-terminal tail possesses a microtubule-binding domain that is a rather weak microtubule binder.

Figure 2

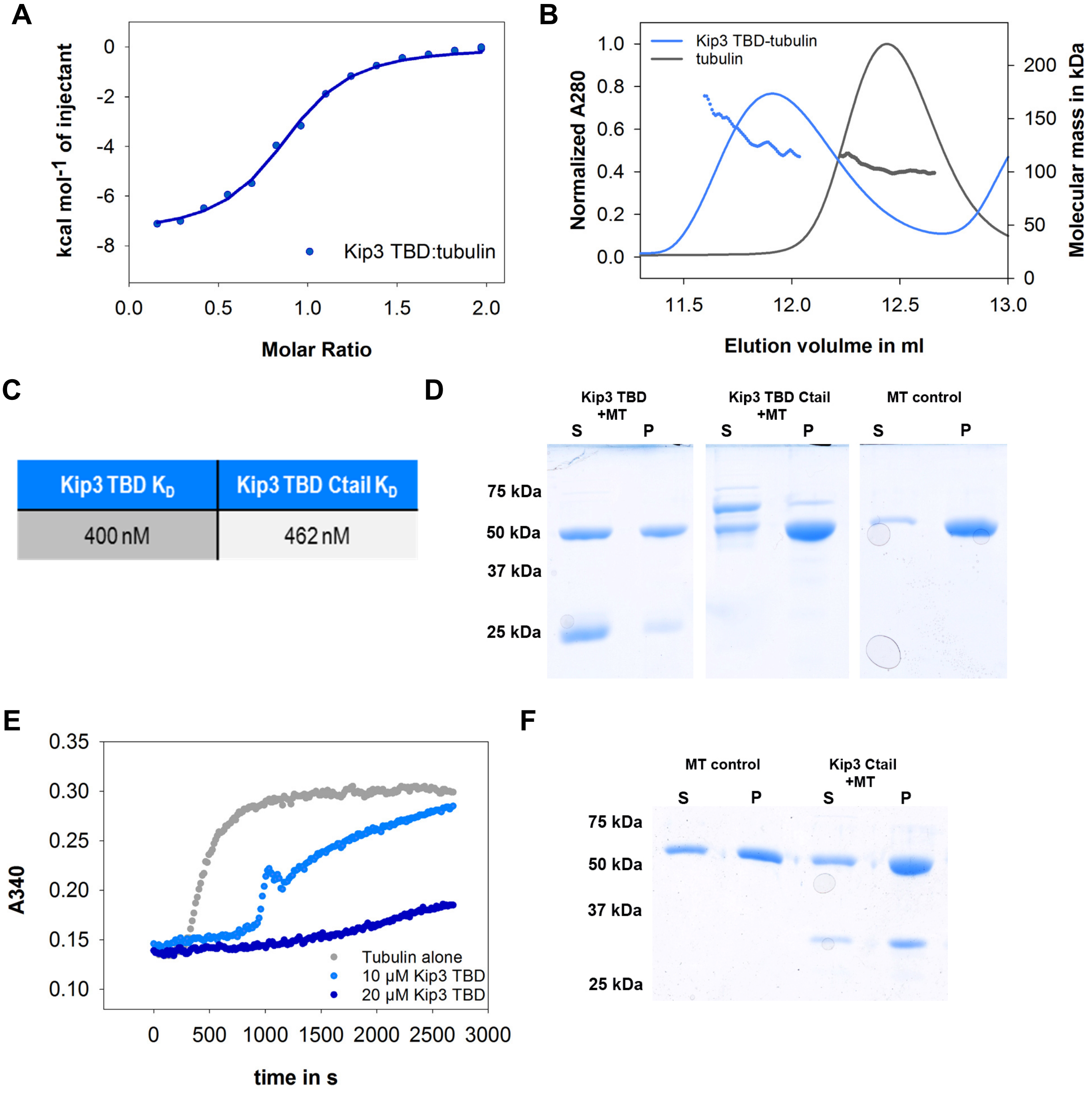

Kip3 TBD K_D	Kip3 TBD Ctail K_D
400 nM	462 nM

Figure 2. Interaction of the Kip3 C-terminal part with tubulin and microtubules.

(A) ITC experiment for Kip3 TBD:tubulin. The solid line represents the fit that was obtained by using the dimer concentration of the Kip3 TBD and the concentration of the tubulin heterodimer.

(B) SEC-MALS experiment of the Kip3 TBD with tubulin and tubulin as a reference. The UV absorption at 280 nm and the molecular masses across the peak determined by MALS are plotted.

(C) Comparison of the KDs of the Kip3 TBD and the Kip3 TBD Ctail obtained by ITC experiments.

(D) Microtubule-pelleting assay in which the Kip3 TBD or the Kip3 TBD Ctail was mixed in an equimolar ratio with tubulin in BRB80 buffer. As controls, the Kip3 TBD domain or microtubules were processed alone. The supernatants (S) and pellets (P) were separated on a 12 % SDS-PAGE and stained with Coomassie.

(E) Microtubule-polymerization assay of the Kip3 TBD. Various concentrations of Kip3 TBD were mixed with 20 µM tubulin, and the A340 signal was measured over time.

(F) Microtubule-pelleting assay in which the Kip3 Ctail was mixed in an equimolar ratio with tubulin in BRB40 buffer. As a control, microtubules were processed alone. The supernatants (S) and pellets (P) were separated on a 12 % SDS-PAGE and stained with Coomassie.

Structure of the Kip3 TBD

It was unknown how the Kip3 TBD can interact with tubulin. Due to this, we aimed to crystallize the Kip3 TBD. The obtained crystals of the Kip3 TBD diffracted to 2 Å, and the structure was solved by Se-Met phasing because no suitable model was available for molecular replacement. Inside the asymmetric unit, four Kip3 chains were located (Figure 3A). Only the two Kip3 chains in the middle of the asymmetric unit exhibited a significant amount of interaction between the chains and a hydrophobic core. In addition, the neck coiled-coil existed only between these two chains. Due to this, we propose that these two Kip3 chains represent the functional dimer (Figure 3B). The structure of the Kip3 TBD reveals that the predicted short neck coiled-coil seamlessly continues into an assembly of parallel α-helices. Inside the arrangement of α-helices, a second coiled-coil-like structure can be identified as the core of the domain, which contains a large number of aromatic residues for mediating hydrophobic interactions (Figure 3C). Additionally, various salt bridges are observed inside the arrangement of helices (Figure 3D). A two-fold symmetry axis passes through the two coiled-coil parts. The two helices of the neck coiled-coil separate from each other after the neck coiled-coil residues, and they connect with the coiled-coil-like structure. Around this connection interface, an α-helix respectively attaches to the continued helices of the neck coiled-coil. The coiled-coil-like structure is surrounded by three helices on both sides, forming an α-helical bundle. Moreover, the neck coiled-coil exhibits a kink inside the coiled-coil, and this introduces an asymmetry in this region of the protein. Therefore, one site of this coiled-coil in combination with the assembly of α-helices slightly resembles a cradle. On the surface of the Kip3 TBD, no prominent positively charged patches can be found because positively charged arginines and lysines occur in the vicinity of negatively charged aspartates and glutamates (Figure 3E). This observation fits to the predicted neutral pI of the Kip3 TBD. Based on the structure alone, it turns out to be difficult to determine which region of Kip3 would bind to tubulin. Nevertheless, the cradle of the neck coiled-coil displays some positively charged patches due to the asymmetry of this region, providing a potential binding interface for tubulin (Figure 3E).

Figure 3

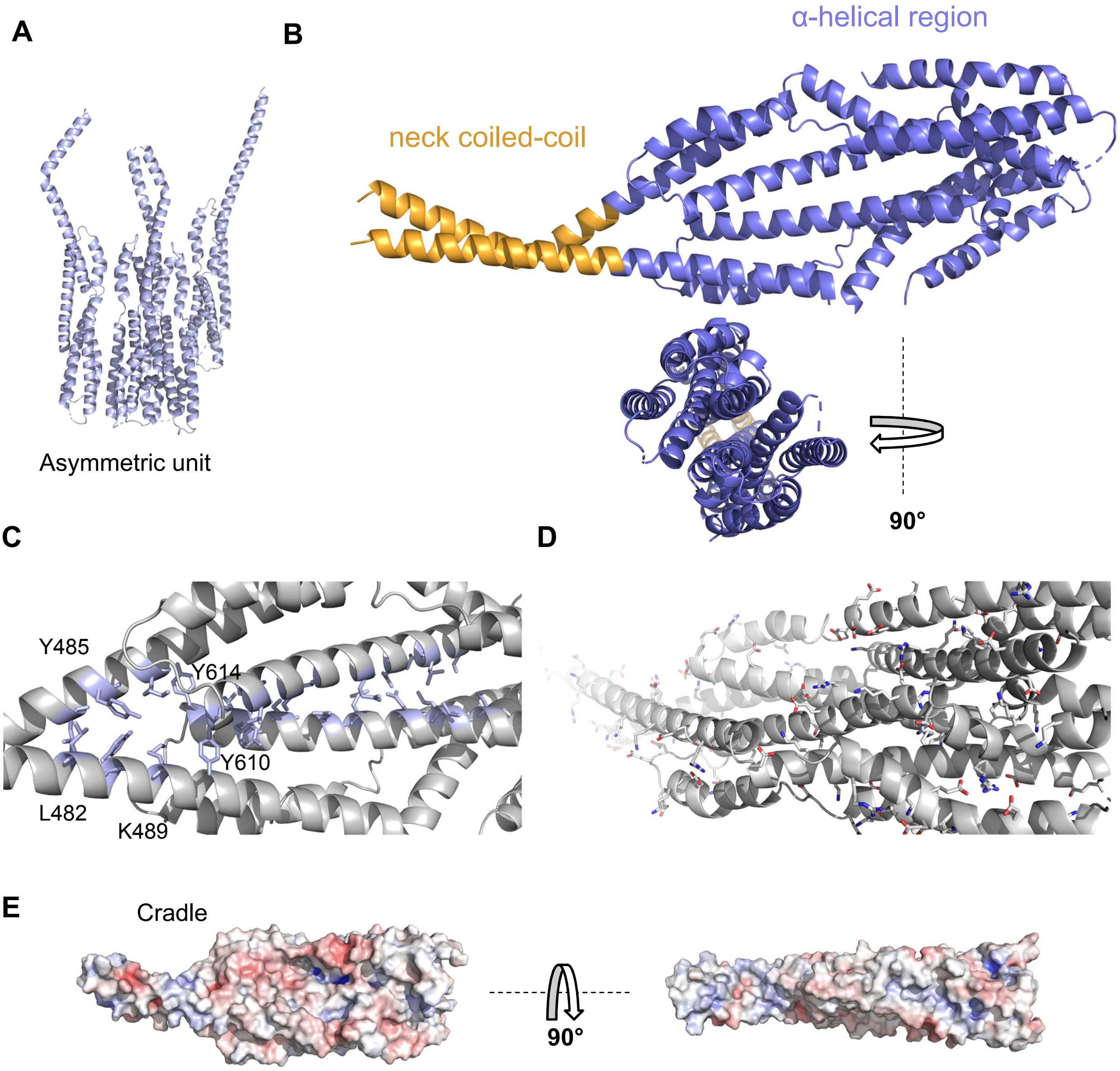
A
B
α-helical region
neck coiled-coil
Asymmetric unit
90°
C
D
Y485
Y614
Y610
L482
K489
E
Cradle
90°

Figure 3. Crystal structure of the Kip3 TBD.

(A) Asymmetric unit of the Kip3 TBD crystal with four Kip3 TBD chains displayed in the cartoon representation.

(B) Two overall views of the structure of the Kip3 TBD dimer in the cartoon representation with the neck coiled-coil highlighted in orange.

(C) and (D) Close-up on the dimerization interface with various important aromatic or other residues (C) and charged residues depicted (D) in the carton representation.

(E) Charged surface of the Kip3 TBD dimer with positive charges in blue and negative charges in red.

Characterization of the tubulin-binding mode of the Kip3 TBD

In order to further understand the tubulin-binding mode of the Kip3 domain TBD, we aimed to co-crystallize this domain in complex with tubulin. Unfortunately, all crystals that were obtained in the co-crystallization trials contained only Kip3 and no tubulin. Therefore, we contemplated using an auxiliary protein as a crystallization tool to keep tubulin in solution. For instance, the artificial protein DARPin1 or the protein stathmin (RB3) inhibits polymerization of tubulin by blocking key interfaces essential for microtubule polymerization (Gigant et al., 2000; Pecqueur et al., 2012). In order to apply one of these proteins for co-crystallization, the binding interface of tubulin to this protein should not overlap with the tubulin-binding interface of Kip3. In a MALS experiment, Kip3 did bind with a high affinity to the tubulin-DARPin1 (TD1) complex because the TD1 peak was shifted by Kip3, and the observed mass was in the region of the predicted mass (Figure 4A). For the gel filtration run of the Kip3 TBD-TD1 complex, an SDS-PAGE confirmed that all three components were present in the ternary complex (Figure 4B). However, no binding to the tubulin-RB3 complex (T2R) was observed by an ITC experiment (Figure 4C) Thus, it can be concluded that RB3 and Kip3 may share a similar interface for the binding of tubulin. After polishing of the Kip3 TBD-TD1 complex by gel filtration, crystallization trials were performed, but the obtained crystals consisted of only Kip3 again.

Nevertheless, to acquire insights into the interaction interface of Kip3 with tubulin, we envisaged exploring the Kip3 TBD-tubulin interaction by mutagenesis of positively charged residues of Kip3 because this approach had been successfully applied for various microtubule-binding proteins in the past. As an example, the CKK domain of CAMSAP can be mentioned (Atherton et al., 2017). Based on the evidence from docking experiments of the Kip3 TBD with TD1 and conservation of Kip3 homologs in yeasts, we selected two positively charged patches of the Kip3 TBD and mutated them to alanine to probe the involvement of these residues in tubulin- binding. The Kip3 TBD mutant R471A R473A did bind weaker to tubulin than the Kip3 wild-type in MALS experiments, indicating a putative involvement of these residues in tubulin binding (figure in preparation, further mutants will be tested in the future).

Figure 4

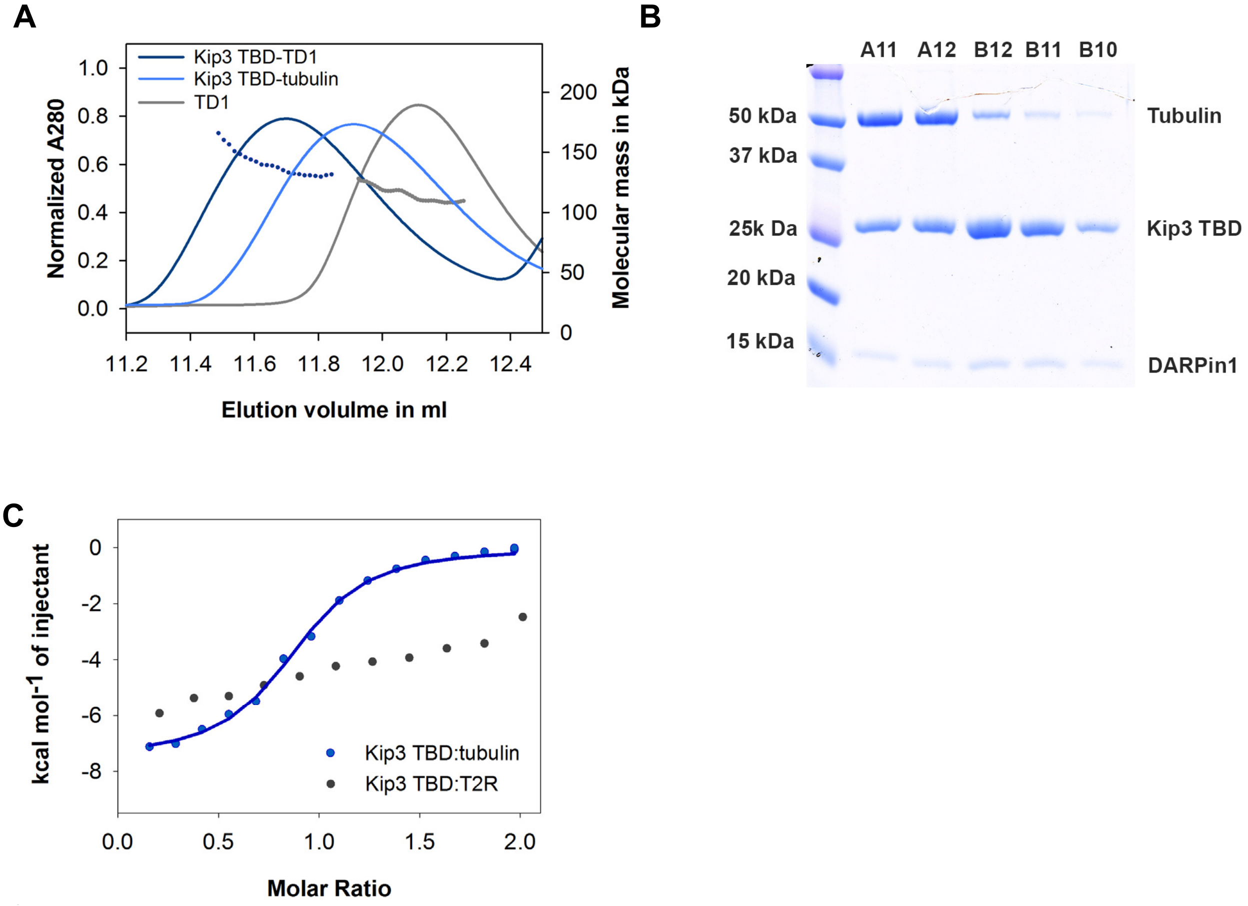

Figure 4. Probing the interaction side of tubulin with Kip3 TBD.

(A) SEC-MALS experiment of the Kip3 TBD with TD1. Kip3-tubulin and TD1 alone were applied as references. UV absorption at 280 nm and the molecular masses across the peak determined by MALS are plotted.

(B) Coomassie-stained SDS-PAGE of the preparative Superdex200 10/300 run of the Kip3-TD1 complex.

(C) ITC experiments for Kip3TBD:tubulin (blue) and Kip3TBD:T2R (grey). The solid line represents the fit that was obtained by using the dimer concentration of the Kip3 TBD and the concentration of the tubulin heterodimer

Investigation of the Kip3 TBD rescue activity in living yeast cells

In order to investigate which additional regions in Kip3 besides the Kip3 TBD are required for the rescue activity, we conceived various truncated constructs of Kip3 for experiments in yeast. The microtubule catastrophe and rescue frequency were determined for these constructs, and wild-type Kip3 together with the *kip3Δ* represented the references (Figure 5 A-C). The deletion of Kip3 resulted both in a reduced catastrophe and rescue frequency, highlighting the dual function of Kip3. When the C-terminal part of Kip3 (TBD and Ctail) was removed, the rescue frequency significantly decreased. This illustrates the essential function of the region containing the Kip3 TBD for rescue. Then, we asked if the Ctail is indispensable for the rescue function. Surprisingly, the construct Kip3 ΔCtail elevated the rescue frequency above the wild-type, suggesting this region is indeed dispensable for rescue. Based on microtubule-pelleting assays, we would have expected participation of this region. When we looked at the catastrophe frequency for the Kip3 ΔCtail, a decrease was observed, indicating an involvement of the Ctail in catastrophe. To analyze the effect of the removal of the motor domain, we expressed the three constructs Kip3 TBD, Kip3 TBD Ctail and Kip3 Ctail at their endogenous level. In the case of Kip3 Ctail, the tail was dimerized by a leucine zipper, and all constructs were tagged with GFP. Interestingly, none of these three constructs localized to microtubules (Figure 6). Therefore, the motor domain appears to be mandatory for Kip3 localization to microtubules, and the putative microtubule-binding domain of the Kip3 Ctail is not able to localize alone to microtubules. Thus, the minimal Kip3 construct that can rescue microtubules was identified as the motor domain together with the Kip3 TBD.

Figure 5

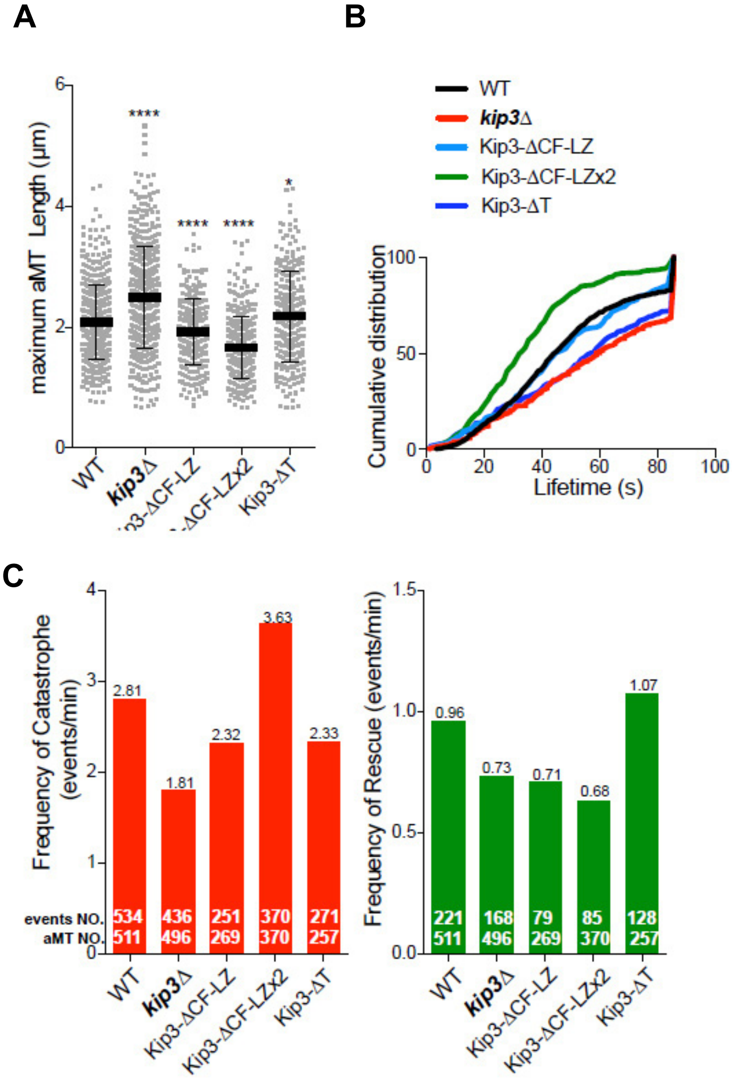

Figure 5. Experimental data of measured astral microtubules dynamics in indicated mutants.

(A) and (B) Maximum length (A) and lifetime (B) of individual pre-anaphase proximal astral microtubules within the 85.6 s image acquisition window represented with column scatter plot (mean ± s.d.) and cumulative distribution plot respectively.

*(C) Catastrophe and rescue frequency of astral microtubules computed by dividing the total number of annotated catastrophe or rescue events with total time spend in growth or shrinkage respectively. The number of annotated events and astral microtubules are marked within corresponding columns. Statistical significance was calculated using two-tailed Student<0.0001, *** p <0.001, ** p <0.01, n.s. = not significant.*

Figure 6

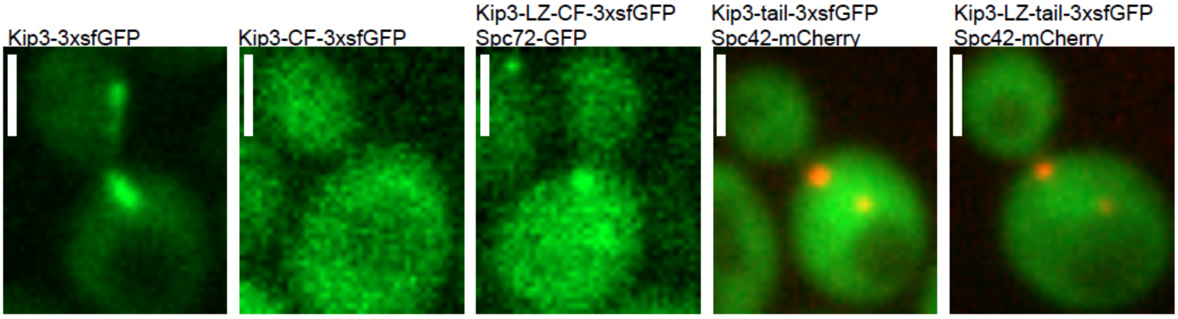

Figure 6. Location of the Kip3 TBD Ctail and Kip3 Ctail in yeast cells.

The Kip3 TBD Ctail (here named Kip3-CF) or Kip3 Ctail (here named Kip3-tail) were expressed with a GFP label in living cells. In addition, the versions of these proteins dimerized by leucine zipper were investigated. Representative images of metaphase cells expressing indicated fusion proteins from endogenous loci. Leucine Zipper (LZ: Gcn5 (250-281) was added for maintaining the dimerization state. White boxes represent scale bars. The low Kip3-CF-3xsfGFP protein level is verified by WB.

Discussion

For the C-terminal part of Kip3, we identified a novel dimeric tubulin-binding domain Kip3 TBD that is essential for microtubule rescue and functionally independent of the Kip3 Ctail. The crystal structure of the Kip3 TBD revealed a sophisticated arrangement of α-helices that is seamlessly followed by the neck coiled-coil. Therefore, the previously reported separation (Su et al., 2011) into the neck coiled-coil and an α-helical C-terminal domain does not reflect the close relationship of these two parts that together form the Kip3 TBD. In addition, the kink in the coiled-coil introduces an asymmetry in the Kip3 TBD that could be the reason why only one tubulin can bind to this dimeric protein. Surprisingly, solved structures of C-terminal domains of kinesins were often simple coiled-coils responsible for dimerization. With the Kip3 TBD structure, we unravel the complexity that these parts of kinesins can possess. For Kip3, the whole C-terminal part was drawn in the literature as a simple dimerization domain. It would be interesting to investigate if Kif18A and Kif19A, the orthologues of Kip3 in higher eukaryotes, feature a similar Kip3 TBD. A sequence alignment of these proteins points toward conservation.

The Kip3 TBD alone depolymerizes microtubules in vitro and prevents microtubule polymerization. This apparent contradiction has also been observed for single domains involved in the microtuble rescue like a TOG domain of the microtubule polymerase Stu2 (Ayaz et al., 2012) and the PN23 domain of the human protein CPAP (Hsu et al., 2008). The Kip3 TBD and these other domains bind curved tubulin with a high affinity so that the depolymerizing activity can be explained by this property. To reconcile this observation with the ability to rescue microtubules, it can be concluded that induvial domains like the Kip3 TBD require additional parts of the respective protein to fulfill their function. In the case of CPAP, the PN23 domain together with a microtubule-binding domain is capable of rescuing microtubules (Sharma et al., 2016). The same applies to a single Stu2 TOG domain that needs further TOG domains and a basic linker. These examples highlight that a domain can functionally behave in the opposite way compared to the full-length protein. In a similar fashion, the Kip3 TBD together with the motor domain can rescue microtubules in the cell. In terms of rescue, the Kip3 motor domain emerges to function as a microtubule-binding domain for the Kip3 TBD so that the high affinity of the Kip3 TBD for curved tubulin results in a rescue event and not in microtubule depolymerization. In this constellation, the Kip3 TBD could enrich soluble tubulin in the GTP-bound state at the microtubule plus-end. After integration of tubulin in the GTP-bound state, the switch to growing microtubules could occur because rescue events are associated with the rebuilding of the GTP cap. There is also the possibility that at the plus-end the curved GDP bound tubulin is substituted directly to GTP-bound tubulin by Kip3 TBD. This would introduce GTP islands, and these GTP islands appear to induce rescue of microtubules (Gardner et al., 2013) Interestingly, the Kip3 motor domain promotes catastrophe itself so that it remains enigmatic how this activity is partially suppressed in the case of rescue events. It has been described that a conformational switch takes place when the Kip3 motor domain binds curved tubulin instead of binding to straight tubulin in microtubules (Arellano-Santoyo et al., 2017). In the case of a rescue by the Kip3 TBD, the Kip3 motor domain could remain bound to straight tubulin. Further research is needed to dissect the interplay between the Kip3 TBD and the motor domain.

Based on the microtubule pelleting assay of the Kip3 TBD Ctail construct, we would have expected an involvement of this tail to tether the Kip3 TBD to microtubules by the putative MBD in the Kip3 Ctail. However, the deletion of the Kip3 Ctail did even increase the rescue frequency. This illustrates that the spatial proximity of these two parts does not lead to a functional activity together. This is in accordance with a recent publication (Dave et al., 2018). Since the Kip3 Ctail seems to facilitate microtubule catastrophe, it can be suggested that the Ctail enhances the processivity of the Kip3 motor domain because this domain is responsible for the catastrophe by binding to curved tubulin at the microtubule plus-ends (Arellano-Santoyo et al., 2017). The motor domain could be tethered by the Ctail at the plus-end, resulting in a stronger depolymerization activity. It has been reported that the C-terminal tail of Kif18A boosts the processivity of this kinesin (Stumpff et al., 2011). In contrast to the Kif18A Ctail in higher eukaryotes (Mayr et al., 2011), the Kip3 Ctail alone failed to localize to microtubules. Nevertheless, the presumed microtubule-binding domain in the Kip3 Ctail showed weak microtubule-binding in vitro. In yeast cells, the affinity of the Kip3 Ctail for microtubules appears to be rather low, and a second microtubule-binding interface in the form of the motor domain is required. As further evidence, it has been observed that deletion of the C-terminal part of Kip3 reduced the dwell time of the Kip3 motor domain (Su et al., 2011). In addition, the fusion of the Kip3 C-terminal part to the motor domain of the kinesin KHC enlarged the dwell time (Su et al., 2011). The elevated processivity of the Kip3 motor domain by the Kip3 Ctail would also explain the increase of the rescue frequency in the Kip3 ΔCtail mutant because the catastrophe frequency decreased. As catastrophe and rescue are antagonistic processes, this could indirectly elevate the rescue frequency. Overall, further research will help to better understand the rescue function of Kip3 and the interplay with the catastrophe function of Kip3.

Table 1. X-ray data collection and refinement statistics.

Data collection*	**Kip3 TBD**
Space group	$P2_1$ 1 1
Cell dimension, Å	81.7 50.6 143.6
Angles, °	90.0 90.6 90.0
Resolution, Å[†]	47.6-2 (2.05-2)
R_{meas}, %	22.2 (203.6)
$CC_{1/2}$[‡]	99.9 (22.5)
I/σI	12.7 (1.6)
Completeness, %	98.3 (91.9)
Refinement	
Resolution, Å	43.5-2.0
No. Unique reflections	78353
Rwork/Rfree, %	21.7/25.3
Average B-factors	59.9
rmsd from ideality	
Bond length, Å	0.004
Bond angles, °	0.93
Ramachandran statistics[#]	
Favored regions, %	98.0
Allowed regions, %	1.5
Outliers, %	0.5

*Highest shell statistics are in parentheses

[†] The resolution cutoff was selected based on I/σI and CC1/2 according to (Karplus and Diederichs, 2012)

[‡] CC1/2 = percentage of correlation between intensities from random half-data sets

[#] As defined by MolProbity (Chen et al., 2010)

Material and Methods

Protein preparations

The DNA encoding the Kip3 tubulin-binding domain of *S. cerevisiae* (Kip3 TBD, residues 445-693; Uniprot ID: P53086) was cloned into the pET-based bacterial expression vector PSPCm2, which encodes for an N-terminal 6x His-tag and a PreScission cleavage site using a positive selection method (Olieric et al., 2010). The same vector was used for the Kip3 TBD together with the C-terminal tail (Kip3 TBD Ctail, residues 445-805). In the case of C-terminal tail of Kip3 (Kip3 Ctail, residues 694-805), the construct was put into a PSPCm9 vector, which encodes for an N-terminal thioredoxin, a 6x His-tag and a PreScission cleavage. In addition, the Kip3 TBD Ctail was cloned in the PSPcm9 as well. The mutants of the Kip3 TBD vector were obtained by PCR-based site-directed mutagenesis applying a 2-step like PCR protocol as described in the literature (Xia et al., 2015).

The production of the proteins was conducted in the *E. coli* strain BL21(DE3) (Stratagene) in LB media containing 50 µg/ml of kanamycin. When the cultures had reached an OD_{600} of 0.6 at 37 °C, they were cooled down to 20 °C, induced with 1 mM isopropyl 1-thio-β-D-galactopyranoside (IPTG) and shaken for another 16 hours at 20 °C. After the cells have been harvested and washed with Dulbecco PBS buffer (Millipore), they were sonicated in the presence of the protease inhibitor cOmplete cocktail (Roche) in lysis buffer (50 mM HEPES, pH 8, supplemented with 500 mM NaCl, 10 mM imidazole, 2 mM β-mercaptoethanol, 0.1% bovine deoxyribonuclease I).

Proteins were purified by immobilized metal-affinity chromatography (IMAC) on a HisTrap HP Ni^{2+}-Sepharose column (GE Healthcare) at 4 °C according to the instructions of the manufacturer. The column was equilibrated in IMAC buffer A (50 mM HEPES, pH 8, supplemented with 500 mM NaCl, 10 mM imidazole, 2 mM β-mercaptoethanol). Proteins were eluted by IMAC buffer B (IMAC buffer A containing 400 mM imidazole in total). The N-terminal 6x His-tag was cleaved off by an in-house produced HRV 3C protease (Cordingley et al., 1990) in IMAC buffer A for 16 hours at 4 °C. The cleaved samples were reapplied on the IMAC column to separate cleaved from uncleaved protein.

Protein samples were concentrated and loaded onto a size exclusion chromatography (SEC) HiLoad Superdex 200 16/60 column (GE Healthcare), which was equilibrated in SEC buffer (20 mM Tris-HCl, pH 7.5, supplemented with 150 mM NaCl and 1 mM DTT). The fractions of the respective main peaks were pooled and concentrated to 10-20 mg/ml. Protein quality and identity were analyzed by SDS-PAGE and mass spectrometry, respectively.

Circular dichroism (CD) spectroscopy

The CD spectra of Kip3 TBD and of the Kip3 TBD mutants (0.2 mg/ml in PBS) were measured at 5 °C on a Chirascan-Plus spectrophotometer (Applied Photophysics Ltd.) equipped with a computer-controlled Peltier element using a quartz cuvette of 1 mm optical path length. Thermal unfolding profiles were recorded by CD at 222 nm by continuous heating at 1 °C min^{-1}. The apparent midpoint of the transition, T_m, was determined by fitting of the data points using the R nonlinear least square fitting function based on a sigmoid model.

Microtubule-pelleting assay

Microtubule-pelleting assays of purified proteins were performed as previously described (Lansbergen et al., 2004). Briefly, 10 mg/ml bovine brain tubulin was diluted in 1×BRB80 buffer (80 mM K-PIPES, pH 6.8, supplemented with 1 mM EGTA, 1 mM MgCl2 and 1 mM DTT) to 2 mg/ml. In case of the Kip3 Ctail 1xBRB40 (40 mM K-PIPES, pH 6.8 instead of 80 mM K-PIPES, pH 6.8) was used. After the addition of 0.5 mM GTP, the sample was incubated on ice for 5 min. The microtubule polymerization was started by transfer to 37 °C. After 10 min, 0.1 µM, 1 µM and 10 µM paclitaxel were added stepwise with incubation times of 5 min each. Pelleting assays in the presence of Kip3 TBD, Kip3 TBD or Kip3 TBD Ctail were performed by mixing 3.8 µM of taxol-stabilized microtubules with an equimolar ratio of the respective protein. In order to separate the Kip3 TBD Ctail from tubulin on an SDS gel, the thioredoxin-tagged version was used. As control treatments, taxol-stabilized microtubules or the respective protein was applied alone. Samples were applied onto a taxol–glycerol cushion that contained 55% 2× BRB80, 44% glycerol and 6% 2 mM paclitaxel. After centrifugation at 174,500g for 30 min at 25 °C, an aliquot was taken from the supernatant. After removal of the supernatant, the pellet was resuspended in SDS sample buffer. Samples were loaded and analyzed on Coomassie-stained 12 % SDS gels.

Size exclusion chromatography followed by multi-angle light scattering (SEC-MALS)

For the SEC-MALS experiment at 25 °C, a Superdex200 10/30 column (GE Healthcare) was equilibrated in BRB80 buffer (80 mM PIPES, pH 6.8, supplemented with 1 mM $MgCl_2$, 1 mM EGTA and 1 mM DTT) at a flow rate of 0.5 ml/min on an Agilent UltiMate3000 HPLC. 30 µl of the respective single protein or complex was injected onto the column, and the mass was determined using the miniDAWN TREOS and Optilab T-rEX refractive index detectors (Wyatt Technology). The concentration in the injected volume was 4-6 mg/ml for tubulin, 5-6 mg/ml for the Kip3 TBD or the respective mutant and 2 mg/ml for DARPin1. In the case of the complexes, the individual concentrations of the components were maintained. The Zimm model was chosen for data fitting, which was performed in the ASTRA 6 software.

Isothermal titration calorimetry (ITC)

All proteins and peptide samples were buffer-exchanged to BRB80 buffer (see SEC-MALS for composition). ITC experiments were performed at 25 °C on an iTC 200 machine (MicroCal) using 15 injections of 2.6 µl. 100-200 µM of Kip3 TBD was loaded into the syringe. 10-20 µM tubulin or tubulin-RB3 (T2R) was put into the sample cell. Fits of the binding isotherms were obtained by using a nonlinear least squares minimization method. The one set of site model provided in the software package of the calorimeter was utilized to determine the equilibrium dissociation constant, K_d.

X-ray data collection and structure determination

The Kip3 TBD labeled with selenomethionine was concentrated to 6 mg/ml, and DTT to a final concentration of 5 mM was added to the sample. The screening of crystallization conditions was performed using a Mosquito robot (TTP Labtech) in 96 well plates using the vapor diffusion hanging drop method at 20 °C. Crystals appeared overnight in drops of a 1:1 (200 nl each) mixture of Kip3 TBD and the mother liquor (0.1 M Bis-Tris propane, pH 7.5, 0.2 M sodium iodide and 20 % w/v PEG 3350). Since diffraction data of these crystals was not sufficient, the crystals were used as a seed stock that was diluted 1:10 with the mother liquor. By micro seeding, the crystals were further optimized, and the best hit appeared in drops of 1:3:4 (50 nl seed stock, 150 nl Kip3 TBD, 200 nl mother liquor) mixture of seed stock, Kip3 TBD and the mother liquor (0.1 M Bis-Tris propane, pH 8.5, 0.2 M sodium iodide and 20 % w/v PEG 3350). The crystals were cryo-protected by transferring them into mother liquor that contained 30 % w/v PEG 3350 and were flash frozen in liquid nitrogen.

X-ray diffraction data of Kip3 TBD crystals were collected at the X06SA macromolecular crystallography beamline at the Swiss Light Source (Paul Scherrer Institut) at a wavelength of 1 Å. The data were indexed with LABELIT (Sauter et al., 2004), and refined and integrated with XDS (Kabsch, 1993). The Kip3 TBD structure was solved by Se-Met phasing with the software package CRANK2 (Skubak and Pannu, 2013). This initial structure was optimized by several rounds of manual model building in COOT (Emsley et al., 2010) and refinement in PHENIX (Adams et al., 2002). The structure was validated by MolProbity (Chen et al., 2010). PyMol (Schrodinger, 2015) was used for the preparation of the figures. Data collection and refinement statistics are given in Table 1.

References

Adams, P.D., Grosse-Kunstleve, R.W., Hung, L.W., Ioerger, T.R., McCoy, A.J., Moriarty, N.W., Read, R.J., Sacchettini, J.C., Sauter, N.K., and Terwilliger, T.C. (2002). PHENIX: building new software for automated crystallographic structure determination. Acta crystallographica. Section D, Biological crystallography *58*, 1948-1954.

Akhmanova, A., and Steinmetz, M.O. (2015). Control of microtubule organization and dynamics: two ends in the limelight. Nat Rev Mol Cell Biol *16*, 711-726.

Al-Bassam, J., Kim, H., Brouhard, G., van Oijen, A., Harrison, S.C., and Chang, F. (2010). CLASP promotes microtubule rescue by recruiting tubulin dimers to the microtubule. Dev Cell *19*, 245-258.

Arellano-Santoyo, H., Geyer, E.A., Stokasimov, E., Chen, G.Y., Su, X., Hancock, W., Rice, L.M., and Pellman, D. (2017). A Tubulin Binding Switch Underlies Kip3/Kinesin-8 Depolymerase Activity. Dev Cell *42*, 37-51 e38.

Atherton, J., Jiang, K., Stangier, M.M., Luo, Y., Hua, S., Houben, K., van Hooff, J.J.E., Joseph, A.P., Scarabelli, G., Grant, B.J., *et al.* (2017). A structural model for microtubule minus-end recognition and protection by CAMSAP proteins. Nat Struct Mol Biol *24*, 931-943.

Aumeier, C., Schaedel, L., Gaillard, J., John, K., Blanchoin, L., and Thery, M. (2016). Self-repair promotes microtubule rescue. Nat Cell Biol *18*, 1054-1064.

Ayaz, P., Ye, X., Huddleston, P., Brautigam, C.A., and Rice, L.M. (2012). A TOG:alphabeta-tubulin complex structure reveals conformation-based mechanisms for a microtubule polymerase. Science *337*, 857-860.

Brouhard, G., and Sept, D. (2012). Microtubules: sizing up the GTP cap. Curr Biol *22*, R802-803.

Cassimeris, L. (2009). Microtubule assembly: lattice GTP to the rescue. Curr Biol *19*, R174-176.

Chen, V.B., Arendall, W.B., 3rd, Headd, J.J., Keedy, D.A., Immormino, R.M., Kapral, G.J., Murray, L.W., Richardson, J.S., and Richardson, D.C. (2010). MolProbity: all-atom structure validation for macromolecular crystallography. Acta crystallographica. Section D, Biological crystallography *66*, 12-21.

Cordingley, M.G., Callahan, P.L., Sardana, V.V., Garsky, V.M., and Colonno, R.J. (1990). Substrate requirements of human rhinovirus 3C protease for peptide cleavage in vitro. J Biol Chem *265*, 9062-9065.

Dave, S., Anderson, S.J., Roy, P.S., Nsamba, E.T., Bunning, A.R., Fukuda, Y., and Gupta, M.L., Jr. (2018). Discrete regions of the kinesin-8 Kip3 tail differentially mediate astral microtubule stability and spindle disassembly. Molecular biology of the cell, mbcE18030199.

Emsley, P., Lohkamp, B., Scott, W.G., and Cowtan, K. (2010). Features and development of Coot. Acta crystallographica. Section D, Biological crystallography *66*, 486-501.

Fukuda, Y., Luchniak, A., Murphy, E.R., and Gupta, M.L., Jr. (2014). Spatial control of microtubule length and lifetime by opposing stabilizing and destabilizing functions of Kinesin-8. Curr Biol *24*, 1826-1835.

Gardner, M.K., Zanic, M., Gell, C., Bormuth, V., and Howard, J. (2011). Depolymerizing kinesins Kip3 and MCAK shape cellular microtubule architecture by differential control of catastrophe. Cell *147*, 1092-1103.

Gardner, M.K., Zanic, M., and Howard, J. (2013). Microtubule catastrophe and rescue. Curr Opin Cell Biol *25*, 14-22.

Gigant, B., Curmi, P.A., Martin-Barbey, C., Charbaut, E., Lachkar, S., Lebeau, L., Siavoshian, S., Sobel, A., and Knossow, M. (2000). The 4 A X-ray structure of a tubulin:stathmin-like domain complex. Cell *102*, 809-816.

Gupta, M.L., Jr., Carvalho, P., Roof, D.M., and Pellman, D. (2006). Plus end-specific depolymerase activity of Kip3, a kinesin-8 protein, explains its role in positioning the yeast mitotic spindle. Nat Cell Biol *8*, 913-923.

Hsu, W.B., Hung, L.Y., Tang, C.J., Su, C.L., Chang, Y., and Tang, T.K. (2008). Functional characterization of the microtubule-binding and -destabilizing domains of CPAP and d-SAS-4. Exp Cell Res *314*, 2591-2602.

Kabsch, W. (1993). Automatic processing of rotation diffraction data from crystals of initially unknown symmetry and cell constants. Journal of applied crystallography *26*, 795-800.

Karplus, P.A., and Diederichs, K. (2012). Linking crystallographic model and data quality. Science *336*, 1030-1033.

Lansbergen, G., Komarova, Y., Modesti, M., Wyman, C., Hoogenraad, C.C., Goodson, H.V., Lemaitre, R.P., Drechsel, D.N., van Munster, E., Gadella, T.W., Jr*., et al.* (2004). Conformational changes in CLIP-170 regulate its binding to microtubules and dynactin localization. J Cell Biol *166*, 1003-1014.

Mayr, M.I., Storch, M., Howard, J., and Mayer, T.U. (2011). A non-motor microtubule binding site is essential for the high processivity and mitotic function of kinesin-8 Kif18A. PLoS One *6*, e27471.

Olieric, N., Kuchen, M., Wagen, S., Sauter, M., Crone, S., Edmondson, S., Frey, D., Ostermeier, C., Steinmetz, M.O., and Jaussi, R. (2010). Automated seamless DNA co-transformation cloning with direct expression vectors applying positive or negative insert selection. BMC biotechnology *10*, 56.

Pecqueur, L., Duellberg, C., Dreier, B., Jiang, Q., Wang, C., Pluckthun, A., Surrey, T., Gigant, B., and Knossow, M. (2012). A designed ankyrin repeat protein selected to bind to tubulin caps the microtubule plus end. Proc Natl Acad Sci U S A *109*, 12011-12016.

Sauter, N.K., Grosse-Kunstleve, R.W., and Adams, P.D. (2004). Robust indexing for automatic data collection. Journal of applied crystallography *37*, 399-409.

Schrodinger, LLC (2015). The PyMOL Molecular Graphics System, Version 1.8.

Seetapun, D., Castle, B.T., McIntyre, A.J., Tran, P.T., and Odde, D.J. (2012). Estimating the microtubule GTP cap size in vivo. Curr Biol *22*, 1681-1687.

Sharma, A., Aher, A., Dynes, N.J., Frey, D., Katrukha, E.A., Jaussi, R., Grigoriev, I., Croisier, M., Kammerer, R.A., Akhmanova, A*., et al.* (2016). Centriolar CPAP/SAS-4 Imparts Slow Processive Microtubule Growth. Dev Cell *37*, 362-376.

Skubak, P., and Pannu, N.S. (2013). Automatic protein structure solution from weak X-ray data. Nat Commun *4*, 2777.

Stumpff, J., Du, Y., English, C.A., Maliga, Z., Wagenbach, M., Asbury, C.L., Wordeman, L., and Ohi, R. (2011). A tethering mechanism controls the processivity and kinetochore-microtubule plus-end enrichment of the kinesin-8 Kif18A. Mol Cell *43*, 764-775.

Stumpff, J., von Dassow, G., Wagenbach, M., Asbury, C., and Wordeman, L. (2008). The kinesin-8 motor Kif18A suppresses kinetochore movements to control mitotic chromosome alignment. Dev Cell *14*, 252-262.

Su, X., Arellano-Santoyo, H., Portran, D., Gaillard, J., Vantard, M., Thery, M., and Pellman, D. (2013). Microtubule-sliding activity of a kinesin-8 promotes spindle assembly and spindle-length control. Nat Cell Biol *15*, 948-957.

Su, X., Qiu, W., Gupta, M.L., Jr., Pereira-Leal, J.B., Reck-Peterson, S.L., and Pellman, D. (2011). Mechanisms underlying the dual-mode regulation of microtubule dynamics by Kip3/kinesin-8. Mol Cell *43*, 751-763.

Varga, V., Leduc, C., Bormuth, V., Diez, S., and Howard, J. (2009). Kinesin-8 motors act cooperatively to mediate length-dependent microtubule depolymerization. Cell *138*, 1174-1183.

Vemu, A., Szczesna, E., Zehr, E.A., Spector, J.O., Grigorieff, N., Deaconescu, A.M., and Roll-Mecak, A. (2018). Severing enzymes amplify microtubule arrays through lattice GTP-tubulin incorporation. Science *361*.

Weaver, L.N., Ems-McClung, S.C., Stout, J.R., LeBlanc, C., Shaw, S.L., Gardner, M.K., and Walczak, C.E. (2011). Kif18A uses a microtubule binding site in the tail for plus-end localization and spindle length regulation. Curr Biol *21*, 1500-1506.

Xia, Y., Chu, W., Qi, Q., and Xun, L. (2015). New insights into the QuikChange process guide the use of Phusion DNA polymerase for site-directed mutagenesis. Nucleic acids research *43*, e12.

5. A structural model for microtubule minus-end recognition by CAMSAPs

5. A structural model for microtubule minus-end recognition by CAMSAPs

5.1 Declaration of contribution

The CAMSAP project represented a collaboration of various research groups. I contributed my solving the crystal structure of the CAMSAP CKK domain, and I characterized various mutants of the CKK domain by CD spectroscopy. In addition, I performed microtubule-pelleting assays of the CKK domain. The various CKK domain constructs were expressed and purified by me. The construct for solving the structure was also cloned by me. Prof. Dr. Michel Steinmetz and I designed and analyzed the in vitro experiments of our group. The crystallization trials were performed by me, and data sets were collected together with other Steinmetz group members at the beam line. Furthermore, I solved the structure of the CKK domain with the support of Dr. Andrea Prota.

The paper about CAMSAPs was published in the year with the title “A structural model for microtubule minus-end recognition and protection by CAMSAP proteins” in the journal Nature Structural and Molecular Biology in 2017.

Bibliographic Information:

Atherton, J., Jiang, K., Stangier, M.M., Luo, Y., Hua, S., Houben, K., van Hooff, J.J.E., Joseph, A.P., Scarabelli, G., Grant, B.J., et al. (2017). A structural model for microtubule minus-end recognition and protection by CAMSAP proteins. Nat Struct Mol Biol 24, 931-943.

nature
structural &
molecular biology

A structural model for microtubule minus-end recognition and protection by CAMSAP proteins

Joseph Atherton[1,11], Kai Jiang[2,11], Marcel M Stangier[3], Yanzhang Luo[4], Shasha Hua[2], Klaartje Houben[4], Jolien J E van Hooff[5–7], Agnel-Praveen Joseph[1], Guido Scarabelli[8], Barry J Grant[9], Anthony J Roberts[1], Maya Topf[1], Michel O Steinmetz[3,10], Marc Baldus[4], Carolyn A Moores[1] & Anna Akhmanova[2]

CAMSAP and Patronin family members regulate microtubule minus-end stability and localization and thus organize noncentrosomal microtubule networks, which are essential for cell division, polarization and differentiation. Here, we found that the CAMSAP C-terminal CKK domain is widely present among eukaryotes and autonomously recognizes microtubule minus ends. Through a combination of structural approaches, we uncovered how mammalian CKK binds between two tubulin dimers at the interprotofilament interface on the outer microtubule surface. *In vitro* reconstitution assays combined with high-resolution fluorescence microscopy and cryo-electron tomography suggested that CKK preferentially associates with the transition zone between curved protofilaments and the regular microtubule lattice. We propose that minus-end-specific features of the interprotofilament interface at this site serve as the basis for CKK's minus-end preference. The steric clash between microtubule-bound CKK and kinesin motors explains how CKK protects microtubule minus ends against kinesin-13-induced depolymerization and thus controls the stability of free microtubule minus ends.

© 2017 Nature America, Inc., part of Springer Nature. All rights reserved.

Microtubules (MTs) are highly dynamic polymers that assemble and disassemble from their two ends: the fast-growing plus end and the slow-growing minus end. Although abundant data are available regarding the regulation of MT plus ends[1,2], much less is known about the proteins that specifically regulate MT minus ends, although MT minus-end organization defines the architecture of cellular MT arrays[3,4]. The best-studied MT-nucleating and minus-end-binding factor is the γ-tubulin ring complex (γ-TuRC)[5]. Recently, the members of calmodulin-regulated spectrin-associated protein (CAMSAP) and the Patronin family have been shown to control noncentrosomal MT minus-end organization independently of γ-TuRC in different systems, including the mitotic spindle in insect cells[6–8], cortically attached MT arrays in epithelial cells[9–13] and MT bundles in neurons[14–17].

CAMSAP1, CAMSAP2 and CAMSAP3 (in vertebrates) and Patronin (in invertebrates) recognize and track uncapped, growing MT minus ends[18,19]. In mammals, CAMSAP2 and CAMSAP3 are deposited on MT lattices formed by MT minus-end polymerization and in this way generate stable MT stretches that can serve as a source of noncentrosomal MT outgrowth[18,20]. In contrast, CAMSAP1 tracks growing MT minus ends but does not decorate them[18]. CAMSAPs and Patronin contain a C-terminal domain common to CAMSAP1, KIAA1078 and KIAA1543 (CKK) as well as an N-terminal Calponin-homology domain and several coiled-coil regions[21]. In mammalian CAMSAPs, minus-end recognition has been shown to depend on the CKK domain, whereas the ability of CAMSAP2 and CAMSAP3 to stay attached to the MT lattice is associated with additional adjacent regions[18]. However, in fly Patronin, minus-end recognition has been proposed to be mediated by the unstructured linker region in combination with the adjacent C-terminal coiled coil[19]. The deletion of the CKK domain in CAMSAP3 causes a loss-of-function phenotype in mice[10], and the CKK domain of Patronin (PTRN-1) in worms is necessary and sufficient for supporting proper MT dynamics and axon regeneration[17], thus demonstrating the functional importance of this domain.

Here, we set out to investigate the nature of the MT minus-end specificity of CAMSAPs. Structural analysis by X-ray crystallography, cryo-EM and solid-state NMR showed that the globular CKK domain binds a unique site between two tubulin dimers at the interprotofilament interface. Fluorescence microscopy demonstrated that the high-affinity site for CKK binding is located several tubulin dimers behind the outmost MT minus end. Cryo-electron tomography (cryo-ET) of MT minus ends revealed a heterogeneous array of gently curved protofilaments that retain lateral interactions. On the basis of these data, we propose that the CKK preferentially

---

[1]Institute of Structural and Molecular Biology, Birkbeck, University of London, London, UK. [2]Cell Biology, Department of Biology, Faculty of Science, Utrecht University, Utrecht, the Netherlands. [3]Laboratory of Biomolecular Research, Division of Biology and Chemistry, Paul Scherrer Institut, Villigen, Switzerland. [4]NMR Spectroscopy, Bijvoet Center for Biomolecular Research, Utrecht University, Utrecht, the Netherlands. [5]Hubrecht Institute, Royal Netherlands Academy of Arts and Sciences (KNAW), Utrecht, the Netherlands. [6]Theoretical Biology and Bioinformatics, Department of Biology, Faculty of Science, Utrecht University, Utrecht, the Netherlands. [7]Molecular Cancer Research, University Medical Center Utrecht, Utrecht, the Netherlands. [8]Department of Computational Medicine and Bioinformatics, University of Michigan Medical School, Ann Arbor, Michigan, USA. [9]Division of Biological Sciences, University of California San Diego, La Jolla, California, USA. [10]University of Basel, Biozentrum, Basel, Switzerland. [11]These authors contributed equally to this work. Correspondence should be addressed to C.A.M. (c.moores@mail.cryst.bbk.ac.uk) or A.A. (a.akhmanova@uu.nl).

Received 4 March; accepted 12 September; published online 9 October 2017; doi:10.1038/nsmb.3483

binds the transition zone between the regular lattice and the curved sheet-like structure of the minus-end extremity, which presents a subtly altered interprotofilament interface that is optimal for CKK binding. Finally, our structural and *in vitro* reconstitution data showed that CKK sterically hinders the interaction of kinesin-13 with MT minus ends, thereby explaining how CAMSAPs and Patronin protect MT minus ends against depolymerization by these factors.

RESULTS

Minus-end recognition by CAMSAPs depends on the conserved CKK domain

We have previously shown that the CKK domain in mammalian CAMSAPs binds minus ends[18]. To investigate whether other CAMSAP domains might also control minus-end recognition, we tested the ability of different purified GFP-tagged CAMSAP1 and CAMSAP3 domains to bind to MT minus ends and lattices *in vitro*. None of the CAMSAP fragments that lacked the CKK domain showed any minus-end preference (**Fig. 1a**–**f** and **Supplementary Fig. 1a**–**c**). For CAMSAP1, we found that the predicted helical domain and the linker, which precede the CKK, had only very weak MT affinity of their own but increased MT binding of CAMSAP1 CKK, though not its minus-end selectivity (**Fig. 1a**–**f**). An additional negatively charged linker region of CAMSAP1 (**Supplementary Fig. 1d**), located upstream of its third coiled-coil domain, suppressed MT-lattice binding and enhanced minus-end selectivity when it was present together with the CKK domain (**Fig. 1a**–**e**; this construct is denoted CAMSAP1$_{\mathrm{mini}}$). For CAMSAP3, we confirmed that the MT-binding domain located between coiled coils 2 and 3 specifically bound to GMPCPP but not GDP MTs, as we have previously demonstrated[18] (**Supplementary Fig. 1a**–**c**). The predicted helical domain of CAMSAP3 together with the adjacent linker also specifically bound to GMPCPP MTs without showing end preference (**Supplementary Fig. 1a**–**c**). We concluded that the minus-end preference of CAMSAPs depends on the CKK domains, whereas additional domains modulate their end selectivity or ability to decorate MT lattices.

To establish whether CKK-mediated minus-end binding defines an evolutionarily conserved mechanism, we screened a set of nearly 100 eukaryotic genomes and found homologs of the CKK domain in all eukaryotic supergroups except for Amoebozoa, although homologs were absent in some well-studied lineages such as dikaryan fungi and land plants (**Supplementary Fig. 2** and **Supplementary Table 1**). Parsimoniously interpreting the occurrence of CKK across eukaryotes, we concluded that this domain was probably already present in the genome of the last eukaryotic common ancestor and did not emerge during early animal evolution, as suggested previously[21]. In particular, our discovery of genes encoding CKK-containing proteins in the genomes of various members of the Excavata, a group that some consider to be sister to all other eukaryotes (discussed in ref. 22), strongly supports an ancient origin of CKK. Whereas in vertebrates, the array of CKK-containing proteins was expanded by gene duplications leading to the three CAMSAP paralogs in mammals, this outcome was not the case in many other genomes (**Supplementary Data Set 1**), thus suggesting that in most eukaryotes, a single copy of the domain fulfils CKK functions.

To test whether the sequence conservation of CKK translates into functional conservation, we next purified GFP-tagged CKK domains derived from flies (*Drosophila melanogaster*) and worms (*Caenorhabditis elegans*), as well as from four more evolutionarily distant eukaryotes (*Trichomonas vaginalis*, *Tetrahymena thermophila*, *Naegleria gruberi* and *Phytophthora infestans*). From these six CKK domains tested, four (*D. melanogaster*, *C. elegans*, *T. vaginalis* and *T. thermophila*) specifically tracked the growing minus ends of MTs assembled from pig-brain tubulin in *in vitro* MT-dynamics reconstitution experiments (**Fig. 1g**), whereas the two others (*N. gruberi* and *P. infestans*) showed strong binding along the entire MT lattice (data not shown). These data demonstrated that CKK is a protein module that recognizes MT minus ends, a property preserved over long evolutionary distances.

CKK domains bind an intradimer site between protofilaments

We determined the crystal structure of the mouse CAMSAP3 CKK-domain core (residues 1121–1239; denoted CKK3$_{\mathrm{core}}$) (**Table 1**). Similarly to a deposited but unpublished NMR structure (PDB 1UGJ), the CKK3$_{\mathrm{core}}$ has a compact, globular structure composed of two N-terminal α-helices, which are connected by a disordered loop (loop1) and pack against a central five-stranded β-sheet (**Supplementary Fig. 3**).

Although CKK shows a clear preference for MT minus ends, at high concentrations it can also decorate the entire MT lattice. We reasoned that a high-resolution structure of the lattice-bound CKK domain might shed light on the mechanism of its MT minus-end recognition. Therefore, we used cryo-EM to analyze extended CKK domains of CAMSAP1 and CAMSAP3 (residues 1474–1613 and 1112–1252, respectively) bound to 13-protofilament (pf) taxol-stabilized MTs. Filtered images of these MTs showed additional density corresponding to CKK domains spaced by 8 nm (**Fig. 2a**), a result indicative of binding every tubulin dimer. A striking feature of these CKK-decorated MTs is the presence of a right-handed skew in the protofilaments. This feature was evident in both the filtered images and the alignment parameters of the MT segments used for reconstruction and was specific to the CKK–MT data sets (**Fig. 2a**,**b** and **Supplementary Fig. 4a**). This result indicated that CKK binding modifies the MT lattice with which it interacts, in agreement with the idea that the regular MT lattice conformation is not the most favored substrate for CKK domains.

Asymmetric 3D reconstructions (~12-Å and ~9-Å resolution for CAMSAP1 and CAMSAP3, respectively) show the CKK domains binding the MT lattice every 8 nm between protofilaments except at the seam (**Fig. 2c** and **Supplementary Fig. 4b**). Using the pseudosymmetry of the MTs, we obtained averaged reconstructions with overall final resolutions that allowed α- and β-tubulin to be clearly distinguished (true Fourier shell correlation (FSCtrue) 0.143 criterion[23] of 5.3 Å (CAMSAP3) and 8 Å CAMSAP1) (**Fig. 2d**,**e**, **Supplementary Fig. 4c**–**e** and **Table 2**). From these data, we concluded that CKK domains bind at the tubulin intradimer B-lattice interface, where conserved differences between α- and β-tubulin explain this binding-site selection (**Fig. 3a**). The binding site of CKK is distinct from those of other proteins known to bind between protofilaments, end-binding proteins (EBs) and Doublecortin, which bind at the vertex of four tubulin dimers and not at the intradimer interface (**Supplementary Fig. 4f**–**h**). However, some overlap was found with the binding site of kinesin (**Supplementary Fig. 4i**).

For ease of description, the four tubulin subunits contacting a single CKK domain are referred to as β1-, β2-, α1- and α2-tubulin (**Figs. 2d**,**e** and **3a**). In general, the CKK wedges snugly between the β-tubulins and forms more extensive contacts with the β-tubulins than with the α-tubulins (**Fig. 3a**). Contacts between the CKK domain and its MT-binding site are distributed across the domain and also involve the N and C termini (**Figs. 2d** and **3a**,**b**). To confirm and extend the cryo-EM data, we also analyzed the structure of the CKK domain of CAMSAP3 bound to MTs, by using solid-state NMR (ssNMR), which provides a sensitive means to study ligand and protein binding to MTs at the atomic level[24,25]. To do so, we compared the solution NMR results (PDB 1UGJ) and our X-ray crystallographic results of free

© 2017 Nature America, Inc., part of Springer Nature. All rights reserved.

© 2017 Nature America, Inc., part of Springer Nature. All rights reserved.

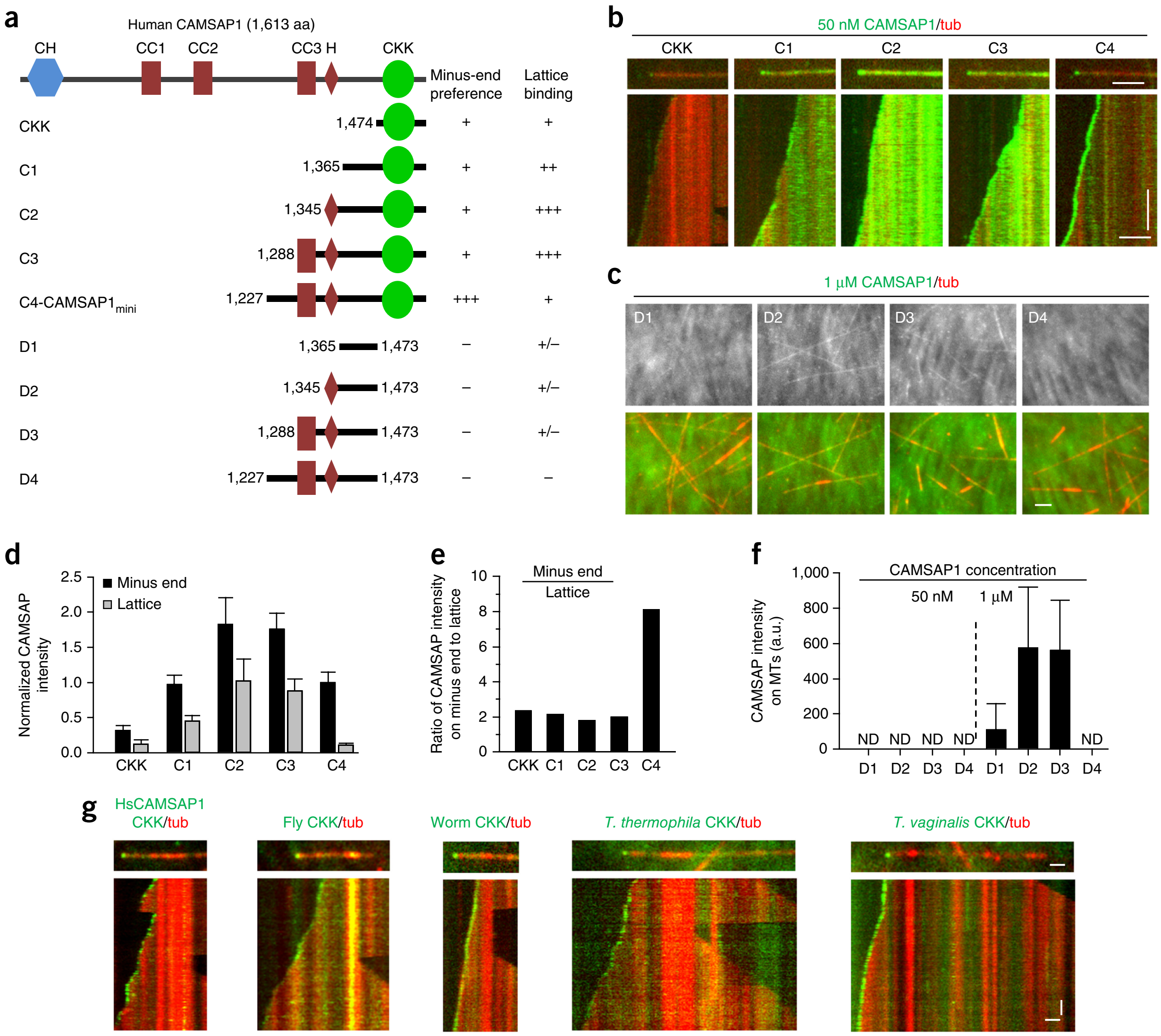

Figure 1 The CKK is a highly conserved domain for MT minus-end tracking. (**a**) Schematic of CAMSAP1 domain organization and the constructs used. (**b**,**c**) TIRFM images (**b**) and corresponding kymographs (**c**). Scale bars: horizontal, 2 µm; vertical, 2 min. (**d**–**f**) Quantification of localization of GFP-CAMSAP1 fragments to MT minus ends and lattice, based on data in **b** and **c**. The intensity was normalized to the average minus-end intensity of the C4 fragment. Data are mean ± s.d., *n* = 30 MTs. ND, not detectable; a.u., arbitrary units. (**g**) TIRFM images (top) and kymographs (bottom) of GFP-tagged CKK domains from humans (CAMSAP1), flies (*D. melanogaster*), worms (*C. elegans*), *T. thermophila* and *T. vaginalis*. Scale bars: horizontal, 1 µm; vertical, 30 s. Additional TIRFM images are shown in **Supplementary Figure 1**, and source data for graphs are in **Supplementary Table 2**. Tub, tubulin.

CKK with 2D ssNMR data recorded on ^{13}C-^{15}N-labeled CKK in complex with MTs. This procedure allowed us to identify CKK residues that underwent significant chemical-shift/intensity changes after MT binding (**Fig. 3c** and **Supplementary Fig. 5a**–**d**, labeled in red) and those that experienced no significant change (labeled in blue). For example, in our EM density, helix α1 of the CKK domain sits across the β1- and β2-tubulins, while beneath it, loop7 and adjacent regions of the β-barrel wedge in between the β-tubulin subunits (**Fig. 3a**–**c** and **Supplementary Fig. 5e**,**f**). Consistently with this configuration, residues from MT-bound CKK helix-α1 and adjacent loop7 displayed ssNMR chemical shifts relative to free CKK. Similarly, our cryo-EM and ssNMR data corroborated interactions between CKK loop1 and β1-tubulin, and CKK loop7 and β2-tubulin, while CKK loop3 lies at the intradimer interface contacting both β1-tubulin and α1-tubulin. CKK loop8 is well positioned to form contacts with α2-tubulin, and our ssNMR data supported the involvement of this loop in the MT interaction. However, loop8 is visible only at less conservative cryo-EM density thresholds (**Supplementary Fig. 5f**), thus suggesting that this loop has greater flexibility than the rest of the CKK domain in this region, in agreement with its *B* factor in the crystal structure. Together, our results demonstrated that residues identified to undergo changes in ssNMR signals cluster on the CKK MT-facing surface. In contrast, residues displaying unaltered ssNMR signals are predominantly solvent exposed (**Fig. 3c** and **Supplementary Fig. 5b**–**d**). The ssNMR data thus supported the EM-derived binding mode at an atomic level.

The CKK N and C termini are not visible in the crystal structure, and both are flexible in solution (PDB 1UGJ). However, our cryo-EM and ssNMR data also supported a role of the CKK N and C termini in MT binding. Density corresponding to the final portion of the N terminus leading into helix-α1 (starting at S1120) is visible in our cryo-EM reconstruction contacting α2-tubulin (**Figs. 2d** and **3a**,**d**), and the additional cryo-EM density suggests that more N-terminal regions make additional contacts with β2-tubulin (red asterisks in

© 2017 Nature America, Inc., part of Springer Nature. All rights reserved.

Table 1 Data collection and refinement statistics

	CKK3 (PDB 5LZN)
Data collection	
Space group	*I*422
Cell dimensions	
a, *b*, *c* (Å)	96.4, 96.4, 63.3
α, β, γ (°)	90.0, 90.0, 90.0
Resolution (Å)	68.1–1.4 (1.45–1.4)
R_{meas} (%)	6.8 (475.0)
R_{pim} (%)	1.3 (99.2)
$I/\sigma(I)$	23.5 (0.8)
$CC_{1/2}$	100 (52.2)
Completeness (%)	100 (99.9)
Redundancy	25.5 (22.4)
Refinement	
Resolution (Å)	68.1–1.4
No. reflections	29,557
R_{work} / R_{free}	16.2 / 19.2
No. atoms	
Protein	897
Water	67
B factors	
Protein	46.0
Water	45.5
R.m.s. deviations	
Bond lengths (Å)	0.01
Bond angles (°)	1.33

Data were collected from one crystal.

Fig. 3a; red dashed line in **Fig. 3d**). The CKK N terminus is therefore partially stabilized in complex with the MT, in agreement with the N-terminal truncation construct having lower MT affinity (**Fig. 3e**). Furthermore, although this region was not readily modeled, cryo-EM density corresponding to the conserved basic C terminus of the CKK domain and/or the β-tubulin C-terminal tail is visible (**Fig. 3f**). ssNMR measurements in the CAMSAP3 CKK–MT complex suggested that the CKK C terminus retains some conformational variability when interacting with MTs (**Fig. 3c**). The location of the CKK C terminus suggested that it interacts with the flexible acidic C-terminal tail of β1-tubulin; this possibility was supported by the observation that the interaction of GFP-tagged CAMSAP3 CKK domain with MTs significantly decreased after the acidic C-terminal tails of tubulin had been cleaved (**Fig. 3g**).

We also used MD-based energy calculations, which can provide an estimate of the relative energetic contributions of individual residues to complex formation[26], to analyze the CKK–MT interaction. This analysis also supported the involvement of the regions described above in the CKK–tubulin interface (**Supplementary Fig. 6a**). Overall analysis of the electrostatic potential of the contact surfaces showed complementary charges between the CKK domain and the MT (**Supplementary Fig. 6b**,**c**). This result was consistent with the large electrostatic contribution to binding energy from MD and the established sensitivity of CAMSAP–MT interaction to ionic strength[18,19] (**Supplementary Fig. 6a**,**d**). CKK residues at the interface with the MT, especially basic ones, are particularly evolutionarily conserved in CKK domains (**Supplementary Fig. 2b** and **6c**,**e**). In addition, these calculations also highlighted the greater energetic contribution of CKK binding to β-tubulin over α-tubulin (with a calculated ΔG of −25.1 ± 5.2 kcal/mol for β-tubulin positions compared with −3.6 ± 5.0 kcal/mol for α-tubulin). Together, our cryo-EM, ssNMR and MD data showed that CKK binds through multiple binding sites across two tubulin dimers at their intradimer interface between protofilaments and associates more closely with β-tubulin than α-tubulin.

Analysis of CKK mutants supports the identified CKK–MT interface

To further validate the identified CKK–MT binding mode, we made a series of CKK mutants in the context of a short version of CAMSAP1 (CAMSAP1$_{\text{mini}}$, residues 1227–1613), which displayed more robust minus-end tracking activity than that of the CKK domain alone (**Fig. 1a**–**e**). Mutations of several conserved positively charged residues decreased the overall binding affinity of CAMSAP1$_{\text{mini}}$ toward MTs and their minus ends (**Fig. 4a**–**c**), although they did not affect the integrity and folding of the CKK domain, on the basis of CD spectra and thermal unfolding profiles in the CAMSAP3 CKK context (**Supplementary Fig. 7a**). Truncation of the N-terminal extension or mutations of positively charged residues in this sequence had a similar effect, as did truncations of the positively charged C-terminal tail region (**Fig. 4a**). These data supported the validity of our CKK–MT lattice reconstruction and its relevance for CKK binding to the MT minus end.

Unexpectedly, a mutation of a conserved asparagine residue (N1492 of CAMSAP1 and N1130 in CAMSAP3) to alanine, which did not affect the integrity of the domain (**Supplementary Fig. 7a**), dramatically increased the ability of CKK to bind to the MT lattice and decreased, though did not abolish, its selectivity toward minus ends (**Fig. 4a**–**c** and **Supplementary Fig. 7b**–**f**). The importance of CAMSAP1's N1492 residue was further emphasized by the observation that mutating it to bulky charged or uncharged amino acids decreased the affinity of CKK for both MT minus ends and lattices, whereas substituting it for either serine or threonine enhanced MT-lattice binding and decreased minus-end selectivity even further (**Fig. 4d** and **Supplementary Fig. 7d**–**f**). CAMSAP1 N1492 is expected to contact the C terminus of helix H4 of β2-tubulin (cyan in **Fig. 4b**), and our data suggested that the formation of the CKK–MT complex is very sensitive to both the size and the chemical nature of the side chain in this position. For example, the potential hydrogen-bond formation between this residue and β-tubulin may affect the affinity of the CKK–MT interaction.

We also mutated several residues close to N1492 in the CKK structure to alanine; several of these substitutions had no effect (**Supplementary Fig. 7g**,**h**), whereas the D1572A mutation also enhanced CKK interaction with the MT lattice and decreased its minus-end selectivity (**Fig. 4a**). Overall, these experiments identified two main classes of mutations: (i) mutations of positively charged CKK residues, which weakened the interaction between CKK and the negatively charged surfaces of the MT ends and lattice, including less structurally ordered regions of both the CKK and MT, and (ii) mutations that specifically increased lattice binding. Remarkably, the effects of these latter mutations were rather subtle, thus suggesting that the mechanism of minus-end discrimination itself is also subtle.

We reasoned that understanding the mechanism underlying the higher affinity of the N1492A mutant for MTs would provide insight into CKK's minus-end specificity. Therefore, we obtained a 3D reconstruction of the CAMSAP1 CKK N1492A mutant by using cryo-EM (**Fig. 4e**, **Supplementary Fig. 8a**–**d** and **Table 2**). As with the wild-type CKK, the N1492A mutant also binds at the tubulin intradimer B-lattice interface with the same overall orientation as the that of the wild-type CKK (**Supplementary Fig. 8a**,**c**,**d**). However, two distinct structural properties were observed for the mutant compared with

© 2017 Nature America, Inc., part of Springer Nature. All rights reserved.

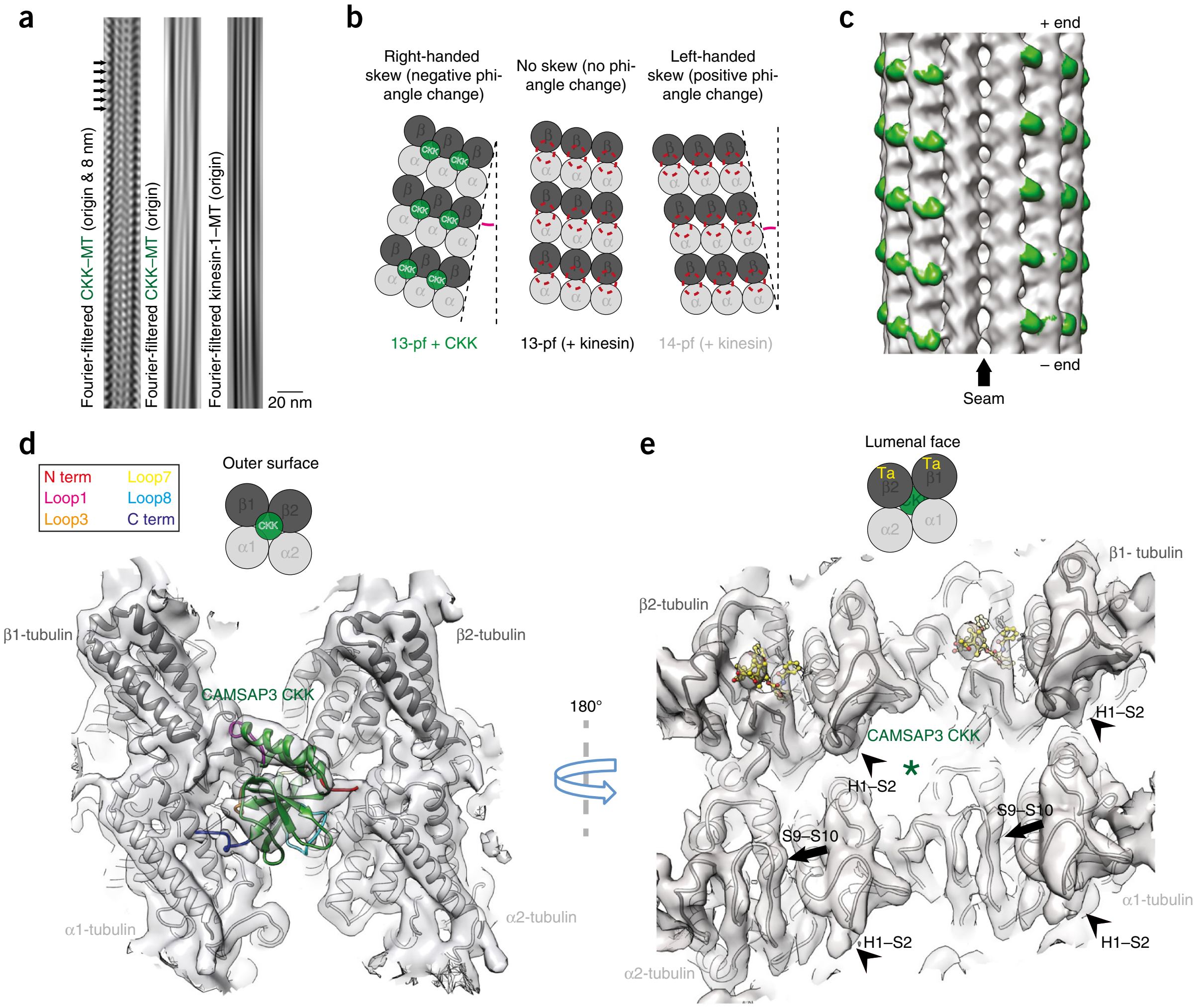
a
Fourier-filtered CKK–MT (origin & 8 nm)
Fourier-filtered CKK–MT (origin)
Fourier-filtered kinesin-1–MT (origin)
20 nm
b
Right-handed skew (negative phi-angle change)
No skew (no phi-angle change)
Left-handed skew (positive phi-angle change)
13-pf + CKK
13-pf (+ kinesin)
14-pf (+ kinesin)
c
+ end
– end
Seam
d
N term
Loop1
Loop3
Loop7
Loop8
C term
Outer surface
β1
β2
CKK
α1
α2
β1-tubulin
β2-tubulin
CAMSAP3 CKK
α1-tubulin
α2-tubulin
180°
e
Lumenal face
Ta
β1- tubulin
β2-tubulin
H1–S2
CAMSAP3 CKK
*
S9–S10
α1-tubulin
α2-tubulin

Figure 2 The unique MT-binding site of the CAMSAP CKK domain. (**a**) Fourier-filtered images of 13-pf MTs. Left, filtering of a CAMSAP3-CKK-decorated 13-pf MT showing density corresponding to the CAMSAP3 CKK domain every tubulin dimer; center, filtering highlighting the MT moiré pattern and the presence of protofilament skew. Right, filtering of a kinesin-1-decorated 13-pf MT, highlighting a comparative lack of skew. (**b**) Schematic of three sets of three protofilaments depicting the skew detected in the CKK 13-pf MT data sets (left) compared with kinesin-bound 13-pf (middle) and 14-pf paclitaxel-stabilized MTs (right). The skew-angle size is exaggerated for ease of viewing. (**c**) The asymmetric reconstruction of the CAMSAP3-CKK-decorated 13-pf paclitaxel-stabilized MT low-pass filtered to 15-Å resolution, showing extra densities (green) every 8 nm corresponding to the CAMSAP3 CKK domains, which are absent at the seam (arrow). (**d**) The averaged reconstruction of the CAMSAP3 CKK domain viewed from the MT surface contacting two β-tubulins and two α-tubulins at the intradimer interprotofilament interface. The CKK is colored as in the X-ray structure (**Supplementary Fig. 3**), except for the N terminus (red) and loop1 (magenta), which are absent in our crystal structure but visible in our EM density. α-tubulin is shown in light gray, and β-tubulin is shown in dark gray. Term, terminus. (**e**) The averaged reconstruction of the MT-bound CAMSAP3 CKK domain viewed from the MT lumen, showing density corresponding to paclitaxel bound to β-tubulin (yellow). Along with the distinctive appearance of the H1–S2 and S9–S10 loops (arrowheads and arrows, respectively), this reconstruction differentiates between β- and α-tubulin, thus allowing for identification of the CKK-binding site at the intradimer interface. In **d** and **e**, schematic drawings appear on top. Ta, paclitaxel-binding site. Additional views are shown in **Supplementary Figures 3** and **4**.

wild type: (i) less protofilament skew in CKK N1492A–decorated MTs (**Supplementary Fig. 8e**) and (ii) a subtle shift of CKK N1492A itself toward the main MT body (**Fig. 4e**). These results suggested that very small changes in the CKK–MT interaction determine the binding selectivity of CKK between the lattice and the minus end. Moreover, the adjustment in the CKK–MT interaction by the N1492A mutant—movement of the CKK domain deeper between protofilaments—may reflect aspects of the mechanism of end selectivity by wild-type CKK via selection of a tubulin conformation present only at MT minus ends.

We also attempted to polymerize tubulin in the presence of a high concentration of CKK. In the presence of wild-type CKK, only very few short microtubules formed, and instead a variety of tubulin oligomers that formed clumps were generated. In contrast, in the presence of saturating concentrations of the N1492A mutant, many longer, predominantly 13-pf, microtubules formed (**Supplementary Fig. 8f**). These data supported the idea that wild-type CKK preferentially interacts with a polymeric conformation of tubulin that is distinct from the normal MT structure, whereas the binding of the N1492A mutant is more compatible with the regular MT lattice.

The high-affinity CKK-binding site at MT minus ends

Having defined the CKK–MT binding mode, we set out to determine whether the state of MT minus ends affects CKK binding. We found that the binding of CAMSAP1$_{\text{mini}}$ to MT minus ends was insensitive to the nucleotide state of MTs, because the protein bound well to

© 2017 Nature America, Inc., part of Springer Nature. All rights reserved.

Table 2 Cryo-EM data collection, refinement and validation statistics

	CAMSAP3 CKK–taxol–GDP 13-pf MTs (EMD-4154, PDB 5M50)	CAMSAP1 CKK–taxol–GDP 13-pf MTs (EMD-4156, PDB 5M54)	CAMSAP1 N1492A CKK–taxol–GDP 13-pf MTs (EMD-3444, PDB 5M5C)
Data collection and processing			
Magnification	41,720	41,477	35,971
Voltage (kV)	300 Kv	200 Kv	300 Kv
Electron exposure (e^-/Å^2)	25	20	25
Defocus range (μm)	−0.4 to −3.5 μm	−0.4 to −3.5 μm	−0.4 to −3.5 μm
Pixel size (Å)	1.534 Å	1.543 Å	1.39 Å
Symmetry imposed[a]	Pseudohelical	Pseudohelical	Pseudohelical
Initial particle images (no.)	66,453	34,122	36,027
Final particle images (no.)	6,530	5,954	4,144
Map resolution (Å)	5.3 Å	8 Å	4.8 Å
FSC threshold[b]	0.143	0.143	0.143
Map resolution range (Å)	5–6.5 Å	7.5–8.5 Å	4.5–6 Å
Refinement			
Initial models used	PDB 5LZN, 1UGJ, 3J6G	PDB 5LZN, 1UGJ, 3J6G	PDB 5LZN, 1UGJ, 3J6G
Refinement resolution (Å)	6.5	8	5.5
$\text{FSC}_{\text{average}}$	0.81	0.91	0.83
Map-sharpening *B* factor (Å^2)	−200	−350	−120
Model composition			
Nonhydrogen atoms	14,600	14,605	14,608
Protein residues	1,826	1,825	1,826
Ligands	6	6	6
R.m.s. deviations			
Bond lengths (Å)	0	0	0
Bond angles (°)	0.78	0.72	0.79
Validation[c]			
MolProbity score	1.70	1.61	1.70
Clashscore	8.94	7.15	7.4
Poor rotamers (%)	0	0	0.06
Ramachandran plot[c]			
Favored (%)	96.58	96.58	95.75
Allowed (%)	100	100	100
Disallowed (%)	0	0	0

[a] Microtubules exhibit pseudohelical symmetry, owing to a symmetry break at the seam. Because CKK domains do not bind at the seam, 12-fold pseudohelical symmetry was applied to the 13-pf microtubule reconstructions. [b] The FSC curves for all reconstructions were subjected to the gold-standard noise-substitution test for overfitting[23]. The resolution value at the gold-standard FSCtrue 0.143 criterion is shown. [c] As defined by the MolProbity[49] validation server.

the minus ends of GMPCPP-stabilized (GTP like) or taxol-stabilized (GDP) MTs, as well as dynamic GTP or GTP-γS-bound (GDP-Pi like) MTs (**Fig. 5a**,**b**). In contrast, we observed no accumulation of CAMSAP1$_{\text{mini}}$ at depolymerizing MT minus ends (**Fig. 5c**), thus suggesting that their structure does not support CKK binding.

To determine the precise localization of CKK on MT minus ends, we implemented the model-convolution method[27,28] to determine the relative positions of the CKK and the MT minus end from their 1D intensity profiles along the MT axis (**Fig. 5d**,**e**). Our data showed that CKK accumulated ~16 nm, equivalent to a few tubulin dimers, behind the outmost MT minus end (estimated measurement error of ~8 nm; Online Methods). This result suggested that some structural features of MT minus ends at this specific location form a preferred CKK-binding site.

Cryo-ET shows preserved interprotofilament contacts at MT ends

To gain insight into the structure of this binding site, we analyzed individual ends of GMPCPP-stabilized MTs by cryo-ET (**Fig. 5f**). Because no averaging was imposed, the tomographic 3D reconstructions contain information about overall polymer configuration and thus allow for direct visualization of the conformation of tubulin that CKK recognizes. The data quality readily allowed for discrimination of individual protofilaments and in many cases individual subunits (**Fig. 5g**), and provided critical 3D information about the MT ends.

Individual protofilament 3D trajectories within five minus and five plus ends (identified through previously established approaches[29]) (**Supplementary Fig. 9a**,**b**) were analyzed. Overall, the individual MT ends are very heterogeneous, and there are no significant differences between minus and plus ends. However, their structures are not blunt but are also distinct from those of a MT-end model constructed on the basis of available high-resolution structures of curved tubulin (**Supplementary Fig. 9c**). First, plots of individual protofilament trajectories at both plus and minus ends show a range of curvatures and lengths of curved regions (example of a minus end in **Fig. 5h**). Second, although there is a wide variation of protofilament curvature, protofilaments at each end are on average less curved than in the model (**Fig. 5i**,**j**). The minus- and plus-end protofilaments are similar with respect to the length (18 ± 15 nm and 11 ± 8 nm at the minus and plus ends, respectively) and the extent of longitudinal curvature, results consistent with those of previous cryo-EM studies in 2D[30,31]. Hence, CKK minus-end preference does not depend on longitudinal curvature alone.

© 2017 Nature America, Inc., part of Springer Nature. All rights reserved.

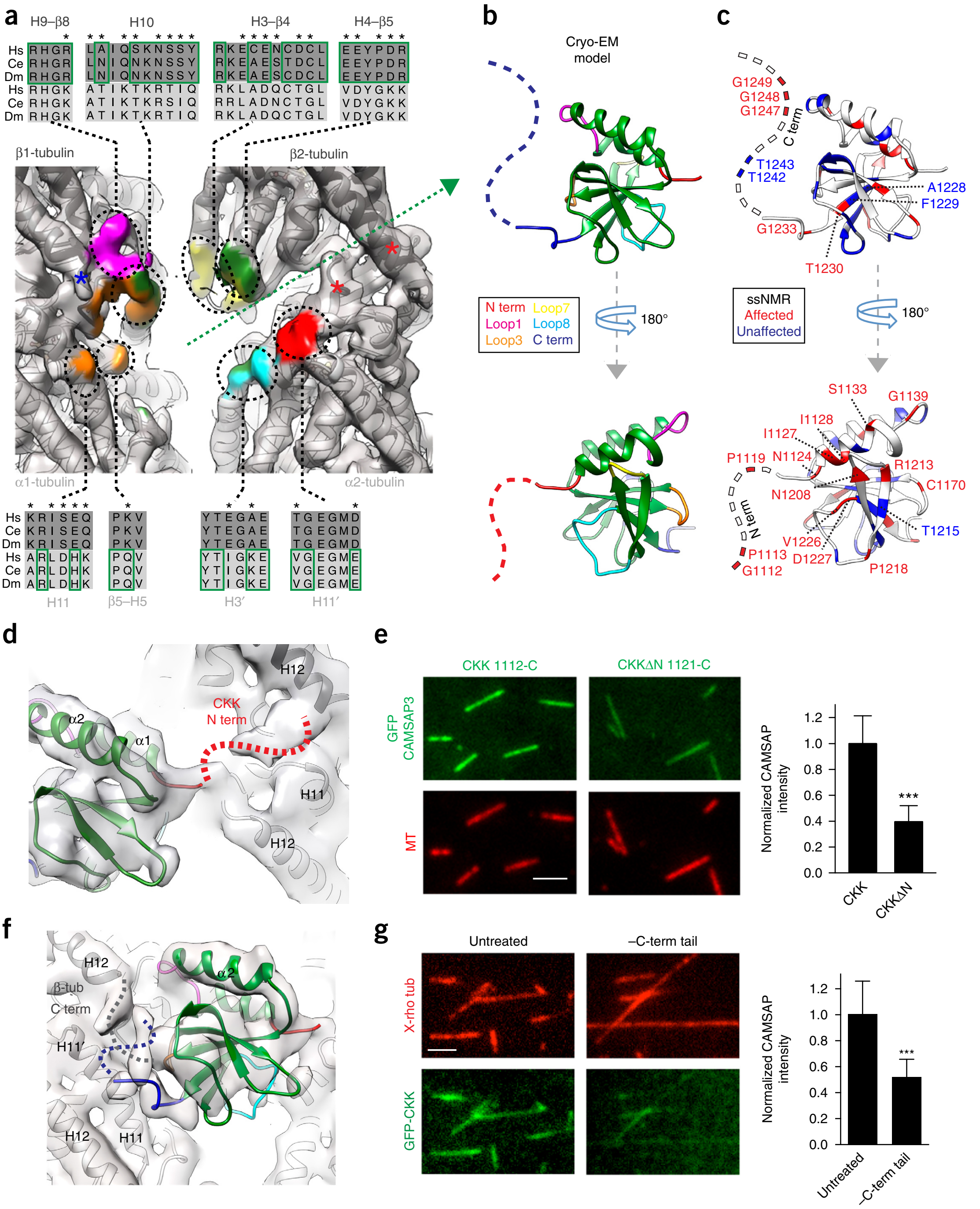
a
H9–β8
H10
H3–β4
H4–β5
Hs RHGR LAIQSKNSSY RKECENCDCL EEYPDR
Ce RHGR LNIQNKNSSY RKEAESTDCL EEYPDR
Dm RHGR LNIQNKNSSY RKEAESCDCL EEYPDR
Hs RHGK ATIKTKRTIQ RKLADQCTGL VDYGKK
Ce RHGK ATIKTKRSIQ RRLADNCTGL VDYGKK
Dm RHGK ATIKTKRTIQ RKLADQCTGL VDYGKK
β1-tubulin
β2-tubulin
α1-tubulin
α2-tubulin
Hs KRISEQ PKV YTEGAE TGEGMD
Ce KRISEQ PKV YTEGAE TGEGMD
Dm KRISEQ PKV YTEGAE TGEGMD
Hs ARLDHK PQV YTIGKE VGEGME
Ce ARLDHK PQV YTIGKE VGEGME
Dm ARLDHK PQV YTIGKE VGEGME
H11
β5–H5
H3′
H11′
b
Cryo-EM model
N term
Loop7
Loop1
Loop8
Loop3
C term
180°
c
G1249
G1248
G1247
C term
T1243
T1242
A1228
F1229
G1233
T1230
ssNMR
Affected
Unaffected
180°
S1133
G1139
I1128
I1127
P1119
N1124
R1213
C1170
N1208
N term
T1215
V1226
P1113
D1227
G1112
P1218
d
H12
CKK
N term
α2
α1
H11
H12
e
CKK 1112-C
CKKΔN 1121-C
GFP CAMSAP3
MT
Normalized CAMSAP intensity
1.2
1.0
0.8
0.6
0.4
0.2
0.0
***
CKK
CKKΔN
f
H12
β-tub
C term
α2
H11′
H12
H11
g
Untreated
–C-term tail
X-rho tub
GFP-CKK
Normalized CAMSAP intensity
1.2
1.0
0.8
0.6
0.4
0.2
0.0
***
Untreated
–C-term tail

Figure 3 The interaction with four tubulin monomers is distributed across the CKK domain. (**a**) CKK-interaction surface of the MT, with cryo-EM density colored according to CKK contacts (<6 Å distance; coloring as in **Fig. 2d**). Sequence alignments for contact regions in β-tubulin (top) and α-tubulin (bottom) indicate sequence differences between human α1a tubulin and β3 tubulins (asterisks) that may contribute to CKK binding to the intra- versus the interdimer site. Comparison between *H. sapiens* (Hs) β3 tubulin and α1a tubulin (most common isoforms in mammalian brain[45]); *C. elegans* (Ce) β1 tubulin and α3 tubulin; and *D. melanogaster* (Dm) β1 tubulin and α-tubulin at 84B. Residues contacting the CKK are within green boundaries. (**b**) 180° rotations of the CKK domain, with loop coloring referring to MT contact sites in **a**. (**c**) CKK views as in **b**, showing ssNMR data on ^{13}C-^{15}N-labeled CKK–decorated MTs relative to free CKK. Red, residues showing significant chemical-shift or intensity changes; blue, residues showing no change; white, residues not analyzed. The unresolved N and C termini are represented as dashed lines with each dash depicting a single residue. (**d**) CAMSAP3 CKK–MT cryo-EM density at lower threshold, showing the CKK N terminus. (**e**) TIRFM experiments showing the importance of the CKK N-terminal extension in MT binding. Intensity is normalized to average CKK lattice intensity. Scale bar, 2 μm. Data are mean ± s.d.; CKK, $n = 104$ MTs; CKKΔN, $n = 118$ MTs. $^{***}P < 0.001$, two-tailed Mann–Whitney *U* test. (**f**) CAMSAP3 CKK–MT cryo-EM density probably corresponding to interaction between the CKK flexible C terminus (blue dotted line) and the β-tubulin C terminus (gray dotted line), not usually seen in MT reconstructions[46]. (**g**) X-rhodamine (rho)-labeled paclitaxel-stabilized MTs (red), either untreated or treated with subtilisin to remove their C-terminal tails, incubated with 200 nM GFP-tagged CAMSAP3 CKK and imaged with TIRFM. Scale bar, 4 μm. The intensity of MT labeling, normalized to that of wild type, is quantified. Data are mean ± s.d., $n = 100$ MTs. $^{***}P < 0.001$, two-tailed Mann–Whitney *U* test. Additional details of the CKK–MT binding site are shown in **Supplementary Figure 5**. Source data for graphs are in **Supplementary Table 2**.

© 2017 Nature America, Inc., part of Springer Nature. All rights reserved.

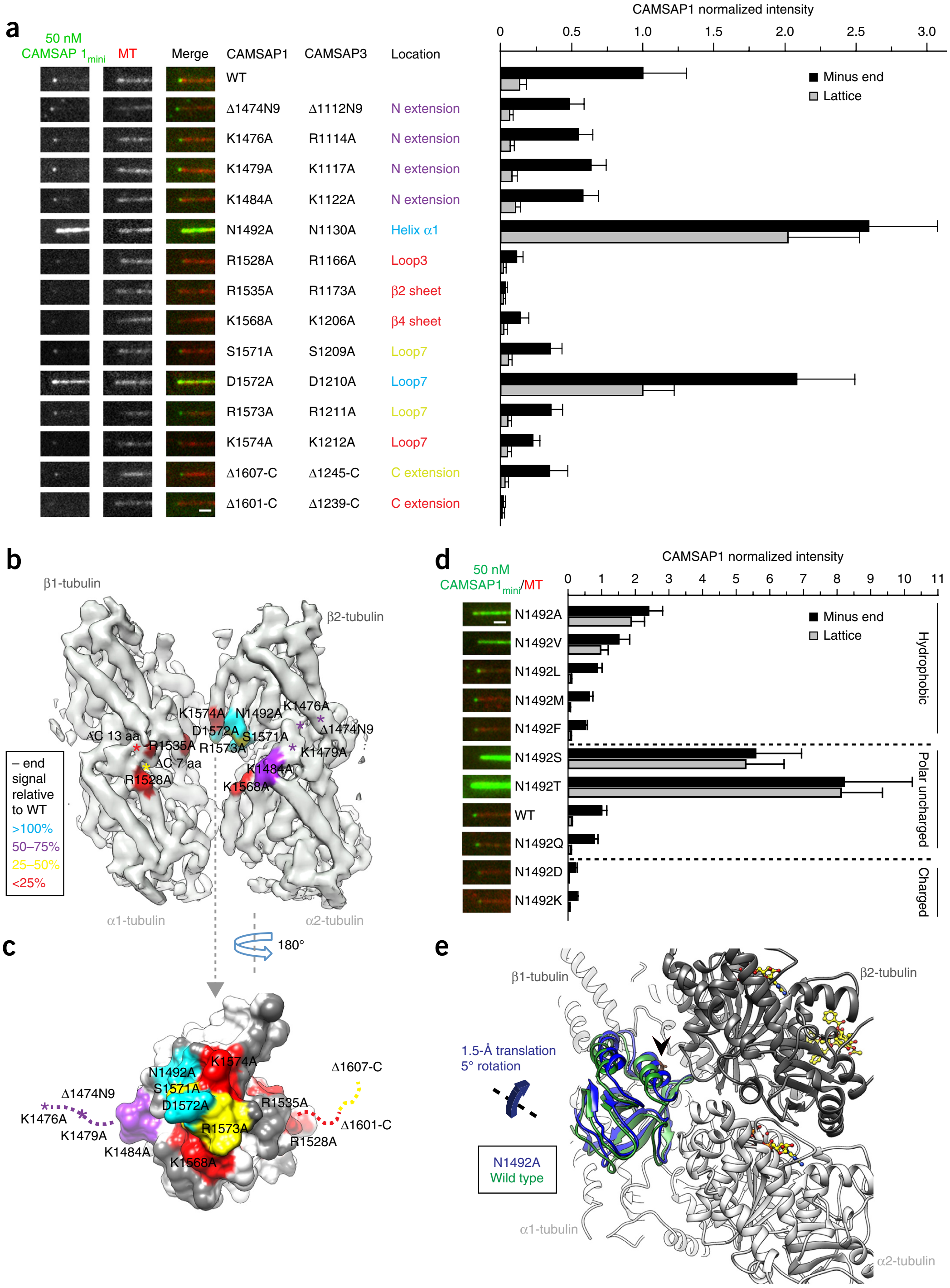

Figure 4 Validation of CKK–MT contact sites with *in vitro* assays and structure of a mutant CKK bound to MTs. (**a**) Left, TIRFM images of GFP-CAMSAP1$_{\mathrm{mini}}$ wild type and mutants binding to the minus ends of dynamic MTs. Scale bar, 1 µm. The corresponding residues in CAMSAP3 and their locations are indicated. Right, quantification of GFP-CAMSAP1$_{\mathrm{mini}}$ intensities at MT minus ends and on MT lattice. The intensity is normalized to the average minus-end intensity of wild type. Data are mean ± s.d.; *n* ranged from 17 to 87 MTs (individual data points in **Supplementary Table 2**). (**b**) View of the CKK-interaction surface of the MT cryo-EM density, with mutated CKK residues mapped (<8 Å distance) and colored according to the percentage change in the minus-end fluorescence signal in mutants relative to wild type (as in **a**). (**c**) Surface representation of the tubulin-interacting face of the CAMSAP1 CKK domain. Mutated CKK residues are colored according to the percentage change in the minus-end fluorescence signal of corresponding mutants relative to wild type in our TIRF assays (as in **a**). (**d**) Left, TIRFM images of GFP-CAMSAP1$_{\mathrm{mini}}$ N1492 mutants; scale bar, 1 µm. Right, quantification of GFP-CAMSAP1$_{\mathrm{mini}}$ intensities at MT minus ends and on MT lattice. The intensity is normalized to the average minus-end intensity of wild type. Data are mean ± s.d., *n* = 30 MTs. (**e**) The N1492A CAMSAP1 CKK binds at the intradimer, interprotofilament MT binding site but in an orientation subtly different from that of wild type. Ribbon representation comparing the position of N1492A CAMSAP1 CKK with wild-type CAMSAP1 CK relative to the tubulin-binding surface. N1492A CAMSAP1 CKK (blue) is rotated 5° around the indicated axis and translated 1.9 Å into the interprotofilament-binding site, relative to wild-type CAMSAP1 CKK (green). Arrowhead depicts the position of N1492. Additional validation of CKK–MT contact sites by mutagenesis and analysis of the N1492A mutant is shown in **Supplementary Figures 7** and **8**. Source data for graphs are in **Supplementary Table 2**.

© 2017 Nature America, Inc., part of Springer Nature. All rights reserved.

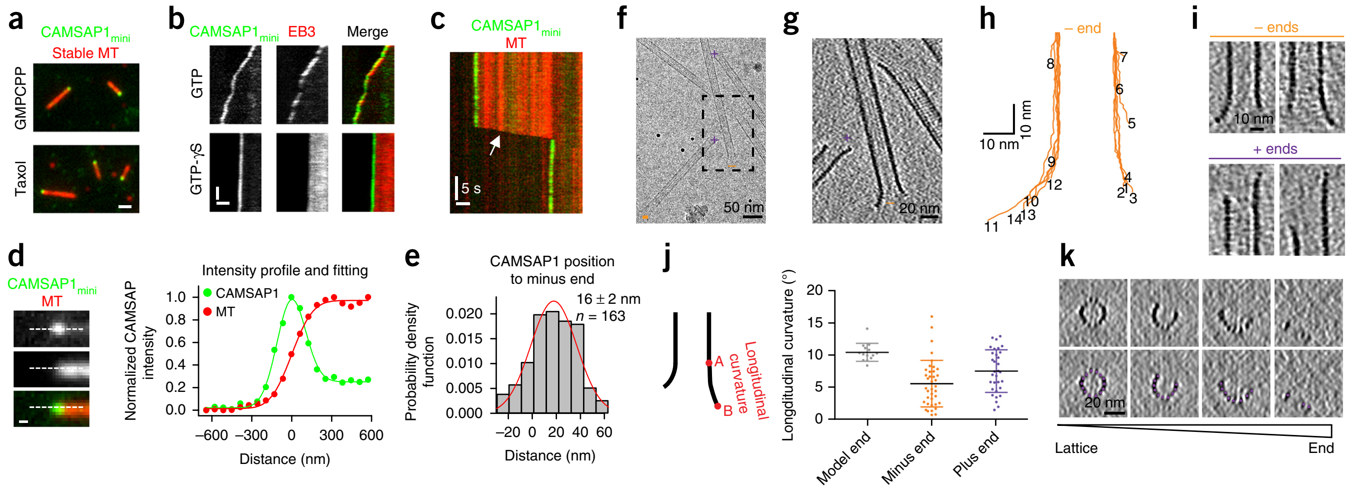

Figure 5 Examining CKK's preferred tubulin conformation. (**a**) TIRFM images of the minus-end localization of GFP-CAMSAP1$_{\mathrm{mini}}$ on GMPCPP or taxol-stabilized MTs. Scale bar, 1 µm. (**b**) Kymographs showing that GFP-CAMSAP1$_{\mathrm{mini}}$ tracks growing MT minus ends when MTs are polymerized in the presence of GTP or GTP-γS, whereas mCherry-EB3 decorates the entire lattice of GTP-γS MTs. Scale bars: horizontal, 1 µm; vertical, 30 s. (**c**) Kymograph showing that GFP-CAMSAP1$_{\mathrm{mini}}$ tracks a growing but not a depolymerizing MT minus end (white arrow). Scale bars: horizontal, 1 µm; vertical, 5 s. (**d**) TIRFM image of rhodamine-labeled stable GMPCPP MT and CAMSAP1$_{\mathrm{mini}}$-GFP. Normalized 1D intensity profiles of CAMSAP1$_{\mathrm{mini}}$-GFP and MT and corresponding fitting of point-spread-function-convoluted models (details in Online Methods). To decrease the error introduced by the flexible linker between CKK and GFP, GFP was inserted at the CKK C terminus. Scale bar, 200 nm. (**e**) Distribution of the position of CAMSAP1$_{\mathrm{mini}}$-GFP relative to the MT minus end. Mean ± s.e.m. are shown; $n = 163$ MTs. (**f**) Projection image from a cryo-ET tilt series showing *in vitro* GMPCPP-stabilized MTs, including several ends. The moiré patterns were used to determine MT polarity (additional data in **Supplementary Fig. 9**). The black dots are gold fiducials for tilt-series alignment. (**g**) Longitudinal slice through MTs in the tomographic volume corresponding to the boxed region in **f**. (**h**) 2D graphical representation of an exemplar minus end, plotting 3D protofilament radial trajectories. Here, for a 14-pf MT, 7 pf are plotted on either side, numbered around the circumference (pf14 is adjacent to pf1). (**i**) Sagittal slices through tomographic volumes showing a range of curvatures and lengths at both ends. Some protofilaments terminate in the lattice before curvature is observed. (**j**) Longitudinal curvature of ends. Left, schematic of longitudinal curvature A–B. Right, graph with only curved end regions longer than one dimer long plotted. Data show individual points, mean ± s.d.; model end (**Supplementary Fig. 9c**), $n = 14$ pf; plus end, $n = 32$ pf (5 MTs); minus end, $n = 38$ pf (5 MTs). Minus end versus plus end, not significant; model versus data, statistically significant ($P < 0.01$, Kolmogorov–Smirnov test). (**k**) Series of transverse sections through an MT from lattice to end. Bottom panels show traced protofilament positions. Additional cryo-ET analyses are shown in **Supplementary Figure 9**, and source data for graphs are in **Supplementary Table 2**.

Intriguingly, adjacent protofilaments within an MT end retain connectivity with their neighbors (**Fig. 5k** and **Supplementary Fig. 9d**), even while the protofilaments spread away from the MT axis, and the total protofilament number is decreased. This behavior is in contrast to the MT-end model in which protofilament separation is an essential consequence of their curvature and is more consistent with the classical 'rams' horns' of depolymerizing MTs[31], to which CAMSAP do not bind (**Fig. 5c**). In other words, in nondepolymerizing MTs, protofilaments curving outward from the MT axis flatten from cylinders into gently curving sheet-like structures, which retain lateral connectivity[30,32,33]. Given that the CKK domain binds at the interprotofilament interface, the tomographic data suggest that potential CKK-binding sites are retained in the end structures characterized here. To determine whether CKK binding perturbs these curved sheet-like structures, we examined MT minus ends in the presence of CKK but detected no differences relative to the control MTs (**Supplementary Fig. 9e–h**). This analysis, when combined with our fluorescence-based localization of the CKK binding site, suggested that the CKK prefers neither the extreme end nor the MT lattice but a transition region from the straight lattice to a curved and flattened polymer.

CKK blocks MCAK interaction with MT minus ends

Fly Patronin and three mammalian CAMSAPs have been shown to protect MT minus ends from depolymerization by kinesin-13 (refs. 6,19), but the underlying mechanism is unknown. By superimposing the human (Hs) MCAK motor structure onto our CKK–MT cryo-EM reconstruction, we found that CKK and HsMCAK would strongly clash with each other at a number of positions (**Fig. 6a**). Hence, CKK and MCAK would be expected to compete for the binding sites at MT minus ends. To test this hypothesis, we measured *in vitro* disassembly of GMPCPP-stabilized MTs by 50 nM MCAK in the presence of different concentrations of CAMSAP1$_{\mathrm{mini}}$ or the isolated CKK domain (**Fig. 6b**,**c**). CAMSAP1$_{\mathrm{mini}}$ and CKK almost completely inhibited the minus-end binding and depolymerization of MCAK at 1.5 nM and 38 nM, respectively, whereas the activity of MCAK on plus ends was largely unaffected at those concentrations (**Fig. 6d**,**e**). Above 1 µM concentration, even though both CAMSAP1$_{\mathrm{mini}}$ and CKK fully decorated the MT shaft with lattice intensities higher than those observed at the minus ends at low concentrations, this decoration did not lead to complete inhibition of MT plus-end accumulation and depolymerization by MCAK (**Fig. 6d**,**e**). This observation suggested that the CKK has the highest affinity for MT minus ends and then for the MT lattice, and has the lowest affinity for MT plus ends. The alternative mechanism—in which displacement of MCAK from MT minus ends is due to CKK-mediated alteration of the MT minus-end structure, which would be less favorable for MCAK binding—is not supported by our cryo-EM images even at a CKK concentration of >50 µM, which was much higher than the concentrations used in our *in vitro* assays (**Supplementary Fig. 9e–h**). This result indicated that the competition between CKK and MCAK on MT minus ends is primarily based on steric hindrance.

© 2017 Nature America, Inc., part of Springer Nature. All rights reserved.

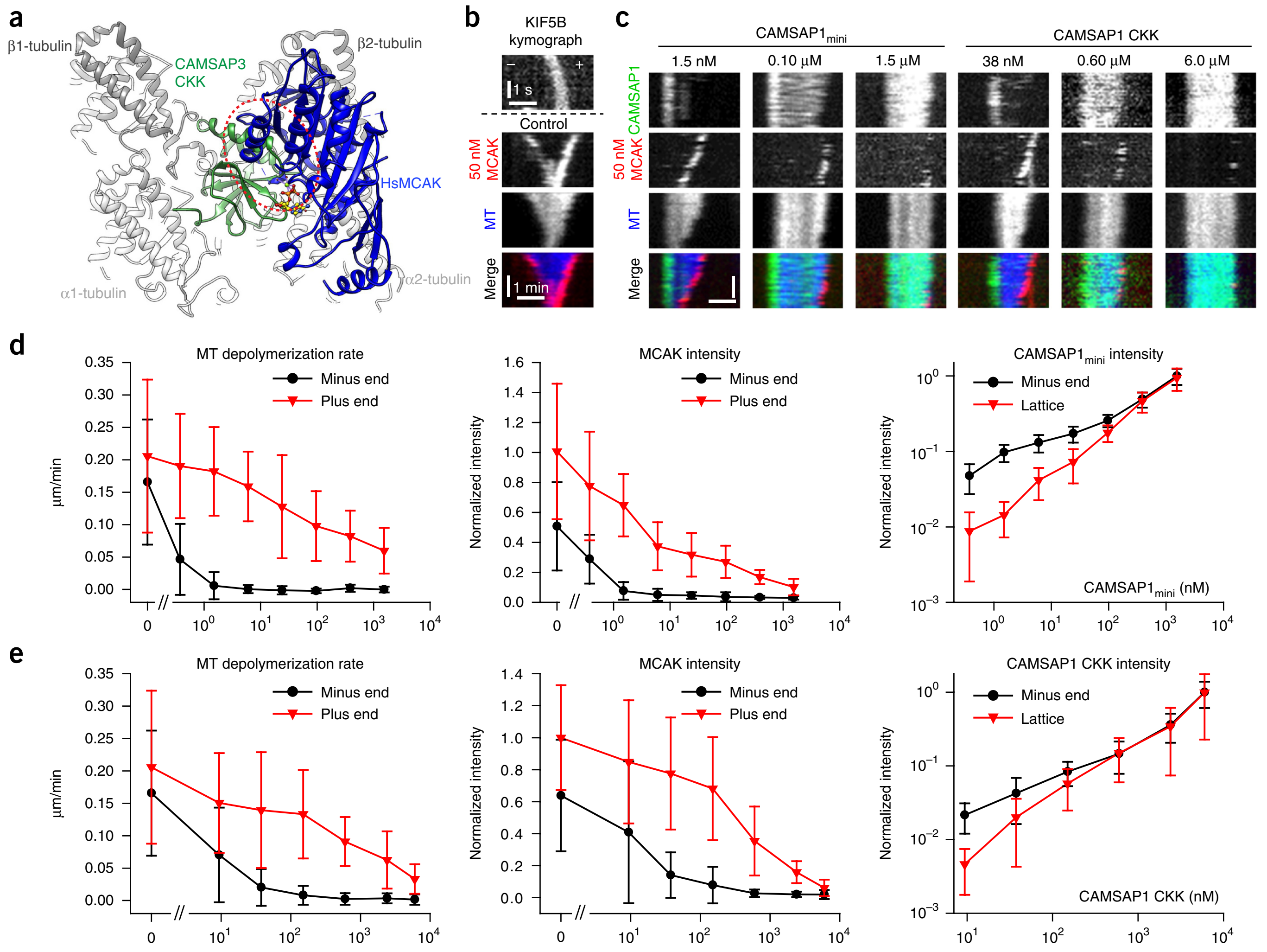

Figure 6 CAMSAP CKKs protect MT minus ends from MCAK-induced depolymerization via steric inhibition. (**a**) An MT tubulin dimer pair bound to CAMSAP3 CKK (green), shown with the expected position of an MD of HsMCAK (in complex with ADP; PDB 4UBF) by alignment with MT-bound kinesin-1 (ref. 47) in Chimera[48]. (**b**) Kymographs of MT-depolymerization assay with GMPCPP-stabilized MTs (blue) and GFP-MCAK (red). Scale bars: horizontal, 1 μm; vertical, 1 s (top) or 1 min (bottom). MT polarity was determined on the basis of the movement of the SNAP-Alexa647-tagged plus-end-directed motor kinesin-1 KIF5B (green, residues 1–560). (**c**) Kymographs of MT-depolymerization assays with GMPCPP-stabilized MTs (blue), GFP-MCAK (red) and different concentrations of SNAP-Alexa647-tagged CAMSAP1$_{\text{mini}}$ or CKK (green). Scale bars: horizontal, 1 μm; vertical, 1 min. In **b** and **c**, MT minus (–) ends are shown on the left, and plus (+) ends are shown on the right. (**d**,**e**) Quantification of MT-depolymerization rate, MCAK intensity and CAMSAP1 intensity at different concentrations of CAMSAP1$_{\text{mini}}$ (**d**) or CKK (**e**). Data are mean ± s.d.; *n* ranged from 17 to 31 MTs (source data and individual data points in **Supplementary Table 2**).

DISCUSSION

In this study, we demonstrated that the CKK is a highly conserved globular-protein module that interacts with an interprotofilament site between two tubulin dimers on the outer surfaces of MTs. Several lines of evidence suggest that an optimal site for CKK binding deviates from the interprotofilament interface within a regular, straight MT structure. First, the decoration by CKK distorts the normal MT lattice, thereby generating a right-handed protofilament skew. Second, tubulin copolymerization with CKK yields mainly non-MT, curved polymers. Third, the interaction between CKK and its binding site is intrinsically asymmetric, with the helical parts of CKK interacting more closely with the β-tubulin pairs, whereas its connectivity with the α-tubulin pair is less compact and is able to accommodate plasticity at minus ends. Fourth, the N1492A mutation increases affinity and subtly alters the CKK position relative to the MT, thus resulting in a deeper insertion between the protofilaments. The size and the chemical nature of the N1492-substituted side chain also affect CKK affinity for the MT lattice, thus suggesting that the optimal binding site for the wild-type CKK domain might depend on specific but subtle conformational features of tubulin dimers at MT minus ends to allow for a more buried fit between protofilaments. Fifth, high-resolution microscopy showed that the high-affinity CKK-binding region is located, on average, two tubulin dimers behind the outmost MT end. This binding site fits very well with the average position of the transition zone between the straight protofilaments in the MT shaft and the mildly curved tubulin sheets identified at MT ends by cryo-ET.

At this transition zone, pairs of α-tubulins would be more laterally flattened and more flexible than the more constrained lattice-like β-tubulin pairs (**Fig. 7a**). In agreement with this scenario, our structures show that the lattice-bound CKK has tight shape complementarity and a large contact surface with the β-tubulin pairs, whereas the α-tubulin pairs surround the CKK more loosely. In contrast, at

© 2017 Nature America, Inc., part of Springer Nature. All rights reserved.

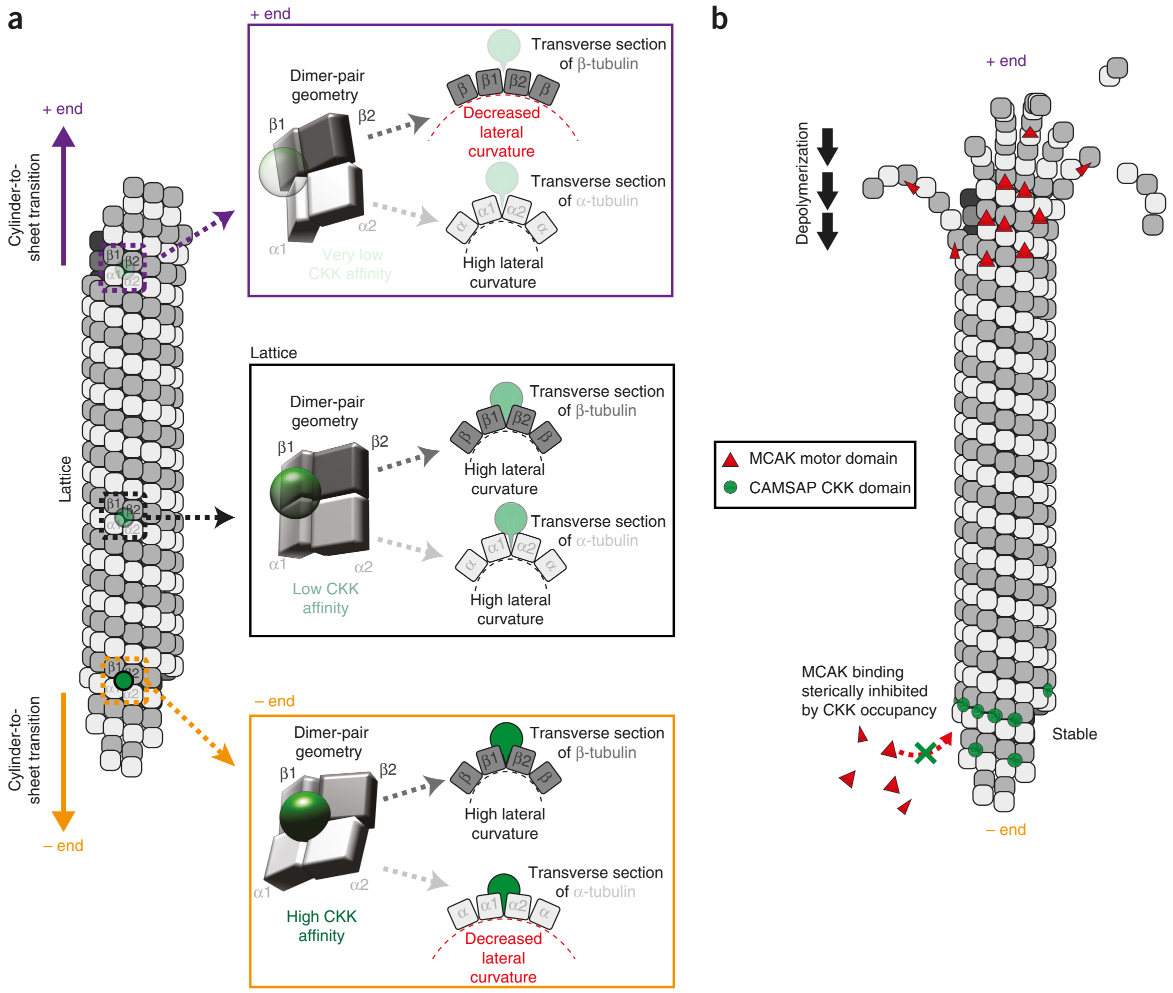
a
+ end
Cylinder-to-sheet transition
Lattice
Cylinder-to-sheet transition
– end
β1
β2
α1
α2
+ end
Dimer-pair geometry
β1
β2
α1
α2
Very low CKK affinity
Transverse section of β-tubulin
β
β1
β2
β
Decreased lateral curvature
Transverse section of α-tubulin
α
α1
α2
α
High lateral curvature
Lattice
Dimer-pair geometry
β1
β2
α1
α2
Low CKK affinity
Transverse section of β-tubulin
High lateral curvature
Transverse section of α-tubulin
High lateral curvature
– end
Dimer-pair geometry
β1
β2
α1
α2
High CKK affinity
Transverse section of β-tubulin
High lateral curvature
Transverse section of α-tubulin
Decreased lateral curvature
b
+ end
Depolymerization
MCAK motor domain
CAMSAP CKK domain
MCAK binding sterically inhibited by CKK occupancy
Stable
– end

Figure 7 Proposed mechanisms of MT minus-end binding and protection from MCAK-induced depolymerization by the CKK domain. (**a**) Toward the ends of stable or growing MTs, there is a transition from the regular lattice to sheet-like regions, with increasing longitudinal curvature and decreasing lateral curvature. Protofilaments retain lateral connectivity, and thus interprotofilament CKK-binding sites are preserved. Given the polar nature of MTs, these lattice-to-sheet transitions create unique conformations of B-lattice tubulin dimer pairs at either end of the MT: at the minus end, α-tubulins in dimer pairs are more flattened than β-tubulins, whereas the opposite is true at the plus end. In this way, we propose that the unique dimer-pair conformation at the minus end, compared with dimer-pair conformations in the lattice or at the plus end, favors CKK binding. (**b**) Model of minus-end-specific protection from MCAK-induced depolymerization by the CKK domains. CKKs (green circles) specifically bind to a curved minus-end region, and steric inhibition thereby prevents the association of MCAK motor domains (red triangles) with the same region. Because the CKKs do not bind to the corresponding region of the plus end, MCAK is free to bind and depolymerize from the plus end.

the plus end, β-tubulin pairs are expected to acquire a more flattened and flexible arrangement than α-tubulins. This arrangement would disfavor the interaction of CKK with the plus end, thereby explaining its inability to effectively compete with MCAK at this location. In summary, flattening of β-tubulin pairs at the plus end may squeeze CKK out of the tubulin groove, thus avoiding steric clashes, whereas flattening of α-tubulin pairs at the minus end may tighten their multiple contacts around the CKK. This tightening would lead to a binding preference for the minus end, some capacity to bind the straight MT lattice and low affinity for MT plus end. The lack of CKK binding at rapidly depolymerizing MT minus ends, where the lateral contacts between protofilaments are expected to be lost, owing to their strong curling, is consistent with the requirement for maintenance of lateral protofilament connectivity and/or more gentle longitudinal curvature for CAMSAP binding.

Importantly, although our analysis showed that CKK was the only CAMSAP part able to autonomously recognize MT minus ends, some longer CAMSAP fragments, such as CAMSAP1$_{mini}$, had a higher affinity for the minus ends. These data indicated that CAMSAP regions outside of the CKK domain contribute to the affinity and selectivity of minus-end binding, and additional work will be needed to decipher the underlying mechanisms.

The MT minus-end-binding mode of the CKK domain is distinct from those of other known MT-tip-interacting proteins. The most conceptually simple mode of MT-end recognition relies on the presence of unique binding sites on α- and β-tubulin exposed on the outermost MT ends, as is the case for the γ-TuRC at the minus end[5] and probably for the centriole protein CPAP at MT plus ends[34]. However, the preference of most known MT regulators is based on recognition of certain MT-lattice features that are different at MT ends compared with the MT shaft. For example, EB proteins bind at the vertex of four tubulin dimers[35,36] and sense a GTP-hydrolysis transition state of tubulin within the MT lattice at both plus and minus ends[37,38]. Doublecortin, which also binds at the vertex of four tubulin dimers[39] and acts as an MT-end-binding protein, is thought to be sensitive to the extent of protofilament longitudinal curvature[40,41]. MT-depolymerizing kinesin-13s can also accumulate at MT ends, probably because of a preference for the more curved or flexible conformations of tubulin located outside the lattice[42,43]. Importantly, none of these mechanisms are specific for the plus or the minus end.

CAMSAPs are similar to most other MT-end-binding proteins in that they bind on the outer surfaces of MTs: in contrast to γ-TuRC binding, which caps MTs, CAMSAP binding is compatible with further MT polymerization at the minus end[18]. CAMSAPs and γ-TuRCs thus do not directly compete for binding to MT minus ends; however, the restricted lattice-like conformation of tubulin at γ-TuRC-capped minus ends probably prevents formation of CAMSAP-preferred binding regions. Importantly, in contrast to EB–MT association, CAMSAP–MT association is insensitive to the hydrolysis state of the tubulin-bound nucleotide. Whereas the tubulin interdimer interface to which EBs bind changes conformation in response to nucleotide, the intradimer interface to which CKKs bind does not[36,44]. This difference in conformational changes accounts for the ability of CAMSAPs to recognize growing GTP- as well as GDP-bound minus ends generated by MT severing[18].

CAMSAP's interaction with MT minus ends can be expected to have several consequences. First, by preferentially binding between laterally connected but curved protofilaments, the CKK, in the context of the full-length protein, might inhibit formation of a regular lattice, thus explaining why CAMSAPs slow down MT minus-end polymerization[18]. Second, CKK binding at intradimer-binding sites can also explain the protection of MT minus ends from kinesin-13-driven depolymerization by direct steric inhibition (**Fig. 7b**).

Together, our data show that the unique MT-binding mode of the CKK domains enables CAMSAPs to combine the ability to recognize MT minus ends with the preservation of the dynamic properties of these ends. Hence, CAMSAPs can be rapidly recruited to MT minus ends generated by release from the sites of MT nucleation, severing or breakage, and consequently protect the ends from disassembly by depolymerases and, by decorating polymerizing minus ends, form stretches of stabilized MT lattice. Future studies will show whether other proteins share the CKK's MT-binding mode or whether this mode is unique to this evolutionarily ancient and widespread protein module.

METHODS

Methods, including statements of data availability and any associated accession codes and references, are available in the online version of the paper.

Note: Any Supplementary Information and Source Data files are available in the online version of the paper.

ACKNOWLEDGMENTS
We thank F. Govers (Wageningen University), V. Gelfand (Northwestern University) and M. Harterink (Utrecht University) for sharing reagents; E. Katrukha for advice on processing fluorescence microscopy data; R. Boelens for providing access to the solution-state NMR instrumentation; and S. Yokoyama and A. Nomura for sharing NMR resonance assignments of free CKK. A.A. was supported by ERC Synergy grant 609822. J.A., C.A.M. (MR/J000973/1), A.-P.J. and M.T. (MR/M019292/1) were supported by the Medical Research Council, UK. A.J.R. was supported by a Sir Henry Dale Fellowship from the Wellcome Trust and Royal Society (104196/Z/14/Z). G.S. and B.J.G. were supported by the National Institutes of Health (R01GM070862). M.B., Y.L. (grant 718.015.001) and K.H. (grant 718.015.001 and 184.032.207) were supported by the Netherlands Organization for Scientific Research (NWO). ssNMR experiments were supported by uNMR-NL, an NWO-funded National Roadmap Large-scale Facility of the Netherlands (grant 184.032.207). M.O.S. was supported by grants from the Swiss National Science Foundation (31003A_166608) and from SystemsX.ch (RTD-TubeX).

AUTHOR CONTRIBUTIONS
J.A., K.J., M.O.S., M.B., C.A.M. and A.A. designed experiments, analyzed data and wrote the paper. C.A.M. and A.A. coordinated the project. J.A. performed and analyzed cryo-EM and cryo-ET experiments; K.J. and S.H. performed *in vitro* reconstitution experiments; M.M.S. performed X-ray crystallography and biophysical experiments; Y.L. and K.H. performed and analyzed NMR experiments; J.J.E.v.H. performed bioinformatics analysis; A.-P.J. and M.T. performed cryo-EM-based molecular modeling; G.S. and B.J.G. performed molecular dynamics calculations; and A.J.R. performed subtilisin–MT TIRFM assays.

COMPETING FINANCIAL INTERESTS

The authors declare no competing financial interests.

Reprints and permissions information is available online at http://www.nature.com/reprints/index.html. Publisher's note: Springer Nature remains neutral with regard to jurisdictional claims in published maps and institutional affiliations.

1. Howard, J. & Hyman, A.A. Dynamics and mechanics of the microtubule plus end. *Nature* **422**, 753–758 (2003).
2. Akhmanova, A. & Steinmetz, M.O. Control of microtubule organization and dynamics: two ends in the limelight. *Nat. Rev. Mol. Cell Biol.* **16**, 711–726 (2015).
3. Dammermann, A., Desai, A. & Oegema, K. The minus end in sight. *Curr. Biol.* **13**, R614–R624 (2003).
4. Akhmanova, A. & Hoogenraad, C.C. Microtubule minus-end-targeting proteins. *Curr. Biol.* **25**, R162–R171 (2015).
5. Kollman, J.M., Merdes, A., Mourey, L. & Agard, D.A. Microtubule nucleation by γ-tubulin complexes. *Nat. Rev. Mol. Cell Biol.* **12**, 709–721 (2011).
6. Goodwin, S.S. & Vale, R.D. Patronin regulates the microtubule network by protecting microtubule minus ends. *Cell* **143**, 263–274 (2010).
7. Derivery, E. *et al.* Polarized endosome dynamics by spindle asymmetry during asymmetric cell division. *Nature* **528**, 280–285 (2015).
8. Wang, H., Brust-Mascher, I., Civelekoglu-Scholey, G. & Scholey, J.M. Patronin mediates a switch from kinesin-13-dependent poleward flux to anaphase B spindle elongation. *J. Cell Biol.* **203**, 35–46 (2013).
9. Khanal, I., Elbediwy, A., Diaz de la Loza, Mdel.C., Fletcher, G.C. & Thompson, B.J. Shot and Patronin polarise microtubules to direct membrane traffic and biogenesis of microvilli in epithelia. *J. Cell Sci.* **129**, 2651–2659 (2016).
10. Toya, M. *et al.* CAMSAP3 orients the apical-to-basal polarity of microtubule arrays in epithelial cells. *Proc. Natl. Acad. Sci. USA* **113**, 332–337 (2016).
11. Wang, S. *et al.* NOCA-1 functions with γ-tubulin and in parallel to Patronin to assemble non-centrosomal microtubule arrays in *C. elegans*. *eLife* **4**, e08649 (2015).
12. Zheng, J. *et al.* Marshalin, a microtubule minus-end binding protein, regulates cytoskeletal structure in the organ of Corti. *Biol. Open* **2**, 1192–1202 (2013).
13. Nashchekin, D., Fernandes, A.R. & St Johnston, D. Patronin/shot cortical foci assemble the noncentrosomal microtubule array that specifies the *Drosophila* anterior-posterior axis. *Dev. Cell* **38**, 61–72 (2016).
14. Yau, K.W. *et al.* Microtubule minus-end binding protein CAMSAP2 controls axon specification and dendrite development. *Neuron* **82**, 1058–1073 (2014).
15. Richardson, C.E. *et al.* PTRN-1, a microtubule minus end-binding CAMSAP homolog, promotes microtubule function in *Caenorhabditis elegans* neurons. *eLife* **3**, e01498 (2014).
16. Marcette, J.D., Chen, J.J. & Nonet, M.L. The *Caenorhabditis elegans* microtubule minus-end binding homolog PTRN-1 stabilizes synapses and neurites. *eLife* **3**, e01637 (2014).
17. Chuang, M. *et al.* The microtubule minus-end-binding protein patronin/PTRN-1 is required for axon regeneration in *C. elegans*. *Cell Rep.* **9**, 874–883 (2014).
18. Jiang, K. *et al.* Microtubule minus-end stabilization by polymerization-driven CAMSAP deposition. *Dev. Cell* **28**, 295–309 (2014).
19. Hendershott, M.C. & Vale, R.D. Regulation of microtubule minus-end dynamics by CAMSAPs and Patronin. *Proc. Natl. Acad. Sci. USA* **111**, 5860–5865 (2014).
20. Tanaka, N., Meng, W., Nagae, S. & Takeichi, M. Nezha/CAMSAP3 and CAMSAP2 cooperate in epithelial-specific organization of noncentrosomal microtubules. *Proc. Natl. Acad. Sci. USA* **109**, 20029–20034 (2012).
21. Baines, A.J. *et al.* The CKK domain (DUF1781) binds microtubules and defines the CAMSAP/ssp4 family of animal proteins. *Mol. Biol. Evol.* **26**, 2005–2014 (2009).
22. Williams, T.A. Evolution: rooting the eukaryotic tree of life. *Curr. Biol.* **24**, R151–R152 (2014).
23. Chen, S. *et al.* High-resolution noise substitution to measure overfitting and validate resolution in 3D structure determination by single particle electron cryomicroscopy. *Ultramicroscopy* **135**, 24–35 (2013).
24. Kumar, A. *et al.* Interaction of epothilone B (patupilone) with microtubules as detected by two-dimensional solid-state NMR spectroscopy. *Angew. Chem. Int. Edn Engl.* **49**, 7504–7507 (2010).
25. Yan, S. *et al.* Atomic-resolution structure of the CAP-Gly domain of dynactin on polymeric microtubules determined by magic angle spinning NMR spectroscopy. *Proc. Natl. Acad. Sci. USA* **112**, 14611–14616 (2015).
26. Scarabelli, G. *et al.* Mapping the processivity determinants of the kinesin-3 motor domain. *Biophys. J.* **109**, 1537–1540 (2015).

© 2017 Nature America, Inc., part of Springer Nature. All rights reserved.

27. Gardner, M.K. *et al.* Model convolution: a computational approach to digital image interpretation. *Cell. Mol. Bioeng.* **3**, 163–170 (2010).
28. Maurer, S.P. *et al.* EB1 accelerates two conformational transitions important for microtubule maturation and dynamics. *Curr. Biol.* **24**, 372–384 (2014).
29. Chrétien, D., Kenney, J.M., Fuller, S.D. & Wade, R.H. Determination of microtubule polarity by cryo-electron microscopy. *Structure* **4**, 1031–1040 (1996).
30. Chrétien, D., Fuller, S.D. & Karsenti, E. Structure of growing microtubule ends: two-dimensional sheets close into tubes at variable rates. *J. Cell Biol.* **129**, 1311–1328 (1995).
31. Mandelkow, E.M., Mandelkow, E. & Milligan, R.A. Microtubule dynamics and microtubule caps: a time-resolved cryo-electron microscopy study. *J. Cell Biol.* **114**, 977–991 (1991).
32. Guesdon, A. *et al.* EB1 interacts with outwardly curved and straight regions of the microtubule lattice. *Nat. Cell Biol.* **18**, 1102–1108 (2016).
33. Jánosi, I.M., Chrétien, D. & Flyvbjerg, H. Modeling elastic properties of microtubule tips and walls. *Eur. Biophys. J.* **27**, 501–513 (1998).
34. Sharma, A. *et al.* Centriolar CPAP/SAS-4 imparts slow processive microtubule growth. *Dev. Cell* **37**, 362–376 (2016).
35. Maurer, S.P., Fourniol, F.J., Bohner, G., Moores, C.A. & Surrey, T. EBs recognize a nucleotide-dependent structural cap at growing microtubule ends. *Cell* **149**, 371–382 (2012).
36. Zhang, R., Alushin, G.M., Brown, A. & Nogales, E. Mechanistic origin of microtubule dynamic instability and its modulation by EB proteins. *Cell* **162**, 849–859 (2015).
37. Maurer, S.P., Bieling, P., Cope, J., Hoenger, A. & Surrey, T. GTPgammaS microtubules mimic the growing microtubule end structure recognized by end-binding proteins (EBs). *Proc. Natl. Acad. Sci. USA* **108**, 3988–3993 (2011).
38. Zanic, M., Stear, J.H., Hyman, A.A. & Howard, J. EB1 recognizes the nucleotide state of tubulin in the microtubule lattice. *PLoS One* **4**, e7585 (2009).
39. Fourniol, F.J. *et al.* Template-free 13-protofilament microtubule-MAP assembly visualized at 8 Å resolution. *J. Cell Biol.* **191**, 463–470 (2010).
40. Bechstedt, S., Lu, K. & Brouhard, G.J. Doublecortin recognizes the longitudinal curvature of the microtubule end and lattice. *Curr. Biol.* **24**, 2366–2375 (2014).
41. Ettinger, A., van Haren, J., Ribeiro, S.A. & Wittmann, T. Doublecortin is excluded from growing microtubule ends and recognizes the GDP-microtubule lattice. *Curr. Biol.* **26**, 1549–1555 (2016).
42. Desai, A., Verma, S., Mitchison, T.J. & Walczak, C.E. Kin I kinesins are microtubule-destabilizing enzymes. *Cell* **96**, 69–78 (1999).
43. Moores, C.A. *et al.* A mechanism for microtubule depolymerization by KinI kinesins. *Mol. Cell* **9**, 903–909 (2002).
44. Alushin, G.M. *et al.* High-resolution microtubule structures reveal the structural transitions in $\alpha\beta$-tubulin upon GTP hydrolysis. *Cell* **157**, 1117–1129 (2014).
45. Tischfield, M.A. & Engle, E.C. Distinct alpha- and beta-tubulin isotypes are required for the positioning, differentiation and survival of neurons: new support for the 'multi-tubulin' hypothesis. *Biosci. Rep.* **30**, 319–330 (2010).
46. Nogales, E. & Zhang, R. Visualizing microtubule structural transitions and interactions with associated proteins. *Curr. Opin. Struct. Biol.* **37**, 90–96 (2016).
47. Atherton, J. *et al.* Conserved mechanisms of microtubule-stimulated ADP release, ATP binding, and force generation in transport kinesins. *eLife* **3**, e03680 (2014).
48. Pettersen, E.F. *et al.* UCSF Chimera: a visualization system for exploratory research and analysis. *J. Comput. Chem.* **25**, 1605–1612 (2004).
49. Davis, I.W., Murray, L.W., Richardson, J.S. & Richardson, D.C. MOLPROBITY: structure validation and all-atom contact analysis for nucleic acids and their complexes. *Nucleic Acids Res.* **32**, W615–W619 (2004).

© 2017 Nature America, Inc., part of Springer Nature. All rights reserved.

© 2017 Nature America, Inc., part of Springer Nature. All rights reserved.

ONLINE METHODS

Sequence analysis. For the detection of CKK homologs, BLASTP/PSI-BLAST[50] and phmmer/jackhmmer[51] searches were performed online across the nr and UniProt databases, respectively, with different sequences used as queries. On the basis of these hits, a multiple sequence alignment was made with MAFFT[52], (v7.149b, option einsi) to make an HMM profile. This profile was used to search for other sequences containing the CKK domain across our own dedicated set of eukaryotic proteomes (**Supplementary Table 1**). The resulting full-length protein sequences can be found in **Supplementary Data Set 1**.

Protein expression and purification for crystallization. The DNA encoding the *Mus musculus* CAMSAP3 CKK core domain (denoted $\text{CKK3}_{\text{core}}$, residues 1121–1239; UniProt Q80VC9) was amplified from the *Mus musculus* CAMSAP3 CKK-domain vector (denoted CKK3) (residues 1112–1252) and cloned into the pET-based bacterial expression vector PSTCm2 (with an N-terminal hexahistidine tag) by positive-selection methods[53]. The CKK3 and the mutants used for biophysics characterization were cloned into the pET28a vector. Protein production was performed in *Escherichia coli* strain BL21(DE3) (Stratagene) in LB medium containing 50 µg/ml kanamycin. When the 1-l cultures had reached an OD_{600} of 0.6 at 37 °C, the medium was cooled to 20 °C, and expression was induced with 1 mM IPTG. Expression was allowed to proceed for 16 h at 20 °C. After cells were harvested and washed with Dulbecco's PBS (Millipore), the cells were sonicated in the presence of cOmplete protease-inhibitor cocktail (Roche) in lysis buffer (50 mM HEPES, pH 8, supplemented with 500 mM NaCl, 10 mM imidazole, 2 mM β-mercaptoethanol and 0.1% bovine DNase I).

Proteins were purified by immobilized metal-affinity chromatography (IMAC) on a HisTrap HP Ni^{2+}–Sepharose column (GE Healthcare) at 4 °C, according to the manufacturer's instructions. The column was equilibrated in IMAC A buffer (50 mM HEPES, pH 8, supplemented with 500 mM NaCl, 10 mM imidazole and 2 mM β-mercaptoethanol). Proteins were eluted with IMAC B buffer containing 400 mM imidazole after being washed with 5% IMAC buffer B. In the case of $\text{CKK3}_{\text{core}}$, the N-terminal histidine tag was cleaved off by an in-house-produced HRV 3C protease in IMAC A buffer for 16 h at 4 °C. The cleaved sample was applied again to the IMAC column to separate cleaved from uncleaved protein.

Proteins were concentrated and loaded on a SEC HiLoad Superdex 75 16/60 column (GE Healthcare) that had been equilibrated in 20 mM Tris-HCl, pH 7.5, supplemented with 150 mM NaCl and 1 mM DTT. The fractions of the main peak were pooled and concentrated to 10 mg/ml. Protein quality and identity were assessed by SDS–PAGE and mass spectrometry, respectively.

Protein expression and purification for cryo-EM. Human CAMSAP1 wild type, N1492A CKK (residues 1474–1613) and mouse CAMSAP3 CKK (residues 1112–1252) were cloned into the pET28a vector. After purification with Ni–NTA resin (Qiagen), proteins were further purified on a MonoS ion-exchange column and a Superose 6 gel-filtration column (GE Healthcare). Purified proteins were concentrated to ~20 mg/ml in BRB20 buffer.

Protein expression and purification for *in vitro* assays. All proteins used for TIRFM (human CAMSAP1 CKK (residues 1474–1613) and $\text{CAMSAP1}_{\text{mini}}$ (residues 1227–1613), fly CKK (residues 1547–1689), worm CKK (residues 982–1128), *T. thermophila* CKK (residues 1635–1770), *T. vaginalis* CKK (residues 650–795), *N. gruberi* CKK (residues 612–788), *P. infestans* CKK (residues 1020–1168), HsMCAK full length and human KIF5B (residues 1–560)) were expressed in HEK293T cells with a modified pTT5 expression vector (Addgene no. 44006 (ref. 54)) bearing Strep-GFP or Strep-SNAP tags at either the N or the C terminus of the protein. The cDNA sequences encoding *T. thermophila*, *T. vaginalis* and *N. gruberi* CKK were codon optimized for human-cell expression and synthesized as gBlocks by IDT. The CKK of *P. infestans* was obtained by PCR from genomic DNA (a gift from F. Govers, Wageningen University). Fly and worm Patronin cDNAs were kindly provided by V. Gelfand (Northwestern University) and M. Harterink (Utrecht University), respectively. In CAMSAP1mini-GFP protein, the GFP tag was inserted directly after the C terminus of the CKK domain and was followed by a short flexible linker ($\text{CAMSAP1}_{1227-1613}$-GGSGGS-GFP)

Cells from one 15-cm dish collected after 36 h transfection were lysed in 900 µl lysis buffer (50 mM HEPES, 300 mM NaCl and 0.5% Triton X-100, pH 7.4) supplemented with protease inhibitors (Roche). After clearing of debris by centrifugation, cell lysates were incubated with 100 µl StrepTactin beads (GE Healthcare) for 45 min. Beads were washed five times with lysis buffer without protease inhibitors and twice with the wash buffer (50 mM HEPES, 150 mM NaCl and 0.01% Triton X-100). The proteins were eluted in 60 µl elution buffer (50 mM HEPES, 150 mM NaCl, 0.01% Triton X-100 and 2.5 mM desthiobiotin).

To label SNAP-tagged proteins with Alexa647 dye (NEB), 20–40 µM dye was incubated with proteins on beads for 1 h between the washing and elution steps. After extensive washing steps, proteins were eluted in elution buffer containing 300 mM instead of 150 mM NaCl.

The HEK293T cell line was obtained from ATCC, was not found in the database of commonly misidentified cell lines maintained by ICLAC and NCBI BioSample, was not authenticated and was negative for mycoplasma contamination.

Total internal reflection fluorescence microscopy (TIRFM). TIRFM was performed on an inverted research microscope Nikon Eclipse Ti-E (Nikon) with the perfect focus system (PFS) (Nikon), equipped with a Nikon CFI Apo TIRF 100× 1.49-NA oil objective (Nikon) and a Photometrics Evolve 512 EMCCD (Roper Scientific) camera, and controlled with MetaMorph 7.7 software (Molecular Devices). Images were projected onto the chip of an Evolve 512 camera with an intermediate 2.5× lens (Nikon C mount adaptor 2.5×). To keep *in vitro* samples at 30 °C, we used an INUBG2E-ZILCS (Tokai Hit) stage-top incubator.

For excitation, we used 491-nm/100-mW Stradus (Vortran), 561-nm/100-mW Jive (Cobolt) and 642-nm/110-mW Stradus (Vortran) lasers. We used an ET-GFP 49002 filter set (Chroma) for imaging proteins tagged with GFP; an ET-mCherry 49008 filter set (Chroma) for imaging X-rhodamine-labeled tubulin or mCherry-EB3; and an ET-405/488/561/647 filter set for imaging SNAP-Alexa647. For simultaneous imaging of green and red fluorescence, we used a triple-band TIRF polychroic filter (ZT405/488/561rpc, Chroma) and triple-band laser emission filter (ZET405/488/561m, Chroma), mounted in the metal cube (91032, Chroma) together with an Optosplit III beamsplitter (Cairn Research) equipped with a double-emission-filter cube configured with ET525/50m, ET630/75m and T585LPXR (Chroma) filters. We used sequential acquisition for triple-color imaging experiments.

***In vitro* MT assays.** The *in vitro* assays with dynamic MTs were performed under the same conditions as described previously[18]. Briefly, after coverslips were functionalized by sequential incubation with 0.2 mg/ml PLL–PEG–biotin (Susos) and 1 mg/ml neutravidin (Invitrogen) in MRB80 buffer, GMPCPP-stabilized MT seeds were attached to the coverslips through biotin–neutravidin interactions. Flow chambers were further blocked with 1 mg/ml ê-casein. The reaction mix with purified proteins (MRB80 buffer supplemented with 20 µM porcine brain tubulin, 0.5 µM X-rhodamine-tubulin, 75 mM KCl, 1 mM GTP, 0.2 mg/ml κ-casein, 0.1% methylcellulose and oxygen scavenger mix (50 mM glucose, 400 µg/ ml glucose oxidase, 200 µg/ml catalase and 4 mM DTT) were added to the flow chamber after centrifugation. The flow chamber was sealed with vacuum grease, and dynamic MTs were imaged immediately at 30 °C with a TIRF microscope.

The conditions for the MT-depolymerization assay were essentially the same as in the assays with dynamic MTs, except that tubulin proteins were not included, and the reaction mix was optimized to image MT depolymerization (MRB80 buffer supplemented with 100 mM KCl, 1 mM GTP, 1 mM ATP, 0.2 mg/ml κ-casein and oxygen scavenger mix). All tubulin products were from Cytoskeleton.

Quantification of the intensity of the wild-type and mutant $\text{CAMSAP1}_{\text{mini}}$ on dynamic MTs. To quantify the minus-end and lattice intensity of $\text{CAMSAP1}_{\text{mini}}$ in a time-lapse movie, kymographs were generated in ImageJ with the KymoResliceWide plug-in. The minus-end positions were marked by 5-pixel-wide linear ROIs corresponding to $\text{CAMSAP1}_{\text{mini}}$ signals. The maximum intensity within the 5-pixel region along the spatial axis of the kymograph was measured with a macro written in ImageJ.

Determination of the CAMSAP1 position on MT ends. To determine the position of $\text{CAMSAP1}_{\text{mini}}$ relative to the MT minus end, we simultaneously imaged $\text{CAMSAP1}_{\text{mini}}$-GFP and X-rhodamine-labeled GMPCPP-stabilized MTs by using a beam splitter. Spatial registration between two channels was performed with a B-spline point-based transform (MathWorks File Exchange: 20057-b-spline-grid--image-and-point-based-registration), by using images of

© 2017 Nature America, Inc., part of Springer Nature. All rights reserved.

a calibration grid featuring 500-nm-diameter transparent circles separated by a 2-μm distance (Compugraphics). To achieve better spatial sampling of the imaging area, an image with a 'denser' grid was obtained by moving the stage eight times with a step of 0.25 μm in both *x* and *y* directions during calibration. After channel registration, we extracted 1D intensity profiles along the MT axis for both CAMSAP1$_{\mathrm{mini}}$ and MT channels. The profiles were fitted to the models previously used for XMAP215 and MT ends[28]. Briefly, the MT-end axis profile was modeled as an error function, which was the result of convolution between the step function representing the density of tubulin-molecule distribution in an MT and a Gaussian representing the optical point-spread function (PSF) of the microscope. The CAMSAP1$_{\mathrm{mini}}$ axis profile was modeled as the combination of a Gaussian peak (representing convoluted point-like accumulation at the edge of the minus end) and an error function (accounting for its weak lattice binding) with different weights. The PSF-size estimation (GFP channel, 108 nm; X-rhodamine channel, 125 nm) was obtained from two-color images of 100-nm diameter fluorescence beads (TetraSpeck, Invitrogen).

The overall displacement error between point images in two channels after registration was estimated to be ~2 nm, on the basis of acquiring an extra set of calibration-grid images and calculating the average distance between corresponding spots in two channels after registration. The average error of fitting for the position parameters was approximately 5 nm and 6 nm for CAMSAP1 (peak position) and MT (edge position), respectively. Thus, according to the propagation of uncertainty, the estimated error of a distance between the peak of the CAMSAP1 distribution and the edge of the MT minus end is approximately $\sqrt{2^2 + 5^2 + 6^2} \approx 8$ nm.

Structure determination of the CAMSAP3 CKK domain. CKK3$_{\mathrm{core}}$ was concentrated to 14 mg/ml, and TCEP to a final concentration of 5 mM was added. The screening of crystallization conditions was performed with a Mosquito robot (TTP Labtech) in 96-well plates by using the hanging-drop vapor-diffusion method. In drops of a 1:1 (200 nl each) mixture of CKK3$_{\mathrm{core}}$ and mother liquor (100 mM citric acid, pH 5, and 1 M NaCl), crystals with a diameter of 100 μm appeared after 1 week. The crystals were cryoprotected by transfer into mother liquor supplemented with 10% glycerol and were flash frozen in liquid nitrogen.

Diffraction data were collected at the X06DA macromolecular crystallography beamline at the Swiss Light Source (Paul Scherrer Institut) at a wavelength of 1 Å. The data were indexed with LABELIT[55], refined and integrated in XDS[56]. The structure was solved by molecular replacement with PHASER[57] with the available NMR structure (PDB 1UGJ) as a search model. Several rounds of manual model building in COOT[58] and refinement in PHENIX.refine[59] and REFMAC5 (ref. 60) produced a final model with satisfactory $R_{\mathrm{work}}/R_{\mathrm{free}}$. The structure was validated with MolProbity and the wwPDB Validation Service. The MolProbity validation indicated zero Ramachandran outliers, 98.1% Ramachandran favored residues, zero rotamer outliers and a clashscore of 0.56. Data collection and refinement statistics are shown in **Table 1**. Figures were created with PyMOL[61].

Circular dichroism (CD) spectroscopy. CD spectra of CKK3 and derived mutants were recorded on a Chirascan-Plus CD instrument (Applied Photophysics) equipped with a computer-controlled Peltier element, with a cuvette with a 1-mm optical path length. 0.25 mg/ml of protein sample was applied in PBS buffer. Thermal unfolding profiles were measured at 206 nm by continuous heating at 1 °C min^{-1}.

MT pelleting assays. MT pelleting assays of purified proteins were performed as previously described[62]. Briefly, 10 mg/ml bovine brain tubulin was diluted in 1× BRB35 buffer (35 mM K-PIPES, pH 6.8, supplemented with 1 mM EGTA, 1 mM $MgCl_2$ and 1 mM DTT) to 1 mg/ml. After the addition of 0.5 mM GTP, the sample was incubated on ice for 5 min. MT polymerization was started by transfer to 37 °C. After 10 min, 0.1 μM, 1 μM and 10 μM paclitaxel were added stepwise with incubation times of 5 min each. Pelleting assays in the presence of CAMSAP3 CKK were performed by mixing 3.8 μM of taxol-stabilized MTs with an equimolar ratio of the CAMSAP3 CKK in the presence of different sodium chloride concentrations. As control treatments, taxol-stabilized MTs or CAMSAP3 CKK was applied alone. Samples were applied onto a taxol–glycerol cushion that contained 55% 2× BRB35, 44% glycerol and 6% 2 mM paclitaxel. After centrifugation at 174,500*g* for 30 min at 25 °C, an aliquot was taken from the supernatant. After removal of the supernatant, the pellet was resuspended in SDS sample buffer. Samples were loaded and analyzed on Coomassie-stained 15% SDS gels.

Cryo-EM. Single-particle cryo-EM data for MT–CAMSAP3 CKK-domain complexes were collected on a Tecnai G2 Polara (FEI) instrument, and data for MT–CAMSAP1 CKK-domain complexes were collected on a Tecnai F20 (FEI) instrument, both with a DE20 direct electron detector (Direct Electron). Data for MT–CAMSAP1 N1492A mutant CKK-domain complexes were collected on a Tecnai G2 Polara with a K2 direct electron detector (Gatan) operating in counting mode. Cryo-ET single-axis tilt series of MT ends were collected on a Tecnai G2 Polara with a K2 Summit direct electron detector (Gatan) operated in counting mode. MTs for single-particle reconstruction were boxed manually and were input to a set of custom-designed semiautomated single-particle-processing scripts with Spider and Frealign, as described previously[63,64]. Additional details are provided in the **Supplementary Note**. The final data-set sizes and resolutions are reported in **Table 2**. For the cryo-ET data, tilt series were processed, and tomograms were generated with IMOD's Etomo graphical user interface (v4.7.15).

CKK domain–MT pseudoatomic-model building. The X-ray structure of the CAMSAP3 CKK domain (PDB 5LZN) was rigidly fitted into the CKK-domain density of the CAMSAP3 CKK-domain map with UCSF Chimera's 'fit in map' tool. A homology model of CAMSAP1 CKK (residues 1474–1600) was generated in MODELLER[65], with the CAMSAP3 CKK crystal structure used as the template. To model missing loops and terminal regions for both CKKs, the previously deposited NMR structure of the CAMSAP3 CKK domain (PDB 1UGJ) was used as a template. CKK models were selected on the basis of MODELLER's statistical potential score, zDOPE[66]. The model of CAMSAP1 CKK was rigidly fitted into its density map, and for both CKKs, the local fits of secondary-structural elements and loops were scored with a local correlation score with TEMPy (SCCC)[67]. Loop regions that had low SCCC scores were further optimized. For each of these loops, 200 loop models were generated with MODELLER's loop-optimization protocol[68] and a top-scoring conformation (based on SCCC) was selected. To create the N1492A CAMSAP1 CKK model, point mutation of the wild-type CAMSAP1 model was performed in Coot[69], and the N1492A-mutant model was rigidly fitted into the corresponding mutant's CKK density.

Final CKK fits were combined with rigid fits (with Chimera's 'fit in map' tool) of two tubulin dimers from the structure of the paclitaxel-stabilized MT[44] (PDB 3J6G). The rigid-fitted models were already a good fit to the experimental density; therefore, the models were subjected to final refinement to their *B*-factor-sharpening resolutions (**Table 2**) with NCS restraints, with the phenix.real_space_refine tool in Phenix[70], to resolve clashes and improve model geometry.

Molecular dynamics simulations. 4,000 cycles of energy minimization without any positional restraints were performed on the refined structural complexes. Two consecutive molecular dynamics simulation runs of 10 ps and 200 ps were then used to increase the temperature from 100 K to 300 K and to equilibrate the systems at 300 K. Four replicate production runs of 40 ns each were then performed starting from the equilibrated system configurations. The simulations were run at constant temperature (300 K) and constant pressure (1 atm) with a 2-fs time step. Periodic boundary conditions and full particle-mesh Ewald electrostatics were used. A 12-Å cutoff value was applied to truncate the nonbonded interactions. The SHAKE algorithm was used to constrain the covalent bonds formed by hydrogen atoms. Each replicate simulation was run with different random starting velocities. All calculations were performed with the AMBER 12 package[71].

MM/GBSA calculations. Molecular mechanics with generalized Born and surface-area solvation (MM/GBSA) calculations were performed with the GB$^{\mathrm{OBC}}$ model in AMBER 12 (ref. 71). For each molecular dynamics simulation, pairwise energetic-interaction values (flag idecomp = 4) were scaled by the average number of CKK domain – tubulin dimers contacts (51 contacts) and averaged over four replica simulations.

NMR sample preparation and experiments. Uniformly ^{13}C-^{15}N-labeled variants of CKK were produced in *E. coli* strain Rosetta 2 in M9 minimum medium containing 25 μg/ml kanamycin and 35 μg/ml chloramphenicol. The cells were induced with 0.3 mM IPTG at 25 °C overnight after the OD_{600} reached 0.6. Proteins were purified as described above with phosphate buffer instead of HEPES buffer. After purification, proteins were loaded onto a SEC HiLoad

Superdex 75 26/60 column (GE Healthcare), which was equilibrated in 40 mM phosphate buffer with 150 mM NaCl and 1 mM DTT, pH 7.0. Proteins were then concentrated and used for solution-state NMR measurements with 5% D_2O supplementation or for ssNMR sample preparation.

For ssNMR experiments, [^{13}C,^{15}N]CAMSAP3 CKK–MT complexes were prepared. 20 mg of lyophilized tubulin was first dissolved in BRB80 buffer to a final concentration of 2 mg/ml. Tubulin was then polymerized with the addition of 20 μM paclitaxel for 30 min at 37 °C. Paclitaxel-stabilized MTs were centrifuged at 55,000 r.p.m. (Beckman TLA-55 rotor) at 30 °C for 30 min. The pellet was resuspended in warm BRB80 buffer, and labeled CKK domain was added to a final concentration of 65.3 μM (4:1 CKK/tubulin). The mixture was incubated at 37 °C for 30 min and then centrifuged at 55,000 r.p.m. (Beckman TLA-55 rotor) at 30 °C for 30 min. The pellet was washed with phosphate buffer without disturbing the pellet. Finally, the pellet was transferred and packed into a 3.2-mm rotor.

Resonance assignments were obtained from previous results (PDB 1UGJ), and additional solution-state NMR experiments on free CKK were recorded on a 600-MHz spectrometer (Bruker Biospin) to assign missing residues (2D HSQCs, 3D HNCA, HNCO, HNCACB, CBCA(CO)NH, HAHB(CO)NH and hCCH-DIPSI). ssNMR experiments involved 2D NCA and CC proton-driven spin-diffusion (PDSD) experiments (temperature 260 K, MAS rate 14 kHz) as well as additional 2Q–1Q experiments (temperature 268 K, MAS 10 kHz). Mixing schemes used SPECIFIC-CP transfers[72] as well as SPC5 (ref. 73) and spin diffusion under weak coupling conditions[74] for longer PDSD mixing times. Data were recorded on a 950-MHz standard-bore spectrometer (Bruker Biospin) equipped with a 3.2-mm triple-channel MAS HCN probe. ssNMR data were analyzed by using NMR assignments obtained on free CKK as a reference. Resolved residues whose signal matched with ssNMR data within 0.5 p.p.m. in ^{13}C and 1 p.p.m. in ^{15}N dimensions[75] were considered unperturbed, whereas resolved residues whose signals matched with ssNMR data within 1 p.p.m. in the indirect dimension and 0.5 p.p.m. in the direct dimension in the CC PDSD experiments were considered unperturbed. Larger deviations were considered altered and are indicated in red.

Analysis of CKK-domain binding to subtilisin-treated MTs. Paclitaxel-stabilized MTs containing 10% rhodamine tubulin, 10% biotinylated tubulin, and 80% unlabeled tubulin (Cytoskeleton) were prepared and then treated with 0.1 mg/ml subtilisin for 30 min to remove predominantly β-tubulin C-terminal tails (CTTs), as verified by western blotting. The reaction was stopped by the addition of 10 mM pefabloc, and MTs were isolated by centrifugation. GFP-CKK-domain binding was analyzed by TIRFM, using flow chambers assembled from plasma-cleaned glass coverslips and microscope slides. Chambers were incubated sequentially with 1 mg/ml PLL–PEG–biotin (Susos), blocking solution (1% plurionic F-127, 4 mg/ml casein), 0.5 mg/ml neutravidin, and MTs with or without CTTs (as indicated). Each incubation was followed by two washes with MRB80 buffer (80 mM PIPES, 4 mM $MgCl_2$ and 1 mM EGTA, pH 6.8) supplemented with 80 mM KCl, 20 μM paclitaxel, 4 mM DTT and 2 mg/ml casein. The final binding reaction contained 200 nM CKK-GFP in MRB80 with 80 mM KCl, 20 μM taxol, 4 mM DTT and 2 mg/ml casein and an oxygen-scavenger mix (400 μg/ml glucose oxidase and 200 μg/ml catalase). TIRFM was performed on an Eclipse Ti-E inverted microscope with a Perfect Focus System, CFI Apo TIRF 1.49-NA oil objective, H-TIRF module and LU-N4 laser unit (Nikon). Images were recorded with 100-ms exposure on an iXon DU888 Ultra EMCCD camera (Andor) controlled with NIS-Elements AR Software (Nikon).

Statistics and reproducibility. The Mann–Whitney *U*-test *P* values were calculated in Matlab (MathWorks). All data shown are mean ± s.d. The sample size is indicated in the figure legends. All data presented in this study were either averages or representative data from at least two independent experiments. For the ssNMR experiments, all spectra were recorded twice on one sample and yielded consistent results. The sample was not altered by measurement of the 1D H–C CP over time.

Code availability. Computer codes used in this study are available from the corresponding authors on request.

Data availability. The structure of CKK3$_{core}$ has been deposited in the Protein Data Bank (PDB) under accession code PDB 5LZN. The CKK–MT models along with their corresponding electron density maps have been deposited in the PDB and Electron Microscopy Data Bank, respectively: CAMSAP1 CKK–MT, PDB 5M54 and EMD-4156; CAMSAP1 N1492A CKK–MT, PDB 5M5C and EMD-3444; and CAMSAP3 CKK–MT, PDB 5M50 and EMD-4154). NMR data have been deposited in the Biological Magnetic Resonance Bank under entry ID 27234. Source data for graphs in **Figures 1** and **3**–**6** and **Supplementary Figures 1**, **4** and **7**–**9** can be found in **Supplementary Table 2**. All data that support the conclusions are available from the authors on request, and/or available in the article itself. A **Life Sciences Reporting Summary** for this paper is available.

50. Altschul, S.F. *et al.* Gapped BLAST and PSI-BLAST: a new generation of protein database search programs. *Nucleic Acids Res.* **25**, 3389–3402 (1997).
51. Finn, R.D. *et al.* HMMER web server: 2015 update. *Nucleic Acids Res.* **43**, W1, W30–W38 (2015).
52. Katoh, K., Misawa, K., Kuma, K. & Miyata, T. MAFFT: a novel method for rapid multiple sequence alignment based on fast Fourier transform. *Nucleic Acids Res.* **30**, 3059–3066 (2002).
53. Olieric, N. *et al.* Automated seamless DNA co-transformation cloning with direct expression vectors applying positive or negative insert selection. *BMC Biotechnol.* **10**, 56 (2010).
54. Scholz, J., Besir, H., Strasser, C. & Suppmann, S. A new method to customize protein expression vectors for fast, efficient and background free parallel cloning. *BMC Biotechnol.* **13**, 12 (2013).
55. Sauter, N.K., Grosse-Kunstleve, R.W. & Adams, P.D. Robust indexing for automatic data collection. *J. Appl. Crystallogr.* **37**, 399–409 (2004).
56. Kabsch, W. Automatic processing of rotation diffraction data from crystals of initially unknown symmetry and cell constants. *J. Appl. Crystallogr.* **26**, 795–800 (1993).
57. McCoy, A.J. *et al.* Phaser crystallographic software. *J. Appl. Crystallogr.* **40**, 658–674 (2007).
58. Emsley, P., Lohkamp, B., Scott, W.G. & Cowtan, K. Features and development of Coot. *Acta Crystallogr. D Biol. Crystallogr.* **66**, 486–501 (2010).
59. Adams, P.D. *et al.* PHENIX: building new software for automated crystallographic structure determination. *Acta Crystallogr. D Biol. Crystallogr.* **58**, 1948–1954 (2002).
60. Vagin, A.A. *et al.* REFMAC5 dictionary: organization of prior chemical knowledge and guidelines for its use. *Acta Crystallogr. D Biol. Crystallogr.* **60**, 2184–2195 (2004).
61. DeLano, W.L. *The PyMOL Molecular Graphics System* (DeLano Scientific, 2002).
62. Lansbergen, G. *et al.* Conformational changes in CLIP-170 regulate its binding to microtubules and dynactin localization. *J. Cell Biol.* **166**, 1003–1014 (2004).
63. Sindelar, C.V. & Downing, K.H. The beginning of kinesin's force-generating cycle visualized at 9-A resolution. *J. Cell Biol.* **177**, 377–385 (2007).
64. Sindelar, C.V. & Downing, K.H. An atomic-level mechanism for activation of the kinesin molecular motors. *Proc. Natl. Acad. Sci. USA* **107**, 4111–4116 (2010).
65. Sali, A. & Blundell, T.L. Comparative protein modelling by satisfaction of spatial restraints. *J. Mol. Biol.* **234**, 779–815 (1993).
66. Kremer, J.R., Mastronarde, D.N. & McIntosh, J.R. Computer visualization of three-dimensional image data using IMOD. *J. Struct. Biol.* **116**, 71–76 (1996).
67. Farabella, I. *et al.* TEMPy: a Python library for assessment of three-dimensional electron microscopy density fits. *J. Appl. Crystallogr.* **48**, 1314–1323 (2015).
68. Fiser, A., Do, R.K. & Sali, A. Modeling of loops in protein structures. *Protein Sci.* **9**, 1753–1773 (2000).
69. Emsley, P. & Cowtan, K. Coot: model-building tools for molecular graphics. *Acta Crystallogr. D Biol. Crystallogr.* **60**, 2126–2132 (2004).
70. Afonine, P.V., Headd, J.J., Terwilliger, T.C. & Adams, P.D. New tool: phenix.real_space_refine. *Comput. Crystallogr. Newsl.* **4**, 43–44 (2013).
71. Case, D.A. *et al. AMBER 12* (University of California, San Francisco, 2012).
72. Baldus, M., Petkova, A.T., Herzfeld, J. & Griffin, R.G. Cross polarization in the tilted frame: assignment and spectral simplification in heteronuclear spin systems. *Mol. Phys.* **95**, 1197–1207 (1998).
73. Hohwy, M., Rienstra, C.M., Jaroniec, C.P. & Griffin, R.G. Fivefold symmetric homonuclear dipolar recoupling in rotating solids: application to double quantum spectroscopy. *J. Chem. Phys.* **110**, 7983–7992 (1999).
74. Seidel, K. *et al.* Protein solid-state NMR resonance assignments from (C-13, C-13) correlation spectroscopy. *Phys. Chem. Chem. Phys.* **6**, 5090–5093 (2004).
75. Seidel, K., Etzkorn, M., Schneider, R., Ader, C. & Baldus, M. Comparative analysis of NMR chemical shift predictions for proteins in the solid phase. *Solid State Nucl. Magn. Reson.* **35**, 235–242 (2009).

© 2017 Nature America, Inc., part of Springer Nature. All rights reserved.

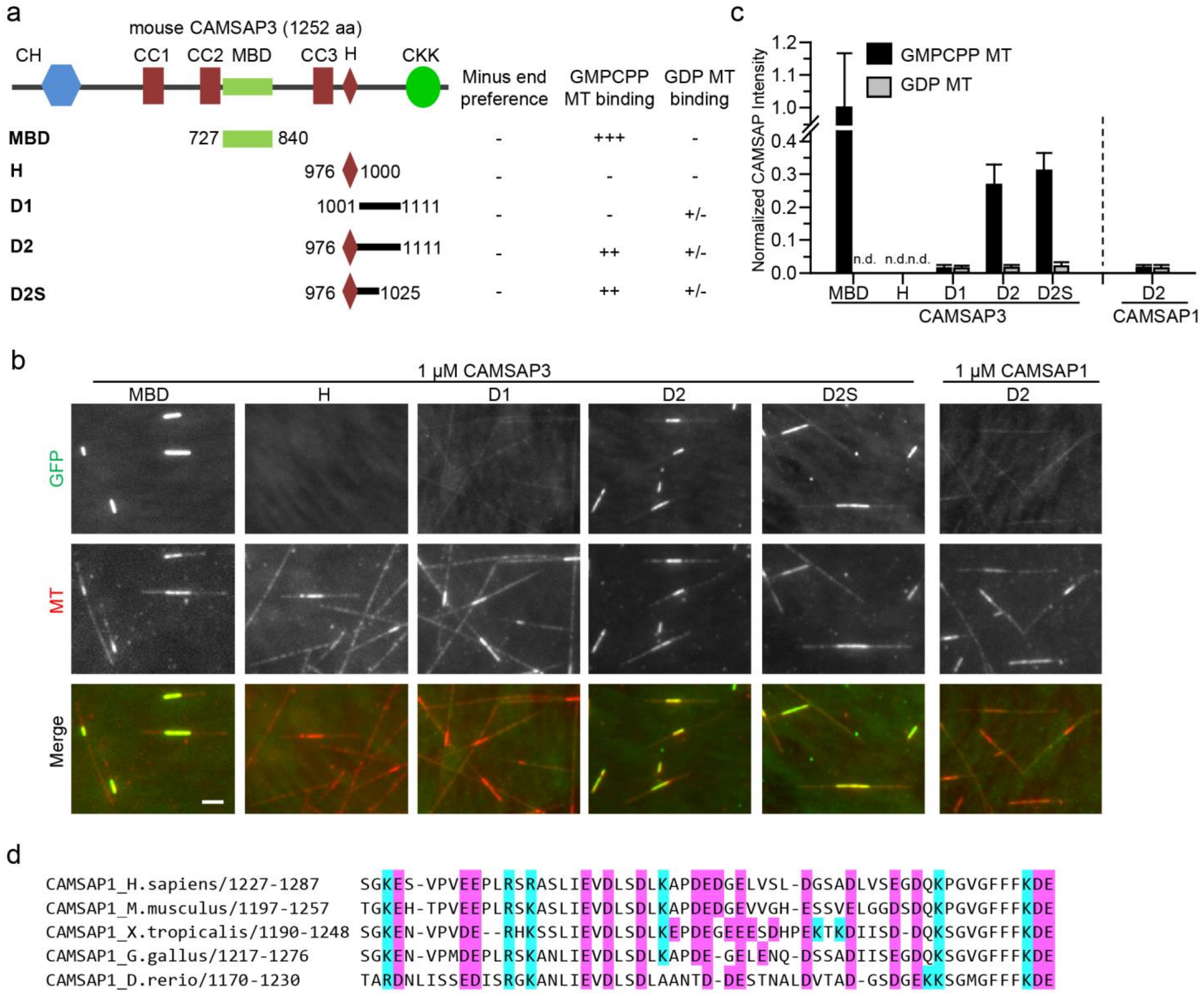

Supplementary Figure 1

C-terminal domains of CAMSAP3 do not confer MT minus-end specificity.

(a) Schematic of the CAMSAP3 domain organization and the constructs used.

(b,c) TIRFM images and quantification of the binding of GFP-CAMSAP3 fragments to GMPCPP-stabilized MTs and dynamic GDP-MTs; values for GFP- CAMSAP1-D2 quantified in the same way are shown for comparison. The intensity is normalized to the average intensity of MBD on GMPCPP MTs. Scale bar, 2 µm.

(d) Sequence alignment of the linker region located upstream of the third coiled-coil in vertebrate CAMSAP1. Negatively and positively charged residues are highlighted in purple and cyan, respectively.

See also Supplementary Table 2.

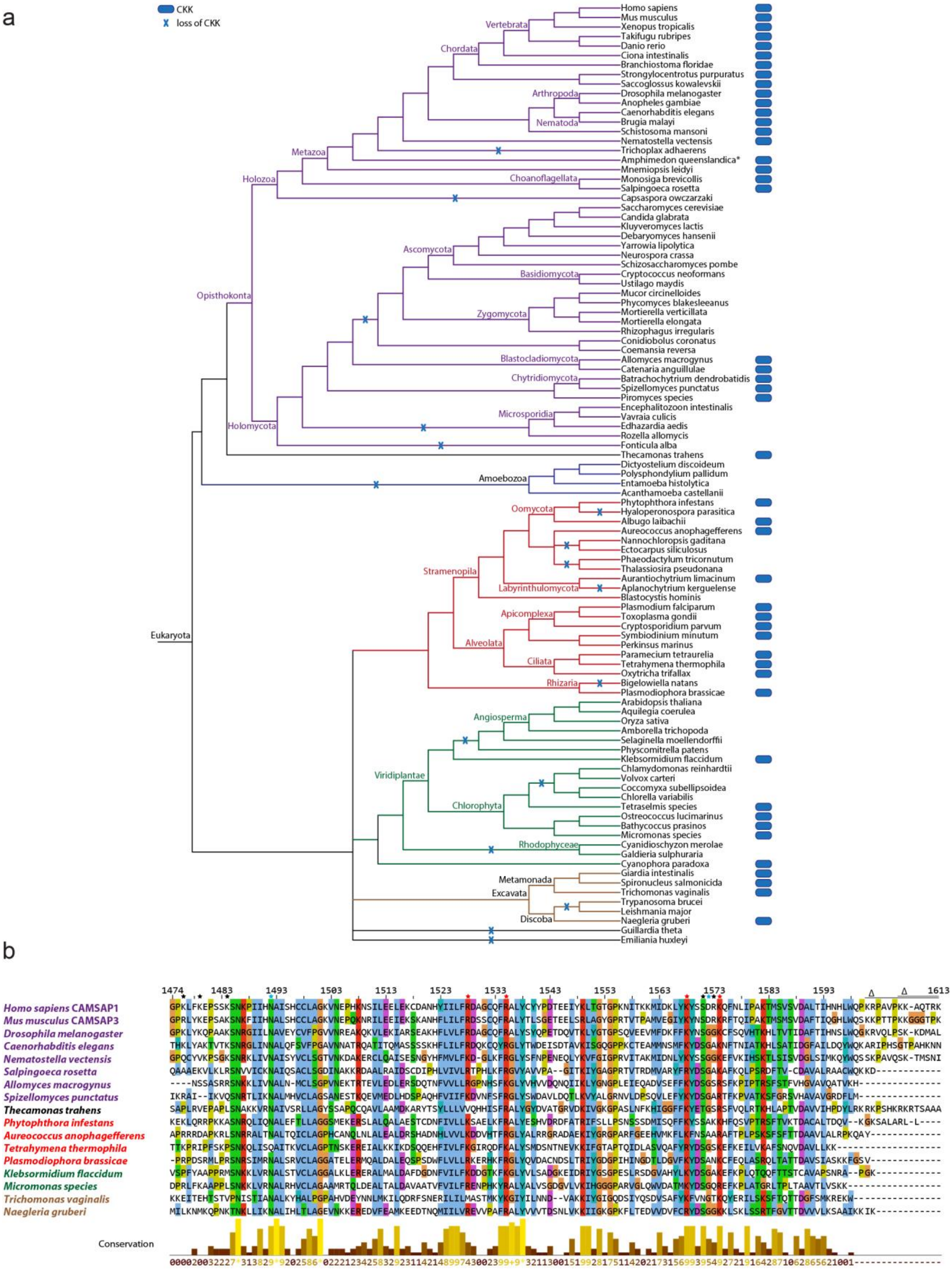a
CKK
loss of CKK
Eukaryota
Opisthokonta
Holozoa
Metazoa
Chordata
Vertebrata
Arthropoda
Nematoda
Choanoflagellata
Holomycota
Ascomycota
Basidiomycota
Zygomycota
Blastocladiomycota
Chytridiomycota
Microsporidia
Amoebozoa
Stramenopila
Oomycota
Labyrinthulomycota
Alveolata
Apicomplexa
Ciliata
Rhizaria
Viridiplantae
Angiosperma
Chlorophyta
Rhodophyceae
Excavata
Metamonada
Discoba
Homo sapiens
Mus musculus
Xenopus tropicalis
Takifugu rubripes
Danio rerio
Ciona intestinalis
Branchiostoma floridae
Strongylocentrotus purpuratus
Saccoglossus kowalevskii
Drosophila melanogaster
Anopheles gambiae
Caenorhabditis elegans
Brugia malayi
Schistosoma mansoni
Nematostella vectensis
Trichoplax adhaerens
Amphimedon queenslandica*
Mnemiopsis leidyi
Monosiga brevicollis
Salpingoeca rosetta
Capsaspora owczarzaki
Saccharomyces cerevisiae
Candida glabrata
Kluyveromyces lactis
Debaryomyces hansenii
Yarrowia lipolytica
Neurospora crassa
Schizosaccharomyces pombe
Cryptococcus neoformans
Ustilago maydis
Mucor circinelloides
Phycomyces blakesleeanus
Mortierella verticillata
Mortierella elongata
Rhizophagus irregularis
Conidiobolus coronatus
Coemansia reversa
Allomyces macrogynus
Catenaria anguillulae
Batrachochytrium dendrobatidis
Spizellomyces punctatus
Piromyces species
Encephalitozoon intestinalis
Vavraia culicis
Edhazardia aedis
Rozella allomycis
Fonticula alba
Thecamonas trahens
Dictyostelium discoideum
Polysphondylium pallidum
Entamoeba histolytica
Acanthamoeba castellanii
Phytophthora infestans
Hyaloperonospora parasitica
Albugo laibachii
Aureococcus anophagefferens
Nannochloropsis gaditana
Ectocarpus siliculosus
Phaeodactylum tricornutum
Thalassiosira pseudonana
Aurantiochytrium limacinum
Aplanochytrium kerguelense
Blastocystis hominis
Plasmodium falciparum
Toxoplasma gondii
Cryptosporidium parvum
Symbiodinium minutum
Perkinsus marinus
Paramecium tetraurelia
Tetrahymena thermophila
Oxytricha trifallax
Bigelowiella natans
Plasmodiophora brassicae
Arabidopsis thaliana
Aquilegia coerulea
Oryza sativa
Amborella trichopoda
Selaginella moellendorffii
Physcomitrella patens
Klebsormidium flaccidum
Chlamydomonas reinhardtii
Volvox carteri
Coccomyxa subellipsoidea
Chlorella variabilis
Tetraselmis species
Ostreococcus lucimarinus
Bathycoccus prasinos
Micromonas species
Cyanidioschyzon merolae
Galdieria sulphuraria
Cyanophora paradoxa
Giardia intestinalis
Spironucleus salmonicida
Trichomonas vaginalis
Trypanosoma brucei
Leishmania major
Naegleria gruberi
Guillardia theta
Emiliania huxleyi
b
1474
1483
1493
1503
1513
1523
1533
1543
1553
1563
1573
1583
1593
1613
Homo sapiens CAMSAP1
Mus musculus CAMSAP3
Drosophila melanogaster
Caenorhabditis elegans
Nematostella vectensis
Salpingoeca rosetta
Allomyces macrogynus
Spizellomyces punctatus
Thecamonas trahens
Phytophthora infestans
Aureococcus anophagefferens
Tetrahymena thermophila
Plasmodiophora brassicae
Klebsormidium flaccidum
Micromonas species
Trichomonas vaginalis
Naegleria gruberi
Conservation

Supplementary Figure 2

The CKK is a highly conserved MT minus-end-tracking domain.

(a) The presence of CKK in extant eukaryotic lineages and its evolutionary history since LECA. The CKK domain can be found in four out of five eukaryotic supergroups: Eukaryotic supergroups are indicated by colored branches (Opisthokonta: purple, Amoebozoa: blue, Stramenopila-Alveolata-Rhizaria (SAR): red, Archaeplastida: green, Excavata: brown). Species tree depicting all species comprising our eukaryotic proteome database and the presences of the CKK domain as well as its inferred losses. The presence of CKK in LECA and indicated subsequent loss events were inferred according to Dollo parsimony, which allows for only a single invention. Asterisk: sequence derived from NCBI. Note that in the oomycetes, the loss of CKK domain seems relatively recent, because *Phytophthora infestans* and *Albugo laibachii* contain CKK, but downy mildew *Hyaloperonospora parasitica* lacks it.

(b) Multiple sequence alignment of the CKK domain in a subset of the species in (a). The supergroups to which the species encoding these sequences belong are indicated by the name colors as in (a). The numbering of amino acids is based on human CAMSAP1 sequence. The colored asterisks indicate the amino acids, which, when mutated to alanine, alter the CAMSAP1$_{mini}$ signal at MT minus ends compared to wild type protein; red asterisk, signal reduced to less than 25%; black asterisk, signal reduced to 25-75%; cyan asterisk, signal increased above 100%.

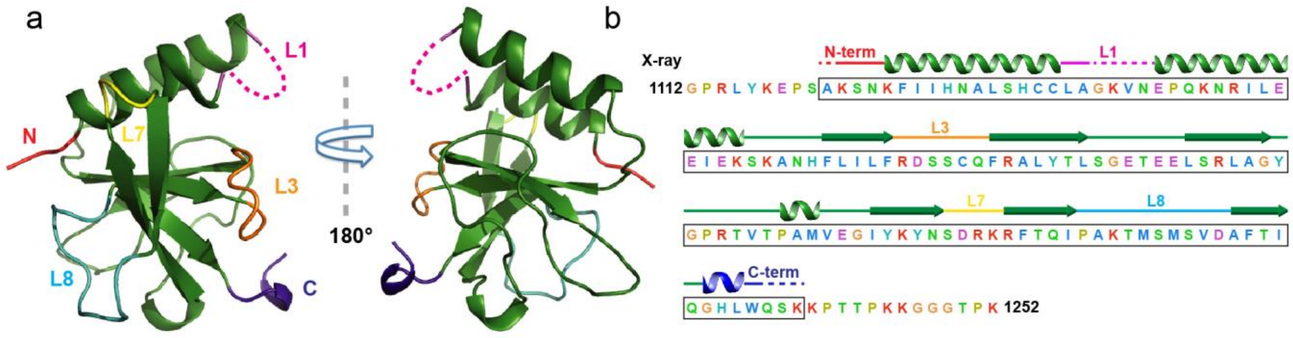
a
L1
N
L7
L3
L8
C
180°
b
X-ray
N-term
L1
1112 GPRLYKEPSAKSNKFIIHNALSHCCLAGKVNEPQKNRILE
L3
EIEKSKANHFLILFRDSSCQFRALYTLSGETEELSRLAGY
L7
L8
GPRTVTPAMVEGIYKYNSDRKRFTQIPAKTMSMSVDAFTI
C-term
QGHLWQSKKPTTPKKGGGTPK 1252

Supplementary Figure 3

The X-ray crystal structure of the mouse CAMSAP3 CKK domain.

(a) Two views 180° apart of the ribbon representation of the *M. musculus* CAMSAP3 CKK domain crystal structure. Key loops as well as the N- and C-termini of the domain are labeled.

(b) The *M. musculus* CAMSAP3 CKK sequence, colored according to side chain property, is shown, with overlying secondary structure based on our crystal structure. The boxed region indicates the construct used for X-ray crystallography. Secondary structure estimations deduced by X-ray crystallography are indicated above, color coded consistent with the scheme in panel a, with unsolved regions indicated with dashed lines.

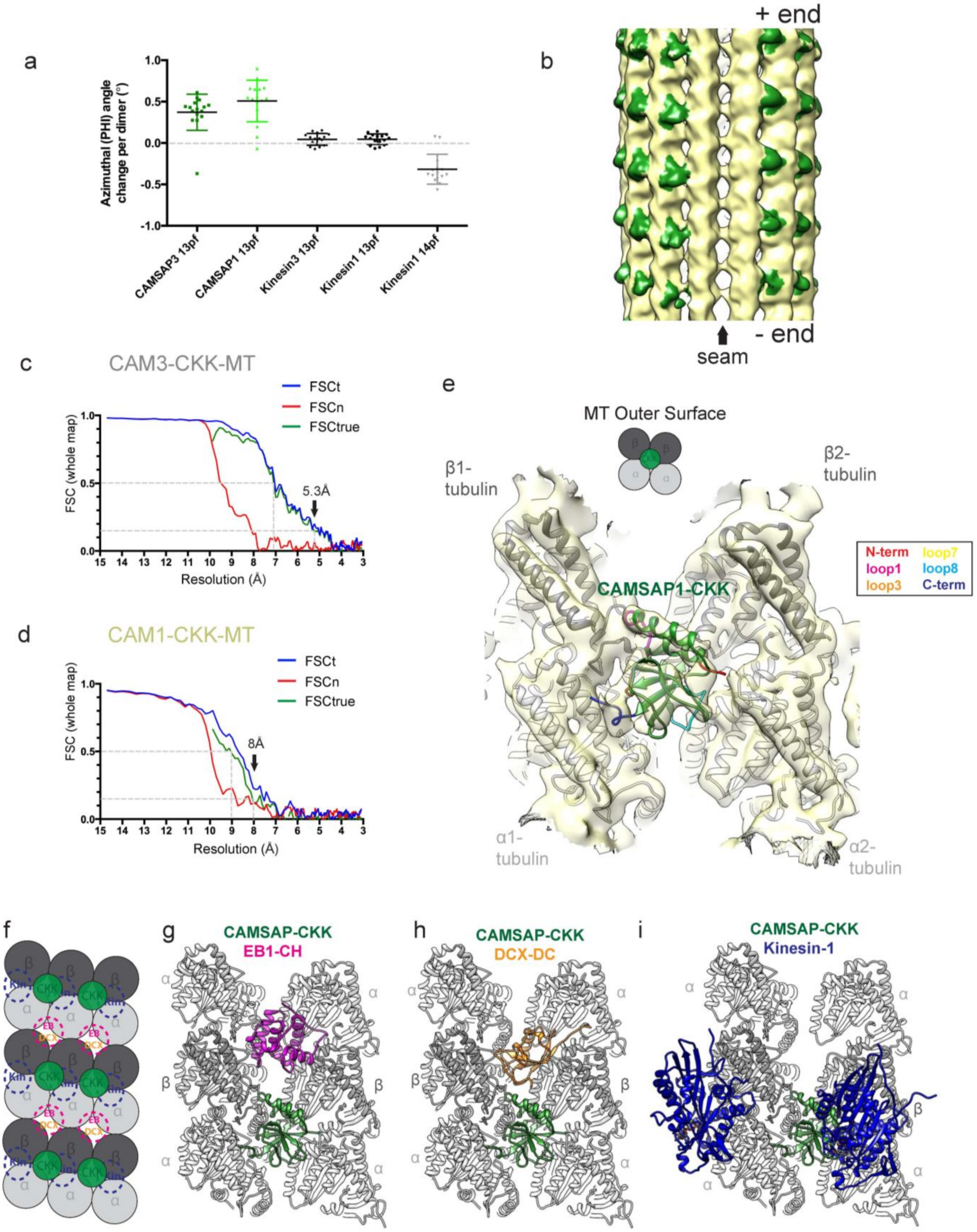
a
Azimuthal (PHI) angle change per dimer (°)
1.0
0.5
0.0
-0.5
-1.0
CAMSAP3 13pf
CAMSAP1 13pf
Kinesin3 13pf
Kinesin1 13pf
Kinesin1 14pf
b
+ end
- end
seam
c
CAM3-CKK-MT
FSCt
FSCn
FSCtrue
FSC (whole map)
1.0
0.5
0.0
5.3Å
15 14 13 12 11 10 9 8 7 6 5 4 3
Resolution (Å)
d
CAM1-CKK-MT
FSCt
FSCn
FSCtrue
FSC (whole map)
1.0
0.5
0.0
8Å
15 14 13 12 11 10 9 8 7 6 5 4 3
Resolution (Å)
e
MT Outer Surface
β
β
α
α
β1-
tubulin
β2-
tubulin
CAMSAP1-CKK
N-term
loop1
loop3
loop7
loop8
C-term
α1-
tubulin
α2-
tubulin
f
β
α
CKK
Kin
EB
DCX
g
CAMSAP-CKK
EB1-CH
α
β
h
CAMSAP-CKK
DCX-DC
α
β
i
CAMSAP-CKK
Kinesin-1
α
β

Supplementary Figure 4

Evaluation of the resolution of CAMSAP–CKK MT reconstructions, conservation of the CKK binding site in CAMSAP1 and comparison of the CKK binding site with those of other MAPs and MT motors.

(a) Protofilament skew for 16 representative MTs from each dataset is depicted by plotting the average rotation angle around the MT axis (PHI) change per dimer moving axially towards the MT plus-end. CAMSAP CKK-decorated MTs are compared to control kinesin decorated paclitaxel-stabilized MTs (datasets from Atherton, J. *et al., eLife* **3**, e03680 ,2014). that show no skew for 13 pfs and a left-handed (negative) skew for 14pfs. PHI angles were determined in Frealign (Grigorieff, N., *Journal of structural biology* **157**, 117-125, 2007). CAMSAP CKK decorated 13pf MTs show right-handed (positive) skew, while control 13pf kinesin decorated MTs show little or no skew. In contrast, control 14pf kinesin decorated MTs show left-handed (negative) skew as expected (Chretien, D. & Wade, R.H., *Biology of the cell / under the auspices of the European Cell Biology Organization* **71**, 161-174, 1991). n=16 MTs per condition. Data represent mean ± SD. CAMSAP-3 13pf vs CAMSAP-1 13pf not significant, one-way ANOVA with Tukey's multiple comparison test. CAMSAP-3 13pf vs kinesin-3 13pf, $p<0.0001$. CAMSAP-3 13pf vs kinesin-1 13pf, $p<0.0001$. CAMSAP-1 13pf vs kinesin-3 13pf, $p<0.0001$. CAMSAP-1 13pf vs kinesin-1 13pf, $p<0.0001$.

(b) The asymmetric reconstruction of the CAMSAP1-CKK decorated 13pf taxol-stabilized MT low-pass filtered to 15Å resolution shows extra densities (green) every 8 nm corresponding to the CAMSAP1-CKK domain, which are absent at the seam (arrow).

(c, d) Fourier shell correlation (FSC) curves utilizing the gold-standard noise substitution method (Chen, S. *et al., Ultramicroscopy* **135**, 24-35, 2013) give an overall resolution estimate for the (c) CAMSAP3-CKK-MT reconstruction of 5.3Å and (d) CAMSAP1-CKK-MT reconstruction of 8Å.

(e) The averaged reconstruction of the CAMSAP1-CKK domain viewed from the MT surface contacting two β-tubulins and two α-tubulins at the intra-dimer, inter-protofilament interface. The CAMSAP-1 CKK is colored as in the CAMSAP3-CKK. α-tubulin is shown in light grey and β-tubulin is shown in dark grey. Above, schematic.

(f-i) Schematic depiction of the CKK binding site compared to other known MT binding partners, and structural models of (g) CAMSAP-CKK and EB1-CH domain (based on PDB ID 3JAK, *Zhang et al.,* E. *Cell* **162**, 849-859, 2015) (h) CAMSAP-CKK and DCX-DC domain (same binding site as EB, based on PDB ID 2XRP, Fourniol, F.J. *et al.*, *The Journal of cell biology* **191**, 463-470, 2010) and (i) CAMSAP-CKKs and kinesin-1 motor domain (based on PDB ID 4UY0, Atherton, J. *et al., eLife* **3**, e03680 ,2014, note steric overlap).

See also Supplementary Table 2.

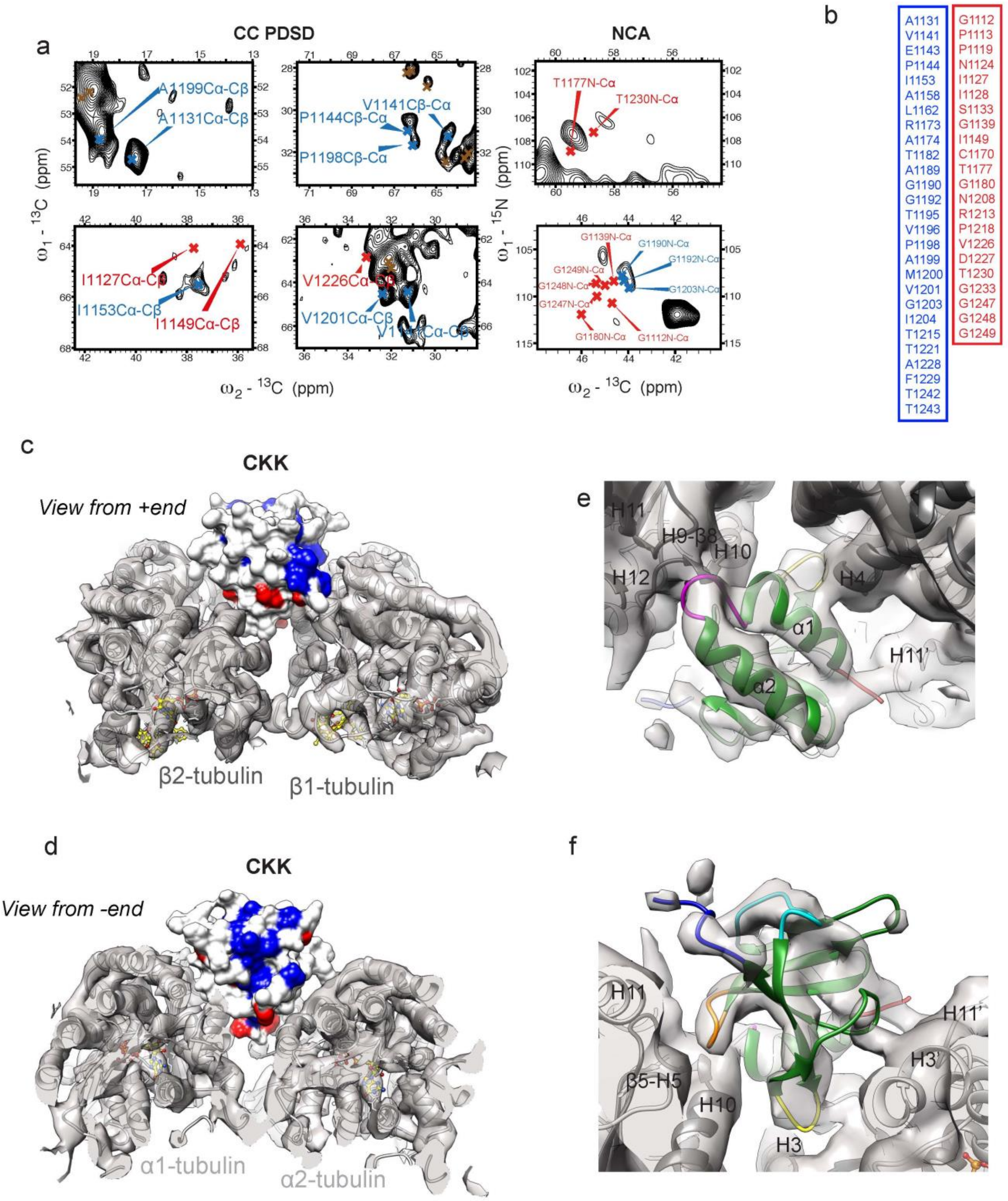

Supplementary Figure 5

Details of the CKK MT-binding site by ssNMR and cryo-EM.

(a) Zooms of well-resolved regions in the solid-state ^{13}C-^{13}C (PDSD, left and middle panels) and NCA (right panel) ssNMR spectra of [^{15}N,^{13}C,] labeled CKK bound to MTs. Crosses indicate expected signals based on solution-state chemical shifts of free CKK in solution.

Signals for which a good match is found between expected and observed chemicals shifts are indicated in blue, while the absence of a corresponding signal is indicated in red. Brown crosses correspond to expected signals in overlapping regions.

(b) Full list of affected (red) and unaffected (blue) residues based on the NMR data.

(c, d) View from the MT plus-end (c) or minus-end (d) of the MT-bound CKK, reporting on ssNMR data obtained on [^{13}C,^{15}N] labeled CKK decorated MTs relative to NMR results on free CKK. The CKK is shown as a color-coded surface representation whilst a ribbon representation of the MT (light grey for α-tubulin and dark grey for β-tubulin) is shown within its respective grey transparent solid cryo-EM density. CKK residues that underwent significant chemical-shift/intensity changes are colored in red (affected) and those that experienced no change are indicated in blue (unaffected). White residues were not analyzed due to signal overlap.

(e) A view from the plus end of the MT, showing details of the tubulin contacts of the CKK N-terminus (red), helix α1, loop1 (magenta) and loop7 (yellow), colored as in Fig. 2d. The experimental density is shown as transparent solid, with tubulin shown as grey ribbons fitted into the experimental density.

(f) A view from the minus end of the MT, showing details of the tubulin contacts of the CKK N-terminus (red), loop7 (yellow), the C-terminus (blue) loop3 (orange) and the position of loop8 (cyan).

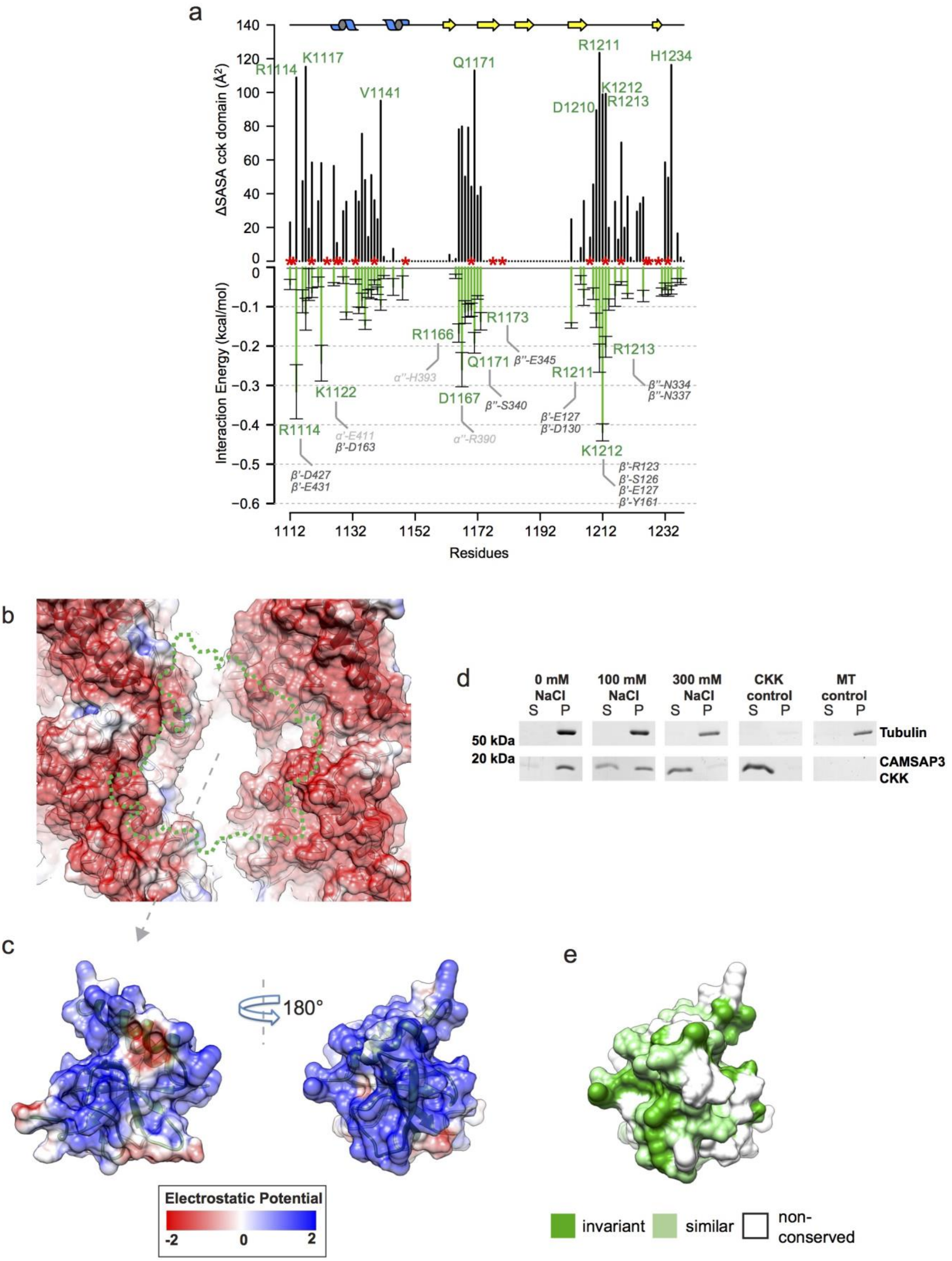
a
140
120
100
80
60
40
20
0
ΔSASA cck domain (Å²)
R1114
K1117
V1141
Q1171
R1211
K1212
D1210
R1213
H1234
0
-0.1
-0.2
-0.3
-0.4
-0.5
-0.6
Interaction Energy (kcal/mol)
R1114
β'-D427
β'-E431
K1122
α'-E411
β'-D163
R1166
α''-H393
D1167
α''-R390
Q1171
β''-S340
R1173
β''-E345
R1211
β'-E127
β'-D130
K1212
β'-R123
β'-S126
β'-E127
β'-Y161
R1213
β''-N334
β''-N337
1112
1132
1152
1172
1192
1212
1232
Residues
b
c
180°
Electrostatic Potential
-2
0
2
d
0 mM NaCl
100 mM NaCl
300 mM NaCl
CKK control
MT control
S
P
50 kDa
20 kDa
Tubulin
CAMSAP3 CKK
e
invariant
similar
non-conserved

Supplementary Figure 6

Characterization of the CKK MT-binding site; energetics and electrostatic contributions.

(a) CAMSAP3 residue-wise variation in solvent accessible surface area (top, black bars) and energetic contributions to MT binding (bottom, green bars). Selected CKK residues showing major solvent accessibility changes and energetic contributions are labelled in green, with corresponding interacting tubulin residues labelled in light grey for α-tubulin and dark grey for β-tubulin. Red stars indicate the location of residues with ssNMR signal shifts. Energetic contributions were determined from molecular dynamics simulations using the Amber MMGBSA routine. Data represent mean ± SD. Solvent accessibility was determined with Bio3D (Grant, B.J. et al., *Bioinformatics* **22**, 2695-2696, 2006, see Methods).

(b) Surface representation of the MT-CKK interface on tubulin colored by electrostatic potential, with the CKK binding site indicated by a green dashed outline. The surface was calculated with the APBS (Baker, N.A. *et al., PNAS* **98**, 10037-10041, 2001) and pdb2pqr (Dolinsky, T.J. *et al., Nucleic acids research* **35**, W522-525, 2007).

(c) The corresponding front view of the surface-represented CKK (left) colored in the same way as panel b, while a 180° rotation of this view illustrating the tubulin-facing surface of the CKK is shown on the right.

(d) MT pelleting assay, in which the CAMSAP3 CKK and MTs were mixed in equimolar ratios at different salt concentrations in BRB35 buffer. As controls, the CKK domain and MTs were processed alone. The supernatants (S) and pellets (P) were separated on a 15 % SDS-PAGE and stained with Coomassie.

(e) Tubulin-facing surface representation of CAMSAP3 CKK surface showing the residue conservation between the *M. musculus*, *C. elegans*, *D. melanogaster* CKK domains. Dark green, invariant residues; light green, similar residues; white, non-conserved residues. Equivalent view to right hand image in panel (c) is shown.

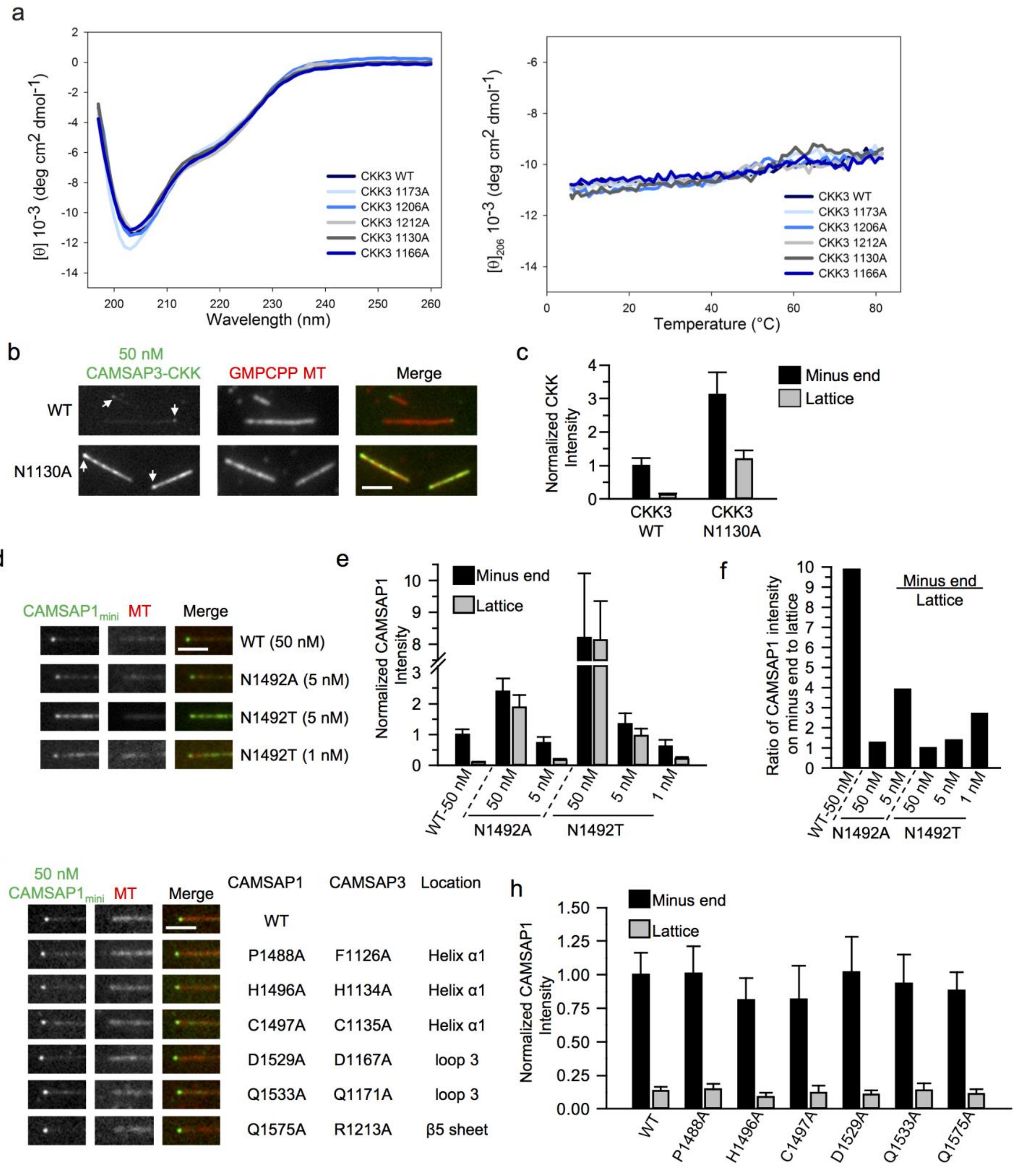

Supplementary Figure 7

Validation of CKK–MT contact sites by using CKK mutants.

(a) CD spectra (left) and thermal unfolding profiles (right) of CAMSAP3 CKK variants. The spectra were recorded at 5 °C in PBS at a protein concentration of 0.25 mg/ml. The thermal unfolding profiles were recorded at 206 nm.

(b,c) TIRFM images and quantification of GFP-CAMSAP3 CKK and N1130A mutant binding to GMPCPP-stabilized MTs. The intensity is normalized to the average minus-end intensity of WT. Similar to CAMSAP1 N1492A mutant, CAMSAP3 N1130A mutant shows increased MT lattice binding. n=80 MTs.

(d-f) TIRFM images and quantifications of the binding of GFP-CAMSAP1$_{mini}$ N1492A and N1492T mutants to the minus ends and lattice of dynamic MTs at different concentrations. Both mutants show minus-end specificity at lower concentrations (see Fig. 4a,d for images at 50 nM). The intensity is normalized to the average minus-end intensity of wild type. n=30-50 MTs. The data for N1492A and N1492T mutants at 50 nM was replotted from Fig. 4d.

(g,h) TIRFM images and quantification of binding of GFP-CAMSAP1$_{mini}$ and mutants to the minus ends and lattice of dynamic MTs. The intensity is normalized to the average minus-end intensity of wild type. n=30 MTs.

Scale bars, 1 μm. Data represent mean ± SD.

See also Supplementary Table 2.

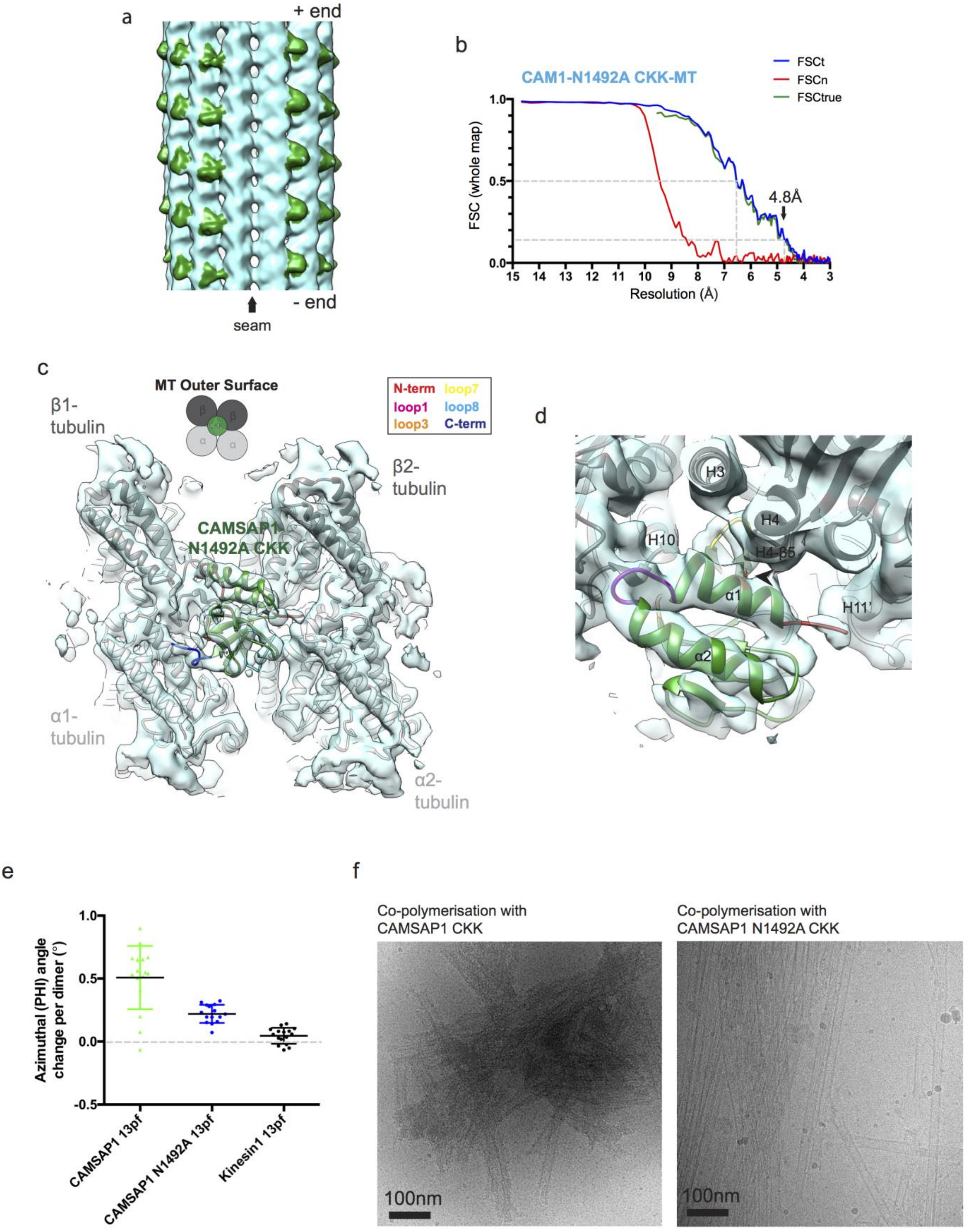
a
+ end
- end
seam
b
CAM1-N1492A CKK-MT
FSCt
FSCn
FSCtrue
FSC (whole map)
1.0
0.5
0.0
4.8Å
15 14 13 12 11 10 9 8 7 6 5 4 3
Resolution (Å)
c
MT Outer Surface
β
β
α
α
N-term
loop1
loop3
loop7
loop8
C-term
β1-tubulin
β2-tubulin
CAMSAP1 N1492A CKK
α1-tubulin
α2-tubulin
d
H3
H4
H10
H4-β5
α1
H11'
α2
e
Azimuthal (PHI) angle change per dimer (°)
1.0
0.5
0.0
-0.5
CAMSAP1 13pf
CAMSAP1 N1492A 13pf
Kinesin1 13pf
f
Co-polymerisation with CAMSAP1 CKK
Co-polymerisation with CAMSAP1 N1492A CKK
100nm
100nm

Supplementary Figure 8

Reconstruction of the CAMSAP1 N1492A CKK mutant and analysis of the effect of CKK on MT polymerization.

(a) The asymmetric reconstruction of the CAMSAP1-N1492A CKK decorated 13pf paclitaxel-stabilized MT low-pass filtered to 15Å resolution shows extra densities (green) every 8nm corresponding to the CAMSAP1-N1492A CKK domain, which are absent at the seam similar to wild type (arrow).

(b) FSC curves utilizing the gold-standard noise substitution method (Chen, S. *et al., Ultramicroscopy* **135**, 24-35, 2013) give an overall resolution estimate for the CAMSAP1-N1492A CKK-MT reconstruction of 4.8Å.

(c) The averaged reconstruction of the CAMSAP1- N1492A CKK domain viewed from the MT surface contacting two β-tubulins and two α-tubulins at the intra-dimer, inter-protofilament interface. The CAMSAP1-N1492A CKK is colored as previously. α-tubulin is shown in light grey and β-tubulin is shown in dark grey. Cryo-EM density is shown as transparent light blue solid. Above, schematic.

(d) View from the plus end of the CAMSAP1-N1492A CKK decorated 13pf MT, showing details of the tubulin contacts of the N-terminus (red), helix α1, loop1 (magenta) and loop 7 (yellow), colored as in Supplementary Fig. 5e. The position of N1492A (brown) is also indicated (arrowhead). The experimental density is shown as blue transparent solid, with tubulin shown as grey ribbons fitted into the experimental density.

(e) Protofilament skew for representative MTs from each dataset is depicted as in Supplementary Figure 4a. The reduced skew produced by CAMSAP1-N1492A CKK-decorated MTs are compared to wild type CKK MTs and control kinesin decorated paclitaxel-stabilized MTs (datasets from Atherton, J. *et al., eLife* **3**, e03680 ,2014). For CAMSAP1 CKK, n=16, for kinesin1 decorated MTs, n=16; for CAMSAP1-N1492A CKK-decorated MTs, n=15. Data represent mean ± SD. 1-way ANOVA, CAMSAP1 CKK N1492A vs CAMSAP1 CKK wild type, $p<0.001$;CAMSAP1 CKK N1492A vs kinesin-1 13pf $p<0.05$.

(f) Copolymerisation of tubulin with CAMSAP1 CKK domain yields few MTs but produces clumps of heterogeneous tubulin oligomers (left), while copolymerisation with CAMSAP-N1492A yields mainly MTs (right). Representative cryo-EM images of the products of each polymerisation reaction are shown.

See also Supplementary Table 2.

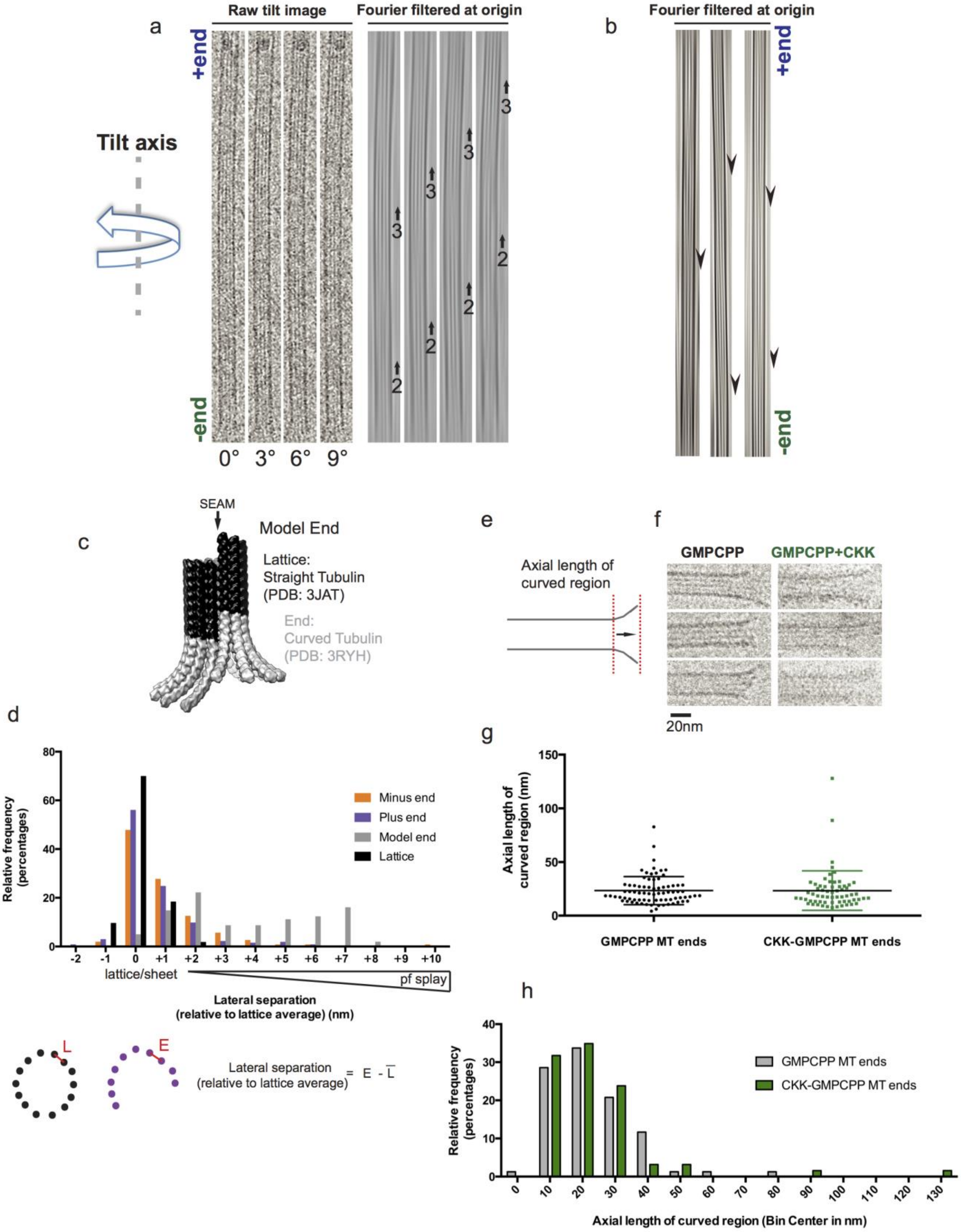
a
Raw tilt image
Fourier filtered at origin
+end
-end
Tilt axis
0° 3° 6° 9°
2
3
b
Fourier filtered at origin
+end
-end
c
SEAM
Model End
Lattice:
Straight Tubulin
(PDB: 3JAT)
End:
Curved Tubulin
(PDB: 3RYH)
d
Relative frequency (percentages)
80
60
40
20
0
-2 -1 0 +1 +2 +3 +4 +5 +6 +7 +8 +9 +10
lattice/sheet
pf splay
Lateral separation (relative to lattice average) (nm)
Minus end
Plus end
Model end
Lattice
L
E
Lateral separation (relative to lattice average) = E - $\overline{L}$
e
Axial length of curved region
f
GMPCPP
GMPCPP+CKK
20nm
g
Axial length of curved region (nm)
150
100
50
0
GMPCPP MT ends
CKK-GMPCPP MT ends
h
Relative frequency (percentages)
40
30
20
10
0
0 10 20 30 40 50 60 70 80 90 100 110 120 130
Axial length of curved region (Bin Center in nm)
GMPCPP MT ends
CKK-GMPCPP MT ends

Supplementary Figure 9

Determination of MT polarity in cryo-tomograms.

(a) The moire pattern from successive raw images in a representative tilt series, and corresponding Fourier filtered images. The tilt method (Chretien, D. *et al., Structure* **4**, 1031-1040, 1996) uses the position of the tilt axis and shift with tilt of the fringes (2 and 3) in the moiré pattern of 14pf MTs to identify MT polarity. The plus (+) end is oriented towards the top of the page.

(b) The moiré pattern of a subset of Fourier filtered MT projections also contain an arrowhead pattern, which arises from pf skew, which can be used to corroborate MT polarity (Chretien, D. *et al., Structure* **4**, 1031-1040, 1996). In 14pf MTs, the arrowheads point towards the minus end; black arrowheads indicate the position of the arrowhead moire patterns on the MTs and thus demonstrate that the MTs are oriented with their plus ends towards the top of the image.

(c) 14 pf MT minus end model built from known tubulin dimer structures (PDB numbers indicated).

(d) Change in lateral pf separation compared to lattice was measured in transverse sections of the MT lattice and ends and plotted as frequency histogram (% of total observations). At both minus and plus ends, most pfs remain laterally closely associated despite longitudinal curvature (0 or +1 nm separation), consistent with a sheet-like structure, and in contrast to the lateral separation of the end model where pfs instead splay apart. Inset; a schematic of a transverse section through the MT lattice and an MT end indicating pf lateral separation distance in the lattice (L) and in the longitudinally curved end region (E).

(e) A scheme illustrating the curved region of a MT end in 2D. The measured axial length of the curved region is the distance between the two red dashed lines.

(f) Gallery of 2D projections of exemplar GMPCPP MT ends with or without 1.5 mg/ml CAMSAP3 CKK domain. Note similar end structures with moderate longitudinal curvature, but also the much higher background in the presence of excess CKK protein.

(g) 2D quantification of the axial length of curved regions of GMPCPP MT ends (as shown in panel e) in the presence or absence of CAMSAP3 CKK domain. No significant difference is observed with added CKK domain, two-tailed Mann-Whitney U test. For GMPCPP-MT ends, n=77 MT ends; for CKK-GMPCPP-MT ends, n=63 MT ends. Data represent mean ± SD.

(h) A histogram of axial length of curved regions of GMPCPP MT ends shows similar length distributions in the presence or absence of CAMSAP3 CKK domain. In both cases, the most common bin center of end lengths is 20 nm (bin width 10 nm).

See also Supplementary Table 2.

Supplementary Note

Details of Cryo-EM methods

Sample preparation for single particle cryo-EM

Bovine brain tubulin (Cytoskeleton Inc, Denver, CO) was polymerized at a final concentration of 5 mg/ml in MES MT polymerization buffer (100 mM MES, pH 6.5, 1 mM $MgCl_2$, 1 mM EGTA, 1 mM DTT, 5 mM GTP) for 1 hour at 37°C. 1 mM paclitaxel in DMSO (Calbiochem) was then added and MTs incubated for a further hour at 37°C. Paclitaxel-stabilized MTs were diluted to 0.25 mg/ml (2.5 µM) in BRB20 (20 mM PIPES, 2 mM $MgCl_2$, 1 mM EGTA, 2 mM DTT, pH 6.8) and 4 µl were applied to glow discharged C-flat holey carbon grids (Protochips, Raleigh, NC). Excess solution was blotted away and either 4 µl of 2 mg/ml (110 µM) CAMSAP1/3-CKK or 1 mg/ml of CAMSAP1-CKK N1492A mutant in BRB20 with an additional 80mM KCl was immediately added. The grid was then incubated for 30 seconds in a Vitrobot (FEI Co.) operating at 23°C and 100% humidity, then blotted and vitrified in liquid ethane. Although full MT binding was observed at 0.2 mg/ml of CAMSAP1-CKK N1492A, 1 mg/ml (55 µM) was used during grid preparation to facilitate subsequent CTF determination.

Sample preparation for cryo-electron tomography and MT end analysis

Double-cycled bovine brain tubulin GMPCPP MTs were polymerized at a final concentration of 5 mg/ml in BRB80 (80 mM PIPES, 2 mM $MgCl_2$, 1 mM EGTA, 2 mM DTT, pH 6.8) with 2 mM GMPCPP for 30 minutes at 37°C. MTs were pelleted for 7 minutes at 18,000 × g in a benchtop centrifuge, the supernatant removed and the MTs depolymerized by resuspension to 5 mg/ml tubulin in 4°C BRB80 and incubation on ice for 5 minutes. GMPCPP was then added to 2 mM and MTs polymerized by incubation at 37°C for 45 minutes. GMPCPP stabilized MTs were pelleted as previously and resuspended to 0.25 mg/ml in 30°C BRB80. 4 µl of 10 nm nanogold fiducial-BSA solution (Sigma) was added to glow discharged C-flat holey carbon grids then blotted prior to addition of MTs. 4 µl MTs was then applied to grids, which was incubated for 30 seconds in a Vitrobot (FEI Co.) operating at 30°C and 100% humidity before blotting and vitrification in liquid ethane. For 2D end analysis, GMPCPP MTs were prepared for cryo-EM in the same way but without addition of nanogold. For CKK-GMPCPP MTs 1.5 mg/ml CAMSAP3 CKK domain was added to GMPCPP MTs sequentially prior to blotting as in preparation for single particle cryo-EM.

Data Collection for single particle cryo-EM

Images of MT-CAMSAP3 CKK domain complexes were collected on a Tecnai G2 Polara (FEI) operating at 300kV with a calibrated final sampling of 1.53Å/pixel and a defocus range of 0.4-3.5µm using a DE20 direct electron detector (Direct Electron). A total electron dose of ~50e-/Å^2 over a 1.5 seconds exposure and a frame rate of 15 frames/second was used, giving a total of 23 frames at ~2.2e-/Å^2/frame. Images of MT-CAMSAP1 CKK domain complexes were collected on a Tecnai F20 (FEI) operating at 200kV with a calibrated final sampling of 1.54Å/pixel and a similar defocus range using a DE20 direct electron detector (Direct Electron). A total electron dose of ~30e-/Å2 over a 1 seconds exposure and a frame rate of 25 frames/second was used, giving a total of 25 frames at ~1.2e-/Å^2/frame.

Images of MT-CAMSAP1 N1492A mutant CKK domain complexes were collected on a Tecnai G2 Polara operating at 300kV with a calibrated final sampling of 1.39Å/pixel and a similar defocus range using a K2 direct electron detector (Gatan) operating in counting mode at 7e-/pixel/second, with a quantum post-column energy-filter (Gatan), operated in zero-loss imaging mode with a 20-eV energy-selecting slit. The total exposure was 35e-/Å^2 over 10 seconds at 4 frames/sec, giving 40 frames at ~0.875e-/Å^2/frame.

Data Collection for MT cryo-electron tomography and MT end analysis

Single-axis tilt series at ~3 or 5 µm defocus were collected on a Tecnai G2 Polara operating at 300kV with a calibrated final sampling of 5.39Å/pixel on a K2 summit direct electron detector (Gatan) operating in counting mode at 5e-/pixel/second with a quantum post-column energy-filter (Gatan), operated in zero-loss imaging mode with a 20-eV energy-selecting slit. Whole tilt series used a total dose of either 60 or 80e-/Å^2 total dose, corresponding to a 12 or 16 second total exposure time. The total dose was divided into bidirectional tilt images from 0° to +60° and 0° to -60° in 3° increments with higher tilts receiving compensatory higher electron doses. Each tilt image was divided into 4 sub-frames, which were aligned on collection with Digital Micrograph prior to creating the final tilt stack. For 2D MT end analysis, images were collected with a total dose of ~25e-/Å^2 on a FEI Tecnai T12 operating at 120 kV using a 4096 × 4096-pixel CCD camera (Gatan Inc.). Axial lengths of curved regions in MT ends were quantified with the straight line and 'measure' tools in FIJI[1].

Sub-frame processing of single particle data for 3D reconstruction

For wild type CAMSAP1 and 3 CKK data collected on the DE20 detector individual frames were globally aligned using Imod scripts[2] then locally aligned using the Optical Flow approach[3], implemented in Xmipp[4]. Sums of all frames were used for particle picking and CTF determination in CTFFind3[5]), whereas the first ~25e-/Å^2 (for CAMSAP3 data obtained at 300kV) or ~20e-/Å^2 (for CAMSAP1 data obtained at 200kV) was used in particle processing and generation of the final reconstructions. For mutant CAMSAP1 N1492A CKK data collected on the K2 detector, individual frames were globally aligned using Motioncorr[6]. The total dose of ~35e-/Å^2 was used for particle picking and CTF determination in CTFFind3[5], whereas ~25e-/Å^2 was used in particle processing and generation of the final reconstructions.

Processing of single particle data

Straight CAMSAP CKK domain-decorated 13pf taxol-stabilized MTs were boxed manually in EMAN boxer, and were input for a set of custom-designed semi-automated single-particle processing scripts utilizing Spider and Frealign as described previously[7, 8], with minor modifications. These custom-designed scripts provide diagnostics for MT architecture and decoration, accurately determine seam location in 13 and 14pf MTs and apply pseudo-symmetry between MT protofilaments during reconstruction and refinement. Eight rounds of refinement are performed in Frealign v8, using information at increasing spatial frequency up to a resolution of 8Å in the final round to generate the final reconstruction. The procedure was modified to avoid using information at the seam in application of symmetry, which was found to be absent of CKK domains in C1 reconstructions.

A kinesin-1-decorated 13pf MT low-pass filtered to 15 Å was used as a reference for initial alignment, yielding ~9Å reconstructions of both wild type and N1492A mutant CAMSAP1 and CAMSAP3 CKK domains and allowing initial docking of the CAMSAP-3 CKK domain (PDB ID 1UGJ; unpublished) into density. This model was filtered to 15Å and used as a reference for further rounds of alignment. This greatly improved the seam-finding process in particular, improving the resolution of the reconstructions. The final dataset sizes and resolutions are reported in Table 2.

Tilt series processing, tomogram generation and analysis

Tilt series were processed and tomograms generated using IMOD's Etomo graphical user interface (v4.7.15). Tilt series were aligned with 10nm gold fiducials, which were selected manually based on minimal observed beam induced movement. Final tomograms were binned by 3 on output to reduce noise. Tomogram slices were analyzed using 3DMOD's 'slicer' viewer with 'high resolution' interpolation mode rendering.

14pf MTs were identified by their moire patterns[9, 10] and confirmed in tomographic volume cross-sections. MT polarity was determined using a combination of previously reported methods that use i) change of moire pattern appearance with tilt angle and ii) directionality of 'arrowhead' moire patterns in 2D projections[11] (see Supplementary Fig. 6a,b). Only MTs where polarity was unambiguously determined were analyzed. Quantitative characterization of MT plus and minus ends was performed in 3DMOD's 'slicer' viewer. Protofilament trajectories were traced manually by plotting their three-dimensional center of mass in successive 1.6nm cross-sections along the MT axis from lattice to end. Coordinates of protofilament positions in 3D space were used to calculate distances both within single protofilaments and between adjacent protofilaments. Protofilament curvatures were calculated as monomer rotation (i.e the rotation needed to superimpose one tubulin monomer onto the next), comparable to e.g.[12] and[13]).

References

1. Schindelin, J. et al. Fiji: an open-source platform for biological-image analysis. Nat Methods 9, 676-682 (2012).

2. Kremer, J.R., Mastronarde, D.N. & McIntosh, J.R. Computer visualization of three-dimensional image data using IMOD. Journal of structural biology 116, 71-76 (1996).

3. Abrishami, V. et al. Alignment of direct detection device micrographs using a robust Optical Flow approach. Journal of structural biology 189, 163-176 (2015).

4. de la Rosa-Trevin, J.M. et al. Xmipp 3.0: an improved software suite for image processing in electron microscopy. Journal of structural biology 184, 321-328 (2013).

5. Mindell, J.A. & Grigorieff, N. Accurate determination of local defocus and specimen tilt in electron microscopy. Journal of structural biology 142, 334-347 (2003).

6. Li, X. et al. Electron counting and beam-induced motion correction enable near-atomic-resolution single-particle cryo-EM. Nat Methods 10, 584-590 (2013).

7. Sindelar, C.V. & Downing, K.H. The beginning of kinesin's force-generating cycle visualized at 9-A resolution. The Journal of cell biology 177, 377-385 (2007).

8. Sindelar, C.V. & Downing, K.H. An atomic-level mechanism for activation of the kinesin molecular motors. Proceedings of the National Academy of Sciences of the United States of America 107, 4111-4116 (2010).

9. Wade, R.H., Chretien, D. & Job, D. Characterization of microtubule protofilament numbers. How does the surface lattice accommodate? Journal of molecular biology 212, 775-786 (1990).

10. Chretien, D. & Wade, R.H. New data on the microtubule surface lattice. Biology of the cell / under the auspices of the European Cell Biology Organization 71, 161-174 (1991).

11. Chretien, D., Kenney, J.M., Fuller, S.D. & Wade, R.H. Determination of microtubule polarity by cryo-electron microscopy. Structure 4, 1031-1040 (1996).

12. Nawrotek, A., Knossow, M. & Gigant, B. The determinants that govern microtubule assembly from the atomic structure of GTP-tubulin. Journal of molecular biology 412, 35-42 (2011).

13. Brouhard, G.J. & Rice, L.M. The contribution of alphabeta-tubulin curvature to microtubule dynamics. The Journal of cell biology 207, 323-334 (2014).

Supplementary Table 1. **List of screened genomes and their sources.**

Scientific name	**Taxonomy ID**	**Download (m/d/y)**	**Assembly version**	**Reference/source**
Aureococcus anophagefferens CCMP1984	44056	6/13/2013	v.1.0 (September 27, 2007)	Gobler CJ, *et al.* (2011) Niche of harmful alga Aureococcus anophagefferens revealed through ecogenomics. *Proceedings of the National Academy of Sciences of the United States of America* 108(11):4352-4357
Acanthamoebe castellanii str. Neff	1257118	6/12/2013	Acastellanii.strNEFF v1 (January 9, 2013)	Clarke M, *et al.* (2013) Genome of Acanthamoeba castellanii highlights extensive lateral gene transfer and early evolution of tyrosine kinase signaling. *Genome biology* 14(2):R11.
Aquilegia coerulea Goldsmith	218851	17/7/2013	Release of the initial 8X unmapped Aquilegia coerulea Goldsmith genome	Aquilegia coerulea Genome Sequencing Project, http://phytozome.jgi.doe.gov/
Anopheles gambiae str. PEST	180454	7/1/2013	AgamP3.7	Holt RA, *et al.* (2002) The genome sequence of the malaria mosquito Anopheles gambiae. *Science* 298(5591):129-149.
Aplanochytrium kerguelense PBS07	702273	4/11/2013	V1	These sequence data were produced by the US Department of Energy Joint Genome Institute http://www.jgi.doe.gov/ in collaboration with the user community.
Albugo laibachii Nc14	890382	7/1/2013	ENA 1 (2011-08-ENA)	Kemen E, *et al.* (2011) Gene gain and loss during evolution of obligate parasitism in the white rust pathogen of Arabidopsis thaliana. *PLoS biology* 9(7):e1001094.
Aurantiochytrium limacinum ATCC MYA-1381	717989	4/11/2013	V1	These sequence data were produced by the US Department of Energy Joint Genome Institute http://www.jgi.doe.gov/ in collaboration with the user community.
Allomyces macrogynus ATCC 38327	578462	6/10/2013	V1, March 1, 2012	Origins of Multicellularity Sequencing Project, Broad Institute of Harvard and MIT (http://www.broadinstitute.org/)
Amphimedon queenslandica	400682	6/12/2013	V1.0, (May 28, 2010)	Srivastava M, *et al.* (2010) The Amphimedon queenslandica genome and the evolution of animal complexity. *Nature* 466(7307):720-726.
Arabidopsis thaliana	3702	7/3/2013	TAIR10, November 17, 2010	Arabidopsis Genome Initiative (2000) Analysis of the genome sequence of the flowering plant Arabidopsis thaliana. *Nature* 408(6814):796-815.
Amborella trichopoda	13333	5/1/2013	Unknown	Amborella Genome Project (2013) The Amborella genome and the evolution of flowering plants. *Science* 342(6165):1241089.
Batrachochytrium dendrobatidis JAM81	684364	6/3/2013	V1	These sequence data were produced by the US Department of Energy Joint Genome Institute http://www.jgi.doe.gov/ in collaboration with the user community

Branchiostoma floridae	7739	7/1/2013	Unknown	Putnam NH, *et al.* (2008) The amphioxus genome and the evolution of the chordate karyotype. *Nature* 453(7198):1064-1071.
Blastocystis hominis	12968	6/13/2013	V1	Denoeud F, *et al.* (2011) Genome sequence of the stramenopile Blastocystis, a human anaerobic parasite. *Genome biology* 12(3):R29.
Brugia malayi	6279	6/27/2013	WS238	Ghedin E, *et al.* (2007) Draft genome of the filarial nematode parasite Brugia malayi. *Science* 317(5845):1756-1760. Yook K, *et al.* (2012) WormBase 2012: more genomes, more data, new website. *Nucleic acids research* 40(Database issue):D735-741.
Bigelowiella natans CCMP2755	753081	6/13/2013	V1	Curtis BA, *et al.* (2012) Algal genomes reveal evolutionary mosaicism and the fate of nucleomorphs. *Nature* 492(7427):59-65.
Bathycoccus prasinos RCC1005	1075084	5/30/2013	V1	Moreau H, *et al.* (2012) Gene functionalities and genome structure in Bathycoccus prasinos reflect cellular specializations at the base of the green lineage. *Genome biology* 13(8):R74.
Catenaria anguillulae PL171	765915	6/10/2013	V1	These sequence data were produced by the US Department of Energy Joint Genome Institute http://www.jgi.doe.gov/ in collaboration with the user community.
Conidiobolus coronatus NRRL28638	796925	6/10/2013	V1	Chang Y, *et al.* (2015) Phylogenomic Analyses Indicate that Early Fungi Evolved Digesting Cell Walls of Algal Ancestors of Land Plants. *Genome Biol Evol* 7(6):1590-1601.
Caenorhabditis elegans	6239	7/1/2013	WBcel235	C. elegans Sequencing Consortium (1998) Genome sequence of the nematode C. elegans: a platform for investigating biology. *Science* 282(5396):2012-2018.
Candida glabrata CBS138	284593	6/13/2013	7/12/2012	Dujon B, *et al.* (2004) Genome evolution in yeasts. *Nature* 430(6995):35-44. Inglis DO, *et al.* (2012) The Candida genome database incorporates multiple Candida species: multispecies search and analysis tools with curated gene and protein information for Candida albicans and Candida glabrata. *Nucleic acids research* 40(Database issue):D667-674.
Ciona intestinalis	7719	6/27/2013	KH (April 29, 2011)	Dehal P, *et al.* (2002) The draft genome of Ciona intestinalis: insights into chordate and vertebrate origins. *Science* 298(5601):2157-2167.
Cyanidioschyzon merolae 10D	280699	6/13/2013	V1	Matsuzaki M, *et al.* (2004) Genome sequence of the ultrasmall unicellular red alga Cyanidioschyzon merolae 10D. *Nature* 428(6983):653-657.
Cryptococcus neoformans	235443	6/12/2013	V4	Cryptococcus neoformans var. grubii H99 Sequencing Project, Broad Institute of Harvard and MIT (http://www.broadinstitute.org/) Loftus BJ, *et al.* (2005) The genome of the basidiomycetous yeast and human pathogen Cryptococcus neoformans.

				Science 307(5713):1321-1324.
Capsaspora owczarzaki ATCC 30864	595528	5/31/2013	V2	Origins of Multicellularity Sequencing Project, Broad Institute of Harvard and MIT (http://www.broadinstitute.org/)
Cryptosporidium parvum Iowa II	414452	5/29/2013	2/23/2007	Abrahamsen MS*, et al.* (2004) Complete genome sequence of the apicomplexan, Cryptosporidium parvum. *Science* 304(5669):441-445.
Cyanophora paradoxa	2762	6/13/2013	V1, November 2010	Price DC*, et al.* (2012) Cyanophora paradoxa genome elucidates origin of photosynthesis in algae and plants. *Science* 335(6070):843-847.
Chlamydomonas reinhardtii	3055	7/2/2013	Unknown	Merchant SS*, et al.* (2007) The Chlamydomonas genome reveals the evolution of key animal and plant functions. *Science* 318(5848):245-250.
Coemansia reversa NRRL 1564	763665	6/10/2013	V1	Chang Y*, et al.* (2015) Phylogenomic Analyses Indicate that Early Fungi Evolved Digesting Cell Walls of Algal Ancestors of Land Plants. *Genome Biol Evol* 7(6):1590-1601.
Coccomyxa subellipsoidea C-169	574566	6/14/2013	V2.0 (April 13, 2012)	Blanc G*, et al.* (2012) The genome of the polar eukaryotic microalga Coccomyxa subellipsoidea reveals traits of cold adaptation. *Genome biology* 13(5):R39.
Chlorella variabilis NC64A	554065	5/30/2013	V1	Blanc G*, et al.* (2010) The Chlorella variabilis NC64A genome reveals adaptation to photosymbiosis, coevolution with viruses, and cryptic sex. *The Plant cell* 22(9):2943-2955.
Dictyostelium discoideum AX4	352472	5/30/2013	Unknown	Eichinger L*, et al.* (2005) The genome of the social amoeba Dictyostelium discoideum. *Nature* 435(7038):43-57.
Debaryomyces hansenii CBS767	284592	6/12/2013	V2, February 9, 2012	Dujon B*, et al.* (2004) Genome evolution in yeasts. *Nature* 430(6995):35-44.
Drosophila melanogaster	7227	6/26/2013	5.51, May 7, 2013	Adams MD*, et al.* (2000) The genome sequence of Drosophila melanogaster. *Science* 287(5461):2185-2195. Attrill H*, et al.* (2015) FlyBase: establishing a Gene Group resource for Drosophila melanogaster. *Nucleic acids research*.
Danio rerio	7955	7/1/2013	Zv9	Howe K*, et al.* (2013) The zebrafish reference genome sequence and its relationship to the human genome. *Nature* 496(7446):498-503.
Edhazardia aedis USNM 41457	1003232	5/27/2013	4/30/2013	Microsporidia Comparative Sequencing Project, Broad Institute of Harvard and MIT (http://www.broadinstitute.org/)
Entamoeba histolytica HM-1:IMSS	294381	5/31/2013	11/27/2009	Loftus B*, et al.* (2005) The genome of the protist parasite Entamoeba histolytica. *Nature* 433(7028):865-868.
Emiliania huxleyi CCMP1516	280463	6/26/2013	V1	Read BA*, et al.* (2013) Pan genome of the phytoplankton Emiliania underpins its global distribution. *Nature* 499(7457):209-213.
Encephalitozoon intestinalis ATCC 50506	876142	5/31/2013	10/18/2010	Corradi N, Pombert JF, Farinelli L, Didier ES, & Keeling PJ (2010) The complete sequence of the smallest known nuclear genome from the microsporidian Encephalitozoon intestinalis. *Nature communications* 1:77.

Ectocarpus siliculosus	2880	6/13/2013	Unknown	Cock JM*, et al.* (2010) The Ectocarpus genome and the independent evolution of multicellularity in brown algae. *Nature* 465(7298):617-621.
Fonticula alba	691883	7/21/2014	V2	Origins of Multicellularity Sequencing Project, Broad Institute of Harvard and MIT (http://www.broadinstitute.org/)
Giardia intestinalis assemblage A	941442	5/29/2013	2/8/2013	Morrison HG*, et al.* (2007) Genomic minimalism in the early diverging intestinal parasite Giardia lamblia. *Science* 317(5846):1921-1926.
Galdieria sulphuraria	130081	6/13/2013	ASM34128v1 (February 25, 2013)	Schonknecht G, *et al.* (2013) Gene transfer from bacteria and archaea facilitated evolution of an extremophilic eukaryote. *Science* 339(6124):1207-1210.
Guillardia theta CCMP2712	905079	7/1/2013	Guith1 (2012-12-EnsemblProtist)	Curtis BA, *et al.* (2012) Algal genomes reveal evolutionary mosaicism and the fate of nucleomorphs. *Nature* 492(7427):59-65.
Hyaloperonospora parasitica	272952	7/5/2013	Unknown	Saprolegnia genome Sequencing Project, Broad Institute of Harvard and MIT (http://www.broadinstitute.org/)
Homo sapiens	9606	7/1/2013	GRCh37.p10	Lander ES, *et al.* (2001) Initial sequencing and analysis of the human genome. *Nature* 409(6822):860-921.
Klebsormidium flaccidum	3175	7/21/2014	V1.0	Hori K, *et al.* (2014) Klebsormidium flaccidum genome reveals primary factors for plant terrestrial adaptation. *Nature communications* 5
Kluyveromyces lactis NRRL Y-1140	284590	6/12/2013	ASM251v1, (July 2, 2004)	Dujon B, *et al.* (2004) Genome evolution in yeasts. *Nature* 430(6995):35-44.
Leishmania major strain Friedlin	347515	5/29/2013	10/20/2010	Ivens AC, *et al.* (2005) The genome of the kinetoplastid parasite, Leishmania major. *Science* 309(5733):436-442.
Monosiga brevicollis MX1 / ATCC 50154	431895 / 487148	6/12/2013	V1.0, (December 20, 2007)	King N, *et al.* (2008) The genome of the choanoflagellate Monosiga brevicollis and the origin of metazoans. *Nature* 451(7180):783-788.
Mucor circinelloides 1006PhL	1220926	6/28/2013	V1	Lee SC, *et al.* (2014) Analysis of a food-borne fungal pathogen outbreak: virulence and genome of a Mucor circinelloides isolate from yogurt. *mBio* 5(4):e01390-01314.
Mortierella elongata	310910	6/10/2013	V1	These sequence data were produced by the US Department of Energy Joint Genome Institute http://www.jgi.doe.gov/ in collaboration with the user community.
Mnemiopsis leidyi	27923	5/29/2013	Initial release	http://research.nhgri.nih.gov/mnemiopsis/
Mus musculus	10090	7/1/2013	GRCm38.p1	Waterston RH, *et al.* (2002) Initial sequencing and comparative analysis of the mouse genome. *Nature* 420(6915):520-562.
Micromonas species RCC299	296587	6/17/2013	ASM9098v1 (April 10, 2009)	Worden AZ, *et al.* (2009) Green evolution and dynamic adaptations revealed by genomes of the marine picoeukaryotes Micromonas. *Science* 324(5924):268-272.
Mortierella verticillata	1069443	6/10/2013	2/17/2011	Origins of Multicellularity Sequencing

NRRL 6337				Project, Broad Institute of Harvard and MIT (http://www.broadinstitute.org/)
Neurospora crassa OR74A	367110	6/12/2013	3/11/2013	Neurospora crassa Sequencing Project, Broad Institute of Harvard and MIT (http://www.broadinstitute.org/) Galagan JE, *et al.* (2003) The genome sequence of the filamentous fungus Neurospora crassa. *Nature* 422(6934):859-868.
Nannochloropsis gaditana CCMP526	1093141	6/13/2013	1.1	Radakovits R, *et al.* (2012) Draft genome sequence and genetic transformation of the oleaginous alga Nannochloropis gaditana. *Nature communications* 3:686.
Naegleria gruberi strain NEG-M	744533	6/19/2013	1	Fritz-Laylin LK, *et al.* (2010) The genome of Naegleria gruberi illuminates early eukaryotic versatility. *Cell* 140(5):631-642.
Nematostella vectensis	45351	5/29/2013	1	Putnam NH, *et al.* (2007) Sea anemone genome reveals ancestral eumetazoan gene repertoire and genomic organization. *Science* 317(5834):86-94.
Ostreococcus lucimarinus CCE9901	436017	7/3/2013	Unknown	Palenik B, *et al.* (2007) The tiny eukaryote Ostreococcus provides genomic insights into the paradox of plankton speciation. *Proceedings of the National Academy of Sciences of the United States of America* 104(18):7705-7710.
Oryza sativa japonica	39947	7/1/2013	MSU6 (2009-01-MSU6)	International Rice Genome Sequencing Project (2005) The map-based sequence of the rice genome. *Nature* 436(7052):793-800.
Oxytricha trifallax	1172189	5/29/2013	2/12/2012	Swart EC, *et al.* (2013) The Oxytricha trifallax macronuclear genome: a complex eukaryotic genome with 16,000 tiny chromosomes. *PLoS biology* 11(1):e1001473.
Phycomyces blakesleeanus NRRL1555	763407	6/10/2013	V2	These sequence data were produced by the US Department of Energy Joint Genome Institute http://www.jgi.doe.gov/ in collaboration with the user community.
Plasmodiophora brassicae	37360	12/30/2015	V1	Schwelm A, *et al.* (2015) The Plasmodiophora brassicae genome reveals insights in its life cycle and ancestry of chitin synthases. *Scientific Reports* 5:11153.
Plasmodium falciparum 3D7	36329	5/29/2013	3	Gardner MJ, *et al.* (2002) Genome sequence of the human malaria parasite Plasmodium falciparum. *Nature* 419(6906):498-511.
Phytophthora infestans T30-4	403677	6/13/2013	ASM14294v1, (June 17, 2009)	Phytophthora infestans Sequencing Project, Broad Institute of Harvard and MIT (http://www.broadinstitute.org/) Haas BJ, *et al.* (2009) Genome sequence and analysis of the Irish potato famine pathogen Phytophthora infestans. *Nature* 461(7262):393-398.
Perkinsus marinus ATCC 50983	423536	5/29/2013	Unknown	
Polysphondylium pallidum PN500	670386	5/31/2013	PolPal_Dec2009, (January 29, 2010)	Heidel AJ, *et al.* (2011) Phylogeny-wide analysis of social amoeba genomes

				highlights ancient origins for complex intercellular communication. *Genome research* 21(11):1882-1891.
Physcomitrella patens subsp. patens	145481	7/4/2013	V1.6	Rensing SA*, et al.* (2008) The Physcomitrella genome reveals evolutionary insights into the conquest of land by plants. *Science* 319(5859):64-69. Zimmer AD*, et al.* (2013) Reannotation and extended community resources for the genome of the non-seed plant Physcomitrella patens provide insights into the evolution of plant gene structures and functions. *BMC genomics* 14:498.
Paramecium tetraurelia	5888	5/29/2013	v1.78	Arnaiz O & Sperling L (2011) ParameciumDB in 2011: new tools and new data for functional and comparative genomics of the model ciliate Paramecium tetraurelia. *Nucleic acids research* 39(Database issue):D632-636.
Phaeodactylum tricornutum CCAP1055/1	556484	6/13/2013	ASM15095v2 (December 12, 2008)	Bowler C*, et al.* (2008) The Phaeodactylum genome reveals the evolutionary history of diatom genomes. *Nature* 456(7219):239-244.
Piromyces species	45796	7/21/2014	v1 (March 2011)	http://genome.jgi.doe.gov
Rozella allomyces	281847	04/08/2014	GCA_000442015.1	Chang Y*, et al.* (2015) Phylogenomic Analyses Indicate that Early Fungi Evolved Digesting Cell Walls of Algal Ancestors of Land Plants. *Genome Biol Evol* 7(6):1590-1601.
Rhizophagus irregularis DAOM 197198	588596	21/07/2014	v1 (March 2012)	Tisserant E*, et al.* (2013) Genome of an arbuscular mycorrhizal fungus provides insight into the oldest plant symbiosis. *Proceedings of the National Academy of Sciences* 110(50):20117-20122.
Saccharomyces cerevisiae S288C	559292	6/13/2013	Release R64-1-1	Goffeau A*, et al.* (1996) Life with 6000 genes. *Science* 274(5287):546, 563-547.
Saccoglossus kowalevskii	10224	7/1/2013	Unknown	Simakov O*, et al.* (2015) Hemichordate genomes and deuterostome origins. *Nature* 527(7579):459-465.
Schistosoma mansoni	6183	5/29/2013	5	Berriman M*, et al.* (2009) The genome of the blood fluke Schistosoma mansoni. *Nature* 460(7253):352-358.
Spironucleus salmonicida	348837	Genome not downloaded, but only accessed online via the nr database of NCBI.		
Symbiodinium minutum	1202447	17/7/13	v1.0	Shoguchi E*, et al.* (2013) Draft assembly of the Symbiodinium minutum nuclear genome reveals dinoflagellate gene structure. *Current biology : CB* 23(15):1399-1408.
Selaginella moellendorffii	88036	7/1/2013	v1.0 (2011-05-ENA)	Banks JA*, et al.* (2011) The Selaginella genome identifies genetic changes associated with the evolution of vascular plants. *Science* 332(6032):960-963.
Strongylocentrotus purpuratus	7668	28/07/2013	Spur_3.1	Sodergren E*, et al.* (2006) The Genome of the Sea Urchin Strongylocentrotus purpuratus. *Science* 314(5801):941-952.
Schizosaccharomyces pombe (strain 972 / ATCC 24843)	4896	7/1/2013	ASM294v1 (2012-03-PomBase)	Wood V*, et al.* (2002) The genome sequence of Schizosaccharomyces pombe. *Nature* 415(6874):871-880.

Spizellomyces punctatus DAOM BR117	645134	6/3/2013 / 6/11/2013	3/1/2012	Origins of Multicellularity Sequencing Project, Broad Institute of Harvard and MIT (http://www.broadinstitute.org/)
Salpingoeca rosetta	946362	5/31/2013	V1	Origins of Multicellularity Sequencing Project, Broad Institute of Harvard and MIT (http://www.broadinstitute.org/)
Trichoplax adhaerens	10228	6/12/2013	V1.0, (June 17, 2008)	Srivastava M, *et al.* (2008) The Trichoplax genome and the nature of placozoans. *Nature* 454(7207):955-960.
Trypanosoma brucei TREU 927	185431	6/19/2013	2013-01-16	Berriman M, *et al.* (2005) The genome of the African trypanosome Trypanosoma brucei. *Science* 309(5733):416-422.
Toxoplasma gondii ME49	508771	5/29/2013	7/23/2012	Lis Caler, J. Craig Venter Institute
Thalassiosira pseudonana	296543	6/13/2013	ASM14940v1 (January 16, 2009)	Armbrust EV, *et al.* (2004) The genome of the diatom Thalassiosira pseudonana: ecology, evolution, and metabolism. *Science* 306(5693):79-86.
Takifugu rubripes	31033	7/1/2013	FUGU5 (October 13, 2011)	Aparicio S, *et al.* (2002) Whole-genome shotgun assembly and analysis of the genome of Fugu rubripes. *Science* 297(5585):1301-1310.
Tetrahymena thermophila	5911	5/29/2013	Oct 2008	Eisen JA, *et al.* (2006) Macronuclear genome sequence of the ciliate Tetrahymena thermophila, a model eukaryote. *PLoS biology* 4(9):e286. Stover NA, *et al.* (2006) Tetrahymena Genome Database (TGD): a new genomic resource for Tetrahymena thermophila research. *Nucleic acids research* 34(Database issue):D500-503.
Tetraselmis sp. GSL018	582737	Genome not downloaded, but only accessed online via the nr database of NCBI.		
Thecamonas trahens ATCC 50062	461836	6/13/2013	10/28/2011	Origins of Multicellularity Sequencing Project, Broad Institute of Harvard and MIT (http://www.broadinstitute.org/)
Trichomonas vaginalis G3	412133	5/29/2013	1/11/2007	Carlton JM, *et al.* (2007) Draft genome sequence of the sexually transmitted pathogen Trichomonas vaginalis. *Science* 315(5809):207-212.
Ustilago maydis	237631	6/12/2013	ASM32847v1 (March 5, 2007)	Kamper J, *et al.* (2006) Insights from the genome of the biotrophic fungal plant pathogen Ustilago maydis. *Nature* 444(7115):97-101.
Volvox carteri	3068	7/3/2013	Unknown	Prochnik SE, *et al.* (2010) Genomic analysis of organismal complexity in the multicellular green alga Volvox carteri. *Science* 329(5988):223-226.
Vavraia culicis floridensis	948595	5/27/2013	4/30/2013	Microsporidia Comparative Sequencing Project, Broad Institute of Harvard and MIT (http://www.broadinstitute.org/)
Xenopus tropicalis	8364	7/1/2013	Xtropicalis_v7 (December 19, 2012)	Hellsten U, *et al.* (2010) The genome of the Western clawed frog Xenopus tropicalis. *Science* 328(5978):633-636.
Yarrowia lipolytica CLIB 122	284591	7/1/2013	ASM252v1 (2012-05-EnsemblFungi)	Dujon B, *et al.* (2004) Genome evolution in yeasts. *Nature* 430(6995):35-44.

6. Conclusion and outlook

The previous four chapters contained the published papers or manuscripts about the +TIPs Bik1, Kip2 and Kip3 and the -TIP CAMSAP. In this last chapter, my Ph.D. thesis will finish with a conclusion and an outlook for the respective proteins.

6.1 The +TIP network in yeast with Bik1 as a major contributor

For the budding yeast +TIP Bik1, the role of Bik1 in the +TIP network was rather poorly understood. Moreover, a structural and quantitative description of interaction such as the Bik1-Bim1 were not available. In this work, new insights about the Bik1 interaction network were obtained because we determined which parts of Bik1 can interact with the proteins Bim1, Kip2 and Stu2 and quantitively characterized these interactions. In addition, the crystal structure of the Bik1-Bim1 complex was solved, and this allowed probing the effect of the perturbation of this interaction in yeast cells to increase the understanding of the yeast +TIP network.

The crystal structure of Bik1 with the C-terminal tail of Bim1

Based on the crystal structure, we discovered that the CAP-Gly domain of Bik1 specifically recognizes the C-terminal phenylalanine in motifs like ETF by a slightly different binding mode compared to CAP-Gly domains of higher eukaryotes. This binding mode employs additional interactions such as a cation-π interaction, and the ETF motif is more deeply buried inside the binding pocket. Therefore, the structure permitted us to explain the higher affinity of Bik1 for ETF motifs and the prevention of tyrosine binding by a steric clash. It would be interesting to investigate if this binding mode is conserved in other yeast CAP-Gly domains like the one of NIP100, the p150Glued orthologue. Since in higher eukaryotes proteins such as CLIP-170 feature a C-terminal phenylalanine as well, in theory there could exist CAP-Gly domains of other proteins that apply a similar binding mode as the Bik1 CAP-Gly domain to target only motifs with a C-terminal phenylalanine and not tails like the α-tubulin tail with a tyrosine.

The ternary complex of Bik1-Bim1 with SxIP or LxxPTPh motifs and the implication of this complex for the +TIP network

Furthermore, it was proved that the binding of Bim1 to Bik1 and to SxIP or LxxPTPh motifs in proteins such as Kar9 is not mutually exclusive due to the longer C-terminal tail of Bim1 compared to mammalian EBs. Before, this was an open question because EBs cannot bind simultaneously to CLIP-170 and SxIP motifs (Duellberg et al., 2014). This result helps to describe the interaction network of +TIPs. For instance, in the Bim1-Bik1-Kip2 complex, Kip2 can interact with Bik1 via its coiled-coil and with Bim1 by its SxIP motif so that this ternary complex possesses strong and redundant interactions for its role in the dynein pathway (Miller et al., 2006; Roberts et al., 2014). A ternary complex between Bik1-Bim1 and Kar9 can be formed in which Bim1 can recruit Kar9 by SxIP and LxxPTPh motifs in the C-terminal tail of Kar9. It will be an interesting question to address which interactions of the Bik1-Bim1 complex with motifs such as the SxIP motif occur at which point during the cell cycle in yeast cells. The possibility of abrogating the binding of a specific SxIP motif harboring protein to Bim1 via phosphorylation (Drechsler et al., 2015; Honnappa et al., 2009) implies a mechanism for regulation. In addition, the individual affinities of the various SxIP and LxxPTPh motifs in yeast could be characterized in a similar fashion as it was performed for EBs (Buey et al., 2012). In the future, these insights together with the dissociation constants of interactions like the Bik1-Bim1 will help to simulate the composition of +TIP complexes and their influence on microtubule dynamics in various stages of the cell cycle.

Perturbations of the Bik1-Bim1 interaction

By the Bik1-Bim1 complex structure, it was possible to conceive two different mutations to perturb the Bik1-Bim1 interaction in yeast cells. In the case of the abrogation of the Bim1 binding by the deletion of the Bim1 ETF tail, the Bik1 localization decreased at the plus-end, but a certain amount of Bik1 was still localized at the plus-end via the transport by Kip2 (Carvalho et al., 2004). This illustrates the redundancy in the yeast +TIP network. The disruption of the Bik1 binding to any ETF-like motif, which can also be found in the C-terminal tail of α-tubulin, significantly reduced the amount of Bik1 on microtubules, and this observation highlights the importance of Bik1 attachment to microtubules by the CAP-Gly domain (Caudron et al., 2008). Without interactions with both Bim1 and microtubules, the Kip2 transport of Bik1 fails to localize a considerable amount of Bik1 at the plus-end. Therefore, it is crucial that Bik1 can either interact with Bim1 or microtubules so that Kip2 can fulfill its function. The binding of Bik1 to microtubules enriches Bik1 at microtubules so that both Bim1 and Kip2 can recruit Bik1 to the plus-end. By this result, we were able to define the minimal requirement for successful localization of Bik1 to the plus-end. Intriguingly, the perturbation of the Bik1-Bim1 interaction yielded longer microtubules in comparison to the wild-type. The deletion of Bim1 caused even longer microtubules. Overall, Bim1 appears to destabilize microtubules by the induction of GTP-hydrolysis (Maurer et al., 2014). Furthermore, the net effect of the recruited proteins by Bim1 could contribute to this effect. In addition, the Bim1-Bik1 interaction seems to participate in this destabilization of microtubules. It could be analyzed in the future if Bik1 enhances the destabilizing effect of Bim1. Besides, the influence of Bik1 and Bim1 on microtubule dynamics could be studied in detail.

Interplay between Bik1 and Kar9

Surprisingly, the abrogation of the Bik1-Bim1 interaction did not change the Kar9 asymmetry or the spindle alignment even though Bik1 participates in the asymmetric distribution of Kar9 (Moore et al., 2006). Thus, the Bim1-Bik1 interaction is not required for Kar9 asymmetry, and Bik1 could be involved by an indirect or unknown mechanism in this process. Additional research on the yeast +TIP network can reveal the relationship between Bik1 and Kar9. As Kip2 is supposed to indirectly interact with Kar9 and promote Kar9 asymmetry, Bik1 could connect Kip2 and Kar9 (Drechsler et al., 2015). A possibility would be to investigate the Kar9 localization in a mutant in which the Bik1-Kip2 interaction is perturbed. Although it has been reported that Bik1 could directly interact with the unstructured region of Kar9 (Moore et al., 2006), this interaction cannot occur by binding of the CAP-Gly domain to the C-terminal PTY motif of Kar9 because the tyrosine inhibits the binding. In order to determine the existence of a direct Bik1-Kar9 interaction, the full-length versions of both proteins should be tested for the complex formation.

Interaction of Bik1 with Stu2 and future experiments to investigate the +TIP network in yeast with a focus on Bik1

Furthermore, the binding of the Stu2 C-terminal tail to the Bik1 coiled-coil was validated by ITC experiments because only a yeast two-hybrid experiment indicated this interaction (Wolyniak et al., 2006). Since Bik1 can interact both with Bim1 and Stu2, these results establish Bik1 as an adaptor protein between Bim1 and Stu2. In contrast to a previous observation, Bim1 was not able to bind directly to Stu2. Due to this, a new function of Bik1 as a mediator of contact between these two proteins is revealed. Co-crystallization of the Bik1 coiled-coil together with a Stu2 C-terminal peptide could be conducted to understand the structural details of this interaction and why only one Stu2 C-terminal tail binds to a Bik1 dimer. In the future, the effect of Bik1 on Stu2 localization and activity should be researched. The available perturbations of the Bik1-Bim1 interaction could be employed, or the binding of Stu2 to Bik1 would be possible to abrogate by deleting the Stu2 C-terminal tail. In addition, Stu2 also attaches to Kar9 so that one indirect interaction to Bim1 would still exist when the binding to the adaptor protein Bik1 is disrupted. This example illustrates the complexity of the +TIP network that is even more multifaceted in higher eukaryotes. Yeast can be used as an excellent model organism to systematically perturb single interactions between +TIPs in order to study the effect of these disruptions. In a later stage, various perturbations of interactions can be combined to unravel the +TIP network. Additionally, it could be envisaged to mutate yeast tubulin because interactions could also be disrupted on the tubulin level. Besides, the full-length proteins of Bik1 and its interaction partners like Bim1 and Stu2 would allow conducting in vitro reconstitution of microtubules with these proteins to thoroughly probe the yeast +TIP network.

Specific mutations and truncations of the respective proteins could be employed for this as well. The in vivo experiments and the in vitro reconstitutions should be combined with further biochemical and structural studies. Altogether, these results would permit to simulate the yeast +TIP network in an elaborated manner.

Interaction of Bik1 with the kinesin Kip2

The determined high affinity of Bik1 binding to Kip2 illustrated that the two coiled-coils form a stable complex to transport Bik1 by Kip2 to the microtubule plus-end. Furthermore, we found that the truncation of Kip2 by the C-terminal unstructured tail abrogated the binding to the Bik1 coiled-coil. This truncation allowed the disruption of the Bik1-Kip2 interaction in an elegant way without removing the Kip2 coiled-coil, and this truncation was applied to study the role of the Bik1-Kip2 interaction for the polymerase activity of Kip2 (see next paragraph). In the literature, the interaction between the coiled-coils of Bik1 and Kip2 is depicted as only the binding of the coiled-coils to each other (Roberts et al., 2014). However, we discovered that C-terminal tail of Kip2 is indispensable for this interaction. In the future, the structure of the Bik1-Kip2 complex could be obtained to understand the role of the unstructured C-terminal tail for the binding of Kip2 to Bik1. In addition, the prediction of the Kip2 coiled-coil indicates that it consists of several shorter coiled-coils connected by loops. Crystallization screens of the Kip2 construct in which the C-terminal tail of Kip2 was truncated resulted in first hits. A structure of the Kip2 coiled-coil would reveal insights of the organization of this part of Kip2 and could help to explain the regulation of Kip2 because the phosphorylated N-terminal unstructured region of Kip2 appears to interact with the coiled-coil part of Kip2 (unpublished data of the Yves Barral group). The structure of the coiled-coil would help to identify the binding interface because it should be positively charged to interact with the negative charges of the phosphorylated sites. Interestingly, the complex of Bik1 and Kip2 is still capable of binding the C-terminal tail of Stu2 by Bik1 (our own unpublished data) so that a quaternary complex of Bim1-Bik1-Kip2-Stu2 can exist in the cell. This highlights that further studies must address these multi-protein complexes and should not only focus on binary interactions. In addition, it becomes important to reveal which subcomplexes occur at respective points of the cell cycle because post-translational modifications such as phosphorylation could disrupt certain interactions.

6.2 The kinesins Kip2 and Kip3 in the regulation of microtubule dynamics

Various kinesins play significant roles in the dynamics of microtubules. In contrast to the depolymerase mechanism of kinesins, their function in both polymerization and rescue of microtubules was mechanistically enigmatic. In this work, a mechanism was postulated how the budding yeast kinesin Kip2 can polymerize microtubule. In addition, we proposed a model for the microtubule rescue function of the budding yeast kinesin Kip3.

Insights into the microtubule polymerase Kip2

It was unresolved how a kinesin can function as a microtubule polymerase. We identified for the budding yeast kinesin-7 protein Kip2 that only the motor domain can bind both to microtubules and to soluble tubulin, and the other parts of Kip2 do not interact with either tubulin or microtubules. Three positively charged patches of the putative microtubule/tubulin-binding interface of the Kip2 motor domain were mutated to alanine. One interface mutant of the motor domain was identified that still localized to microtubules but bound to soluble tubulin with lower affinity in vitro and lost the ability to polymerize microtubules in cells. This highlights the crucial function of the tubulin binding by the Kip2 motor domain for the function as a polymerase. We propose that Kip2 can locally increase the concentration of soluble tubulin at the microtubule plus-end by its motor domain to act as a polymerase in a similar manner as Stu2 (Ayaz et al., 2012). However, Kip2 appears to require the interaction with Bik1 to efficiently function as a microtubule polymerase in the cell because the impairment of the Bik1-Kip2 interaction yielded the same phenotype with short microtubules as the Kip2 delete. An explanation for this could be that the Bik1 binding to microtubules and Bim1 tethers Kip2 at the microtubule plus-end so that the motor domain of Kip2 is only capable of efficiently enriching tubulin together with Bik1. It has been shown that Stu2 attaches with some of its TOG domains to the microtubule lattice and some TOG domains interact with soluble tubulin, indicating a similar mechanism (Ayaz et al., 2014; Geyer et al., 2018). However, Stu2 combines these two functions in one protein. The interaction of Bik1 with Kip2 could be disrupted by phosphorylation of its N-terminal unstructured tail, which seems to interact with the C-terminal part of Kip2 (unpublished data). This would allow the cell to regulate the Kip2 polymerase activity according to the stage of the cell cycle.

Mechanistical details of the Kip2 polymerase mechanism and future experiments

In order to verify the proposed mechanism, further experiments like the in vitro reconstitution of microtubule polymerization by the Bik1-Kip2 complex will be required. In these experiments, the impact of the interface mutant that has a lower affinity for tubulin could be probed. Surprisingly, in a published in vitro reconstitution, it has been reported that Kip2 shows some polymerase activity without Bik1 (Hibbel et al., 2015). Since Kip2 also appears to be a rescue factor for microtubules, this activity could be caused by a mechanism that only requires the motor domain in a dimeric state, and a dimeric construct of only the motor domain should be analyzed in in vitro reconstitutions. For the kinesin-7 CENP-E, it has been speculated that its motor domain could stabilize the transition of tubulin from the curved to the straight state (Sardar et al., 2010). It could be that the motor domain of Kip2 combines two different mechanisms to function efficiently as a polymerase. In the case of the motor domain, binding to soluble tubulin has only been reported for microtubule depolymerases such as the kinesin-13 family member MCAK (Wang et al., 2017). Therefore, this could indicate that some subtle differences exist between tubulin bound to Kip2 and MCAK.

The structural investigation by X-ray crystallography of the Kip2-tubulin complex could provide insights to better understand the Kip2 mechanism. Probably, tubulin capped with DARPin1 would be the best system for the co-crystallization because it has been successfully used for the co-crystallization of other kinesin motor domains with tubulin (Gigant et al., 2013; Wang et al., 2017). Besides, cryo-EM studies would be an option to perform on tubulin mixed with the Kip2 motor domain and microtubule seeds. In our studies, the Kip2 motor domain mixed with ATP and tubulin formed various larger aggregates on EM-grids. In the right condition, intermediates of the polymerization mechanism could be visualized. Furthermore, it remains enigmatic if the microtubule polymerization mechanism of Kip2 depends on ATP hydrolysis. For instance, the Kip3 motor domain depolymerizes microtubules in an ATP-independent mechanism (Arellano-Santoyo et al., 2017). In the Kip2 apo-state motor domain-tubulin mixture, the addition of ATP or ATP analogs like AMP-PNP caused aggregation. For other kinesins, it has been reported that the ATP-bound state displays the high-affinity state for tubulin binding. In order to understand if the aggregation is only a side effect of the high-affinity binding or the binding of tubulin by the ATP-bound Kip2 motor domain induces a transition state between the curved and straight tubulin, further studies will be required. The modulation of the tubulin-binding affinity by the ATPase cycle would explain how Kip2 can efficiently enrich tubulin at the microtubule plus-end because the low-affinity ADP state would allow the release of tubulin at the plus-end. Afterward, the high-affinity ATP state could recruit additional tubulin. Furthermore, the binding of the Bik1 CAP-Gly domain to soluble tubulin could enhances the enrichment of tubulin by Kip2. Overall, further research is indispensable to completely decipher the Kip2 mechanism of microtubule polymerization

The structure of the Kip3 tubulin-binding domain and its involvement in the rescue of microtubules

The work on the budding yeast kinesin Kip3 was motivated by the aim to elucidate its mechanism of microtubule rescue. For Kip3, we discovered that the C-terminal part contains a structured tubulin-binding domain (TBD) and an unstructured C-terminal tail providing a second weak microtubule-binding site in addition to the motor domain. The existence of two different interfaces in the C-terminal part was suggested in the literature (Su et al., 2011), but no boundaries or the preference for tubulin or microtubules were known. We were able to crystallize the Kip3 TBD, and the structure revealed a sophisticated structure instead of a simple dimerization domain that was assumed in the literature for this region of Kip3 (Su et al., 2011).

The Kip3 TBD bound to tubulin with a high affinity, and a construct consisting only of this domain depolymerized microtubules. However, in the context of the full-length Kip3, this domain is crucial for the microtubule rescue activity. This highlights that isolated domains can show the opposite activity as the full-length proteins. For instance, a similar observation has been reported for a single TOG domain of Stu2. We were able to define the minimal Kip3 construct that can induce microtubule rescue as a combination of the Kip3 motor domain and the Kip3 TBD. Furthermore, it was determined that the unstructured C-terminal tail does not participate in the rescue of microtubules. In the literature (Fukuda et al., 2014; Su et al., 2011), it had been assumed that the full C-terminal part of Kip3 is involved in rescue and could function without the motor domain.

The microtubule rescue mechanism of Kip3

A potential mechanism for the microtubule rescue by Kip3 could be the local increase of the tubulin concentration at the plus-end by the Kip3 TBD, which exhibits a high affinity for soluble tubulin. The microtubule-bound Kip3 motor domain would function as an anchor to microtubules. Stu2 applies a similar mechanism for microtubule polymerization by binding with some TOG domains to microtubules, and the other TOG domains recruit soluble tubulin. It would be interesting to fuse the Kip3 TBD to a TOG domain of Stu2 or the microtubule-binding domain of CPAP to observe the function of this chimeric protein. As the Kip3 motor domain can interact with curved tubulin at the very end of the plus-end as well, the Kip3 TBD would be perfectly positioned for this activity. At the microtubule plus-end, the enrichment of soluble tubulin by the Kip3 TBD would allow a transition to growing microtubules from shrinking ones because soluble tubulin mainly occurs in the GTP state. By the formation of a new GTP cap, the shrinkage could be stopped, and the microtubule would be rescued. Since the Kip3 TBD binds to curved tubulin, it does not only bind to the soluble tubulin, which always occurs in the curved state, but the Kip3 TBD can interact with the curved tubulin at microtubule ends as well. Therefore, the Kip3 TBD could substitute this GDP-bound curved tubulin to GTP-bound curved tubulin. By this, a GTP island would be established that can promote rescue of microtubules by inducing a switch from shrinkage to growing microtubules due to the formation of a new GTP cap. As the Kip3 motor domain on its own can depolymerize microtubules, it could stop this activity while serving as an anchor for the Kip3 TBD. A switch from the motile state to the depolymerizing state occurs in the Kip3 motor domain. Due to this, the Kip3 motor domain could remain in a state without depolymerizing activity. Since Kip3 appears to rescue microtubules at lower concentrations of Kip3 and induces catastrophe at higher concentrations, it is attractive to assume that a regulation mechanism must exist that deactivates the depolymerizing mechanism at lower concentrations.

Additional experiments to understand the Kip3 rescue function

In order to unravel the Kip3 rescue mechanism further and the interplay between the Kip3 TBD and the motor domain, additional research will be required, and various methods like cryo-EM tomography of microtubule ends and in vitro reconstitution of microtubules should be combined to address this question. In addition, it remains unknown if the Kip3 motor domain functions as an anchor by binding to straight tubulin or tubulin in the curved state at the very end of microtubules. In vitro reconstitutions of microtubule dynamic could assist to resolve this question by the observation of the Kip3 position on microtubules in the case of rescue events. Overall, the rescue of microtubules is still poorly understood, and the difference between proteins that function as a rescue factors or a microtubule polymerase has not been completely determined. The microtubule polymerase Kip2 can also rescue microtubules, indicating the close relationship between these two activities. Therefore, research combined on Kip2 and Kip3 can provide insights into the mechanisms of both microtubule rescue and polymerization.

Although the Kip3 C-terminal tail (Ctail) plays no role in the rescue function, this region can improve the microtubule-depolymerizing activity of the Kip3 motor domain. This is most likely achieved by increasing the processivity of the motor domain so that the Kip3 Ctail tethers the motor domain at microtubules. Therefore, these two parts are spatially separated but function in a synergistic fashion. In contrast to Kip3 orthologs in higher eukaryotes, the Kip3 Ctail did not localize on its own to microtubules in cells. Further research will be needed to confirm the function of the Ctail. In in vitro reconstructions, constructs encompassing the Kip3 motor domain dimerized by a leucine zipper together with the Kip3 Ctail are an option to investigate the influence of the Kip3 Ctail on the catastrophe frequency.

Future experiments to investigate the interaction of the Kip3 TBD with tubulin

A structure of the Kip3 TBD in complex with tubulin would reveal details how tubulin is bound by this domain. This could help to explain the rescue mechanism of Kip3 because depending on the binding site of tubulin a mechanism could be inferred. Based on ITC experiments, it appeared that the Kip3 TBD could bind to tubulin on a similar site as RB3. Unfortunately, extensive co-crystallization trials of the Kip3 TBD with tubulin were not successful. By chemical cross-linking of Kip3 with tubulin and rationally designed mutants of positively charged conserved residues, the potential tubulin-binding interface could be revealed. We have started a collaboration with a research group in Munich for the chemical cross-linking of the complex. Furthermore, a combination of docking Kip3 to tubulin and conservation of residues in Kip3 permitted to design various alanine substitutions of positively charged residues to screen for the tubulin-binding interface. One mutant in which two arginines of the neck coiled-coil were mutated showed weaker tubulin binding, indicating a potential involvement of these two residues. Based on the position of these two residues in the neck coiled-coil and some docking experiments, it can be hypothesized that Kip3 probably binds tubulin in a lateral manner. This would correspond to the similar binding mode as RB3. Since the kinked coiled-coil is involved, this binding mode would explain why only one tubulin is capable of binding to the Kip3 homodimer. Additional mutants will be screened in the future to identify further mutants to disrupt the binding of Kip3 to tubulin. The tubulin-binding interface mutants permit the perturbation of tubulin binding by Kip3 in yeast cells without deleting the C-terminal part. In the near future, the group of Yves Barral will probe the effect of various interface mutants on microtubule dynamics with a focus on the changes of catastrophe and rescue frequency. These experiments will provide new insights on how the tubulin binding of the Kip3 TBD achieve the microtubule rescue because these mutants will eliminate or reduce tubulin binding but otherwise will completely resemble the wild-type.

In terms of the co-crystallization of Kip3 together with tubulin, the bovine brain tubulin could be replaced by recombinant yeast tubulin because the two available structures of the Stu2 TOG domains with tubulin (Ayaz et al., 2014; Ayaz et al., 2012) were obtained by using a polymerization-blocked mutant of yeast tubulin (Johnson et al., 2011). Furthermore, the presumed tubulin-binding domain of the Kip3 orthologues, Kif18a and Kif19a, could be characterized regarding their ability to bind to tubulin. It represents an attractive question if the rescue mechanism of Kip3 is conserved in higher eukaryotes. As an additional approach, the co-crystallization of Kif18a or Kif19a with bovine brain tubulin would be worth an attempt. Since the recent technical advances in the cryo-EM field allow the structural determination of protein complex in the 100 kDa range (Khoshouei et al., 2017; Merk et al., 2016), the Kip3-tubulin-DARPin1 complex could be also investigated by this method. Furthermore, Bio-SAXS experiments of this complex would be a possible approach to obtain a low-resolution structure that could be combined with the results of the mass spectrometry.

6.3 Emerging regulation of the minus-end by -TIPs such as CAMSAPs

The recognition of the microtubule minus-end by CAMSAP proteins

The publication about the CAMSAP CKK domain provided the first structural description of how a -TIP targets the minus-end of microtubules. Cryo-EM tomography allowed understanding how the CKK domain binds to the unique curved state of tubulin at the microtubule minus-end. Although both the microtubule plus-end and the microtubule minus-end feature curved tubulin, it was discovered that the β-tubulin has a higher lateral curvature at the minus-end. In contrast, the α-tubulin occurs in a low lateral curvature state at the minus-end. On the plus-end, the opposite states of curvature exist for α/β-tubulin. The CKK domain requires the highly curved β-tubulin to interact strongly with microtubules. This explains the preference for the minus-end because other parts of the microtubule provide less favorable interactions. Therefore, the CKK domain allows CAMSAPs to discriminate between the plus-end and the minus-end in contrast to EBs that are capable of tracking both the plus-end and minus-end by recognizing an intermediate state of GTP hydrolysis near the GTP cap (Maurer et al., 2014). Especially, further research on microtubule ends will improve our understanding of the subtle differences between these two ends, and how +TIPs and -TIPs have adapted to recognize them. Cryo-EM tomography is an invaluable method to investigate microtubule ends due to its ability to probe only the end compared to the average of the full microtubule lattice by single particle analysis. In the case of CAMSAP2 and CAMSAP3, other parts of the CAMSAP proteins like the unstructured microtubule-binding domain increase affinity for microtubules and selectivity for the minus-end. In the future, the role of these part should be analyzed to reveal their contribution. This will help explain why CAMSAP2/3 can not only track the minus-end but stabilize it as well (Jiang et al., 2014). Furthermore, CAMSAP proteins are capable of interacting with additional proteins such as Calmodulin and Spectrin (Akhmanova and Hoogenraad, 2015). The role of these interactions for the CAMSAP function should be addressed in further research.

Combination of various methods to investigate the function of -TIPs

Since in the CAMSAP publication a combination of the structural biology methods X-ray crystallography, cryo-EM single particle analysis, cryo-EM tomography and solid-state NMR was applied, this highlights the importance of combining the strengths of various methods to investigate the microtubule-binding mechanism of a protein in the case of future projects. Besides, we also found a mutant of the CKK domain with increased affinity for microtubule binding but less specificity for the minus-end. Based on our structural analysis, the mutant with the increased affinity seemed to partially lose the ability to differentiate between the special curved state at the minus-end and tubulin inside other parts of microtubules. This exemplifies that in evolution the highest affinity version of a protein is not always preferred, but a combination of decent affinity with elevated selectivity is chosen. In addition, we have identified a CKK domain of a protist organism that possesses no specificity for the microtubule minus-end. The aim of this ongoing research is to understand how this CKK domain bind to microtubules, and this could help reveal the specificity of CKK domains of higher eukaryotes in more detail by comparing the differences.

Future work on further -TIPs

In the future, the mechanism of recently discovered -TIPs such as the protein ASPM, which autonomously track the minus-end, should be investigated to elucidate their minus-end recognition mechanism. ASPM seems to track the minus-end by combining four CH domains and a C-terminal HEAT-repeat domain (Jiang et al., 2017) (unpublished data). Since EBs contain a single CH domain, it is enigmatic what the mechanism of the four CH domains in combination with the C-terminal domain for minus-end tracking could be. A similar approach as for the CKK domain would be an option to apply. However, the apparent combination of various domains could increase the difficulty. Nevertheless, ASPM, which plays a significant role in spindle positioning in higher eukaryotes (Gai et al., 2016), represents a very interesting protein from the medical point of view because it is crucial for neuronal development, and mutations in ASPM are linked to microcephaly.

6.4 Final outlook

In this thesis, important insights into the role of Bik1 in the +TIP network were obtained. In order to understand this network better, simulations of the +TIPs composition at various points of the cell cycle represent an attractive approach. Results such as the determined dissociation constants together with previous findings will allow the simulation of a part of the +TIP network in the future. Recent research on +TIPs has discovered that the phenomenon of liquid-liquid phase separation appears to play a crucial role in various +TIPs (posters at the EMBO Symposium Microtubules 2018). Interestingly, both Bik1 and Kar9 show phase separation under certain conditions in vitro (unpublished results of our group). Therefore, future research on +TIP should take into account the existence of the phase separation to permit a holistic understanding of the +TIP network. In the phase-separated droplets, weak interactions between +TIPs that are normally not observable could be pivotal. In addition, it has been reported that phase separation might occur during the polymerization of tubulin into microtubules (Hernandez-Vega et al., 2017; Woodruff et al., 2017). Although the understanding of the microtubule polymerase Kip2 was significantly expanded in this thesis, some details about the polymerase mechanism remain enigmatic. One route worth testing is to assess whether Kip2 phase separates or induce phase separation in the presence of tubulin. Due to the crucial function of Bik1 for the polymerase activity of Kip2, Bik1 could cause this phase separation as well. For the microtubule rescue function of Kip3 and the minus-end tracking by -TIPs such as CAMSAPs, properties of the microtubule ends seem to be crucial. Advancements in our knowledge of the structure of both microtubule ends will reveal, for instance, how rescue events of microtubules and minus-end tracking are brought about at unprecedented resolution. In this context, cryo-EM tomography of microtubule ends represents the key methods to investigate the microtubule ends on a molecular level.

Overall, this thesis contributes to the understanding of the +TIP network, the function of kinesins as microtubule polymerases, the rescue of microtubules by kinesins and the microtubule minus-end tracking by -TIPs. For all these four areas, attractive future research topics have been identified.

7. Further manuscripts in preparation

During my Ph.D. work, I was also involved in additional projects. For the following projects, it is envisaged to submit manuscripts in the future.

Chen, X., Widmer, L., Stangier, M.M., Steinmetz, M.O., Stelling, J., Barral, Y., A mechanism for the control of microtubule plus-end dynamics from the minus-end

One manuscript about the protein Kar9 in collaboration with Anil Kumar (group of Prof. Dr. Michel Steinmetz) and the group of Prof. Dr. Yves Barral

One manuscript about the microtubule binding of the *N. gruberi* CKK domain with the group of Prof. Dr. Carolyn Moores

8. References

Aher, A., and Akhmanova, A. (2018). Tipping microtubule dynamics, one protofilament at a time. Curr Opin Cell Biol *50*, 86-93.

Akhmanova, A., and Hoogenraad, C.C. (2015). Microtubule minus-end-targeting proteins. Curr Biol *25*, R162-171.

Akhmanova, A., and Steinmetz, M.O. (2010). Microtubule +TIPs at a glance. Journal of cell science *123*, 3415-3419.

Akhmanova, A., and Steinmetz, M.O. (2015). Control of microtubule organization and dynamics: two ends in the limelight. Nat Rev Mol Cell Biol *16*, 711-726.

Al-Bassam, J., Ozer, R.S., Safer, D., Halpain, S., and Milligan, R.A. (2002). MAP2 and tau bind longitudinally along the outer ridges of microtubule protofilaments. J Cell Biol *157*, 1187-1196.

Al-Bassam, J., van Breugel, M., Harrison, S.C., and Hyman, A. (2006). Stu2p binds tubulin and undergoes an open-to-closed conformational change. J Cell Biol *172*, 1009-1022.

Allen, R.D., Metuzals, J., Tasaki, I., Brady, S.T., and Gilbert, S.P. (1982). Fast axonal transport in squid giant axon. Science *218*, 1127-1129.

Amos, L.A., and Schlieper, D. (2005). Microtubules and maps. Advances in protein chemistry *71*, 257-298.

Arellano-Santoyo, H., Geyer, E.A., Stokasimov, E., Chen, G.Y., Su, X., Hancock, W., Rice, L.M., and Pellman, D. (2017). A Tubulin Binding Switch Underlies Kip3/Kinesin-8 Depolymerase Activity. Dev Cell *42*, 37-51 e38.

Arnal, I., Heichette, C., Diamantopoulos, G.S., and Chretien, D. (2004). CLIP-170/tubulin-curved oligomers coassemble at microtubule ends and promote rescues. Curr Biol *14*, 2086-2095.

Atherton, J., Farabella, I., Yu, I.M., Rosenfeld, S.S., Houdusse, A., Topf, M., and Moores, C.A. (2014). Conserved mechanisms of microtubule-stimulated ADP release, ATP binding, and force generation in transport kinesins. eLife *3*, e03680.

Ayaz, P., Munyoki, S., Geyer, E.A., Piedra, F.A., Vu, E.S., Bromberg, R., Otwinowski, Z., Grishin, N.V., Brautigam, C.A., and Rice, L.M. (2014). A tethered delivery mechanism explains the catalytic action of a microtubule polymerase. eLife *3*, e03069.

Ayaz, P., Ye, X., Huddleston, P., Brautigam, C.A., and Rice, L.M. (2012). A TOG:alphabeta-tubulin complex structure reveals conformation-based mechanisms for a microtubule polymerase. Science *337*, 857-860.

Badin-Larcon, A.C., Boscheron, C., Soleilhac, J.M., Piel, M., Mann, C., Denarier, E., Fourest-Lieuvin, A., Lafanechere, L., Bornens, M., and Job, D. (2004). Suppression of nuclear oscillations in Saccharomyces cerevisiae expressing Glu tubulin. Proc Natl Acad Sci U S A *101*, 5577-5582.

Baines, A.J., Bignone, P.A., King, M.D., Maggs, A.M., Bennett, P.M., Pinder, J.C., and Phillips, G.W. (2009). The CKK domain (DUF1781) binds microtubules and defines the CAMSAP/ssp4 family of animal proteins. Mol Biol Evol *26*, 2005-2014.

Berlin, V., Styles, C.A., and Fink, G.R. (1990). BIK1, a protein required for microtubule function during mating and mitosis in Saccharomyces cerevisiae, colocalizes with tubulin. J Cell Biol *111*, 2573-2586.

Bezanilla, M., Gladfelter, A.S., Kovar, D.R., and Lee, W.L. (2015). Cytoskeletal dynamics: a view from the membrane. J Cell Biol *209*, 329-337.

Blake-Hodek, K.A., Cassimeris, L., and Huffaker, T.C. (2010). Regulation of microtubule dynamics by Bim1 and Bik1, the budding yeast members of the EB1 and CLIP-170 families of plus-end tracking proteins. Molecular biology of the cell *21*, 2013-2023.

Blanchoin, L., Boujemaa-Paterski, R., Sykes, C., and Plastino, J. (2014). Actin dynamics, architecture, and mechanics in cell motility. Physiological reviews *94*, 235-263.

Brinkley, W. (1997). Microtubules: a brief historical perspective. J Struct Biol *118*, 84-86.

Brouhard, G.J. (2015). Dynamic instability 30 years later: complexities in microtubule growth and catastrophe. Molecular biology of the cell *26*, 1207-1210.

Brouhard, G.J., and Rice, L.M. (2014). The contribution of alphabeta-tubulin curvature to microtubule dynamics. J Cell Biol *207*, 323-334.

Brouhard, G.J., and Rice, L.M. (2018). Microtubule dynamics: an interplay of biochemistry and mechanics. Nat Rev Mol Cell Biol *19*, 451-463.

Buey, R.M., Sen, I., Kortt, O., Mohan, R., Gfeller, D., Veprintsev, D., Kretzschmar, I., Scheuermann, J., Neri, D., Zoete, V.*, et al.* (2012). Sequence determinants of a microtubule tip localization signal (MtLS). J Biol Chem *287*, 28227-28242.

Campbell, J.N., and Slep, K.C. (2011). alphabeta-Tubulin and microtubule-binding assays. Methods in molecular biology (Clifton, N.J.) *777*, 87-97.

Carvalho, P., Gupta, M.L., Jr., Hoyt, M.A., and Pellman, D. (2004). Cell cycle control of kinesin-mediated transport of Bik1 (CLIP-170) regulates microtubule stability and dynein activation. Dev Cell *6*, 815-829.

Caudron, F., Andrieux, A., Job, D., and Boscheron, C. (2008). A new role for kinesin-directed transport of Bik1p (CLIP-170) in Saccharomyces cerevisiae. Journal of cell science *121*, 1506-1513.

Chaaban, S., and Brouhard, G.J. (2017). A microtubule bestiary: structural diversity in tubulin polymers. Molecular biology of the cell *28*, 2924-2931.

Chen, Y., and Hancock, W.O. (2015). Kinesin-5 is a microtubule polymerase. Nat Commun *6*, 8160.

Chretien, D., Kenney, J.M., Fuller, S.D., and Wade, R.H. (1996). Determination of microtubule polarity by cryo-electron microscopy. Structure (London, England : 1993) *4*, 1031-1040.

Cottingham, F.R., and Hoyt, M.A. (1997). Mitotic Spindle Positioning inSaccharomyces cerevisiaeIs Accomplished by Antagonistically Acting Microtubule Motor Proteins. The Journal of Cell Biology *138*, 1041-1053.

Cross, R.A. (2004). The kinetic mechanism of kinesin. Trends Biochem Sci *29*, 301-309.

Dasso, M. (2016). Kar9 Controls the Cytoplasm by Visiting the Nucleus. Dev Cell *36*, 360-361.

Dave, S., Anderson, S.J., Roy, P.S., Nsamba, E.T., Bunning, A.R., Fukuda, Y., and Gupta, M.L., Jr. (2018). Discrete regions of the kinesin-8 Kip3 tail differentially mediate astral microtubule stability and spindle disassembly. Molecular biology of the cell, mbcE18030199.

Davidson, A.J., and Wood, W. (2016). Unravelling the Actin Cytoskeleton: A New Competitive Edge? Trends in cell biology *26*, 569-576.

Desai, A., and Mitchison, T.J. (1997). Microtubule polymerization dynamics. Annu Rev Cell Dev Biol *13*, 83-117.

Dominguez, R., and Holmes, K.C. (2011). Actin structure and function. Annual review of biophysics *40*, 169-186.

Domnitz, S.B., Wagenbach, M., Decarreau, J., and Wordeman, L. (2012). MCAK activity at microtubule tips regulates spindle microtubule length to promote robust kinetochore attachment. J Cell Biol *197*, 231-237.

Doodhi, H., Prota, A.E., Rodriguez-Garcia, R., Xiao, H., Custar, D.W., Bargsten, K., Katrukha, E.A., Hilbert, M., Hua, S., Jiang, K.*, et al.* (2016). Termination of Protofilament Elongation by Eribulin Induces Lattice Defects that Promote Microtubule Catastrophes. Curr Biol *26*, 1713-1721.

Dorleans, A., Gigant, B., Ravelli, R.B., Mailliet, P., Mikol, V., and Knossow, M. (2009). Variations in the colchicine-binding domain provide insight into the structural switch of tubulin. Proc Natl Acad Sci U S A *106*, 13775-13779.

Drechsler, H., Tan, A.N., and Liakopoulos, D. (2015). Yeast GSK-3 kinase regulates astral microtubule function through phosphorylation of the microtubule-stabilizing kinesin Kip2. Journal of cell science *128*, 3910-3921.

Drummond, D.R. (2011). Regulation of microtubule dynamics by kinesins. Semin Cell Dev Biol *22*, 927-934.

Duellberg, C., Trokter, M., Jha, R., Sen, I., Steinmetz, M.O., and Surrey, T. (2014). Reconstitution of a hierarchical +TIP interaction network controlling microtubule end tracking of dynein. Nat Cell Biol *16*, 804-811.

Endow, S.A., Kull, F.J., and Liu, H. (2010). Kinesins at a glance. Journal of cell science *123*, 3420-3424.

Erickson, H.P. (2007). Evolution of the cytoskeleton. Bioessays *29*, 668-677.

Fletcher, D.A., and Mullins, R.D. (2010). Cell mechanics and the cytoskeleton. Nature *463*, 485-492.

Forth, S., and Kapoor, T.M. (2017). The mechanics of microtubule networks in cell division. J Cell Biol *216*, 1525-1531.

Frixione, E. (2000). Recurring views on the structure and function of the cytoskeleton: a 300-year epic. Cell motility and the cytoskeleton *46*, 73-94.

Fukuda, Y., Luchniak, A., Murphy, E.R., and Gupta, M.L., Jr. (2014). Spatial control of microtubule length and lifetime by opposing stabilizing and destabilizing functions of Kinesin-8. Curr Biol *24*, 1826-1835.

Gai, M., Bianchi, F.T., Vagnoni, C., Verni, F., Bonaccorsi, S., Pasquero, S., Berto, G.E., Sgro, F., Chiotto, A.M., Annaratone, L.*, et al.* (2016). ASPM and CITK regulate spindle orientation by affecting the dynamics of astral microtubules. EMBO reports *17*, 1396-1409.

Gandhi, S.R., Gierlinski, M., Mino, A., Tanaka, K., Kitamura, E., Clayton, L., and Tanaka, T.U. (2011). Kinetochore-dependent microtubule rescue ensures their efficient and sustained interactions in early mitosis. Dev Cell *21*, 920-933.

Gardner, M.K., Zanic, M., and Howard, J. (2013). Microtubule catastrophe and rescue. Curr Opin Cell Biol *25*, 14-22.

Geyer, E.A., Miller, M.P., Brautigam, C.A., Biggins, S., and Rice, L.M. (2018). Design principles of a microtubule polymerase. eLife *7*.

Gigant, B., Curmi, P.A., Martin-Barbey, C., Charbaut, E., Lachkar, S., Lebeau, L., Siavoshian, S., Sobel, A., and Knossow, M. (2000). The 4 A X-ray structure of a tubulin:stathmin-like domain complex. Cell *102*, 809-816.

Gigant, B., Wang, W., Dreier, B., Jiang, Q., Pecqueur, L., Pluckthun, A., Wang, C., and Knossow, M. (2013). Structure of a kinesin-tubulin complex and implications for kinesin motility. Nat Struct Mol Biol *20*, 1001-1007.

Gong, T., Yan, Y., Zhang, J., Liu, S., Liu, H., Gao, J., Zhou, X., Chen, J., and Shi, A. (2018). PTRN-1/CAMSAP promotes CYK-1/formin-dependent actin polymerization during endocytic recycling. EMBO J *37*.

Gordon, N.K., and Gordon, R. (2017). Embryogenesis explained (Singapore ; Hackensack, NJ : World Scientific Publishing Co. Pte. Ltd.).

Guesdon, A., Bazile, F., Buey, R.M., Mohan, R., Monier, S., Garcia, R.R., Angevin, M., Heichette, C., Wieneke, R., Tampe, R.*, et al.* (2016). EB1 interacts with outwardly curved and straight regions of the microtubule lattice. Nat Cell Biol *18*, 1102-1108.

Gupta, K.K., Paulson, B.A., Folker, E.S., Charlebois, B., Hunt, A.J., and Goodson, H.V. (2009). Minimal plus-end tracking unit of the cytoplasmic linker protein CLIP-170. J Biol Chem *284*, 6735-6742.

Hardin, J., Bertoni, G., Kleinsmith, L.J., and Becker, W.M. (2012). Becker's World of the Cell (Benjamin Cummings).

Hayashi, I., and Ikura, M. (2003). Crystal structure of the amino-terminal microtubule-binding domain of end-binding protein 1 (EB1). J Biol Chem *278*, 36430-36434.

Hendershott, M.C., and Vale, R.D. (2014). Regulation of microtubule minus-end dynamics by CAMSAPs and Patronin. Proc Natl Acad Sci U S A *111*, 5860-5865.

Hernandez-Vega, A., Braun, M., Scharrel, L., Jahnel, M., Wegmann, S., Hyman, B.T., Alberti, S., Diez, S., and Hyman, A.A. (2017). Local Nucleation of Microtubule Bundles through Tubulin Concentration into a Condensed Tau Phase. Cell Rep *20*, 2304-2312.

Herrmann, H., and Aebi, U. (2016). Intermediate Filaments: Structure and Assembly. Cold Spring Harbor perspectives in biology *8*.

Herrmann, H., Strelkov, S.V., Burkhard, P., and Aebi, U. (2009). Intermediate filaments: primary determinants of cell architecture and plasticity. The Journal of clinical investigation *119*, 1772-1783.

Hibbel, A., Bogdanova, A., Mahamdeh, M., Jannasch, A., Storch, M., Schaffer, E., Liakopoulos, D., and Howard, J. (2015). Kinesin Kip2 enhances microtubule growth in vitro through length-dependent feedback on polymerization and catastrophe. eLife *4*.

Hirose, K., Akimaru, E., Akiba, T., Endow, S.A., and Amos, L.A. (2006). Large conformational changes in a kinesin motor catalyzed by interaction with microtubules. Mol Cell *23*, 913-923.

Honnappa, S., Gouveia, S.M., Weisbrich, A., Damberger, F.F., Bhavesh, N.S., Jawhari, H., Grigoriev, I., van Rijssel, F.J., Buey, R.M., Lawera, A.*, et al.* (2009). An EB1-binding motif acts as a microtubule tip localization signal. Cell *138*, 366-376.

Honnappa, S., John, C.M., Kostrewa, D., Winkler, F.K., and Steinmetz, M.O. (2005). Structural insights into the EB1-APC interaction. EMBO J *24*, 261-269.

Honnappa, S., Okhrimenko, O., Jaussi, R., Jawhari, H., Jelesarov, I., Winkler, F.K., and Steinmetz, M.O. (2006). Key interaction modes of dynamic +TIP networks. Mol Cell *23*, 663-671.

Howard, J., and Hyman, A.A. (2003). Dynamics and mechanics of the microtubule plus end. Nature *422*, 753-758.

Howes, S.C., Geyer, E.A., LaFrance, B., Zhang, R., Kellogg, E.H., Westermann, S., Rice, L.M., and Nogales, E. (2017). Structural differences between yeast and mammalian microtubules revealed by cryo-EM. J Cell Biol *216*, 2669-2677.

Howes, S.C., Geyer, E.A., LaFrance, B., Zhang, R., Kellogg, E.H., Westermann, S., Rice, L.M., and Nogales, E. (2018). Structural and functional differences between porcine brain and budding yeast microtubules. Cell Cycle *17*, 278-287.

Huber, F., Schnauss, J., Ronicke, S., Rauch, P., Muller, K., Futterer, C., and Kas, J. (2013). Emergent complexity of the cytoskeleton: from single filaments to tissue. Advances in physics *62*, 1-112.

Ishikawa, H., and Marshall, W.F. (2013). Isolation of mammalian primary cilia. Methods Enzymol *525*, 311-325.

Janke, C. (2014). The tubulin code: molecular components, readout mechanisms, and functions. J Cell Biol *206*, 461-472.

Jiang, K., Faltova, L., Hua, S., Capitani, G., Prota, A.E., Landgraf, C., Volkmer, R., Kammerer, R.A., Steinmetz, M.O., and Akhmanova, A. (2018). Structural Basis of Formation of the Microtubule Minus-End-Regulating CAMSAP-Katanin Complex. Structure (London, England : 1993) *26*, 375-382 e374.

Jiang, K., Hua, S., Mohan, R., Grigoriev, I., Yau, K.W., Liu, Q., Katrukha, E.A., Altelaar, A.F., Heck, A.J., Hoogenraad, C.C.*, et al.* (2014). Microtubule minus-end stabilization by polymerization-driven CAMSAP deposition. Dev Cell *28*, 295-309.

Jiang, K., Rezabkova, L., Hua, S., Liu, Q., Capitani, G., Altelaar, A.F.M., Heck, A.J.R., Kammerer, R.A., Steinmetz, M.O., and Akhmanova, A. (2017). Microtubule minus-end regulation at spindle poles by an ASPM-katanin complex. Nat Cell Biol *19*, 480-492.

Johnson, V., Ayaz, P., Huddleston, P., and Rice, L.M. (2011). Design, overexpression, and purification of polymerization-blocked yeast alphabeta-tubulin mutants. Biochemistry *50*, 8636-8644.

Kapoor, T.M., Lampson, M.A., Hergert, P., Cameron, L., Cimini, D., Salmon, E.D., McEwen, B.F., and Khodjakov, A. (2006). Chromosomes can congress to the metaphase plate before biorientation. Science *311*, 388-391.

Keating, T.J., Peloquin, J.G., Rodionov, V.I., Momcilovic, D., and Borisy, G.G. (1997). Microtubule release from the centrosome. Proc Natl Acad Sci U S A *94*, 5078-5083.

Kellogg, E.H., Hejab, N.M.A., Poepsel, S., Downing, K.H., DiMaio, F., and Nogales, E. (2018). Near-atomic model of microtubule-tau interactions. Science *360*, 1242-1246.

Khoshouei, M., Radjainia, M., Baumeister, W., and Danev, R. (2017). Cryo-EM structure of haemoglobin at 3.2 A determined with the Volta phase plate. Nat Commun *8*, 16099.

Kollman, J.M., Merdes, A., Mourey, L., and Agard, D.A. (2011). Microtubule nucleation by gamma-tubulin complexes. Nat Rev Mol Cell Biol *12*, 709-721.

Komarova, Y., De Groot, C.O., Grigoriev, I., Gouveia, S.M., Munteanu, E.L., Schober, J.M., Honnappa, S., Buey, R.M., Hoogenraad, C.C., Dogterom, M.*, et al.* (2009). Mammalian end binding proteins control persistent microtubule growth. J Cell Biol *184*, 691-706.

Kozielski, F., Sack, S., Marx, A., Thormahlen, M., Schonbrunn, E., Biou, V., Thompson, A., Mandelkow, E.M., and Mandelkow, E. (1997). The crystal structure of dimeric kinesin and implications for microtubule-dependent motility. Cell *91*, 985-994.

Kull, F.J., Sablin, E.P., Lau, R., Fletterick, R.J., and Vale, R.D. (1996). Crystal structure of the kinesin motor domain reveals a structural similarity to myosin. Nature *380*, 550-555.

Kumar, A., Manatschal, C., Rai, A., Grigoriev, I., Degen, M.S., Jaussi, R., Kretzschmar, I., Prota, A.E., Volkmer, R., Kammerer, R.A.*, et al.* (2017). Short Linear Sequence Motif LxxPTPh Targets Diverse Proteins to Growing Microtubule Ends. Structure (London, England : 1993) *25*, 924-932.e924.

Kurihara, L.J., Beh, C.T., Latterich, M., Schekman, R., and Rose, M.D. (1994). Nuclear congression and membrane fusion: two distinct events in the yeast karyogamy pathway. J Cell Biol *126*, 911-923.

Kusch, J., Liakopoulos, D., and Barral, Y. (2003). Spindle asymmetry: a compass for the cell. Trends in cell biology *13*, 562-569.

Lansbergen, G., Komarova, Y., Modesti, M., Wyman, C., Hoogenraad, C.C., Goodson, H.V., Lemaitre, R.P., Drechsel, D.N., van Munster, E., Gadella, T.W., Jr.*, et al.* (2004). Conformational changes in CLIP-170 regulate its binding to microtubules and dynactin localization. J Cell Biol *166*, 1003-1014.

Lawrence, C.J., Dawe, R.K., Christie, K.R., Cleveland, D.W., Dawson, S.C., Endow, S.A., Goldstein, L.S., Goodson, H.V., Hirokawa, N., Howard, J.*, et al.* (2004). A standardized kinesin nomenclature. J Cell Biol *167*, 19-22.

Lee, S.H., and Dominguez, R. (2010). Regulation of actin cytoskeleton dynamics in cells. Molecules and cells *29*, 311-325.

Leisner, C., Kammerer, D., Denoth, A., Britschi, M., Barral, Y., and Liakopoulos, D. (2008). Regulation of mitotic spindle asymmetry by SUMO and the spindle-assembly checkpoint in yeast. Curr Biol *18*, 1249-1255.

Li, R., and Gundersen, G.G. (2008). Beyond polymer polarity: how the cytoskeleton builds a polarized cell. Nat Rev Mol Cell Biol *9*, 860-873.

Liakopoulos, D., Kusch, J., Grava, S., Vogel, J., and Barral, Y. (2003). Asymmetric loading of Kar9 onto spindle poles and microtubules ensures proper spindle alignment. Cell *112*, 561-574.

Lin, H., de Carvalho, P., Kho, D., Tai, C.Y., Pierre, P., Fink, G.R., and Pellman, D. (2001). Polyploids require Bik1 for kinetochore-microtubule attachment. J Cell Biol *155*, 1173-1184.

Locke, J., Joseph, A.P., Pena, A., Mockel, M.M., Mayer, T.U., Topf, M., and Moores, C.A. (2017). Structural basis of human kinesin-8 function and inhibition. Proc Natl Acad Sci U S A *114*, E9539-E9548.

Lowe, J., Li, H., Downing, K.H., and Nogales, E. (2001). Refined structure of alpha beta-tubulin at 3.5 A resolution. Journal of molecular biology *313*, 1045-1057.

Maekawa, H., Usui, T., Knop, M., and Schiebel, E. (2003). Yeast Cdk1 translocates to the plus end of cytoplasmic microtubules to regulate bud cortex interactions. Embo j *22*, 438-449.

Manatschal, C., Farcas, A.M., Degen, M.S., Bayer, M., Kumar, A., Landgraf, C., Volkmer, R., Barral, Y., and Steinmetz, M.O. (2016). Molecular basis of Kar9-Bim1 complex function during mating and spindle positioning. Molecular biology of the cell.

Mandelkow, E., and Mandelkow, E.M. (1995). Microtubules and microtubule-associated proteins. Curr Opin Cell Biol *7*, 72-81.

Martin, M., and Akhmanova, A. (2018). Coming into Focus: Mechanisms of Microtubule Minus-End Organization. Trends in cell biology *28*, 574-588.

Marx, A., Hoenger, A., and Mandelkow, E. (2009). Structures of kinesin motor proteins. Cell motility and the cytoskeleton *66*, 958-966.

Maurer, S.P., Cade, N.I., Bohner, G., Gustafsson, N., Boutant, E., and Surrey, T. (2014). EB1 accelerates two conformational transitions important for microtubule maturation and dynamics. Curr Biol *24*, 372-384.

Maurer, S.P., Fourniol, F.J., Bohner, G., Moores, C.A., and Surrey, T. (2012). EBs recognize a nucleotide-dependent structural cap at growing microtubule ends. Cell *149*, 371-382.

Merk, A., Bartesaghi, A., Banerjee, S., Falconieri, V., Rao, P., Davis, M.I., Pragani, R., Boxer, M.B., Earl, L.A., Milne, J.L.S., *et al.* (2016). Breaking Cryo-EM Resolution Barriers to Facilitate Drug Discovery. Cell *165*, 1698-1707.

Miller, R.K., D'Silva, S., Moore, J.K., and Goodson, H.V. (2006). The CLIP-170 orthologue Bik1p and positioning the mitotic spindle in yeast. Current topics in developmental biology *76*, 49-87.

Miller, R.K., Heller, K.K., Frisen, L., Wallack, D.L., Loayza, D., Gammie, A.E., and Rose, M.D. (1998). The kinesin-related proteins, Kip2p and Kip3p, function differently in nuclear migration in yeast. Molecular biology of the cell *9*, 2051-2068.

Miller, R.K., and Rose, M.D. (1998). Kar9p is a novel cortical protein required for cytoplasmic microtubule orientation in yeast. J Cell Biol *140*, 377-390.

Mitchison, T., and Kirschner, M. (1984). Dynamic instability of microtubule growth. Nature *312*, 237-242.

Moore, J.K., D'Silva, S., and Miller, R.K. (2006). The CLIP-170 homologue Bik1p promotes the phosphorylation and asymmetric localization of Kar9p. Molecular biology of the cell *17*, 178-191.

Moore, J.K., and Miller, R.K. (2007). The cyclin-dependent kinase Cdc28p regulates multiple aspects of Kar9p function in yeast. Molecular biology of the cell *18*, 1187-1202.

Moore, J.K., Stuchell-Brereton, M.D., and Cooper, J.A. (2009). Function of dynein in budding yeast: mitotic spindle positioning in a polarized cell. Cell motility and the cytoskeleton *66*, 546-555.

Newman, J.R., Wolf, E., and Kim, P.S. (2000). A computationally directed screen identifying interacting coiled coils from Saccharomyces cerevisiae. Proc Natl Acad Sci U S A *97*, 13203-13208.

Niwa, S., Nakajima, K., Miki, H., Minato, Y., Wang, D., and Hirokawa, N. (2012). KIF19A is a microtubule-depolymerizing kinesin for ciliary length control. Dev Cell *23*, 1167-1175.

Nogales, E. (2000). Structural insights into microtubule function. Annual review of biochemistry *69*, 277-302.

Nogales, E., and Scheres, S.H. (2015). Cryo-EM: A Unique Tool for the Visualization of Macromolecular Complexity. Mol Cell *58*, 677-689.

Nogales, E., Wolf, S.G., and Downing, K.H. (1998). Structure of the alpha beta tubulin dimer by electron crystallography. Nature *391*, 199-203.

Pecqueur, L., Duellberg, C., Dreier, B., Jiang, Q., Wang, C., Pluckthun, A., Surrey, T., Gigant, B., and Knossow, M. (2012). A designed ankyrin repeat protein selected to bind to tubulin caps the microtubule plus end. Proc Natl Acad Sci U S A *109*, 12011-12016.

Perez, F., Diamantopoulos, G.S., Stalder, R., and Kreis, T.E. (1999). CLIP-170 highlights growing microtubule ends in vivo. Cell *96*, 517-527.

Peris, L., Thery, M., Faure, J., Saoudi, Y., Lafanechere, L., Chilton, J.K., Gordon-Weeks, P., Galjart, N., Bornens, M., Wordeman, L., *et al.* (2006). Tubulin tyrosination is a major factor affecting the recruitment of CAP-Gly proteins at microtubule plus ends. J Cell Biol *174*, 839-849.

Podolski, M., Mahamdeh, M., and Howard, J. (2014). Stu2, the budding yeast XMAP215/Dis1 homolog, promotes assembly of yeast microtubules by increasing growth rate and decreasing catastrophe frequency. J Biol Chem *289*, 28087-28093.

Prota, A.E., Bargsten, K., Zurwerra, D., Field, J.J., Diaz, J.F., Altmann, K.H., and Steinmetz, M.O. (2013). Molecular mechanism of action of microtubule-stabilizing anticancer agents. Science *339*, 587-590.

Ravelli, R.B., Gigant, B., Curmi, P.A., Jourdain, I., Lachkar, S., Sobel, A., and Knossow, M. (2004). Insight into tubulin regulation from a complex with colchicine and a stathmin-like domain. Nature *428*, 198-202.

Rizk, R.S., Discipio, K.A., Proudfoot, K.G., and Gupta, M.L., Jr. (2014). The kinesin-8 Kip3 scales anaphase spindle length by suppression of midzone microtubule polymerization. J Cell Biol *204*, 965-975.

Roberts, A.J., Goodman, B.S., and Reck-Peterson, S.L. (2014). Reconstitution of dynein transport to the microtubule plus end by kinesin. eLife *3*, e02641.

Rogers, S.L., Rogers, G.C., Sharp, D.J., and Vale, R.D. (2002). Drosophila EB1 is important for proper assembly, dynamics, and positioning of the mitotic spindle. J Cell Biol *158*, 873-884.

Roostalu, J., and Surrey, T. (2017). Microtubule nucleation: beyond the template. Nat Rev Mol Cell Biol *18*, 702-710.

Sardar, H.S., Luczak, V.G., Lopez, M.M., Lister, B.C., and Gilbert, S.P. (2010). Mitotic kinesin CENP-E promotes microtubule plus-end elongation. Curr Biol *20*, 1648-1653.

Severin, F., Habermann, B., Huffaker, T., and Hyman, T. (2001). Stu2 Promotes Mitotic Spindle Elongation in Anaphase. The Journal of Cell Biology *153*, 435-442.

Sheeman, B., Carvalho, P., Sagot, I., Geiser, J., Kho, D., Hoyt, M.A., and Pellman, D. (2003). Determinants of S. cerevisiae dynein localization and activation: implications for the mechanism of spindle positioning. Curr Biol *13*, 364-372.

Slep, K.C., Rogers, S.L., Elliott, S.L., Ohkura, H., Kolodziej, P.A., and Vale, R.D. (2005). Structural determinants for EB1-mediated recruitment of APC and spectraplakins to the microtubule plus end. J Cell Biol *168*, 587-598.

Slep, K.C., and Vale, R.D. (2007). Structural basis of microtubule plus end tracking by XMAP215, CLIP-170, and EB1. Mol Cell *27*, 976-991.

Steinmetz, M.O., and Akhmanova, A. (2008). Capturing protein tails by CAP-Gly domains. Trends Biochem Sci *33*, 535-545.

Steinmetz, M.O., and Prota, A.E. (2018). Microtubule-Targeting Agents: Strategies To Hijack the Cytoskeleton. Trends in cell biology.

Stumpff, J., Du, Y., English, C.A., Maliga, Z., Wagenbach, M., Asbury, C.L., Wordeman, L., and Ohi, R. (2011). A tethering mechanism controls the processivity and kinetochore-microtubule plus-end enrichment of the kinesin-8 Kif18A. Mol Cell *43*, 764-775.

Stumpff, J., von Dassow, G., Wagenbach, M., Asbury, C., and Wordeman, L. (2008). The kinesin-8 motor Kif18A suppresses kinetochore movements to control mitotic chromosome alignment. Dev Cell *14*, 252-262.

Su, X., Arellano-Santoyo, H., Portran, D., Gaillard, J., Vantard, M., Thery, M., and Pellman, D. (2013). Microtubule-sliding activity of a kinesin-8 promotes spindle assembly and spindle-length control. Nat Cell Biol *15*, 948-957.

Su, X., Qiu, W., Gupta, M.L., Jr., Pereira-Leal, J.B., Reck-Peterson, S.L., and Pellman, D. (2011). Mechanisms underlying the dual-mode regulation of microtubule dynamics by Kip3/kinesin-8. Mol Cell *43*, 751-763.

Tanaka, N., Meng, W., Nagae, S., and Takeichi, M. (2012). Nezha/CAMSAP3 and CAMSAP2 cooperate in epithelial-specific organization of noncentrosomal microtubules. Proc Natl Acad Sci U S A *109*, 20029-20034.

Tirnauer, J.S., O'Toole, E., Berrueta, L., Bierer, B.E., and Pellman, D. (1999). Yeast Bim1p promotes the G1-specific dynamics of microtubules. J Cell Biol *145*, 993-1007.

Tortosa, E., Kapitein, L.C., and Hoogenraad, C.C. (2016). Microtubule Organization and Microtubule-Associated Proteins (MAPs). In Dendrites, pp. 31-75.

Tran, P.T., Walker, R.A., and Salmon, E.D. (1997). A metastable intermediate state of microtubule dynamic instability that differs significantly between plus and minus ends. J Cell Biol *138*, 105-117.

Trueheart, J., Boeke, J.D., and Fink, G.R. (1987). Two genes required for cell fusion during yeast conjugation: evidence for a pheromone-induced surface protein. Molecular and cellular biology *7*, 2316-2328.

Tulu, U.S., Fagerstrom, C., Ferenz, N.P., and Wadsworth, P. (2006). Molecular requirements for kinetochore-associated microtubule formation in mammalian cells. Curr Biol *16*, 536-541.

Varga, V., Leduc, C., Bormuth, V., Diez, S., and Howard, J. (2009). Kinesin-8 motors act cooperatively to mediate length-dependent microtubule depolymerization. Cell *138*, 1174-1183.

Veigel, C., and Schmidt, C.F. (2011). Moving into the cell: single-molecule studies of molecular motors in complex environments. Nat Rev Mol Cell Biol *12*, 163-176.

Verhey, K.J., and Hammond, J.W. (2009). Traffic control: regulation of kinesin motors. Nat Rev Mol Cell Biol *10*, 765-777.

Walker, J.E., Saraste, M., Runswick, M.J., and Gay, N.J. (1982). Distantly related sequences in the alpha- and beta-subunits of ATP synthase, myosin, kinases and other ATP-requiring enzymes and a common nucleotide binding fold. Embo j *1*, 945-951.

Wang, D., Nitta, R., Morikawa, M., Yajima, H., Inoue, S., Shigematsu, H., Kikkawa, M., and Hirokawa, N. (2016). Motility and microtubule depolymerization mechanisms of the Kinesin-8 motor, KIF19A. eLife *5*.

Wang, P.J., and Huffaker, T.C. (1997). Stu2p: A microtubule-binding protein that is an essential component of the yeast spindle pole body. J Cell Biol *139*, 1271-1280.

Wang, W., Cantos-Fernandes, S., Lv, Y., Kuerban, H., Ahmad, S., Wang, C., and Gigant, B. (2017). Insight into microtubule disassembly by kinesin-13s from the structure of Kif2C bound to tubulin. Nat Commun *8*, 70.

Wang, W., Cao, L., Wang, C., Gigant, B., and Knossow, M. (2015). Kinesin, 30 years later: Recent insights from structural studies. Protein Sci *24*, 1047-1056.

Wang, Y., and Mandelkow, E. (2016). Tau in physiology and pathology. Nat Rev Neurosci *17*, 5-21.

Weaver, L.N., Ems-McClung, S.C., Stout, J.R., LeBlanc, C., Shaw, S.L., Gardner, M.K., and Walczak, C.E. (2011). Kif18A uses a microtubule binding site in the tail for plus-end localization and spindle length regulation. Curr Biol *21*, 1500-1506.

Weisbrich, A., Honnappa, S., Jaussi, R., Okhrimenko, O., Frey, D., Jelesarov, I., Akhmanova, A., and Steinmetz, M.O. (2007). Structure-function relationship of CAP-Gly domains. Nat Struct Mol Biol *14*, 959-967.

Welburn, J.P. (2013). The molecular basis for kinesin functional specificity during mitosis. Cytoskeleton (Hoboken, N.J.) *70*, 476-493.

Wells, W.A. (2005). The discovery of tubulin. The Journal of Cell Biology *169*, 552-552.

Winder, S.J., and Ayscough, K.R. (2005). Actin-binding proteins. Journal of cell science *118*, 651-654.

Wolyniak, M.J., Blake-Hodek, K., Kosco, K., Hwang, E., You, L., and Huffaker, T.C. (2006). The regulation of microtubule dynamics in Saccharomyces cerevisiae by three interacting plus-end tracking proteins. Molecular biology of the cell *17*, 2789-2798.

Wood, K.W., Sakowicz, R., Goldstein, L.S., and Cleveland, D.W. (1997). CENP-E is a plus end-directed kinetochore motor required for metaphase chromosome alignment. Cell *91*, 357-366.

Woodruff, J.B., Ferreira Gomes, B., Widlund, P.O., Mahamid, J., Honigmann, A., and Hyman, A.A. (2017). The Centrosome Is a Selective Condensate that Nucleates Microtubules by Concentrating Tubulin. Cell *169*, 1066-1077.e1010.

Yin, H., Pruyne, D., Huffaker, T.C., and Bretscher, A. (2000). Myosin V orientates the mitotic spindle in yeast. Nature *406*, 1013-1015.

Zampieri, F., Coen, M., and Gabbiani, G. (2014). The prehistory of the cytoskeleton concept. Cytoskeleton (Hoboken, N.J.) *71*, 464-471.

Zhang, C., Zhu, C., Chen, H., Li, L., Guo, L., Jiang, W., and Lu, S.H. (2010). Kif18A is involved in human breast carcinogenesis. Carcinogenesis *31*, 1676-1684.

Zhang, R., Alushin, G.M., Brown, A., and Nogales, E. (2015). Mechanistic Origin of Microtubule Dynamic Instability and Its Modulation by EB Proteins. Cell *162*, 849-859.

Zhang, R., LaFrance, B., and Nogales, E. (2018). Separating the effects of nucleotide and EB binding on microtubule structure. Proceedings of the National Academy of Sciences *115*, E6191-E6200.

Zimniak, T., Stengl, K., Mechtler, K., and Westermann, S. (2009). Phosphoregulation of the budding yeast EB1 homologue Bim1p by Aurora/Ipl1p. J Cell Biol *186*, 379-391.

9. Acknowledgements

It is impossible to mention all the people who supported me during my Ph.D. research. Nevertheless, I would like to emphasize the contribution of various persons.

Foremost, I would like to thank my supervisor Prof. Dr. Michel Steinmetz for the opportunity to perform my Ph.D. thesis in his laboratory. I genuinely enjoyed working in your laboratory on the various projects. Furthermore, I am very glad to learn from you so much about science and how to improve as a scientist. I also liked the freedom very much to develop a project such as the Kip3 project. Overall, it was a fantastic time in your laboratory, and I was fond of the group activity like the hikes as well.

Then, I am very grateful to the two further members of my Ph.D. committee Prof. Dr. Timm Maier and Prof. Dr. Jean Pieters. I liked the Ph.D. committee meetings very much and the valuable suggestions that you provided.

As next, I would like to thank Prof. Dr. Yves Barral (ETH Zürich), Prof. Anna Akhmanova, Prof. Carolyn Moores and their respective group members for the great collaborations on the various projects. It was a wonderful time to collaborate with you.

From the Steinmetz group, I would like to thank all current and former members for the amazing work atmosphere in the group. I am especially thankful to Anil, Ashwani, Gregory and Natacha for the amazing time in the laboratory and also outside of it. Besides, they taught me a lot about protein expression and other methods. Additionally, I would like to thank Andrea very much for teaching me protein crystallography and for a great time with you. I am also very thankful to the Sun, Tobias, Wouter, Sandro and Shoib for the very good time together in the group.

Furthermore, I am very grateful to the Xiuzhen Cheng and Lukas Wiedmer for the excellent collaboration in the TubeX project. I enjoyed our meetings and to work with you very much. In addition, I would like to thank all other members of the TubeX project like Prof. Dr. Jörg Stelling and Dr.Ana Maria Farcas for this fantastic project.

It was a great idea of Prof. Dr. Jan Pieter Abrahams to create the LYRN. I enjoyed a lot to organize all the different events with the LYRN members. Especially, I am thankful to Fabian, Thomas, Irene, Elisabeth and Valtteri for the very good time.

I am very grateful to all members of the LBR for a perfect time at PSI.

Finally, I would like to thank my parents very much for all their support during my Ph.D. Thesis. I am also most thankful to the support of my love Anna.

Curriculum Vitae

Kontaktinformationen:

Name: Marcel Stangier
Adresse: Spinnereistr. 12a, CH-5210 Windisch
E-Mail: Marcel.Stangier@psi.ch
Telefon: 0041 76 451 17 41
Geburtsdatum: 06.08.1988
Staatsbürgerschaft: Deutsch

Ausbildung:

Seit Januar 2015 Promotion in der Biochemie am Paul-Scherrer-Institut (ETH-Bereich) und der Universität Basel

2011-2013 TU München Master of Science in Biochemie mit den Schwerpunkten NMR-Spektroskopie, Strukturbiologie und Biophysik mit Auszeichnung (1,2)

2008-2011 TU München Bachelor of Science in Biochemie mit Auszeichnung (1,4)

1999-2008 Besuch der Kurt-Schumacher-Schule Karben, Abitur (1,0)

Praktika- und Arbeitserfahrung:

Seit Januar 2015 wissenschaftlicher Mitarbeiter am Paul-Scherrer-Institut (ETH-Bereich)

- Forschungsprojekte im Bereich der +TIPs Bik1, Kip2 und Kip3, sowie des -TIPs CAMSAP
- Fokus auf die Proteinkristallographie, biochemische und biophysikalische Methoden
- Kooperationen mit Forschungsgruppen in Oxford, London, Utrecht und München
- Erste Publikation in Nature Structural and Molecular Biology, weitere in Vorbereitung
- Mitarbeit im TubeX SystemX.ch Projekt (führende Systembiologieinitiative der Schweiz)

Januar-März 2014 Praktikum bei Booz & Company (nun Strategy&) in Frankfurt am Main

Oktober-Dezember 2013 Visiting Associate bei der Stratley AG, Köln

März-September 2013 Masterarbeit in der Gruppe von Prof. Sattler Untersuchung der Interaktion des Hetereodimers des Splicing Factors U2AF bestehend aus U2AF65 und U2AF35 und der RS-Domäne der Untereinheit U2AF65 mittels NMR-Spektroskopie

Februar-März 2013 Forschungspraktikum in der Gruppe von Prof. Eppinger an der KAUST (Saudi-Arabien) über die Charakterisierung neuer Metalloproteine aus der Tiefsee mittels bioinformatischer Methoden

September-Oktober 2012 Forschungsaufenthalt an der Harvard Medical School in der Gruppe von Prof. Wagner über den Einsatz von Nanodiscs zur Untersuchung von Membranproteinen mittels NMR-Spektroskopie

Mai-Juli 2012 Forschungspraktikum in der Gruppe von Prof. Reif am Helmholtz-Zentrum München und der TU München Untersuchung im Bereich der Alzheimerforschung über die Interaktion eines Moleküls mit Aß40

TU München:

März-April 2012 Forschungspraktikum in der Gruppe Prof. Sattler Untersuchung der Interaktion der phosphorylierten NTD des Splicing Factor 1 mit dem Protein U2AF65 mittels NMR-Spektroskopie

September-Oktober 2011 Forschungspraktikum in der Gruppe von Prof. Kiefhaber
Untersuchung der Faltung von α-Helices in Peptiden mittels Ultrakurzeitspektroskopie (TTET)

April-Juni 2011 Bachelorthesis in der Gruppe von Prof. Buchner über den Einfluss von C-terminaler posttranslationaler Modifikationen auf das Tumorsuppressorprotein p53 und die Interaktion von p53 mit Hsp90

August-September 2010 Forschungspraktikum in der Gruppe von Prof. Sattler
Untersuchung eines epigenetisch relevanten Proteins mittels NMR-Spektroskopie

2010-2012 Tutor für organische Chemie an der TU München

2006-2008 Life-Science Lab des Deutschen Krebsforschungszentrum in Heidelberg (DKFZ)

Oktober 2006 Praktikum in der R&D Abteilung im Bereich Dispersionsfarben bei der Celanese AG in Frankfurt Höchst

Stipendien und Sonstiges:

2012-2013 Deutschlandstipendium gefördert durch die Clariant AG

2012-2013 E-Fellow Stipendium

2012 Endrunde der Ideenphase des Science4Life Businessplan-Wettbewerbs

Engagement:

Mitarbeit bei der Organisation und Durchführung von Informationstagen am Paul-Scherrer-Institut, um Schülerinnen und Schülern aus der Schweiz praxisnahe Forschung zu zeigen

Seit 2015 Mitarbeit im LYRN (beispielsweise Organisation eines mehrtätigen Workshops zu einem wissenschaftlichen Thema oder von Vorträgen und Diskussionsrunden)

Seit 2009 Alumniverein des Heidelberger Life-Science Labs, u.a. Mitarbeit in dem Auswahlkomitee des Heidelberger Life-Science Lab

Sprachkenntnisse:

Deutsch (Muttersprache), Englisch (fließend), Latinum

Interessen:

Reisen, Fotografie, Fitness, Ski fahren